

**MATERIALS AND PROCESSES IN THE FABRICATION OF  
PARTICULATE-FREE AND PARTICULATE-BASED  
SCREEN-PRINTED METAL AND METAL OXIDE FILMS  
FOR ELECTRONIC APPLICATIONS**

Thesis

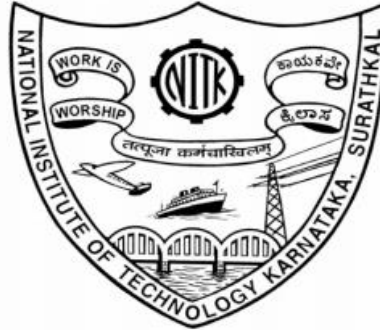
Submitted in partial fulfilment of the requirements for the degree of

**DOCTOR OF PHILOSOPHY**

By

MANJUNATH G

(165019MT16F03)



**DEPARTMENT OF METALLURGICAL AND MATERIALS  
ENGINEERING**

**NATIONAL INSTITUTE OF TECHNOLOGY KARNATAKA  
SURATHKAL, MANGALURU – 575025**

**JUNE 2021**

**MATERIALS AND PROCESSES IN THE FABRICATION OF  
PARTICULATE-FREE AND PARTICULATE-BASED  
SCREEN-PRINTED METAL AND METAL OXIDE FILMS  
FOR ELECTRONIC APPLICATIONS**

Thesis

Submitted in partial fulfilment of the requirements for the degree of

**DOCTOR OF PHILOSOPHY**

**By**

MANJUNATH G

(165019MT16F03)

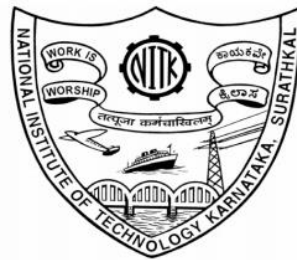
**Under the guidance of**

**Dr. Saumen Mandal**

Assistant Professor

Dept. of Metallurgical and Materials Engineering

NITK Surathkal



**DEPARTMENT OF METALLURGICAL AND MATERIALS  
ENGINEERING**

**NATIONAL INSTITUTE OF TECHNOLOGY KARNATAKA  
SURATHKAL, MANGALURU – 575025**



## DECLARATION

I hereby *declare* that the Research Thesis entitled “**MATERIALS AND PROCESSES IN THE FABRICATION OF PARTICULATE-FREE AND PARTICULATE-BASED SCREEN-PRINTED METAL AND METAL OXIDE FILMS FOR ELECTRONIC APPLICATIONS**” which is being submitted to the National Institute of Technology Karnataka, Surathkal in partial fulfillment of the requirements for the award of the Degree of **Doctor of Philosophy** in the Department of **Metallurgical and Materials Engineering**, is a *bonafide report of the research work carried out by me*. The material contained in this Research Thesis has not been submitted to any University or Institution for the award of any degree.



Place: NITK, Surathkal  
Date: 30-06-2021

Name: MANJUNATH G  
Register Number: 165019MT16F03

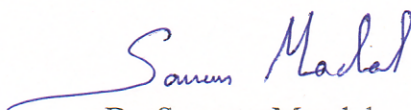
Department of Metallurgical and  
Materials Engineering



## CERTIFICATE

This is to certify that the Research Synopsis entitled “**MATERIALS AND PROCESSES IN THE FABRICATION OF PARTICULATE-FREE AND PARTICULATE-BASED SCREEN-PRINTED METAL AND METAL OXIDE FILMS FOR ELECTRONIC APPLICATIONS**” submitted by Mr. Manjunath G (Register Number: 165019MT16F03) as the record of the research work carried out by him, is *accepted as the Research Thesis submission* in partial fulfillment of the requirements for the award of degree of Doctor of Philosophy.

Research supervisor



Dr. Saumen Mandal

Assistant Professor

Department of Metallurgical and Materials Engineering

NITK Surathkal



Chairman- DRPC

Chairman - DRPC  
Dept. of Metallurgical and Materials Engineering  
National Institute of Technology Karnataka, Surathkal  
Post Srinivasnagar, Mangaluru - 575 025  
Karnataka, India

**DEDICATED TO  
THE ALMIGHTY GOD.....**





## **ACKNOWLEDGEMENTS**

I express my sincere thanks to the almighty whose divine intervention was instrumental in the proceedings of this work. I express my sincere gratitude to my parents and family for their constant and encouraging support throughout my doctoral study.

My sincere graceful acknowledgement to my research supervisor Dr. Saumen Mandal, Assistant Professor, Department of Metallurgical and Materials Engineering, National Institute of Technology Karnataka Surathkal for their valuable guidance, support and help throughout the research. It has been an honor to be his Ph.D. student. I heartily thank him for his kindness, valuable suggestions, and constant encouragement, which I received during tough times in the Ph.D. pursuit. His constant guidance, cooperation and moral support has always kept me going ahead. The research work presented here would have been impossible without support and guidance of my supervisor. I would also like to thank his family members for their relentless love, care, and support they showered on me as part of their family.

My sincere graceful acknowledgement to our research collaborator Dr. Nagraju P Nanosensor Research Laboratory, CMR Technical Campus, Hyderabad for his valuable inputs, laboratory facility, and support throughout the research.

I would like to thank Prof. K Narayan Prabhu, Head of the Department, Metallurgical and Materials Engineering, National Institute of Technology Karnataka Surathkal for the constant encouragement and support. I would like take this opportunity to thank members of my research programme assessment committee (RPAC), Dr. Jagannath Nayak Dept. of Metallurgical and Materials Engineering and Dr. Dr.Hari Prasad Dasari, Dept. of Chemical Engineering, National Institute of Technology Karnataka Surathkal for their valuable suggestions and the comments during the progress and pre-synopsis seminars.

I am obliged to Ministry of Human Resource Development (MHRD), New Delhi, and NITK for their financial assistance to conduct my research work in the form of contingency and for the research fellowship. I also express my sincere thanks to all

research colleagues of both NITK Surathkal and CENSE IISc Bangalore, for their constant help and support and fruitful discussions on concepts.

I express deep and sincere thanks to Dr. Pavan Pujar, Mr. Komal Krishna, Ms. Ashritha Salian, Mr. Robbi Vivek Vardhan, Mr. Praveen Lakkmishetti, Mr. Bikesh Gupta, Mr. Dr. Ritesh Kumar, Mr. Anjan, Mr. Kumar Karthik, Mr. Gajanan Naik, Mr. Maruthi Prasad and Mr. Sandeep Kumar C for their constant support throughout my research work.

I am thankful to all teaching and non-teaching staff of the Dept. of Metallurgical and Materials Engineering, National Institute of Technology Karnataka Surathkal for constant support and help in various aspects of my course. Special thanks to Mrs. Sharmila Dinesh for helping me in necessary documentation at various stages of Ph.D.

The dissertation must surely bear the imprint of the prayers, sacrifices made, love, and affection showered on me by my family members. A very special thanks to my father Late. K. Gangaiah, and my mother Mrs. Susheela, who supported me throughout my life and during this study. I am grateful to my parents, friends and relatives for their care and love.

Finally, I thank all my friends, well-wishers, and anonymous souls for their love and regards, prayers and wishes, that directly and indirectly helped me for completing this research work.

MANJUNATH G

## Abstract

In the present study, approaches towards the processing of screen-printed metal and metal oxide films for the optoelectronic and gas sensing applications are elaborated. Phase pure, highly reactive, nanocrystalline functional materials namely conducting (Ag and Ag-Cu) and semiconducting ( $\text{CaVO}_3$ , pristine and doped ZnO) particles of nano to sub-micro size, which are decent for the formulation screen printing inks are obtained using polyol and facile solution combustion synthesis route respectively. A novel aqueous based combustible particle-free silver and ZnO screen printing inks possess the desirable thixotropic and shear thinning properties for the screen printing, are formulated by using eco-friendly binder Na-CMC and solvent water. The conventional particle based pristine and Sr-doped ZnO screen printing inks are comprised of 60 wt % of functional materials (ZnO/Sr-doped ZnO) and remaining organic vehicle made of Na-CMC and water. Crystalline silver films are processed by depositing particle free silver screen printing inks followed by annealing at 200 °C, displays electrical conductivities in the range of  $2\text{-}8 \times 10^6 \text{ Sm}^{-1}$ . High conductive films with minimal thickness (3  $\mu\text{m}$ ) and high dimensional accuracy used as electrode for TFTs exhibit a  $\mu_{\text{sat}}$ ,  $I_{\text{on}}/I_{\text{off}}$ , and  $V_{\text{th}}$  of  $0.88 \text{ cm}^2 \text{ V}^{-1}\text{s}^{-1}$ ,  $10^2$ , and  $\sim 0.3 \text{ V}$ , respectively. High crystalline screen printed ZnO sensor processed at 500 °C from aqueous particle free-ZnO inks showed significantly high gas response ( $S = 336$ ) and selectivity towards 5 ppm of  $\text{NH}_3$  under ambient conditions. Porous, well-adhered particle-based screen printed ZnO sensors processed from glycine fuel system exhibited good gas sensitivity towards  $\text{NH}_3$ ,  $\text{C}_2\text{H}_5\text{OH}$ ,  $\text{Cl}_2$ . Sr-doped ZnO sensor with smaller crystallite size and lesser lattice distortion exhibited highest gas response 70 towards the 50 ppm of  $\text{NH}_3$  gas at room temperature and also high selectivity to ammonia against various gases such as xylene, acetone and toluene. Upon  $\text{RuO}_2$  activation,  $\text{NH}_3$  response of  $\text{RuO}_2/\text{Sr-doped ZnO}$  heterostructure sensor was diminished to  $\sim 2$ . La-doped  $\text{BaSnO}_3$  sensor exhibited superior gas response upon exposure of both the  $\text{NH}_3$  and  $\text{HCHO}$  gases than the  $\text{BaSnO}_3$ , ceria and ruthenate sensitized La-doped  $\text{BaSnO}_3$  sensors.

**Keywords:** *Screen printing, solution combustion, Ag, Ag-Cu alloy,  $\text{CaVO}_3$ , ZnO, gas sensors, TFTs.*



<b>CHAPTER 1</b> .....	<b>1</b>
<b>INTRODUCTION</b> .....	<b>1</b>
<b>CHAPTER 2</b> .....	<b>5</b>
<b>LITERATURE REVIEW</b> .....	<b>5</b>
2.1 Printing technology .....	5
2.2 Screen printing .....	9
2.3 Formulation of screen-printing inks .....	11
2.4 Rheological properties of screen-printable ink .....	14
2.5 Synthesis of functional materials .....	19
2.5.1 Polyol method.....	19
2.5.2 Solution combustion method .....	29
2.6 Semiconducting metal oxide for gas sensing applications.....	32
2.6.1 Undoped metal oxide.....	32
2.6.2 Doped metal oxide.....	40
2.6.2.1 Gas sensing mechanism of doped semiconducting metal oxides.....	43
2.6.3 Heterostructure metal oxides .....	48
2.6.3.1 Mechanisms to improve gas sensing performance of heterostructure metal oxides.....	48
2.7 Reported screen-printed metal and metal oxide films.....	53
2.7.1 Screen-printed Ag films and their applications.....	53
2.7.2 Screen printed semiconducting thick films for gas sensing applications .....	55
2.8 Scope and objectives of the research work .....	57
2.8.1 Scope .....	57
2.8.2 Objectives .....	58
<b>CHAPTER 3</b> .....	<b>59</b>
<b>SYNTHESIS OF METAL, METAL ALLOY, METAL - OXIDE AND DOPED METAL-OXIDE FUNCTIONAL MATERIAL FOR THE FORMULATION OF SCREEN-PRINTING INKS</b> .....	<b>59</b>
3.1 Introduction .....	59
3.2 Experimental procedure .....	59
3.2.1 Materials .....	59
3.2.2 Synthesis of silver (Ag) and silver-copper (Ag-Cu) alloy nanoparticles .....	60

3.2.2 Synthesis of calcium vanadium oxide (CaVO <sub>3</sub> ).....	61
3.2.3 Synthesis of pristine and strontium (Sr) doped zinc oxide (ZnO).....	61
3.2.3.1 ZnO particles using three fuels .....	61
3.2.3.2 Sr-doped ZnO particles using fuel-glycine.....	62
3.2.4 Measurement and characterization .....	62
3.3 Results and discussion .....	66
3.3.1 Characterization of synthesized silver (Ag) and silver-copper (Ag-Cu) alloy nanoparticles.....	66
3.3.2 Characterization of calcium vanadium oxide (CaVO <sub>3</sub> ).....	78
3.3.3 Characterization of undoped and strontium doped zinc oxide particles .....	86
3.3.3.1 ZnO particles using three fuels.....	86
3.3.3.2 Sr-doped ZnO particles using fuel-glycine.....	91
3.4 Conclusions.....	91
<b>CHAPTER 4.....</b>	<b>93</b>
<b>FORMULATION OF PARTICLE-FREE AND PARTICLE BASED SCREEN PRINTING INKS .....</b>	<b>93</b>
4.1 Introduction.....	93
4.2. Experimental procedure .....	93
4.2.1 Materials.....	93
4.2.2 Formulation of particle-free screen-printing inks .....	94
4.2.2.1 Formulation of particle free silver screen printing inks.....	94
4.2.2.2 Formulation of particle free ZnO screen printing inks.....	94
4.2.3 Formulation of particle-based screen-printing inks .....	95
4.2.3.1 Particle-based pristine and Sr-doped ZnO screen printing inks.....	95
4.2.3.2 Particle-based pristine and La-doped BaSnO <sub>3</sub> screen printing inks.....	95
4.2.4 Characterization .....	95
4.3 Results and Discussion .....	96
4.3.1 Particle-free screen-printing inks .....	96
4.3.1.1 Particle-free silver screen printing inks.....	96
4.3.1.2 Particle-free ZnO screen printing inks.....	102
4.3.2 Particle-based metal oxide screen-printing inks.....	104
4.3.2.1 Pristine and Sr-doped ZnO screen printing inks.....	104

4.3.2.2 Pristine and La-doped BaSnO <sub>3</sub> screen printing inks.....	105
4.4 Conclusions .....	106
<b>CHAPTER 5 .....</b>	<b>109</b>
<b>SCREEN PRINTED FILMS OF METAL, PRISTINE AND DOPED METAL OXIDE – THEIR APPLICATIONS .....</b>	<b>109</b>
5.1. Introduction .....	109
5.2. Experimental Procedure .....	109
5.2.1 Fabrication of screen-printed silver patterns as bottom gate electrode in TFTs .	109
5.2.2 Fabrication of ZnO based screen printed films - gas sensing applications .....	110
5.2.3 Fabrication of BaSnO <sub>3</sub> based screen printed films - gas sensing applications....	110
5.2.3 Measurements and characterization.....	110
5.3. Results and Discussion.....	113
5.3.1 Characterization of Ag screen printed films and its applications.....	113
5.3.2 Combustion derived ZnO based screen printed films – A UV and Gas Sensor..	119
5.3.2.1 Undoped particle-free screen printed ZnO films.....	119
5.3.2.2 Undoped particle-based screen printed ZnO films.....	130
5.3.2.3 Pristine, Sr-doped ZnO and RuO <sub>2</sub> activated Sr doped ZnO screen printed films.....	140
5.3.3 Screen printed pristine and La-doped BaSnO <sub>3</sub> films – gas sensing applications	152
5.4 Conclusions .....	166
<b>CHAPTER 6.....</b>	<b>169</b>
<b>CONCLUSIONS .....</b>	<b>169</b>
<b>APPENDIX .....</b>	<b>171</b>
<b>REFERENCES.....</b>	<b>179</b>
<b>LIST OF PUBLICATIONS AND CONFERENCES .....</b>	<b>209</b>
<b>BIO DATA.....</b>	<b>211</b>





## NOMENCLATURE

$\mu_{\text{sat}}$	:	Saturated mobility
$\delta$	:	Phase angle
$e^-$	:	Electrons
$\Delta G_v$	:	Free energy due to new volume formation
$h^+$	:	Holes
$\gamma$	:	Surface free energy
$\gamma_o$	:	Maximum strain
$\tau_o$	:	Applied stress
Al	:	Aluminium
$\text{Al}_2\text{O}_3$	:	Aluminum Oxide
Ag	:	Silver
Ag-Cu	:	Silver-Copper
$\text{AgNO}_3$	:	Silver nitrate
Au	:	Gold
$\text{BaSnO}_3$	:	Barium stannate
BMNPs	:	Bimetallic Nanoparticles
$\text{CaVO}_3$	:	Calcium Vanadium oxide
$\text{CeO}_2$	:	Cerium Oxide
$\text{C}_6\text{H}_8\text{O}_6$	:	Ascorbic acid
Co	:	Cobalt
$\text{Co}_3\text{O}_4$	:	Cobalt Oxide
CO	:	Carbon monoxide
$\text{CO}_2$	:	Carbon dioxide
Cu	:	Copper
$\text{Cu}_2(\text{OAc})_4$	:	Copper (II) Acetate
CuO	:	Copper Oxide
DSC	:	Differential Scanning Calorimetry

EG	:	Ethylene glycol
F/O	:	Fuel to Oxidizers ratio
Fe <sub>2</sub> O <sub>3</sub>	:	Iron (III) Oxide
FTIR	:	Fourier-Transform InfraRed
G'	:	Elastic/storage modulus
G''	:	Viscous/loss modulus
G*	:	complex modulus
H <sub>2</sub>	:	Hydrogen gas
HCHO	:	Formaldehyde
HCl	:	Hydrochloric acid
HAuCl <sub>4</sub>	:	Chloroauric acid
H <sub>2</sub> S	:	Hydrogen sulfide
ICs	:	Integrated Circuits
In <sub>2</sub> O <sub>3</sub>	:	Indium Oxide
ITO	:	Indium Tin Oxide
I <sub>on</sub> :I <sub>off</sub>	:	On:off ratio
KBr	:	potassium bromide
LVR	:	Linear Viscoelastic Region
LOD	:	Limit of detection
LPG	:	Liquefied petroleum gas
LTCC	:	Low temperature co-fired ceramics
NiO	:	Nickel Oxide
NiScSZ	:	Nickel-scandium stabilized zirconia
NaBH <sub>4</sub>	:	Sodium borohydride
NaBr	:	Sodium Bromide
NaCl	:	Sodium chloride
Na <sub>3</sub> C <sub>6</sub> H <sub>5</sub> O <sub>7</sub>	:	Trisodium citrate
NaH <sub>2</sub> PO <sub>2</sub> .H <sub>2</sub> O	:	Sodium phosphinate
N <sub>2</sub> H <sub>4</sub>	:	Hydrazine

NaOH	:	Sodium hydroxide
Na <sub>2</sub> S	:	Sodium sulfide
NPs	:	Nanoparticles
PDDA	:	Poly(diallyldimethylammonium) chloride
PEG	:	Polyethylene glycol
PET	:	Polyethylene terephthalate
PI	:	Polyimide and PET
Pd	:	Palladium
Pt	:	Platinum
PVA	:	Polyvinyl alcohol
PVP	:	Polyvinylpyrrolidone
r <sup>*</sup>	:	Critical nuclei size
R <sub>a</sub>	:	Resistance in air
R <sub>g</sub>	:	Resistance in the presence of analyte gas
RuO <sub>2</sub>	:	Ruthenium Oxide
Sc <sub>2</sub> O <sub>3</sub>	:	Scandium oxide
SCS	:	Solution Combustion Synthesis
SMO	:	Semiconducting Metal Oxide
SOFC	:	Solid-Oxide Fuel Cell
SO <sub>2</sub>	:	Sulphur dioxide
SnO <sub>2</sub>	:	Tin Oxide
Sr	:	Strontium
TA	:	Tartaric acid
TFT	:	Thin Film Transistors
TGA	:	Thermogravimetric Analysis
Ti	:	Titanium
TiO <sub>2</sub>	:	Titanium Oxide
UV	:	Ultraviolet
V <sub>o</sub>	:	Oxygen Vacancy

$V_{th}$	:	Threshold voltage
VOCs	:	Volatile Organic Compounds
$V_2O_5$	:	Vanadium (V) oxide
$WO_3$	:	Tungsten Oxide
XRD	:	X-Ray Diffraction
XPS	:	X-ray Photoelectron Spectroscopy
YSZ	:	Yttria stabilized zirconia
ZnO	:	Zinc Oxide
$ZnSnO_3$ ,	:	Zinc stannate

# CHAPTER 1

## INTRODUCTION

Nowadays, printed electronics is a prominent technology that would likely to be alternative to the conventional silicon-based electronics in innumerable applications and with huge market potential (Lupo et al. 2013). According to Nano Markets report, there are three main reasons which brief why the printable electronics is grabbing the substantial attention. Primarily, the printing process can be extended to various kinds of substrates which allows the modification of the system for fabrication of electronic devices such as material selection, design and manufacturing phases. Secondly, printing technology offers new business models, in the sense which makes provision for establishment of small-scale industries with low investment say desktop manufacturing. Further the conventional electronics is cost-effective only on the mass production scale, but printed electronics offers flexible and economical approach for the production of tailored small-volume products with large scale (Kunnari et al. 2009). The use of printing technology for manufacturing electronically active components (semiconductor layer, electrodes, diodes, dielectrics etc) in a large manner is a current development, even though printing technology has existed for several decades (Singh et al. 2006). Significant reasons behind the crawling into the printing technology in electronic industry are better economics and environmental issues. Accuracy, stability and reliability with the new functional conductive ink in the printing process made printing technology as the necessitate approach for the development of the following flexible electronic devices such a resistor, antennas, capacitors, diodes, sensors, photovoltaic cells, displays, batteries and thin-film transistors (TFTs) (Sowade et al. 2016).

The unique difference between the manufacturing of convectional and printed electronics is that printing is an additive process whereas the fabrication of electronic circuitry using lithography demands subtractive processes mainly etching and cleaning. Fig. 1.1 depicts the steps such as etching and cleaning are replaced by a one-step process comprising of depositing functional material on the suitable substrate. From the

viewpoint of environmental aspects use of corrosive chemicals for etching and cleaning leads the process is less eco-friendly; printing technology absolutely offers appreciable reduction of wastage, ensure that all the material which is involved in the fabrication ends up into the final product. On the other hand, the processes employed in fabrication of silicon-based electronics are, well-established methods with remarkable accuracy, stability and reliability. Printing methods are usually uncompetitive, in terms of aforementioned features compared to conventional silicon technologies. In an additive process, fabrication of device was enabled by adding electronic materials layer over layer and functionality is completely independent of substrate. The accomplishment of the printing on various substrates makes component at low cost, large-area and at low processing temperature compared to thermal evaporation and sputtering (Cui 2016).

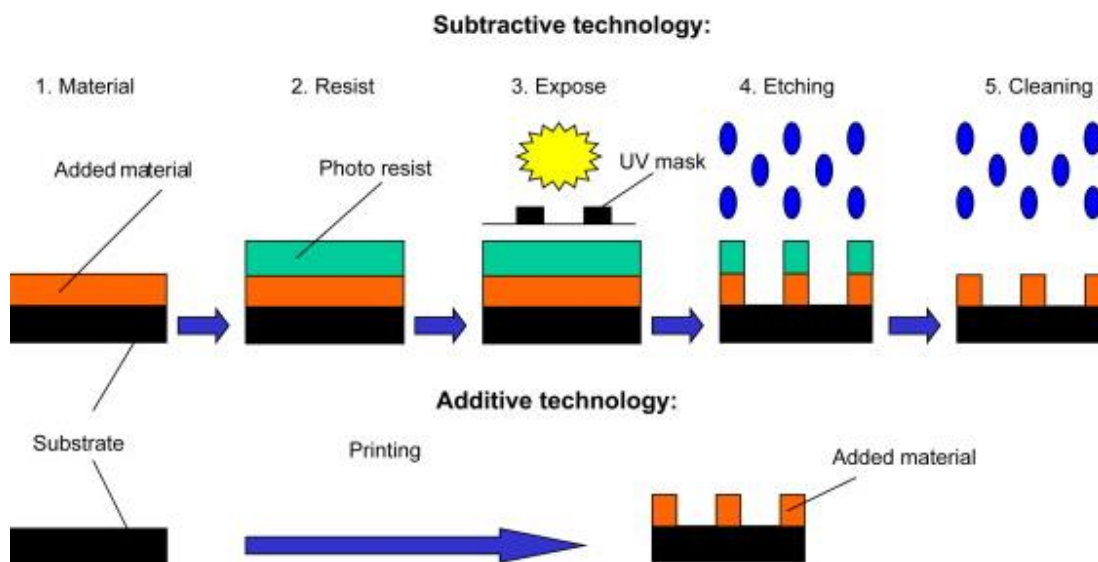


Fig. 1.1 Difference between subtractive and additive manufacturing technologies (Kunnari et al. 2009)

One of the advantages of printed electronics over the conventional electronics is the prospect of low-cost devices. In general, there are two major ways to minimize the cost of electronics; (i) by increasing the packaging efficiency of the IC's which is defined by ratio of all devices on system-level board compared to the area of the board and (ii) increasing the cost effectiveness by working on larger but cheaper substrates. Except additive process, no other techniques can be employed to achieve large area

patterning on inexpensive substrates like plastic, ceramics, laminates, and metals. Using the printing techniques like gravure, screen, offset and ink-jet printing, high-resolution, low-cost and large area flexible electronics can be produced (Parashkov et al. 2005). The selection and adaption of the existing printing processes towards the deposition of functional layers in the fabrication of devices are still current topics of research and might have high appropriateness for the future industry of electronics manufacturing.

There are plenty of peer-reviewed studies reported on the usage of different printing techniques. Among existing printing techniques, the screen-printing technique is a cost-effective and reliable method which can be used to print on substrate of interest in large-volume without the requirement of the sophisticated printing environment, such as high vacuum, inert gas-flow, high-grade clean rooms and so on. No necessity of a sophisticated environment and large volume production make provision for the establishment of low-cost manufacturing in mass quantities. By considering these, conductive electrodes for the various devices, specifically TFTs and active layer for the gas sensors, can be printed through the screen-printing technique, thereby time and cost required can be reduced considerably compared to other printing processes (Cerdà et al. 2002; Liang et al. 2016).

**CHAPTER 2** briefs the existing literature in the area of research namely printing technique, synthesis of functional materials, formulation of screen-printing inks, printed devices etc.

**CHAPTER 3** is dedicated to the synthesis of functional materials (Ag, Ag-Cu alloy,  $\text{CaVO}_3$ , ZnO and Sr-doped ZnO) for the formulation of screen-printing inks. The experimental results confirmed that Ag and Ag-Cu alloy NPs capped with PVP of an average size of  $33 \pm 19$  and  $48 \pm 15$  nm, respectively were synthesized. Phase pure, non-stoichiometric, nanocrystalline pristine and Sr-doped ZnO particles were synthesized by the SCS route with an average particle size of 0.84 and 0.45  $\mu\text{m}$ , respectively. The properties of synthesised functional materials are suitable for the formulation of screen-printing inks.

**CHAPTER 4** is assigned to the formulation of particle-free and particle-based screen-printing inks of metal and metal oxide. The obtained results assured that the formulated

particle-free and particle-based screen-printing inks to obtain the desired films with the acceptable rheological properties, required a low annealing temperature.

**CHAPTER 5** is dedicated to the fabrication and characterisation of metal (Ag) and metal oxide (ZnO, Sr-doped ZnO, BaSnO<sub>3</sub> and La-doped BaSnO<sub>3</sub>) screen printed films and their applications. The results revealed that the high conductive silver films processed at 200 °C having electrical conductivities of the order 10<sup>4</sup> S.cm<sup>-1</sup> and minimum thickness (~ 3 μm) were used as the bottom gate electrode for TFTs, which exhibited an acceptable performance with static performance parameters, such as μ<sub>sat</sub>, I<sub>on</sub>/I<sub>off</sub>, and V<sub>th</sub> of 0.88 cm<sup>2</sup> V<sup>-1</sup> s<sup>-1</sup>, 10<sup>2</sup>, and ~ 0.3 V, respectively. Particle-free screen printed ZnO sensors processed at 500 °C showed a significantly high gas response (S = 336) and selectivity towards 5 ppm of NH<sub>3</sub> under ambient conditions. La-doped BaSnO<sub>3</sub> sensor exhibited superior gas response upon exposure of both the NH<sub>3</sub> and HCHO gases than the BaSnO<sub>3</sub> and sensitized La-doped BaSnO<sub>3</sub> sensors.



## **CHAPTER 2**

### **LITERATURE REVIEW**

The current demand in the electronic industries is concerned mainly on the reduction in the wastage of functional materials and environmental issues. Presently, subtractive technologies have been adopted for the manufacturing of electronics on costly substrates. Even though the performance of the electronics is good, but the fabrication involves using of environmental hazardous chemicals for etching, considerable wastage of functional materials and also time-consuming, makes to discern an alternative. Printed electronics may help in bypassing the above-mentioned problems which come across in subtractive technology. Printed electronics ensures that the functional materials deposited on the substrates will end up into final product and completely rule out the etching process for the development of patterns. In the forthcoming sections of this chapter dealt with the selection of facile and versatile printing technique, preparation for the fabrication of electronically active components (conducting and semiconducting layers) using the selected printing technique and its applications in various fields such as TFTs, gas sensors, etc.

#### **2.1 Printing technology**

Printing (Press) is a reproductive method which replicates the information (such as a text, graphics, pictures) by depositing the inks on the image-carrying medium (substrates). In the fifteenth century, Gutenberg's work on printing with movable lead type, triggered a revolution in multiple duplication of the same picture on the substrate from the format using ink.

Paper was used as the first printing substrate, still continues as a dominant one. During 1912, production of cellophane film (derived from regenerated cellulose) is inclined due to its transparency and barrier properties, and it is employed as a substrate for multicolour printing. Another stage in printing, plastics which are obtained from petroleum derivatives emerged as the first plastic films in the 1950s. Later, situation emerged in which the plastics played a vital role in various fields, including as printed

materials (Izdebska et al. 2015). General printing processes exist today are broadly classified as follows (Michel et al. 2001):

1. Relief printing.
2. Gravure printing.
3. Offset (lithographic - planographic) printing.
4. Screen (permeographic) printing.
5. Digital Printing.

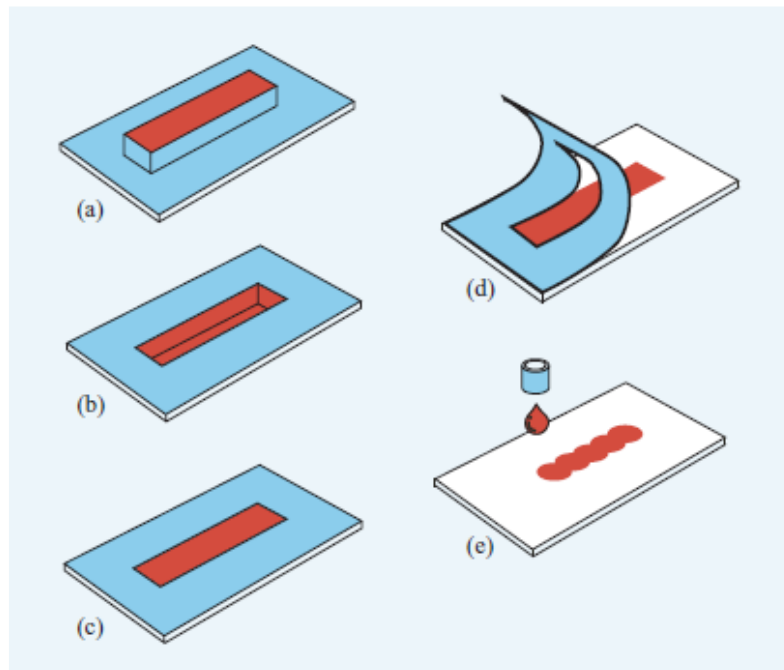


Fig. 2.1 Diagram of the patterning elements (blue) with the ink (red) of major print techniques: (a) Relief printing, (b) intaglio printing (c) lithographic printing, (d) screen or stencil printing, and (e) ink-jet printing (Michel et al. 2001).

Relief printing (fig. 2.1 (a)) the printing elements are located above the nonprinting ones. The substrates are to be printed, brought into firm contact with the protruded surface that already inked. Flexographic printing, letterpress printing, and other processes of transferring an image from a raised surface comes under relief printing technique. In this printing, important aspect is the selection of suitable printing plates for the type of inks used. The wrong choice can lead to bulging of the plates during printing, which may affect the quality of the prints adversely.

Gravure or intaglio printing (fig. 2.1 (b)) is the converse process of relief printing, in which ink is transferred from the sunken surface of printing plate and is pressed against the substrate. Printing cylinders with recessed surfaces are created using laser engraving technology facilitates very high-quality prints, on both absorbent and non-absorbent substrates. Due to the high implementation cost, gravure is restricted only for high-volume or luxury work. Switching of lab-scale process to a large-scale production is the main challenge.

At the end of the eighteenth century, lithographic printing (fig. 2.1 (c)) was invented by Alois Senefelder. It uses a chemically patterned flat surface with areas that accept ink (oleophilic-ink friendly) and areas that repel ink (dampening-hydrophilic friendly). The parameters which define the printing and nonprinting elements during conventional offset printing process are ink, dampening solution and surface tension property of the substrate.

Fig. 2.1 (d) depicts the stencil/screen printing. Screen printing transfers an information by passing ink through openings in a stencil onto the substrates. This technology is being used for mass production due to its advantages including simple, low cost, versatility, miniaturization and offers no restriction on any type of substrates. The technique has a typical resolution of about 50–150  $\mu\text{m}$ . It is widely used for all printing paper mainly newspaper etc. for paper publications (Schüler et al. 2009). Achieving the lesser thickness through this technology is the main challenge.

Digital printing (ink jet printing) is a noncontact process, is able to unload a required quantity of materials directly from a computer-designed image onto a selected area of a substrate with minimal human involvement. It is a flexible and cost-effective method for micro- and nano-fabrication. Nozzle clogging is the challenge in the digital printing, as the inks of inkjet printing consists of insoluble micro- or nanoparticles that can aggregate and precipitate (Haverinen et al. 2010).

A clear scrutiny of the recent development in the field of printed electronics is needed, in order to make some perception regarding printing techniques. There are plenty of studies have done regarding usage of these techniques in fabrication of electronic devices, reported in the peer viewed journal. Despite of challenges such as low performance, less accuracy and reliability of electronic devices, a mammoth work

is being carried out in electronic industries for adapting printing methods rather than convention techniques due to its advantages and efforts to minimize the concerned drawbacks. Table 2.1 gives consolidated information on the different parameters of the printing techniques so far used in electronic industries.

Table 2.1 Comparison of various printing techniques (Khan et al. 2014).

<b>Parameter</b>	<b>Gravure</b>	<b>Offset</b>	<b>Flexography</b>	<b>Screen</b>	<b>Inkjet</b>
<b>Print Resolution (<math>\mu\text{m}</math>)</b>	50-200	20-50	30-80	30-100	15-100
<b>Print thickness (<math>\mu\text{m}</math>)</b>	0.02-12	0.6-2	0.17-8	3-30	0.01-0.5
<b>Printing Speed (m/min)</b>	8-100	0.6-2	5-180	0.6-100	0.02-5
<b>Req. Solution Viscosity (Pa.S)</b>	0.01-1.1	5-2	.010-0.500	0.500-5	00.1-0.10
<b>Surface Tension (mN/m)</b>	41-44	-	13.9-23	38-47	15-25
<b>Material Wastage</b>	Yes	Yes	Yes	Yes	No
<b>Controlled Environment</b>	Yes	Yes	Yes	No	No
<b>Experimental Approach</b>	Contact	Contact	Contact	Contact	Contact-less
<b>Process Mode</b>	Multi-steps	Multi-steps	Multi-steps	Multi-steps	Multi-steps
<b>R2R Compatibility</b>	Yes	Yes	Yes	Yes	Intermediate
<b>Hard Mask Requirement for each printing setup</b>	No	No	No	Yes	No
<b>Printing area</b>	Large	Large	Large	Medium	Large

Generally, all electronics industries are aiming for the high profit which is defined as high productivity with less effort, without compromise in performance as well. After putting glance over the different printing methods, screen printing method is found to be a facile, reliable and user friendly and ability to print on any type substrates under ambient conditions. Screen printing process offers advantage such as no requirement of the sophisticated environment which leads to a less investment. On the other side, it is suitable for large-volume production, these two makes provision for the establishment of low-cost manufacturing (Faddoul et al. 2012). Despite of all advantages, chemicals

which are used to avoid clogging of mesh pores, have adverse effects on environment; the resolution is limited to 100  $\mu\text{m}$ . Furthermore, screen printing speed is lower compared to roll-to-roll processes (Pudas et al. 2005). Rotogravure entertains a printing at speed of 100  $\text{m min}^{-1}$ , whereas screen-printing speed is limited to 30  $\text{m min}^{-1}$  (Faddoul et al. 2012).

## 2.2 Screen printing

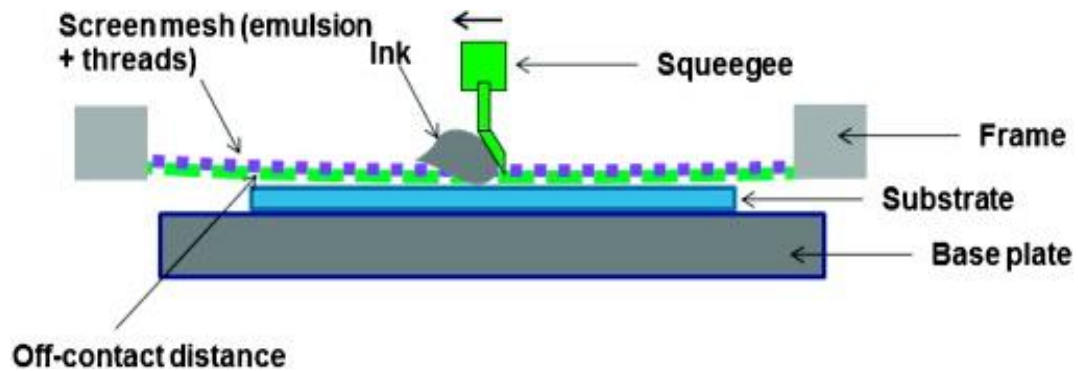


Fig. 2.2 Schematic of screen-printing process (Faddoul et al. 2012).

Screen printing, sometimes is referred to as serigraphy or silk screen printing. A screen-printing process encompasses the pushing of viscous paste (5-50 Poise) through a permeable patterned fabric screen to deposit on the substrates (Krebs et al. 2009). The main components of screen printing are namely screen comprises frame and mesh, coater and squeegee as shown in fig.2.2. As, earlier mentioned, screen has two parts frame and mesh; usually screen frame is made of metals such as aluminum, stainless steel or wood. Another part, screen mesh consists of silk, nylon, polyester or stainless steel, with mesh counts ranging from 10 to 450 openings per inch. Screen web/mesh is mounted on a screen frame under tension (20-30 N/cm) effectively by using suitable adhesives. Screen web/mesh mounted on a screen frame is coated with photosensitive emulsion followed by drying for a few minutes. The film containing the pattern is placed on the screen mesh coated with photosensitive emulsion is finally exposed to UV light. Emulsion layer of the unexposed areas are removed and it leaves the pattern in the screen mesh mounted on the frame.

Screen-printing process is performed in two stages, the screen-printing paste spread over the fixed screen so that the pores in the screen web are filled with the paste.

Concurrently, the screen does not come in contact with substrate as shown in fig. 2.3 (a) and it is called flood stroke.

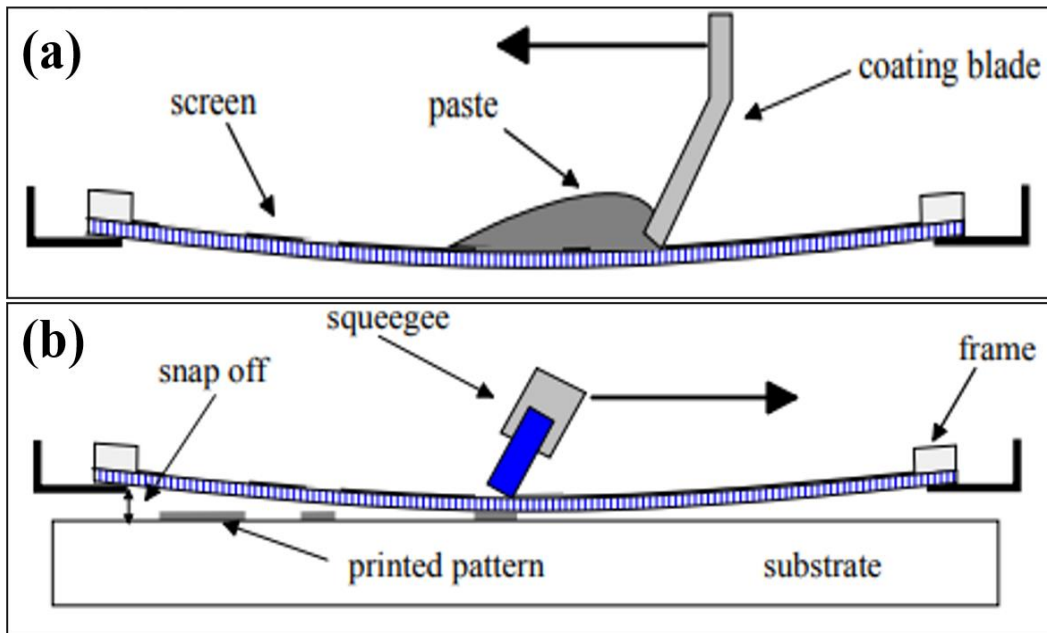


Fig. 2.3 Screen printing process, (a) scheme of the flood stroke and (b) scheme of the print stroke.

During the print stroke (fig. 2.3 (b)), the screen web contacts the substrate when the squeegee pushes the paste through the pores of the screen mesh and deposit it onto the substrate. Squeegees are of different shapes, such as U or V-shapes with different hardness and materials. Usually, squeegees are made of polyurethane with hardness shore A. The parameters like squeegee load, squeegee speed, geometry, type and hardness of squeegee, snap-off distance, screen printing angle, screen mesh type etc., are play a vital role in a screen printing process. (J. Pan et al. 1999). If the squeegee load is increased, then the squeegee speed should be decreased or vice-versa. It has been recommended that the squeegee load and squeegee speed should be in range of 6-9 kg and 20-50 mm/s respectively (Somalu et al. 2017). Squeegee load can be increased, if the inks are too tacky and low thickness are needed. A study reported that squeegee load of 5 and 9 kg was applied to obtain the metal oxide film with thickness 40 and 20  $\mu\text{m}$  respectively. It revealed that thickness was decreased with increased load (Phair et al. 2009). Snap-off distance needs to be maintained in the range of 1.5-2 mm; it can be tuned based on the film thickness requirement. More snap-off distance has been advised to fabricate the film with high thickness. Usually, rectangular shaped squeegee made

up of polyurethane polymer with hardness shore-B are used to fabricate the metal and metal oxides films. Dollen *et al.*, revealed that films fabricated using softer squeegee (60 durometer) with lower squeegee speed (2.54 cm/s) possessed accurate dimensions compared to the films obtained by using harder squeegee (80 durometer) with higher speed (5.58 cm/s) (Von Dollen and Barnett 2005). Yttria stabilized zirconia (YSZ) films with thickness (23-100  $\mu\text{m}$ ) were processed using screen printing parameters such as squeegee pressure (0.3 MPa), printing speed (150 mm/s) and snap-off distance (2.0 mm) (Mücke et al. 2014). Somalu *et al.*, produced nickel-scandium stabilized zirconia (Ni/ScSZ) anode films with thickness 10  $\mu\text{m}$ , by using squeegee speed, squeegee load and snap-off distance of 20 mm/s, 6 Kg and 2.0 mm respectively (Somalu et al. 2012). Above-mentioned results confirm that thickness of films can be tuned by varying the screen-printing parameters mainly squeegee load and squeegee speed. From the viewpoint of film quality, it is concluded that lower squeegee speed improves the surface levelling of the screen-printed films by providing ample time for the ink to flow, particularly for the high viscous screen-printing inks (Somalu et al. 2017). Screen mesh made of nylon, polyester, and stainless steel with mesh number range from 300 to 600 are used. Screen mesh with high mesh number is preferred, when the sharp edge lines need to be printed. Sharp edged lines with 100  $\mu\text{m}$  width or freckle of 70  $\mu\text{m}$  on glass substrates for electronic application, can be printed successfully by using 400 mesh number stainless steel web under the tension of 20 N/cm, whose thread diameter is 18  $\mu\text{m}$  and mesh pore size of 45  $\mu\text{m}$  and tension of the mesh (Karaguzel et al. 2009). Recently, silver (Ag) films used for silicon solar cell applications were fabricated using screen mesh of different mesh no. 300, 325, and 400. This study suggested that selection of silver screen printing inks was more important than the mesh- type and mesh number to obtain high resolution of the printed patterns (Thibert et al. 2014).

### **2.3 Formulation of screen-printing inks**

Screen printing inks are made of three main components, (i) the functional material, (ii) the organic vehicle and (iii) additives such as a promoter and a dispersant. The functional materials mixed into the solution consist of organic vehicle and additives using hand mixer. Nano- or micro-sized particles of various class of materials such as metal, metal oxides, graphene, polymers, nitrides, hydrides can be served as a

functional material (Do et al. 2003; Faddoul et al. 2012; Joseph et al. 2016; Mbarek et al. 2006). Solid loading of the functional material is in the range of 60-70 wt. % of screen-printing inks. In order to fabricate the pattern with minimum defects, functional particles with size lesser than 3  $\mu\text{m}$  are used. In order to develop, a high conductive screen-printing ink, metal particles of gold (Au), platinum (Pt), silver (Ag), copper (Cu), nickel (Ni) palladium (Pd), or mixture of these particles etc. were used as functional material. The sintering of the Cu and Ni particles were carried out in inert or reducing atmosphere, to avoid oxidization. In addition to this, non-metallic materials such as carbon, graphite, graphene, polyaniline etc., were also used as functional materials of conductive screen-printing inks (Gallo Stampino et al. 2010). Conductive particles-based screen-printing inks were employed in fabrication of conductive circuits, electrodes for TFTs, supercapacitors, electrochemical devices etc. Based on functionality requirement various metal oxides such as ZnO, WO<sub>3</sub>, ITO, SnO<sub>2</sub>, BaSnO<sub>3</sub>, NiO, etc were printed by using screen printing technique. Screen printed metal oxide films have potential applications in various fields such as gas sensing, photovoltaic, solid-oxide fuel cells (SOFCs), TFTs, catalytic activities, energy storage devices, biosensors etc.

Process such as particle wetting, formation and adhesion of film on the substrate results from the main element of the screen-printing ink i.e., the vehicle. It comprises of organic binders and solvents. It contributes dispersion stability and rheological behavior. Organic vehicle should possess not only chemical inertness but also its decomposition temperature should be lower than the softening point of additives and melting point of the functional micro/nanoparticles (Wang et al. 1994). Traditionally, solvents used in the screen-printing inks are terpeneol, texanol, diethyl glycol, diethylene glycol, methyl ethyl ketone, N,N'-dimethylpropyleneurea, N-methyl-2-pyrrolidone, glycol ethers (propylene and Di-propylene),butyl carbitol, carbitol acetate, butyl carbitol acetate, acetone, cyclohexane, epoxy and phenoxy resin, etc (Xiao 2001). Nowadays, water as an eco-friendly solvent is used in order to overcome the adverse effects on the environment, raised by the use of previously mentioned solvents. Solvents dominate over the wetting and drying behavior of formulated screen-printing inks. Defects such as cracks, pores, unfilled area in the patterns arises due to the fast-drying behavior of the screen printing inks, whereas slow drying behavior



makes the printed pattern wet for a longer time, resulted into problems such as loosing accurate dimensions, phase separation and difficult in handling. Binder is the main ingredient of the screen-printing ink, which improves the particle network, prevents defects and enables the adhesion of ink on the substrates. Some of the long-chain molecular organic compounds used as an organic binder in screen printing inks are ethyl cellulose, carboxy methyl cellulose, butyl cellulose, polyvinyl acetate, polyvinyl butyral, etc. During formulation of screen-printing inks, the irritant and volatile organic compounds (VOCs) solvents are preferred more than the water, because water-based screen-printing inks are less stable and dry very quickly. Rane *et al.* prepared the organic vehicle made of ethyl cellulose (binder) and butyl carbitol (solvent) to formulate silver screen printing inks (Rane et al. 2003). Ethyl cellulose and terpineol were mixed to obtain organic vehicle, and this organic vehicle was added to nickel/scandia-stabilized-zirconia powders for the fabrication of anode of the SOFCs (Somalu and Brandon 2012). Organic vehicle obtained from the mixing of methyl cellulose in water, facilitates the formulation of water based silver screen printing inks (Liang et al. 2016). Nearly, 20-45 wt.% of screen-printing inks are comprised with organic vehicle. Rheology properties of inks can be tuned by varying the quantities of binder and solvent. Usage of non-degradable binder and non-polar solvents lead to the production of toxic compounds, which may cause adverse effect to the environment. In order to overcome this problem, usage of bio-degradable binders and polar solvents should be encouraged (Liang et al. 2016). S. Merilampi et al, studied the adhesion properties of screen-printed films using silver inks obtained from vinyl chloride and polyester resin-based solvents, where adhesion of film on the substrate was influenced by the organic vehicle. Screen printed films obtained from the vinyl chloride-based inks showed an adhesion classification of 4B and 5B on PI and PET substrates respectively. Whereas adhesion on films from polyester resin-based ink designated as 3B and 4B on PI and PET substrates (Merilampi et al. 2009).

Additives comprises of inorganic binder and dispersants, which enhance the functionality of the inks during screen printing and sintering. An inorganic binder is added when sintering is going to be happening at high temperature. It behaves as an adhesion promoter and activates the sintering process at lower temperatures. Nowadays glass frits, mixture of bismuth, alumina, magnesium, zinc oxides, sodium and calcium

carbonates are used as an inorganic binder (Hashimoto et al. 2002). Densification and adherence of thick films can also be achieved without inorganic binder. Dispersants are long-chain molecules, which are known as additives in the screen-printing inks. It stabilizes the particles by ensuring the repulsive forces between particles and also enhances the long-term stability of formulated inks. Commonly used dispersants are phosphoric acid ester, pentastearic acid oligomer, polyethylene glycol, and alcohol polyoxyethylene. Solid loading of the additives in the screen-printing inks varies from 3-5 wt. %. Glass frits were added in the SnO<sub>2</sub> screen inks, where mechanical strength of the films were improved, but the conductivity of the films were affected. (Viricelle et al. 2005). Hypermer KD15 was used as a dispersant in the nickel/scandia-stabilized-zirconia screen printing ink (Somalu and Brandon 2012). Importantly, screen printing inks should have two contradictory requirements in screen printing. One is that the ink should flow otherwise causes local starvation of ink leads to phenomenon called mesh marking and surface imperfections (Aleeva and Pignataro 2014). On the other hand, ink should not run unnecessarily since it leads to expansion of the width of lines (Vest 1986). Ink properties such as, viscosity, colloidal properties, particle size distribution and surface tension effect on printed characteristics. Moreover, deposited film quality depends on the substrate characteristics (surface energy, porosity, roughness) and compatibility with the inks. Lower surface energies of the substrates improve the screen-printing resolution (Liang et al. 1996). The printed characteristics such as aspect ratio of the printed pattern is controlled by the viscosity (Lin et al. 2008).

#### **2.4 Rheological properties of screen-printable ink**

The quality and characteristics of the screen printed films depend on the various factors which include fingerprinting settings, screen parameters, rheological properties of inks, substrate preparation etc., (Goldberg et al. 1994; Rudež et al. 2015). Unlike other factors, rheology of inks cannot be adjusted during the screen-printing process and also impact the printing definition of the films. Therefore, optimization of rheological properties is necessity for the fabrication of good quality films. As well-known that the screen printing inks usually consist of three components, the functional material, organic vehicle (organic binder and solvent) and additives (Rudež et al. 2015).

Rheology of inks can be understood by evaluating the steady and dynamic properties using the three tests; steady-state, oscillation, and creep-recovery.

The steady-state test is performed to study the properties such as viscosity, yield stress and thixotropy. Viscosity is one of the steady state rheology properties and depends on the percentage of functional material and/or binder. Ried *et al.*, proposed that metal oxide inks possessed viscosity in the range of 5- 15 Pa. s, at shear rate of  $100 \text{ s}^{-1}$ , was suitable screen-printing techniques (Ried et al. 2008). Liang *et al.*, fabricated the silver electrodes for the TFTs with high aspect ratio using the water-based silver screen printing inks with viscosity in the range of 2-10 Pa.s at a shear rate of  $200 \text{ s}^{-1}$  (Liang et al. 2016). Viscosity of the screen-printing inks increases as the composition of the functional material and/or binder in the screen-printing inks are increased. Viscosity of the Ag inks increases from 0.7 to  $5.5 \pm 1.4 \text{ Pa.s}$  under shear rate of  $100 \text{ s}^{-1}$ , when the Ag content increases from 67 to 75 wt. %. Similar trend was also found that as the content of Ag nanowires increased from 6.0 to 7.3 wt.%, the viscosity also enhanced from 2 to 10 Pa.s at a shear rate of  $200 \text{ s}^{-1}$  (Faddoul et al. 2012; Liang et al. 2016). Yield stress is a steady state property and it is defined as a minimum stress at which elastic solid-like behavior of the ink's changes to liquid-like behavior. It gives information about the strength of the particle network and elasticity of the inks. Normally, inks with high viscosity due to the improved particle network strength, possess high yield stress. Faddoul *et al.* determined the yield stress using Hershel-Bulkley model for the formulated water based silver pastes, was found to be in the range of  $36\text{-}508 \pm 31 \text{ Pa}$  and also revealed that yields stress increased with increasing Ag content in the inks (Faddoul et al. 2012). Therefore, the yield stress of the inks greatly depends on the composition of the ingredients such as functional materials, binder, solvents and additives. Thixotropy is a time-dependent shear thinning property of viscous fluids. Any fluid will be over flown with decreasing viscosity, when it is subjected to an applied stress and takes a certain time to recover its original viscosity are known as thixotropic fluid. This property greatly influences on the dispersion of the ink on the substrate and surface levelling of screen-printed films. Terpeneol based metal oxide anode inks with functional materials and binder content 20-26 % and 0-2% respectively, showed the poor thixotropic properties and concluded that formulated anode inks were not suitable for screen printing (Somalu and Brandon 2012). Further,

water based gadolinia doped ceria screen printing inks with hydroxy cellulose binder exhibited poor thixotropic properties and resulted into the cracked films due to the low particle network structure (Sanson et al. 2010).

Viscoelastic properties of inks are studied using the oscillation test, while the creep-recovery test is carried out to understand the slump characteristics of inks (Somalu and Brandon 2012; M. R. Somalu et al. 2013). Elastic/storage ( $G'$ ) and viscous/loss ( $G''$ ) moduli are the two components, which interprets the viscoelastic properties of inks. The elastic modulus and viscous modulus provide information on the solid-like and liquid-like properties of the ink, respectively. Generally, ink with a high elastic modulus (a high resistance to separation and slumping) is known as a well-structured ink, and high viscous modulus ink is known as an in-elastic one (Durairaj 2006). For emulsions, pastes, gels, slurries and dispersions, complex modulus ( $G^*$ ) is a measure of material's resistance to deformation. Complex modulus is a ratio of applied stress ( $\tau_o$ ) to the maximum strain ( $\gamma_o$ ) and is shown in equation 2.1. Complex modulus can be resolved into elastic and viscous components and are called as storage modulus or elastic modulus ( $G'$ ) and viscous modulus or loss modulus ( $G''$ ). Mathematically, components of complex modulus are denoted in equations 2.2 and 2.3.

$$G^* = \frac{\tau_o}{\gamma_o} \quad (2.1)$$

$$G' = G^* \cos \delta \quad (2.2)$$

$$G'' = G^* \sin \delta \quad (2.3)$$

The complex modulus ( $G^*$ ) and phase angle ( $\delta$ ) can be written in terms of storage modulus and viscous modulus as shown in equation 2.4 and 2.5 and can be correlated to the structure of screen printing ink and its printing (Barnes et al. 1989).

$$G^* = G' + iG'' \quad (2.4)$$

$$\tan \delta = \frac{G''}{G'} \quad (2.5)$$

It is expected that phase angle ( $\delta$ ) of the formulated inks with good printability should lies in between  $30^\circ$  -  $50^\circ$ . However, it is revealed the magnitude of  $G'$  and  $G''$  confirms the printability of the formulated inks than the phase angle ( $\delta$ ) (Durairaj et al. 2006). Ink with very high  $G'$  value may require high squeegee pressure and slower printing speed and get struck during print stroke. On the other side, ink with large  $G''$  results in

slumping and ink bleeding (M. R. Somalu et al. 2013). Further, the fingerprinting parameters which affect the quality of the films such as speed, angle, geometry of squeegee, snap-off distance, squeegee pressure, dwell time between flood and print stroke, etc. (Phair et al. 2009). An intensive understanding of both rheology of ink and screen-printing parameters are essential to fabricate high-quality films.

The magnitude of  $G'$  and  $G''$  helps in determining the linear viscoelastic region (LVR) of formulated inks. LVR is defined as a region under which the formulated inks retain its particle network strength when it is subjected to the applied stress. It gives the information about the minimum applied stress required to destroy the particle network strength is called as cross-over point. Ratio of  $G''/G'$  as a function of applied shear stress indicates the viscoelastic behavior of the inks. If the ratio is  $< 1$  then, the inks possess linear viscoelastic behavior under the particular applied stress and suitable for printing process. When it goes beyond the unity ( $>1$ ), then liquid-like structure dominates the solid-like structure and makes it unsuitable for the printing process. It is demonstrated that cross-over point of the conductive formulated ink with 67 % Ag loading found at  $42 \pm 9$  Pa, which was lower than the ink with 72 % ( $492 \pm 39$  Pa) and 75 % ( $7512 \pm 586$ ) Ag loading (Faddoul et al. 2012). Screen printing ink consisting of mixture of metal oxides (NiO/Sc<sub>2</sub>O<sub>3</sub>/CeO<sub>2</sub>/ZrO<sub>2</sub>), terpineol, ethyl cellulose and Hypermer KD15 as functional material, solvent, binder and dispersant respectively were formulated for the fabrication of SOFCs electrodes. With increasing the vol. % of functional loading from 20-34, cross over point of inks also shifted from 100 to 200 Pa (M. Somalu et al. 2013). It is noted that minimum the applied stress at which the particle network strength of inks destroys, increases with increasing solid loading. Table 2.2 shows the different formulated silver screen printing inks consisting of various organic vehicle and additives.

Table 2.2 Summary of different formulated silver screen printing inks consisting of various organic vehicle and additives.

Functional Material			Organic Vehicle		Additives	Curing conditions		Results	Reference
Morphology	Particle size ( $\mu\text{m}$ )	Particle loading (Wt.%)	Solvent	Binder		Curing Temp. ( $^{\circ}\text{C}$ )	Curing Time (Min)	Resistivity ( $\mu\Omega\text{-cm}$ )	
Nanoparticle	0.2	77	Ethylene glycol	Polyacrylic acid	-	200	30	5.5	Hyun et al. 2015
Flakes	3	70	Ethylene glycol + glycerol	acrylic polymers	*Hydropalat -216 #Foamaster -8034	875	60	3	Faddoul et al. 2012
Nanoparticle	0.05 - 0.1	80			Pb-frits	450	15	4	Park et al. 2008
Microparticle	2	70	Ethylene glycol + glycerol		*Hydropalat 216 #Foamster 8034	700	15	6	Faddoul et al. 2012
Microparticle	3-5	60-70			Glass frits	850	15	15	Songping 2007
Microparticle	<5	70	Vinyl chloride		-	120	30	19	Merilampi et al. 2009
Nanoparticle	0.08	60%	Diethylene glycol + water	-	-	200	60	33	Yin et al. 2008
Nano wires	500 (L:D)	6.6%	Water	Hydroxypropyl methyl cellulose	#Defoamer MO-2170	150	15	21	Liang et al. 2016

\*Dispersant agents      #Anti-foaming agents

## **2.5 Synthesis of functional materials**

For the synthesis of nanoparticles, two types of approaches are available, they are top-down approach and bottom-up approach. In the top-down approach, the materials in bulk size are reduced to nanoscale by the means of physical, chemical or mechanical process. The physical method requires high temperature, vacuum and expensive instruments. Examples of top-down methods are mechanical grinding, ball milling, chemical etching, electro -explosion etc. In the bottom-up approach, the atoms or molecules are the starting material to synthesize nanoparticles. Examples of bottom-up approach are conventional solid-state reaction, polyol, hydrothermal, sol-gel, solution combustion synthesis, chemical co-precipitation, microwave, emulsion method, etc (Hornyak et al. 2008).

### **2.5.1 Polyol method**

Polyol process is a unique soft chemical method and largely employed for the synthesis of wide variety of the nanoparticles (mainly monometallic and bimetallic) which have huge demand in the technological fields. In the late 80's, researchers namely Fievet, Lagier, and Figlarz established a liquid phase synthesis technique to prepare metal nanoparticles from their salts, hydroxides, oxides etc. using polyols and termed as polyol process. In this process, polyols such as ether glycols and 1,2 -diols act not only as a solvent for the metal salts but also serves as a reducing agent. Polyols being used as a medium of the nanoparticles synthesis offer some advantages such as (i) polyol protects the synthesised reactive metal nanoparticles from the oxidation, (ii) high boiling point of polyols allows synthesis to be performed at high temperature, to obtain well crystallized materials. Researchers demonstrated the synthesis of high crystalline nanoparticles of noble metals (Au, Pd, Ag), readily reducible metals (Cu), and less reducible metals (Ni, Co, etc.,) using polyols without subsequent heat treatment, hence further energy consumption was avoided. This process grabbed the attention of many companies, for example: In 90's the Eurotungstene company started the synthesis of Ni and Co metal particles on a large-scale using polyol. In 2007, SEMCO adopted the polyol to prepare polymer-stabilized Ag nanoparticles for the production of water-based silver inks to be utilized in the screen printing and inkjet printing.

Different steps are involved in the synthesis of nanoparticles using polyol method; (i) the dissolution of metal salts in the polyols before or during the heating, (ii) dissociation of precursor to form cations reservoir, (iii) the formation of nuclei and (iv) successive growth of nuclei to form nanoparticles. Metal cations obtained in the polyol's solvents are reduced to metal atoms. These reduced metal atoms arbitrarily move and collides the metal cations or other reduced atoms present within the solution and lead to the formation of clusters. Due to repeated collision of cations, atoms and clusters, development of nucleus happens, when the developed nucleus achieved a critical size, nanoparticle is formed. There are two theories cover best about aforementioned mechanism are thermodynamics and kinetic rate. Thermodynamics explains the formation of nuclei i.e., nucleation. The overall free energy ( $\Delta G$ ) change required to form the spherical particles is the total sum of free energy due to new volume formation ( $\Delta G_v$ ) and surface free energy ( $\gamma$ ) of new surface generated and it is shown in equation 2.6.

$$\Delta G = -\frac{4}{3}\pi r^3 \Delta G_v + 4\pi r^2 \gamma \quad (2.6)$$

The critical nuclei size  $r^*$  can be obtained by equating  $d(\Delta G/\Delta r)=0$  and it is shown in equation 2.7. The developed nucleus with radius  $r > r^*$  will be grown to nanoparticles or else nucleus will be dissolved ( $r < r^*$ ).

$$r^* = \frac{2\gamma}{\Delta G} \quad (2.7)$$

After the formation of nuclei, its growth and disappearance phenomena can be explained by kinetic rate theory. Foremost, Continuous growth of nuclei to form nanoparticles happen either via molecular addition, secondary growth or Ostwald ripening. In molecular addition, growth of nuclei to nanoparticles are taken place by the continuous aggregation of metal atoms on the nuclei surface. In secondary growth, nanoparticles are obtained by the agglomeration and collision between particles. During this growth, possibility of obtaining large particles is more, because relative rate of the secondary growth is higher than molecular addition. The process in which, large sized particles ( $r > r^*$ ) are continued to grow larger and to form nanoparticles, whereas small sized particles ( $r < r^*$ ) are dissolved, which is known as Ostwald ripening. In summary, relative rate of nucleation and growth influence the size of the metal nanoparticles



formed. Including polyols, initial elements such as metal salts, reducing agents and stabilizers also influence the relative rate of nucleation and growth. When the polyol is not having sufficient reducing power, then the auxiliary reducing agents need to be added. For example, high nucleation rate during metal reduction process can be obtained, when reducing agent with strong reducing power is employed, and finally smaller nanoparticles can be synthesized. In addition to the above-mentioned parameters, operating conditions such as reaction time, and temperature also play a vital role in the synthesis of metal nanoparticles.

So far, the synthesis of Ag nanoparticles (NPs) by facile polyol process was reported in several literature. In the first report, quasi-spheric and mono-disperse silver particles obtained in ethylene glycol (EG), when the  $\text{AgNO}_3$  and PVP were used as metal precursor and stabilizers. It was also observed that particle size and yield increased with increasing PVP/silver nitrate weight ratio and reaction temperature. PVP/silver nitrate weight ratio of 1:1 yielded 91 % of particles with size of  $0.37 \mu\text{m}$  at reaction temperature  $160^\circ\text{C}$  whereas, weight ratio of 1.2:1 offered particles of size  $0.81 \mu\text{m}$  with 93 % yield at reaction temperature of  $180^\circ\text{C}$  (Ducamp-Sanguesa et al. 1992). Sun *et al.* synthesised cube-shaped Ag NPs from the silver nitrate using ethylene glycol and PVP stabilizers. It is also found that reaction temperature, concentration of  $\text{AgNO}_3$  have influence on the size of the synthesised Ag particles (Sun and Xia 2002). Benjamin *et al.* used  $\text{AgNO}_3$ , ethylene glycol and PVP as a metal precursor, solvent and reducing agent and the stabilizers respectively, for the synthesis of the truncated pyramid shaped Ag NPs with edge length varying from 75-150 nm (Schuette and Buhro 2013). Microwave assisted polyol method was adopted to synthesis Ag nanowires of diameter in the range varying from 45 nm to 200 nm in 3 min using ingredients such as ethylene glycol as a solvent, silver nitrate as metal salt, sodium bromide (NaBr) as auxiliary reducing agent and PVP serves as a capping agent. The size, shape and yield of nanoparticles was controlled by synthesis parameters such as microwave power, PVP/ $\text{AgNO}_3$  molar ratio and concentration of NaBr (Yi et al. 2017). Fereshtah *et al.*, investigated the influence of different polymers on the size and morphology of Ag NPs. It was found that three different polymers such as polyvinylpyrrolidone (PVP), polyvinyl alcohol (PVA), and polyethylene glycol (PEG) were used as a both stabilizers and solvent along with metal precursor,  $\text{AgNO}_3$  and reducing agent, sodium

borohydride ( $\text{NaBH}_4$ ), where the reaction temperature was maintained at  $160\text{ }^\circ\text{C}$  for 4 h. Size of Ag particles synthesised using PEG polymers were smaller ( $352 \pm 20\text{ nm}$ ) than particles obtained using other polymers PVP and PVA. By the incorporation of strong reducing agent  $\text{NaBH}_4$  to solution of PEG and  $\text{AgNO}_3$ , the size of the synthesised particles were reduced from  $352 \pm 20\text{ nm}$  to  $220 \pm 30$  (Fereshteh et al. 2016). Tolaymat *et al.*, documented the different Ag precursor used in the synthesis of silver nanoparticles systematically and almost 83 % literature reported that silver nitrate ( $\text{AgNO}_3$ ) emerged as a most widely used salt precursor (Tolaymat et al. 2010). The reasons behind the use of  $\text{AgNO}_3$  are: low cost and less chemical stability compared to other silver salts. During synthesis of Cu NPs via polyol method, there is a possibility of formation of the copper oxide particles than the Cu particles, in order to overcome this problem, synthesis should be carried out in inert gas atmosphere and auxiliary reducing agents are employed. Commonly used reducing agents are sodium phosphinate ( $\text{NaH}_2\text{PO}_2 \cdot \text{H}_2\text{O}$ ), sodium borohydrides ( $\text{NaBH}_4$ ), ascorbic acid ( $\text{C}_6\text{H}_8\text{O}_6$ ), trisodium citrate ( $\text{Na}_3\text{C}_6\text{H}_5\text{O}_7$ ), potassium bromide (KBr), hydrazine ( $\text{N}_2\text{H}_4$ ) etc. Park *et al.*, studied the influence of concentration of the reducing agents on the size of synthesized Cu nanoparticles using polyol method. It is found that copper sulfate, diethylene glycol, PVP and  $\text{NaH}_2\text{PO}_2 \cdot \text{H}_2\text{O}$  served as metal precursor, solvent, stabilizers and reducing agents respectively. Size of synthesised Cu nanoparticles was decreased from  $72 \pm 17\text{ nm}$  to  $54 \pm 14\text{ nm}$ , when the concentration of reducing agent was increased from 12.75 mmol to 19.10 mmol respectively (Park et al. 2007). The synthesis conditions and observed results for the different metal NPs prepared via polyol method are reported in Table 2.3.

Moreover, from the point of both scientific and technological views, controlled synthesis of bimetallic nanoparticles (BMNPs) via polyol method has grabbed great attention of researchers than monometallic, due to their different morphologies and change in electronic structure. BMNPs exhibit distinctive properties in applications such as electronics, catalysts, bio-medical, optical etc. For example Au-Ag alloy NPs exhibit excellent antibacterial activity against Gram+ bacteria *Staphylococcus aureus* than the monometallic particles Au and Ag (Ramakritinan et al. 2013). Ag-Cu bimetallic nano-alloy have potential applications in printed electronics, lead-free inter-

connects, catalysis, dental amalgams, antibacterial coatings, heat transfer fluids etc (Ferrando et al. 2008). Other than the polyol process conditions, parameters such as relative strength of metal to metal bond strength, atomic size and structure of elements have prominent influence on processing of the four different integrated patterns of BMNPs; (i) random alloy NPs, (ii) core-shell NPs, (iii) multi-shell NPs, and (iv) sub clusters NPs (Ferrando et al. 2008).

Tsuji *et al.*, adopted microwave assisted polyol method to synthesis Au@Ag core shell NPs. It was found that AgNO<sub>3</sub> and HAuCl<sub>4</sub> were used as respective metal precursors, whereas PVP and ethylene glycol served as a stabilizers and solvent respectively. Here, different shapes of Au core (50 nm) such as triangular, square, pentagonal was found inside the triangular, square shaped Ag shell (Tsuji et al. 2006). Au@Cu core-shell NPs were prepared via microwave assisted polyol two-step reduction method. Firstly, Chloroauric acid (HAuCl<sub>4</sub>) precursor was dissolved in ethylene glycol (EG) and heated at 198 °C for 1.5 min, cooled colloidal solution was centrifuged at 15,000 rpm for 30 min using ethanol to obtain Au seeds. Again, Au seeds dispersed in the EG was added into the solution of PVP and EG which was heated at 175 °C, followed by injecting the solution of Cu<sub>2</sub>(OAc)<sub>4</sub> and EG at a rate 0.3 mL/min. Then the solution was kept undisturbed for 5 min after addition of all reagents. Mixture of triangular, square, rhombic, pentagonal shaped Au@Cu NPs were obtained under normal atmosphere (Tsuji et al. 2010). Jiang *et al.*, synthesized the Ag-Cu BMNPs via polyol method aiming towards the application such as lead-free interconnect material. In this study, two solutions of PVP and Cu<sub>2</sub>(OAc)<sub>4</sub> in 20 ml of EG were transferred into another vessel which was under the purged N<sub>2</sub> atmosphere and this solution was heated to 175 °C for 20 min. Afterwards the solution of AgNO<sub>3</sub> and EG was added into the heated solution and left for 5 min. UV-visible spectroscopy confirmed that synthesized NPs were of Ag-Cu alloys with size varying from 100-120 nm, rather than a blend of Ag and Cu monometallic particles (Jiang et al. 2005). Tsuji *et al.*, synthesized the Ag-Cu bimetallic NPs with various AgNO<sub>3</sub>/Cu(OAc)<sub>2</sub> molar ratio using polyol technique at reaction temperature of 175 °C under argon atmosphere. Ag-Cu bimetallic NPs with average size of 406 ± 80, 81 ± 20, 144 ± 85, 173 ± 48 nm were obtained, when the precursors molar ratio was 2, 1, 0.5 and 0.25 respectively (Tsuji et al. 2010). Bonet *et*

*al.*, studied the effect of different precursor on the type of Ni-Cu BMNPs. In this study, Ni-Cu random alloy NPs of size 100-300 nm were synthesised from suspensions of copper carbonate and nickel carbonate in ethylene glycol after the reaction time 39 h at 140 °C, whereas solution of copper nitrate and nickel nitrate in ethylene glycol exhibited the Cu core and a nickel shell BMNPs of size 140 nm at reaction temperature 196 °C for 4 h (Bonet et al. 2003). Table 2.4 summarizes the characteristics of the main bimetallic NPs synthesized by the polyol method.

Table 2.3 A summary of metal salts, reducing agents, stabilizers, solvents during synthesis of metals NPs synthesis via polyol method.

Au nanoparticles

<b>Metal salt precursor</b>	<b>Reducing agent</b>	<b>Stabilizer / surfactant</b>	<b>Solvent</b>	<b>Reaction temp. (°C)</b>	<b>Shape</b>	<b>Size (nm)</b>	<b>Reference</b>
Chloroauric acid (HAuCl <sub>4</sub> )	Ethylene glycol	NaOH	Ethylene glycol	R. T	Multispiked nanoparticles	75	Nalawade et al. 2012
HAuCl <sub>4</sub>	Ethylene glycol	poly(diallyldimethylammonium) chloride (PDDA)	Ethylene glycol	195	Octahedra	50	Li et al. 2008
HAuCl <sub>4</sub>	Ethylene glycol	PDDA, HCl	Ethylene glycol	195	Octahedra	60-320	Li et al. 2008
HAuCl <sub>4</sub>	Ethylene glycol	PDDA, NaOH	Ethylene glycol	195	Octahedra	20	Li et al. 2008
HAuCl <sub>4</sub>	Di-ethylene glycol	PVP	Di-ethylene glycol	240	Decahedra, truncated tetrahedra	50-100	Seo et al. 2008
HAuCl <sub>4</sub>	1,5-Pentanediol	PVP/AgNO <sub>3</sub>	1,5-Pentanediol	240	Polyhedra	64-140	Seo et al. 2006

Ag nanoparticles

<b>Metal salt precursor</b>	<b>Reducing agent</b>	<b>Stabilizer / surfactant</b>	<b>Solvent</b>	<b>Reaction temp. (°C)</b>	<b>Shape</b>	<b>Size (nm)</b>	<b>Reference</b>
Silver nitrate	Ethylene glycol	PVP	Ethylene glycol	160	Spheres	10	T. Zhao et al. 2010
Silver nitrate	Ethylene glycol	PVP	Ethylene glycol	148	Truncated cubes and tetrahedrons	20-80	Wiley et al. 2004
Silver nitrate	Ethylene glycol,	PVP	Ethylene glycol	160	Polyhedrons	175 ± 13	Y. Sun and Xia 2002
Silver nitrate	Ethylene glycol, NaOH, KBr	PVP	Ethylene glycol	160	Nanowires	Dia. 16–22 nm & 20 nm long	Lee et al. 2016
Silver nitrate	Ethylene glycol	polyacrylamide	Ethylene glycol	135	Triangular nanoplates	Length 25 nm & 10 nm thickness	Xiong et al. 2007
Silver nitrate	Ethylene glycol NaCl	PVP	Ethylene glycol	180	Nanowires	2.2–11.4 µm long	Schuette and Buhro 2013
Silver nitrate	1,2-PD/toluene	Dodecanethiol	1,2-PD/toluene	188	Nanowires	< 50 µm long	Viau et al. 2003
Silver nitrate	Ethylene glycol	PVP + Na <sub>2</sub> S (1 mM) + Na <sub>2</sub> S (1 mM)	Ethylene glycol	microwave	Spheres Cubes Nanowires	80–100 nm 70–90 nm 60–100 nm	Liu et al. 2016

## Cu nanoparticles

<b>Metal salt precursor</b>	<b>Reducing agent</b>	<b>Stabilizer / surfactant</b>	<b>Solvent</b>	<b>Reaction temp. (°C)</b>	<b>Shape</b>	<b>Size</b>	<b>Reference</b>
Copper (II) sulfate	Sodium phosphinate monohydrate	(PVP)	Di-ethylene glycol	200 & 140	spheres	53± 13 nm & 48 ± 8 nm	B. K. Park et al. 2007
Copper acetate	ethylene glycol	Tween 80	Ethylene glycol	190	spheres	36 ± 8 nm	Ramyadevi et al. 2012
Copper oxides	D-sorbitol	PVP	Ethylene glycol	195	Spheres	0.46 - 4.23 μm	Fievet et al. 1993
Copper sulfate	NaOH/NaBH <sub>4</sub>	PVP	Ethylene glycol	R.T. (N <sub>2</sub> atm.)	Spheres	1.4 – 3.1 nm	Zhang et al. 2009
Copper chloride	NaOH	-	Ethylene glycol	185 (N <sub>2</sub> atm.)	Spheres	2.3 ± 0.8 nm	Zhang et al. 2014
Copper chloride	Na <sub>3</sub> C <sub>6</sub> H <sub>5</sub> O <sub>7</sub> / NaBH <sub>4</sub>	-	Di-ethylene glycol	100 (N <sub>2</sub> atm.)	Spheres	20 ± 3 nm	Kind et al. 2012
Copper nitrate	-	PVP	Ethylene glycol	160 (N <sub>2</sub> atm.)	Nanowires	Dia. 30–50 nm & 20 mm long	Zhao et al. 2012
Copper (II) hydroxide	L-ascorbic acid	Polyethylene glycol	Ethylene glycol	80	Spheres	150 nm	Zhang et al. 2014

R.T.-Room temperature

Table 2.4 Synthesis parameters and observed results of the different bimetallic NPs prepared via polyol method.

<b>Metal salt precursor</b>	<b>Reducing agent</b>	<b>Stabilizer / surfactant</b>	<b>Solvent</b>	<b>Reaction temp. (°C)</b>	<b>Bimetallic NPs</b>	<b>Shape</b>	<b>Size (nm)</b>	<b>Ref.</b>
Chloroauric acid & silver nitrate	Cetyltrimethyl ammonium bromide	PVP	Ethylene glycol	40	Au-Ag	Nanowires	70-80	Gu et al. 2009
Palladium (II) trifluoroacetate & silver trifluoroacetate	Ethylene glycol	PVP	Ethylene glycol	160	Pd-Ag	Porous coral-like structure	400	Song et al. 2015
Silver nitrate & copper acetate	Ethylene glycol	PVP	Ethylene glycol	175 (Ar atmosphere)	Ag@Cu	Spheres	200-250	Tsuji et al. 2010
Silver nitrate & copper nitrate	Ammonium hydroxide	PVP	Ethylene glycol	160	Ag-Cu	Spheres	40-150	Niknafs et al. 2017
Silver nitrate & copper acetate	Ethylene glycol	PVP	Ethylene glycol	196 (N <sub>2</sub> atmosphere)	Cu@Ag	Spheres	80	Tsuji et al. 2009
Silver nitrate & copper acetate	Ethylene glycol	PVP	Ethylene glycol	175 (N <sub>2</sub> atmosphere)	Ag-Cu	Spheres	40	Yun et al. 2008
Copper carbonate & nickel carbonate	Ethylene glycol	PVP	Ethylene glycol	140 for 39 h	Cu-Ni	Spheres	100-300	Bonet et al. 2003
Copper nitrate & Nickel nitrate	Ethylene glycol	PVP	Ethylene glycol	196 for 4 h	Cu@Ni	Spheres	140	Bonet et al., 2003

- Random alloys, @ core-shell alloy



## 2.5.2 Solution combustion method

In mid-80's an unusual time- and energy-saving approach for synthesis of nanoscale materials was invented and termed as solution combustion synthesis (SCS). SCS is emerging as a low temperature, facile and economically feasible technique, where sufficient heat generates during the redox reaction between the oxidizers and organic fuel compensates the external heat needs to be supplied to synthesize oxides with high purity and well-crystallized nanostructure. During the redox reaction, electrons are transferred between the fuel and oxidizer; chemical energy of the fuel is converted into heat. The number of electrons involved in the reaction decides the intensity of redox reaction, but effective complexation of metal cations with fuel reduces the number of electrons, which participate in the redox reaction. Fig. 2.4 illustrates the procedure involved in the SCS; (1) preparation of homogeneous solution made of oxidizer, fuel and solvent, (2) formation of gel by heating the solution to the temperature near or above the boiling point of solvent, and (3) combustion of gel. After few seconds, soft and fluffy foam is obtained, which is further crushed into the powders by simple mechanical means (Deganello and Tyagi 2018).

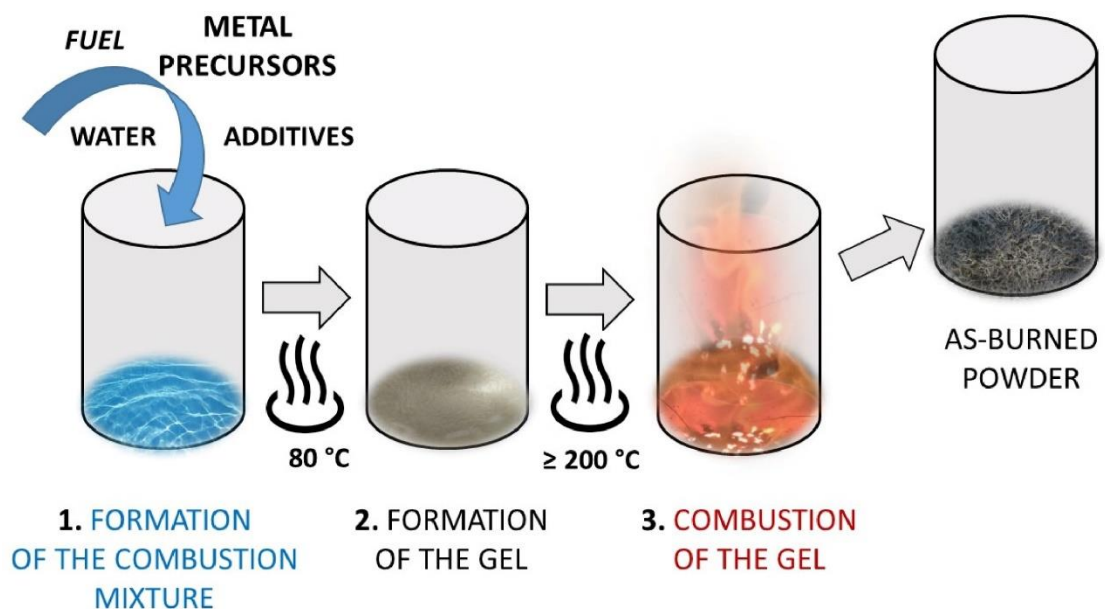


Fig. 2.4. Schematic illustration of solution combustion synthesis method (Deganello and Tyagi 2018).

The components of SCS can be categorised based on the chemical composition as follows; (i) oxidizers such as ammonium nitrates, nitric acid, metal salts including sulphates, carbonates, nitrates, (ii) fuels serve as reducer and complexing agents such as urea, glycine, citric acid, sucrose, glucose, carbohydrazide, acetylacetone and starch etc. and (iii) solvents, like water, kerosene, ethanol, methanol, formaldehydes etc (Varma et al. 2016). SCS offers phase purity materials with high reactivity and tailored defects, which have potential applications in different fields namely energy storage devices, catalysis, sensoristics and electronics.

The solution combustion reactions occurred in any systems (oxidizers and fuel) can be affirmed on the basis of thermogravimetric analysis (TGA) and differential scanning calorimetry (DSC) plot of solution containing oxides, fuels and solvent. Guo et al illustrated the combustion reaction of zinc nitrate and citric acid system, in which zinc nitrate and citric acid were dissolved in the deionised water. Fig. 2.5 depicts the TGA/DSC plot for the combustion reaction of zinc nitrate - citric acid system.

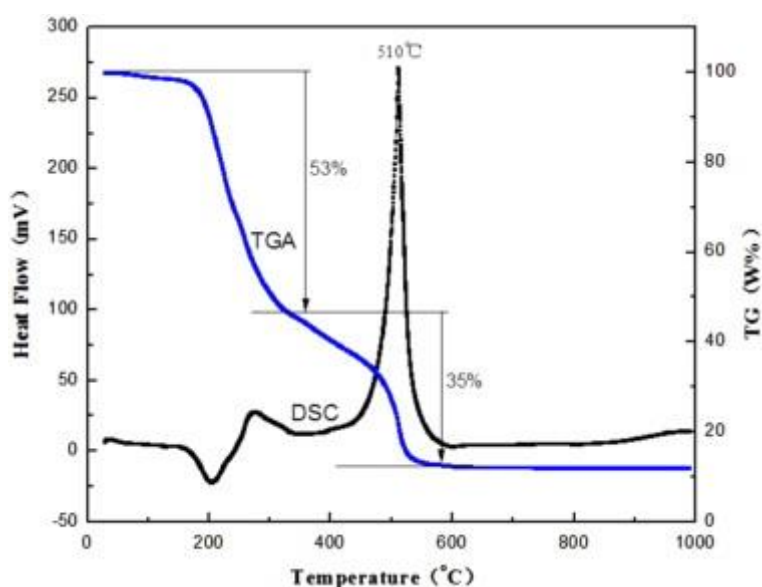


Fig. 2.5 TGA/DSC curve of the zinc nitrate and citric acid precursor system (Guo and Peng 2015).

The TGA curve showed the about 53 % and 35 % weight loss occurred in the temperature range 200-300 °C and 480-520 °C respectively; whereas in DSC curve, high amount of heat was released at temperature 510 °C. An intense and sudden mass loss accompanied with heat generation was observed at temperature 510 °C, which

affirmed that the occurrence of combustion reaction. After 550 °C, no peaks were found in either of the curves which confirmed the formation of nanocrystalline ZnO as decomposition product (Guo and Peng 2015).

In SCS process, structural, optical, textural and electrical properties of synthesized metal oxides are influenced by the choice of fuel and fuel to oxidizer ratio (F/O) ratio. Potti *et al.*, synthesized ZnO with variable crystallite sizes (31–80 nm) and band gap (3.13–3.25 eV) using different fuels, like urea, glycine, citric acid, dextrose, oxalyl dihydrazide and oxalic acid (Potti and Srivastava 2012). Pathak *et al.*, synthesized ZnO with three fuels-glycine, citric acid, urea, where the luminance and antibacterial properties were investigated. ZnO powders obtained using citric acid were smaller in size and exhibited high antibacterial properties compared to the ZnO powders synthesised using urea and glycine as a fuel. It can be concluded that antibacterial properties are greatly affected by choice of fuels (Pathak et al. 2016). The particle size, electrical properties and photocatalytic activity of synthesized ZnO powder by using zinc nitrate as oxidizers and glycine as fuel with varying molar ratio of F/O. ZnO from the F/O ratio as 0.1 and 1.7 showed electrical conductivity in order of  $10^{-5}$  and  $10^{-7}$   $\text{Sm}^{-1}$  respectively. Electrical conductivity of ZnO increases with increasing in the F/O molar ratio (Naveen et al. 2013). The luminance properties of ZnO were also affected by the molar ratio of citric acid as fuel to zinc nitrate as oxidizer (Zhao et al. 2011).

Previously sol-gel techniques were employed for the fabrication of metal oxides films including thin and thick films, which found applications in sensors, TFTs, solar cells etc. The steps involved in the fabrication of metal oxides using sol-gel technique are sol-gel densification and removal of impurities; both steps require a processing temperature nearly more than  $> 500$  °C which is incompatible to plastic/flexible and inexpensive glass substrates. Recently, Kim et al., reported the fabrication of metal oxide films ( $\text{In}_2\text{O}_3$ ,  $\text{ZnSnO}_3$ ,  $\text{InZnO}_{2.5}$ ) at relatively lower processing temperature ( $< 450$  °C) using the solution combustion approach. Here, precursor solutions were obtained using indium nitrate, zinc nitrate and tin chloride as metal salts with ammonium nitrate as an oxidiser, acetylacetone or urea as a fuel and 2-methoxyethanol as a solvent. Prepared solutions were spin-coated on the silicon wafers followed by annealing at  $150 - 450$  °C for 30 min. The formation of high crystalline metal oxides ( $\text{In}_2\text{O}_3$ ,  $\text{ZnSnO}_3$ ,  $\text{InZnO}_{2.5}$ ) on silicon substrates through the combustion precursor was

confirmed by XRD and XPS (Kim et al. 2011). Chaudhary *et al.*, developed the pristine and La-doped ZnO screen printed films using the viscous combustion precursor. In this study, zinc acetate dihydrate and lanthanum trinitrate used as a metal precursor was dissolved in the solution made of ethylene glycol (solvent and binder) and monoethanolamine (fuel and stabilizer). The obtained solution was deposited on the glass substrates using screen printing and printed films were subjected to two-step annealing process first at 100 °C for 1 h which was followed by 500 °C for 10 min. XRD revealed the formation of nanocrystalline pristine and La-doped ZnO screen printed films with no secondary phases (Chaudhary et al. 2018).

## **2.6 Semiconducting metal oxide for gas sensing applications**

With the rapid and massive development of urbanization and industrialization in the past few decades, mainly by chemical, fertilizers, pharmaceuticals, explosives, pesticides, cosmetics, fabrics and petrochemical industries severely contributed to the air pollution. Health-related problems, causalities and property damages due to leakage and explosion become a big threat to the survival of living creatures. Exposure to small concentrations of gases causes irritation, which effects over eyes, nose, mouth, throat, etc. Serious health problems like dyspnea, pulmonary edema, long-term respiratory system disorder and even death may cause with exposure to high concentrations of gases (Liu et al. 2015; Pang et al. 2014). Higher concentrations of gases can be detected by smell because each gas have unique odours. But the human nose fails to detect a lower concentration of vapours and also to quantify the gas concentration. Hence it is extremely important to develop highly sensitive and reliable gas sensors able to trace low concentration of gases with low-cost. So, potent and real-time detection of the toxic and damaging gases using gas sensors at low cost, versatility with production, user-friendly and ability to detect a wide range of gases are needed (Barsan et al. 2007). Semiconductor metal oxides based conductometric gas sensors have dragged the great attention around the globe, because of its high gas response, less-toxic, good selectivity and portability (Wang et al. 2010).

### **2.6.1 Undoped metal oxide**

Many researches have been observed that the reversible interaction between the surface of a solid-state material and gas is a characteristic of gas sensors. These solid-

gas interactions can be detected by measuring the change in resistance, work function, capacitance, optical characteristics etc.; are recorded via electrodes, transistors, thickness mode transducers, diode arrangements and optical arrangements. Synthesized particles with different size and morphology, are processed in the form of pellets, thin and thick films, which are employed as a functional layer of gas detecting devices. Over the past decades, gas sensors have been classified based on the different sensing measurement methods and materials. Korotcenkov has classified the gas sensors based on the different measurement method and materials, such as electrochemical, thermal conductivity, catalytic combustion, infrared absorption and semiconducting metal oxide (SMO) gas sensor. Table 2.5 shows the comparison of classified gas sensors with respect to different parameters (Korotcenkov 2007).

Table 2.5 Comparison of performance of the different types of gas sensors (Korotcenkov 2007).

Parameters	Types of gas sensors				
	Electro-chemical	Thermal conductivity	Catalytic combustion	Infrared absorption	SMO
Sensitivity	B	D	B	A	A
Accuracy	B	B	B	A	B
Selectivity	B	D	D	A	C
Response Time	C	B	B	C	A
Stability	D	B	B	B	B
Durability	C	B	B	A	B
Maintenance	B	B	A	C	A
Cost	B	B	A	C	A
Suitability to portable instruments	D	B	B	D	A

A: Excellent, B: Good, C: Fair, D: Poor

The SMO gas sensor has advantages such as high sensitivity, easy maintenance, low cost and simplicity in function. In addition to this, versatility in various sensor architecture and ease integration with other components of the gas sensing devices makes the SMO gas sensors better than the other gas sensors as shown in fig 2.6. A SMO gas sensor is chemiresistive type sensor in which modulation in electrical

resistance of sensing layer is observed upon interaction with analyte gases. In this, sensing layer is positioned on the insulating substrates between two high conductive electrodes (commonly Au, Pt, Ag). It is also possible to use a SMO in the form of compressed pellet with sintered metal electrodes for the gas sensing measurements (fig. 2.6 (a)). Monica *et al.*, fabricated sensors to detect the water and oxygen adsorption on tin oxide ( $\text{SnO}_2$ ), where powdered tin oxide was positioned between the concentric tantalum cylinder electrodes (fig. 2.6 (b)) (Căldăraru et al. 1996). Gas sensing devices consist of sensing materials, which are deposited as a thin or thick film on substrates (fig. 2.6 (c-f)). Sensing materials can be fabricated on the substrates either above or beneath the two metallic electrodes.

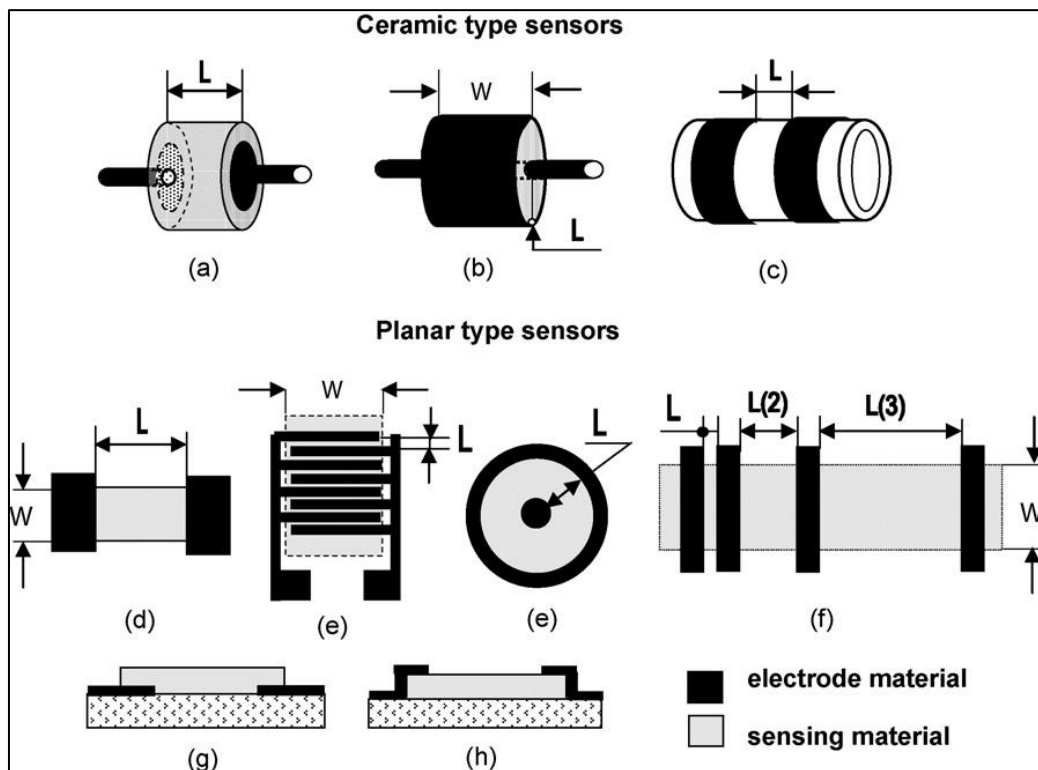


Fig. 2.6 Reported gas sensor geometries with different topologies of electrodes (Korotcenkov 2007).

The working principle of SMO gas sensors depend on the increase/decrease in electrical resistance of SMO in the presence of analyte gas, while retaining its original resistance in the absence of analyte gas. Electrical resistance of the SMO may decrease or increases upon exposure of analyte gas depending on the dominant charge carriers and type of gases as shown in Table 2.6. Gas sensing mechanism of n-type

semiconductor such as ZnO is described here. Under ambient conditions, adsorption of atmospheric oxygen on the gas sensing surface is taken place. These physio adsorbed oxygen molecules get disintegrate and extract the electrons from the material resulted in the formation of chemisorbed oxygen species ( $O^-$  or  $O^{2-}$ ). Disassociate oxygen molecules can extract the electrons from materials which are available within a certain depth (2 -100 nm) from the periphery is called as Debye-length ( $2L$ ). Due to electrons extraction, the region within Debye length depletes with dominant charge carriers ( $e^-$ ) caused to the formation of depletion region. Thereby, electron density in the gas sensing material decreases and causes to increase the resistance of the metal oxides. The Debye-length of the material influences the number of electrons which participate in the formation of chemisorbed oxygen species under ambient conditions. Particularly, crystallite size of the materials decides the Debye-length of the materials (Yamazoe et al. 2003). When the reducing gas is introduced, the chemisorbed oxygen species oxidize the analyte gases and release electrons to the material. When electrons are moved inside, electron density is increased and resistance of the oxide decreases. This modulation of resistance in the presence and absence of analyte gas is defined as the gas response.

Table 2.6 Electrical resistance of p- and n-type materials upon exposure of reducing and oxidizing gases.

Type of gases	Type of semiconductor materials	
	p-type (Holes ( $h^+$ ))	n-type (Electrons ( $e^-$ ))
Reducing gases Ex. $NH_3$ , $HCHO$ , $H_2$ , $H_2S$ , etc.	Resistance increases	Resistance decreases
Oxidizing gases Ex. $O_2$ , $O_3$ , $NO_x$ , $CO_2$ , $SO_2$ . etc.	Resistance decreases	Resistance increases

In the case of p-type semiconductor with holes as dominant charge carriers exhibits reverse modulation in resistance during loading and unloading of the analyte gases (Miller et al. 2014).

Gas response/sensitivity, selectivity, response and recovery time, resolution, limit of detection, stability are the main characteristics of gas sensors. Gas

response/sensitivity is defined in different ways depending on the type of semiconductor (p- and n-type) and type of gases (reducing and oxidizing). For n-type semiconductors, gas response is defined as a ratio of electrical resistance ( $R_g$ ) in the presence of analyte gas to electrical resistance ( $R_a$ ) in air when exposed to oxidizing gases, whereas it becomes  $R_a/R_g$  upon exposure of reducing gases. In the case of p-type semiconductors, these are exactly reversed. Gas response is a unitless parameter, is expressed as  $\left(\frac{R_a}{R_g} - 1\right)$  and sometimes it is also expressed in percentage as  $\left(\frac{R_a}{R_g} - 1\right) \times 100$  (Miller et al. 2014). Selectivity refers to an ability of a gas sensor to respond to the particular gas in a mixture of gases. Response and recovery times are defined as the time taken to achieve 90% of electrical resistance change during adsorption and desorption of the analyte gases, respectively. Resolution is defined as an ability of a gas sensor to distinguish the minimum difference of concentration. Limit of detection (LOD) is the lowest concentration of analyte gas, which can be detected by the sensor. Stability is referred to an ability of a gas sensor to reproduce the gas sensing results including response, selectivity, response and recovery time and LOD for a definite period of time (Bochenkov and Sergeev 2010; Dey 2018). High sensitivity, selectivity, resolution, and stability, faster response and recovery, small value of LOD are characteristics of an ideal gas sensor.

Gas sensing characteristics of semiconducting metal oxide gas sensors greatly depend on several factors such as grain size, particle size, thickness, surface area, morphology, porosity, lattice distortion, presence of additives and heterostructures, operating temperature, the concentration of oxygen vacancies and chemisorbed oxygen etc., (Zhu & Zeng 2017). Grain size is the important among the factors which influence the gas sensing characteristics. When the size of the grains becomes lower than the Debye length i.e., two times the depth of the space charge layer, then each and every grain is fully participated in the charge transfer mechanism. According to Ogawa *et al.*, when the grain size becomes smaller than Debye-length, whole crystallite act as a space-charge layer, which is caused to the maximum sensor response (Ogawa et al. 1982). When the grain size is same as the Debye-length, then the electrons flow through the necks formed between the grains, then the sensitivity defines as size dependency effect. For polycrystalline metal oxides with grain size which are larger



than the Debye-length, conductance of the sensing material is limited by Schottky barrier at inter-grain contact. Hence, the gas sensitivity is not solely dependent on the size effect (Dey 2018). Grains with smaller size cause the maximum gas response, but the extreme smaller grains depreciate temporal stability and structural stability by agglomeration (Korotcenkov 2008).

At present gas sensing properties of SMOs are evaluated using various gas sensor design, mainly – (i) thick film and (ii) thin film. G. Korotcenkov *et al.*, studied the influence of thickness on the gas response of  $\text{In}_2\text{O}_3$  thin film sensors towards the ozone and hydrogen gases. The response to ozone was declined to more than 100 times with increase of thickness from 20 to 400 nm. But in the case of  $\text{H}_2$  detection, response was increased with increased thickness from 20 to 400 nm. Researchers stated that larger grain size and diminished permeability are responsible for the decreased gas response towards ozone, whereas higher diffusion coefficient of  $\text{H}_2$  is reason for the increased gas response (Korotcenkov et al. 2004). Park *et al.*, observed that gas response of dip-coated  $\text{SnO}_2$  thin films towards the 1000 ppm of ethanol, increased from 4 to 11 with increase in film thickness up to 70 nm, afterwards it was started to decrease and ended up with gas response 7 against the film thickness 150 nm. The reason behind the cut-off point of the thickness, film with thickness up to 70 nm possessed the high porosity compared to other films with thickness 150 nm (Park and Mackenzie 1996). It is well known that gas response of thick film sensors is also dependent on thickness of the films. However, different researchers have noticed the effect of film thickness on the sensitivity in a different way. Some authors reported that gas response increased with increasing in film thickness, while others observed in a reverse trend and some studies revealed that high sensitivity achieved at lower thickness. Such disagreements reports confirm that the gas response/sensitivity of SMOs depends on numerous factors. But the parameter such as film thickness affects the sensor kinetics like response and recovery time. It is observed that response and recovery time increase with increasing in the film thickness of  $\text{In}_2\text{O}_3$  gas sensors upon exposure of ozone and  $\text{H}_2$ . Response and recovery times of gas sensor were spiked by 10-fold and increased to nearly two orders of magnitude, when exposed to  $\text{H}_2$  and ozone gases respectively (Korotcenkov et al. 2004). It is observed that quicker response and

recovery can be achieved in the gas sensors with lesser thickness, hence gas sensor designers should carefully consider the film thickness during fabrication.

Lattice disorder or lattice distortion in the film-based gas sensors is also an influencing parameter on the gas sensing characteristics mainly the sensitivity. The methanol gas sensing characteristics of Al-doped ZnO thin films fabricated using spray pyrolysis technique at different operating temperature were studied. The 0.5 at. % Al-doped ZnO thin film with smaller crystallites and less lattice distortion exhibited response nearly 3-fold higher than the undoped ZnO film (Sahay and Nath 2008). Lesser lattice disorder causes minimum scattering of the charge carrier, leads to larger change in resistance of the sensor upon exposure to target gases which results in higher sensitivity.

Apart from the factors such as grain size, lattice distortion, thickness etc., surface morphology of SMOs nanostructure also plays a vital role in gas diffusion during adsorption and desorption process. Various morphologies of SMOs nanostructures possess different specific areas and spatial structures which facilitates the gas diffusion in different ways. The desirable surface morphologies for the gas sensing applications can be obtained by controlling the relevant parameters of the synthesis methods. One dimensional nanostructure of SMOs such as nanorods, nanofibers, nanotubes, nanowires exhibited the excellent gas sensing performance. The aligned ZnO nanorods of flower-like shaped obtained by vapor phase transport technique showed a maximum sensitivity of 581 towards 5 ppm of H<sub>2</sub>S at room temperature and also good selectivity to H<sub>2</sub>S (Hosseini and Mortezaali 2015). Tungsten oxide (WO<sub>3</sub>) nanotubes synthesised by facile solvo-thermal method, exhibited the ultra-fast response (1 s) and recovery (19 s) during ethanol detection and also demonstrated the good selectivity to ethanol (Song et al. 2015). Cui *et al.*, studied the formaldehyde (HCHO) sensing performance of ZnO with different morphologies such as nanoplates, nanoflowers and nanofibers. 1D ZnO nanofibers were prepared by electrospinning process, whereas 2D ZnO nanoplates and 3D ZnO nanoflowers were obtained by sol-gel and hydrothermal methods respectively. 1D ZnO nanofibers sensor exhibited high response of 12 towards 100 ppm of HCHO at room temperature compared to sensors made of 2D nanoplate and 3D nanoflower-like ZnO structure (Cui et al. 2016).

In order to achieve good sensing characteristics of the film-based gas sensors, analyte gases should interact with volume area rather than the geometric layer of sensors. For example, in the compact films, analyte gases have interaction only with geometric layer, whereas porous film provides the volume area to interact with analyte gases. Therefore, the concentration of chemisorbed oxygen species formed in the volume interaction will be more than the geometric layer interaction, and it results in the high sensitivity. It is observed that gas sensing characteristics of  $\text{In}_2\text{O}_3$  films obtained by spray pyrolysis, mainly depend on the gas permeability or porosity than the grain size while detecting the reducing gases such as CO and  $\text{H}_2$  (Korotcenkov et al. 2004).

As well known, that, upon the introduction of oxygen vacancies in metal oxides, charge carrier concentration raises and affects the electrical properties. In the viewpoint of gas sensing properties, oxygen vacancies play a vital role in the enhancement of the adsorption process by triggering a pile of unpaired electrons to appear near the material surface, thus create a large number of active sites where the oxygen species get chemisorbed. The reasons for existence of oxygen vacancy ( $V_o$ ) in the metal oxides are (i) the non-stoichiometric relationship between the anions and cations and (ii) incorporation of impurities into the lattice. Usually, oxygen vacancies can be directly introduced during the synthesis of SMOs by tuning the pertinent conditions such as reaction temperature and time, the type and concentration of the precursor, etc. Oxygen vacancies can be generated by a post treatment of a synthesised SMOs. Peng *et al.*, employed one-step autocatalytic process to fabricate  $\text{ZnFe}_2\text{O}_4$  (ZFO)-based acetone sensors using the precursors tartaric acid (TA) and industrial  $\text{ZnFe}_2\text{O}_4$  (I-ZFO). During processing, different molar ratio of TA/I-ZFO was maintained to be 5:1 and 10:1. The XPS revealed that an around  $\sim 24.83\%$  of oxygen vacancies was present in I-ZFO, whereas the concentration of oxygen vacancies was increased to 28% and 40.22% in ZFO after autocatalytic reaction using molar ratio of 5:1 and 10:1 respectively. The gas sensing performance of ZFOs against 600 ppm of acetone were evaluated at optimal working temperature 280 °C. It was found that I-ZFO showed a sensitivity of 16, whereas as sensitivity of ZFO using molar ratio of 5:1 and 10:1 was found to be 36 and 70 respectively (Peng et al. 2019). Zeng *et al.*, studied the ethanol sensing performance of pristine and  $\text{SnO}_2$  samples after the  $\text{NaBH}_4$  treatment. The  $\text{NaBH}_4$  treated  $\text{SnO}_2$

sensors exhibited response of 120 towards 300 ppm of ethanol which was nearly 3 times higher than the pristine SnO<sub>2</sub>. XPS and PL detailed the reasons of enhanced response; the increased concentration of oxygen vacancies in the treated SnO<sub>2</sub> sensors triggers the strong chemisorption process and caused to generate the large number of chemisorbed oxygen species over the surface (Zeng et al. 2020). It was observed that solvothermal method employed to prepare In<sub>2</sub>O<sub>3</sub> with spindle-like nanostructure and rich oxygen vacancies. Sensor made of In<sub>2</sub>O<sub>3</sub> was subjected to methanol detection test at optimal working temperature 240 °C. Sensors exhibited superfast response (1 s) and recovery (10 s) along with sensitivity 27 against 100 ppm of methanol. It is found that two reasons are responsible for its excellent gas sensing performance: first, morphology offers larger specific surface area; second, presence of abundant V<sub>o</sub> increases the active centres on the surface of the materials. It is concluded that V<sub>o</sub> encourages to widen the electron depletion layer and facilitates the channels for electrons exchange between the adsorbed oxygen and conduction band of the material (Ma et al. 2019).

Unique characteristics such as wide bandgap of 3.37 eV, high mobility of charge carriers, high chemical and thermal stability, cohesive energy of 1.89 eV, made ZnO (n-type semiconductor) to detect the wide range of reducing gases and oxidizing gases by altering the resistance upon exposure to these gas molecules (Zhu and Zeng 2017). Moreover, non-toxic, ease of fabrication, low-cost, suitable for bulk production and also robustness in practical applications enhanced the usage of ZnO as a better sensing material than the other semiconducting metal oxides such as SnO<sub>2</sub>, In<sub>2</sub>O<sub>3</sub>, Fe<sub>2</sub>O<sub>3</sub>, NiO, WO<sub>3</sub>, RuO<sub>2</sub>, V<sub>2</sub>O<sub>5</sub>, Co<sub>3</sub>O<sub>4</sub>, MgO, CuO, CeO<sub>2</sub>, ZrO<sub>2</sub>, etc. (Eranna et al. 2004; Zhu and Zeng, 2017). Room temperature operated ZnO based gas sensors eliminate heaters thereby make still more portable and economical. In addition to this, room temperature operation facilitates the minimum usage of energy, limits the risk of a gas explosion, maintains the long-term stability of sensors and also avoid problems of the gas diffusion at the grain boundaries due to an unenviable drift problem raised by temperature-induced grain growth (Cui et al. 2016; Zhu and Zeng 2017).

### **2.6.2 Doped metal oxide**

Doping of elements during synthesis and deposition methods modify the properties of the SMOs, which helps in detection of the various analyte gases. Dopants

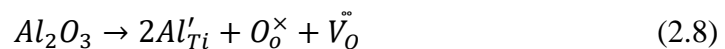
plays vital role in enhancing the pristine SMOs gas sensing characteristics like gas response, selectivity, LOD, stability, response and recovery time. Usually, dopants improve the properties of metal oxides, which are desirable for gas sensors, while the undesirable properties are suppressed or eliminated. Small addition of catalytically active materials to SMOs improves the response and selectivity of the gas sensors. Catalytic activity, microstructure and morphology of films can be modified with doping of transition metal in the SMOs. Dopants/impurities improve the gas sensing properties of the SMOs by (i) modifying the grain size and lattice distortion, (ii) transforming the morphology and porosity, and (iii) increasing the concentration of oxygen vacancies.

As well known, the grain size and lattice distortion are the factors which influence gas sensing performance. Doping of elements in the SMOs modifies its microstructural parameters such as grain size and lattice distortion. The sensors performance increases as the grain size decreases and most importantly sensor response spikes high, when the grains size becomes smaller than the Debye-length. The inhibition of grain growth of the metal oxides takes place, when the impurities/dopants are added. Dopants also play a vital role in the inhibition of grain growth even at high temperature results in the formation of smaller grains (Dey 2018). Renitta *et al.*, reported that a smaller crystallite size and the lesser strain was obtained due to chromium doping in ZnO films, enhanced the sensing performance from 10 to 50 towards hydrogen (H<sub>2</sub>) gas (Renitta and Vijayalakshmi 2016). Similar results were found in the Al-doped ZnO films fabricated using spray pyrolysis technique for detecting the methanol gas. 0.5 at. % of Al dopant reduced the crystallite size of ZnO from 396 nm to 97 nm; smaller crystallite and smaller lattice disorder upon Al doping helped in enhancing the gas response from 16 to 40 towards 500 ppm concentrations at operating temperature 280 °C (Sahay and Nath 2008). Satya *et al.*, investigated the effect of dopant concentration on acetylene sensing performance of In-doped ZnO (IZO) based sensors. The pristine and 1%, 3% and 5% of In (at. %) doped IZO films of thickness 100 nm were fabricated using thermal vacuum deposition. As the dopant concentration increased, the crystallite size also decreased from 20.4 to 14.5 nm. Gas response of IZO films increased with increasing dopant concentration up to 3 at. % and afterwards showed a decreasing trend with doping concentration. Not only smaller crystallite enhances the gas response, but also the smaller lattice distortion obtained

during doping plays a vital role (Dev et al. 2020). Selectivity of undoped ZnO was improved by doping 6 wt.% of Cu towards the 100 ppm of ammonia gas along with other gases such as acetone, LPG, CO<sub>2</sub> and SO<sub>2</sub> (Ganesh et al. 2018).

Some researchers studied the influence of dopant concentration on structural, morphological and gas sensing properties of In-doped ZnO films with different dopant concentration of 1%, 3%, 5% and 7% (in at. %), which were fabricated using SILAR method. Crystallite size was decreased with increased doping concentration. IZO films with dopant concentration 1 at. % showed granular structure, which transformed to nanoflower morphology with 3 at. %. Again, morphology of IZO films turned into the porous and granular after doping with 5 and 7 at. %. The 3 at. % In doped ZnO films with nanoflower morphology exhibited high gas response compared to the other films towards to 50 ppm of NO at working temperature of 167 °C (Soltabayev et al. 2019). Mani et al, investigated the effect of various transition metal dopants on morphological and gas sensing properties of ZnO thin films. Spray pyrolysis technique employed to fabricate a pristine and Co, Cu, and Ni-doped ZnO thin films. It was observed that upon doping Co element, nanorods structure was turned to tiny particles and irregular shaped nanorod. A greater agglomeration of particles was observed in Cu-doped ZnO, whereas randomly dispersed nanorods of length 200 nm was found in the Ni-doped ZnO. Pristine and Co, Cu, and Ni-doped ZnO thin films were subjected to detect the various analyte gases such as ammonia, acetone, ethanol, methanol, formaldehyde, toluene and acetaldehyde. Co-doped ZnO thin films with tiny particles with irregular shaped nanorods exhibited high response towards all the analyte gases compared to the other thin films (Mani and Rayappan 2016).

In addition to the modification of grains size and morphology in the SMOs upon doping, dopants also alter the concentration of oxygen vacancies which act as an electron donor site for the chemisorption process in the gas sensing mechanism. Doping of aluminium (Al) in TiO<sub>2</sub>, generates the oxygen vacancies and enhances the conductivity of TiO<sub>2</sub> metal oxide (equation 2.8). During Al doping, Al<sup>3+</sup> (ionic radius 0.067 Å) occupies the regular position of Ti<sup>4+</sup> (ionic radius 0.074 Å) in the TiO<sub>2</sub> lattice. In the TiO<sub>2</sub> lattice, Al will remain there as a defect with lone negative charge.



Studies on the effect of dopant on the oxygen vacancies of the SMOs gas sensors were reported (Al-Hashem et al. 2019), where concentration of oxygen vacancies were enhanced in Al-doped ZnO than the pristine ZnO nanoparticles synthesized through hydrothermal method, as a result the doped ZnO nanoparticles exhibited high gas response towards 20 ppm of 2-chloroethyl ethylsulfide. Similar results were observed in the Al-doped ZnO nanoparticles synthesized by flame spray pyrolysis method, amount of oxygen vacancies increased from 21 % to 37 % in doped ZnO, which led to the enhancement of gas response from 13 to 245 towards the 10 ppm of acetone at operating temperature of 450 °C. Gallium doped film fabricated using RF sputtering techniques exhibited high sensing performance towards 5 ppm of H<sub>2</sub>S than the pristine films because of the increased oxygen vacancies (Girija et al. 2018). Addition of nickel in SnO<sub>2</sub> nanoparticles increased the oxygen vacancies from 41 % to 50 %, thereby the gas response increased to 104 against 50 ppm of formaldehyde (Hu et al. 2018).

#### **2.6.2.1 Gas sensing mechanism of doped semiconducting metal oxides**

Fig. 2.7 illustrates the gas sensing mechanism of Cu-doped SnO<sub>2</sub>, which leads to an improved CO gas sensing performance compared to the pristine SnO<sub>2</sub> gas sensors (Karthik et al. 2016). Fig. 2.7 (a) depicts the adsorbed oxygen molecules present on the SnO<sub>2</sub> surface, which extract the electrons from the conduction band of SnO<sub>2</sub> and become chemisorbed oxygen species. Upon extraction of electrons from conduction band, electron depletion layer was formed in SnO<sub>2</sub> which result in increment of the electrical resistance. When the CO is exposed, chemisorbed oxygen species distributed over the SnO<sub>2</sub> surface oxidize the CO to CO<sub>2</sub> and result into the increment of electrical resistance (fig. 2.7 (b)). Modulation of electrical resistance in the absence and presence of analyte gas represents the gas sensing. In the case of Cu doped SnO<sub>2</sub> (ig. 2.7 (c)), pronounced chemisorption process was carried out by extracting the greater number of electrons and widens the electron depletion layer than the pristine SnO<sub>2</sub>. Reasons behind this could be due to (i) smaller crystallite size, (ii) morphology modification and (iii) increased oxygen vacancies. When CO comes in contact with surface, chemisorbed oxygen species, which spread in larger extent to participate in oxidization of CO gas into CO<sub>2</sub> (fig. 2.7 (d)). Simultaneously, large number electrons release back to the conduction band, which leads to formation of small charge depletion layer, thereby

electrical resistance decreases. The modulation of electrical resistance in doped SnO<sub>2</sub> is larger than the pristine SnO<sub>2</sub>, as a result gas sensing performance of doped SnO<sub>2</sub> increases. As Table 2.7, Table 2.8, and Table 2.9 show the effect of dopant on improved gas sensing performance through the modification of properties of the ZnO, SnO<sub>2</sub> and other SMOs.

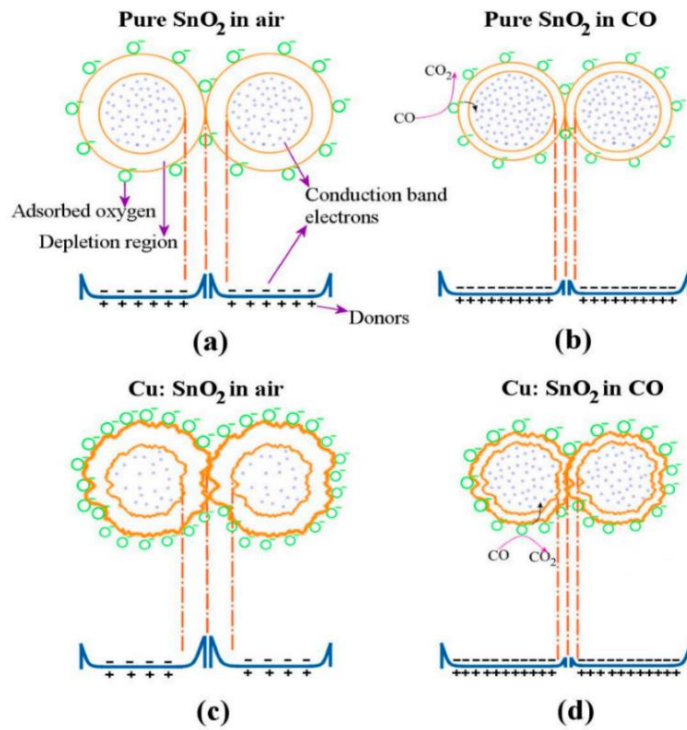


Fig. 2.7 Schematic gas sensing mechanism of (a) pristine SnO<sub>2</sub> and (b) Cu-doped SnO<sub>2</sub> towards CO (Karthik et al. 2016).



Table 2.7 A summary of doped ZnO gas sensors citing crystallite size, lattice distortion, morphology and oxygen vacancies ( $V_o$ ) as factors for improving the gas sensing.

Material	Dopant	Method	Morphology	Analyte gas	Gas Conc. (ppm)	Operating temp. ( $^{\circ}$ C)	Response	Cited effects	Reference
ZnO	Al 0.5 at. %	Spray pyrolysis	N. R	Methanol	500	275	44 <sup>b</sup>	Smaller crystallite and lattice distortion	Sahay and Nath 2008
ZnO	In 3 at. %	Thermal vapor deposition	Granular	Acetylene	100	150	29 <sup>c</sup>	Smaller crystallite and lattice distortion	Dev et al. 2020
ZnO	In 3 wt. %	SILAR	Nanoflower	NO	50	167	24.2 <sup>c</sup>	Crystallite and morphology	Soltabayev et al. 2019
ZnO	Al 1 at. %	Hydrothermal	Spherical	CH <sub>3</sub> CHO	10	500	2250 <sup>d</sup>	Increased specific surface area and $V_o$	Yoo et al. 2018
ZnO	Au 0.5 wt. %	Hydrothermal	Nanorods	CO NH <sub>3</sub> H <sub>2</sub> CH <sub>4</sub>	100 100 100 100	400 R. T. 400 R. T.	275 <sup>a</sup> 1546 <sup>a</sup> 350 <sup>a</sup> 360 <sup>a</sup>	Spill over mechanism	Shingange et al. 2016
ZnO	W 1 at. %	Spray pyrolysis	Granular	NH <sub>3</sub>	100	R. T.	2.2 <sup>a</sup>	Increased $V_o$	Ravichandran et al. 2020
ZnO	Al 6 at. %	Sol-gel	Nanoparticles	NH <sub>3</sub>	100	R. T.	350 <sup>a</sup>	Increased $V_o$	Navaneethan et al. 2017
ZnO	Al 1 wt.%	Flame spray pyrolysis	Nanoparticles	Acetone	10	450	245 <sup>d</sup>	High specific area and increased $V_o$	Yoo et al. 2019
ZnO	Ce 0.5 at. %	Precipitation	Flower-like	Ethanol	100	300	73 <sup>a</sup>	Increased $V_o$ and chemisorbed oxygen	Zhang et al. 2018

<sup>a</sup>  $\frac{R_a}{R_g}$    <sup>b</sup>  $\frac{R_a - R_g}{R_a} \times 100$    <sup>c</sup>  $\frac{R_g}{R_a}$    <sup>d</sup>  $\frac{R_a - R_g}{R_g}$    <sup>e</sup>  $\frac{R_a - R_g}{R_g} \times 100$    R. T. – Room Temperature   N. R. – Not Reported

Table 2.8 A summary of doped SnO<sub>2</sub> gas sensors citing crystallite size, lattice distortion, morphology and oxygen vacancies (V<sub>o</sub>) as factors for improving the gas sensing.

Material	Dopant	Method	Morphology	Analyte gas	Gas Conc. (ppm)	Operating temp. (° C)	Response	Cited effects	Reference
SnO <sub>2</sub>	Cd 3 wt. %	Hydrothermal	Nanorods	H <sub>2</sub> S	10	275	31 <sup>a</sup>	Increased V <sub>o</sub>	Sun et al. 2014
SnO <sub>2</sub>	Sm 1.5 at. %	Hydrothermal	Nanorods	Isopropanol	200	251	74 <sup>a</sup>	Increased V <sub>o</sub> and Spill-over mechanism	Zhao et al. 2018
SnO <sub>2</sub>	Co 3 mol. %	Electrospinning	Nanofibers	Ethanol	100	300	40.1 <sup>a</sup>	Crystallite size and Increased V <sub>o</sub>	Kou et al. 2016
SnO <sub>2</sub>	Er 3 %	Chemical method	Nanoparticles	Ethanol	100	280	48 <sup>a</sup>	High specific surface area and increased V <sub>o</sub>	Singh and Singh 2019
SnO <sub>2</sub>	Eu 2 mol. %	Electrospinning	Nanofibers	Acetone	100	280	32.2 <sup>a</sup>	Increased V <sub>o</sub>	Z. Jiang et al. 2016
SnO <sub>2</sub>	Zn 2.4 wt. %	Spray pyrolysis	Nanoparticle	CO <sub>2</sub>	500	310	94.4 <sup>b</sup>	Increased V <sub>o</sub>	Deepa et al. 2017
SnO <sub>2</sub>	Gd 3%	Co-precipitation	Irregular	Ethanol	250	280	138 <sup>a</sup>	Smaller crystallite size and increased V <sub>o</sub>	Singh and Singh 2017)
SnO <sub>2</sub>	Ni 5 at. %	Hydrothermal	Nanoparticles	HCHO	50	200	100 <sup>a</sup>	Increased V <sub>o</sub>	Hu et al. 2018
SnO <sub>2</sub>	Rh 0.5 mol. %	Electrospinning	Nanofibers	Acetone	50	200	61 <sup>a</sup>	Increased V <sub>o</sub>	Kou et al. 2018
SnO <sub>2</sub>	Ce 5 wt. %	Hydrothermal	Nanoparticles	Acetone	100	270	100 <sup>a</sup>	High specific surface area	Lian et al. 2017)

<sup>a</sup>  $\frac{R_a}{R_g}$    <sup>b</sup>  $\frac{R_a - R_g}{R_a} \times 100$    <sup>c</sup>  $\frac{R_g}{R_a}$    <sup>d</sup>  $\frac{R_a - R_g}{R_g}$    <sup>e</sup>  $\frac{R_a - R_g}{R_g} \times 100$    R. T. – Room Temperature   N.R. – Not Reported.

Table 2.9 A summary of doped In<sub>2</sub>O<sub>3</sub> and TiO<sub>2</sub> gas sensors citing crystallite size, lattice distortion, morphology and oxygen vacancies (V<sub>o</sub>) as factors for improving the gas sensing.

Material	Dopant	Method	Morphology	Analyte gas	Gas Conc. (ppm)	Operating temp. (° C)	Response	Cited effects	Reference
In <sub>2</sub> O <sub>3</sub>	Sn 5 wt. %	Solution combustion	Nanoparticles	Ethanol	1000	200	24 <sup>b</sup>	Smaller crystallite and High specific surface area	Ayeshamariam et al. 2014
In <sub>2</sub> O <sub>3</sub>	Pb 1 mol. %	Sonochemical	Nanoparticles	Ethanol	100	250	33 <sup>a</sup>	Increased defects	Montazeri and Jamali-Sheini 2017
In <sub>2</sub> O <sub>3</sub>	Ce 3 mol. %	Hydrothermal	Flower-like	Acetone	200	250	42 <sup>a</sup>	High specific surface area and carrier concentration	Wei et al. 2018
In <sub>2</sub> O <sub>3</sub>	Pr 3 mol. %	Solvothermal	Non-spherical	Ethanol	50	240	106 <sup>a</sup>	Increased V <sub>o</sub>	Ma et al. 2020
In <sub>2</sub> O <sub>3</sub>	Fe 5 mol. %	One-step Impregnation	Nanospheres	Ethanol	100	350	133 <sup>a</sup>	Small crystallite and morphology	Chen et al. 2019
In <sub>2</sub> O <sub>3</sub>	Mn 3 mol. %	Sol-gel	Nanoparticles	Methanol	50	300	17 <sup>a</sup>	Increased V <sub>o</sub>	Anand et al. 2016
				NH <sub>3</sub>		400	3.5 <sup>a</sup>		
				Ethanol		300	23 <sup>a</sup>		
				LPG		400	8 <sup>a</sup>		
In <sub>2</sub> O <sub>3</sub>	Ag 8 wt. %	Sol-gel	Nanoparticles	Acetone	25	350	18 <sup>a</sup>	High oxygen adsorption	Wang et al. 2009
				HCHO		100	28 <sup>c</sup>		
TiO <sub>2</sub>	Zr 7.5 wt. %	Nebuliser spray pyrolysis	Granular	NH <sub>3</sub>	450	250	118 <sup>d</sup>	Increased V <sub>o</sub>	Ravikumar et al. 2020
TiO <sub>2</sub>	Y 2 mol. %	Sol-gel	Nanoparticles	Ethanol	100	R. T.	225 <sup>a</sup>	Smaller crystallite Increased V <sub>o</sub>	Nithya et al. 2019
TiO <sub>2</sub>	Mn 1 mol. %	Hydrothermal	Nanoparticles	NH <sub>3</sub>	20	R. T.	378 <sup>a</sup>	Increased V <sub>o</sub>	Tshabalala et al. 2017

<sup>a</sup>  $\frac{R_a}{R_g}$    <sup>b</sup>  $\frac{R_a - R_g}{R_a} \times 100$    <sup>c</sup>  $\frac{R_g}{R_a}$    <sup>d</sup>  $\frac{R_a - R_g}{R_g}$    R. T. – Room Temperature   N. R. – Not Reported

### 2.6.3 Heterostructure metal oxides

A survey of literature informs that the heterostructure material also influence the gas sensing performance of the SMOs. Usually, dopants occupy the lattice position in the SMOs by substituting the parent cation, hence the modification of properties supports in improving the gas sensing performance. Heterostructure materials such as metals, metal oxide, polymers, etc., are added to the parent SMOs to improve the gas sensing characteristics mainly sensitivity and selectivity by the following mechanisms: (i) p-n and n-n potential barrier adjustment, (ii) catalytic spill-over, (iii) synergic effect and (iv) microstructure manipulation (Miller et al. 2014).

#### 2.6.3.1 Mechanisms to improve gas sensing performance of heterostructure metal oxides

##### Effect of p-n and n-n nanojunctions

The presence of secondary materials has a drastic effect on the improving gas sensing performance due to the formation of junction/interface between the heterostructure materials. Woong *et al.*, investigated the sensitivity and selectivity of p-type  $\text{Co}_3\text{O}_4$  decorated n-type ZnO nanowires gas sensors. In the  $\text{Co}_3\text{O}_4$ -ZnO heterostructure metal oxides, equilibrant fermi energies are achieved along with formation of depletion layer at p-n junction by transferring the electrons from high energy states to lower energy (fig 2.8 (a)). Depletion layer is formed at heterostructure junction due to the electron-hole recombination, which acts as the potential barrier for the movement of electrons (fig 2.8 (b)). The resistance of the  $\text{Co}_3\text{O}_4$ -ZnO heterostructure metal oxide is higher than the n-type ZnO under ambient. When  $\text{NO}_2$  (oxidising gas) was introduced, resistance was increased in a smaller extent, whereas the resistance of the material was decreased in a larger extent upon exposure to reducing gas ethanol. The value of  $R_a/R_g$  upon ethanol vapor exposure is higher than the  $\text{NO}_2$  gas exposure. Authors cited that  $\text{Co}_3\text{O}_4$ -ZnO heterostructure gas sensor showed a high sensitivity and selectivity towards the ethanol vapor due to the formation of depletion layer at the p-n junction (Na et al. 2011). Zeng *et al.*, reported that sensitivity of n-type  $\text{TiO}_2$  and n-type  $\text{SnO}_2$  heterostructure gas sensors was higher than the pristine  $\text{SnO}_2$  towards 50 ppm of VOCs such as methanol, ethanol, formaldehyde and acetone at operating temperature of 360 °C. It is proposed that electrons are flow from  $\text{TiO}_2$  to the  $\text{SnO}_2$  across the n-n heterojunction as shown in fig. 2.8 (c and d); hence there is a

formation of the electron depletion layer at  $\text{TiO}_2$ , and accumulation layer at  $\text{SnO}_2$ .  $\text{SnO}_2$  with high electron density facilitates the formation of additional chemisorbed oxygen species at the surface (Zeng et al. 2010).

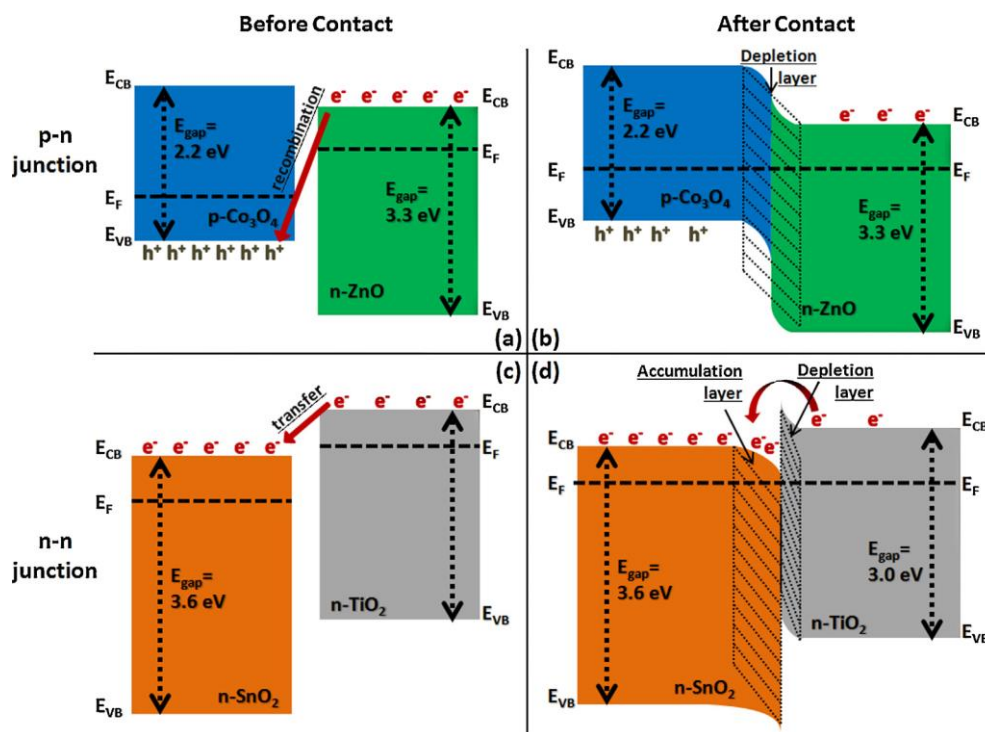


Fig. 2.8. Schematic illustration of band bending at interface of the heterostructure semiconducting (n and p-type) materials (Miller et al. 2014).

### Catalytic spill-over effect

The spill-over effect can be illustrated using heterostructure gas sensors in which noble metal nanoparticles such as Au, Pt, Pd are dispersed over the surface of the primary metal oxide. Nadargi *et al.*, studied the gas sensing performance of Ag loaded ZnO nanocomposites, when exposed to acetone vapor. The gas response was increased enormously from 56 to 71 upon loading of Ag on ZnO due to spill-over mechanism. The incorporated Ag not only acted as the surface sites for adsorption but also activated the surface catalysis and caused to the formation of high concentration of ionosorbed oxygen species (Nadargi et al. 2019). Liu *et al.*, demonstrated the spill-over and no spill-over effect on the ethanol sensing performance of the noble metals loaded  $\text{SnO}_2$ . The sensitivity ( $S$ ) of different noble metals loaded  $\text{SnO}_2$  was compared with the pristine and found as  $S_{\text{Au}} > S_{\text{pristine}} > S_{\text{Pd}} > S_{\text{Pt}}$ . The reason behind the enhanced

sensitivity is the spill-over effect due to an incorporation Au, which offers more sites for the adsorbates on the surface. Whereas in the case of Pd and Pt decorated SnO<sub>2</sub>, Pd and Pt nanoparticles were partially oxidised to PdO and PtO respectively. These oxides (PdO and PtO) inhibits the formation of active sites on the surface of the SnO<sub>2</sub>, hence the lesser concentration of chemisorbed oxygen species are generated and this mechanism is known as no spill-over effect (Liu et al. 2015).

### **Synergic effect**

It is an interesting mechanism in which two different ingredients of heterostructure materials comes in contact with analyte gas and serve the different purposes. In most of the literature, synergic effect is often called either as a non-interface dependent complementary behaviour or decomposition of intermediate reaction products. Sensitivity of the metal oxides towards the alcohol vapor was enhanced by further decomposition of intermediate products, which were generated from the oxidation reaction between alcohol and chemisorbed oxygen species dispersed over the surface of the metal oxide. Costello *et al.*, studied the gas sensing properties of SnO<sub>2</sub>, ZnO and SnO<sub>2</sub>-ZnO heterostructure towards the 1-butanol and found that SnO<sub>2</sub> was oxidised the butanol to butanal effectively and ZnO was failed to oxidise the butanol, but readily decomposed the butanal to CO<sub>2</sub> and H<sub>2</sub>O. Thus SnO<sub>2</sub>-ZnO heterostructure performed synergistically, completed the decomposition of butanol to end products and exhibited the high sensing performance(de Lacy Costello et al. 1999).

### **Manipulation of microstructure**

The Microstructural parameters such as grain size, lattice distortion influence the gas sensing performance of SMOs. Some literature reported that elemental doping offered desirable manipulation in grains and lattice disorder which helped in improving gas sensing performance. A series of literatures reported that an incorporation of secondary oxides such as ZnO, In<sub>2</sub>O<sub>3</sub>, TiO<sub>2</sub> and WO<sub>3</sub> restricted the grain growth of the SnO<sub>2</sub> nanoparticles effectively during crystallization at high-temperature. Hence, the controlled grain-growth phenomenon offered high gas sensing performance of the SnO<sub>2</sub> heterostructure gas sensors (Miller et al. 2014). Chen *et al.* studied the gas sensing performance of the ZnO-SnO<sub>2</sub> heterostructure which was synthesised by microemulsion method. Heterostructure with 40 mol% ZnO- 60 mol % SnO<sub>2</sub> exhibited

highest response 35 towards  $\text{NO}_2$ , while the pure crystalline  $\text{SnO}_2$  showed  $\text{NO}_2$  response of 7. The augmented gas response could be due to the smaller grains (5 nm) of  $\text{SnO}_2$  in 40 mol. %  $\text{ZnO-SnO}_2$  heterostructure compared to the pure crystalline  $\text{SnO}_2$  (19 nm) (Liangyuan et al. 2008). An addition of 20 mol. % of  $\text{WO}_3$  powders to  $\text{SnO}_2$  nanoparticles followed by a calcination at 600 °C, exhibited a higher response towards  $\text{NO}_2$  than the pristine  $\text{SnO}_2$ .  $\text{WO}_3$  suppressed the grain growth of  $\text{SnO}_2$ , which was ended-up with smaller crystallites and high specific surface area (S. Bai et al., 2010).  $\text{SnO}_2$  based heterostructure metal oxides exhibited high response towards the analyte gases CO and NO upon incorporation of 40 mol. %  $\text{In}_2\text{O}_3$ . Incorporation of secondary component  $\text{In}_2\text{O}_3$ , helps in formation of smaller grains, thereby the gas sensing ability of  $\text{In}_2\text{O}_3$  - $\text{SnO}_2$  heterostructure was enhanced compared to the pure  $\text{SnO}_2$  (Chen et al. 2006). Different heterostructure metal oxides sensors along with cited effects which are responsible for improving the gas sensing performance are tabulated in the Table 2.10.

Table 2.10 A summary of heterostructure metal oxide gas sensors citing mechanism responsible for improving sensitivity.

Material	Secondary component	Method	Morphology	Analyte gas	Conc. (ppm)	Operating temp. (° C)	Response	Cited effects	Reference
SnO <sub>2</sub>	TiO <sub>2</sub>	Colloidal mixing	Mixed nanoparticles	Ethanol Acetone	200 200	360	70 <sup>a</sup> 55 <sup>a</sup>	Electron accumulation layer at n-n junction	Zeng et al. 2010
ZnO	Cr <sub>2</sub> O <sub>3</sub>	Thermal evaporation	Nanowires	Trimethyl amine Ethanol	5 5	400	18 <sup>c</sup> 7.3 <sup>a</sup>	electron depletion layer at p-n junction	Woo et al. 2012
SnO <sub>2</sub>	WO <sub>3</sub> 20 mol. %	Two step sol-precipitation	Nanoparticles	NO <sub>2</sub>	200	200	186 <sup>c</sup>	Smaller crystallite and high specific surface area	Bai et al. 2010
SnO <sub>2</sub>	Ag 1 mol. %	Green synthesis	Nanoparticles	Acetone	1000	175	71 <sup>a</sup>	Spill-over	Nadargi et al. 2019
Au/SnO <sub>2</sub>	Au	Hydrothermal	Octahedral	Ethanol	400	350	230 <sup>a</sup>	Spill-over	Liu et al. 2015
SnO <sub>2</sub>	ZnO 40 mol. %	Microemulsion	Nanoparticles	NO <sub>2</sub>	500	250	35 <sup>c</sup>	Smaller crystallite	Liangyuan et al. 2008
SnO <sub>2</sub>	In <sub>2</sub> O <sub>3</sub> 40 mol. %	Co-precipitation	Nanoparticles	CO NO <sub>2</sub>	1000 450	250 150	16 <sup>a</sup> 7.5 <sup>c</sup>	Smaller crystallite and high specific surface area	Chen et al. 2006
SnO <sub>2</sub>	NiO 1 mol. %	Template-assisted	Flower-like	Ethanol	1000	320	576 <sup>a</sup>	p-n heterojunction	G. Sun et al. 2016
SnO <sub>2</sub>	Ni <sub>2</sub> O <sub>3</sub>	Arc-discharge deposition	Irregular	CH <sub>4</sub>	200	400	127 <sup>d</sup>	Synergic effects	Vuong et al. 2014
SnO <sub>2</sub>	NiO	Pulsed laser deposition	Nanoparticles	Trimethyl amine	10	220	48.6	p-n heterojunction	Ju et al. 2015

$$^a \frac{R_a}{R_g} \quad ^b \frac{R_a - R_g}{R_a} \times 100 \quad ^c \frac{R_g}{R_a} \quad ^d \frac{R_a - R_g}{R_g}$$



## **2.7 Reported screen-printed metal and metal oxide films**

### **2.7.1 Screen-printed Ag films and their applications**

Significant numbers of works have been carried out on the fabrication of thin films by screen printing process and performance of the thin films put into the applications. Prepared silver paste composed of 80 % of silver particles of size 50-100 nm, Pb free frit (< 1 %) and inorganic vehicle (20 %) were screen printed on alumina substrates and annealed at different temperatures from 250 °C to 450 °C with 50 °C increment and resistivity was found to be 7.14  $\mu\Omega\text{cm}$  at 250 °C, which was decreased to 4.11  $\mu\Omega\text{cm}$  at 450 °C. Thickness decreased from 8.8  $\mu\text{m}$  to 6.6  $\mu\text{m}$  with annealing temperature (Park et al. 2008). A resistivity of  $15 \times 10^{-8} \Omega\text{m}$  was measured to the screen printed film on the ferrite substrates at 850 °C for 10 min, in which paste was comprised of flake shaped silver particles (60-70%) (Songping 2007). Commercially available high viscous silver paste was deposited on a flexible polyethylene terephthalate (PET) substrate through screen printing technique and film was characterized with rms roughness of 7.986 nm, thickness of 12.2  $\mu\text{m}$  and electrical resistivity of  $5 \times 10^{-8} \Omega\text{m}$  (Adhikari et al. 2015). Formulated screen printing paste with 70-77% silver with particles size 2-3  $\mu\text{m}$  was transferred on the alumina substrates and sintered at 900 °C for 15 min, an electrical resistivity of 2.4  $\mu\Omega\text{cm}$  was reported (Faddoul et al. 2012). Screen paste consists of 70% of silver with particles size 3  $\mu\text{m}$  was screen printed on the Low temperature co-fired ceramics (LTCC) substrates which was annealed at 875 °C for 1 h and exhibited electrical resistivity of  $3 \times 10^{-8} \Omega\text{m}$ . Commercial Ag paste was screen printed on LTCC and cured at 875 °C, possessed an electrical resistivity of  $3 \times 10^{-8} \Omega\text{m}$  (Lahti and Lantto 2001). Formulated silver paste composed of silver with particles size 5  $\mu\text{m}$  and vinyl chloride based copolymer resin was screen printed on paper (square mass 80  $\text{g/m}^2$  and thickness 100  $\mu\text{m}$ ) substrate and sintered at 160 °C for 50 min exhibited resistivity of  $19 \times 10^{-8} \Omega\text{m}$  (Merilampi et al. 2009). The screen-printed patterns obtained from paste consists of silver particles of size 80 nm with an annealing temperature 200 °C, exhibited the resistivity of  $15 \times 10^{-8} \Omega\text{m}$  (Yin et al. 2008). Formulated ink containing a mixture of silver neodecanoate, solvent, and ethyl cellulose was printed on kapton substrates and sintered thermally at 250 °C, later found resistivity

$10.7 \pm 1.1 \times 10^{-8} \Omega\text{m}$  (Kell et al. 2017). Fig. 2.9 shows the resistivity of screen-printed silver films obtained from various formulated silver inks.

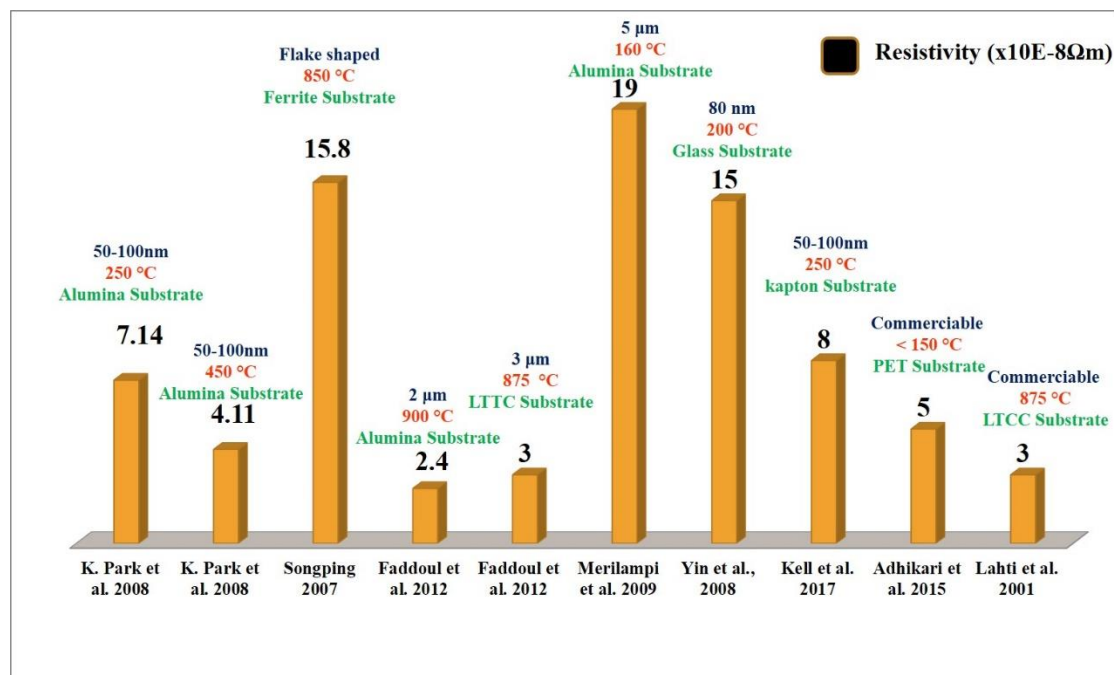


Fig. 2.9 Resistivity of screen-printed silver films reported in the literature.

Screen printing provides compact, robust, rugged and low-cost version reference electrode to replace the conventional electrodes. Zhou *et al.*, reported the array of top gated TFTs on rigid and flexible substrates in which source, drain and gate electrodes were screen printed using silver based conductive inks. Printed TFTs exhibited mobility up to  $7.67 \text{ cm}^2 \text{ V}^{-1} \text{ s}^{-1}$ , on/off ratio of  $10^4$ - $10^5$  with low voltage operation and excellent mechanical flexibility (Cao et al. 2014). Ag nanowires (6.6 % loading) based screen printing inks were used to fabricate source and drain electrodes in the array of TFTs. In this study, fabricated devices showed an average mobility of  $33.8 \pm 3.7 \text{ cm}^2 \text{ V}^{-1} \text{ s}^{-1}$  and on/off ratio of  $10^3$  (Liang et al. 2016). Screen printed electrodes obtained from the silver and carbon based conductive inks used in the organic thin film transistors with a channel length of  $30 \mu\text{m}$  (Lim et al. 2009). Ag nanoparticle-based screen-printed drain and source electrodes were used in the amorphous In-Ga-Zn-O TFTs array; devices exhibited high on/off ratio of  $\sim 10^7$  and the field effect mobility of  $2.8 \text{ cm}^2/\text{V s}$  (Ito et al. 2008).

### **2.7.2 Screen printed semiconducting thick films for gas sensing applications**

Numerous works have been reported on the screen-printed semiconducting films as a functional layer for the detection of various types of gases. Functional materials usually SMOs mixed with organic vehicles are screen printed on rigid and flexible type of substrates. Screen printing technique offers highly porous thick films which enhances the diffusion air/gas through underneath layer; hence effective extraction and insertion of electrons from and to the materials during adsorption and desorption respectively is possible. Patil *et al.*, reported that commercial ZnO powder was screen printed on a glass substrates and subjected to gas sensing characterisation and found highest response ( $S=21$ ) towards chlorine gas with concentration of 300 ppm at operating temperature 400 °C (Patil and Patil 2007). The granular and porous screen printed tin doped indium oxides (Sn-doped  $\text{In}_2\text{O}_3$ ) films on stainless steel substrates were employed for the detection of ammonia vapor. Sn-doped  $\text{In}_2\text{O}_3$  thick films exhibited high response to vapor concentration of 500 ppm of  $\text{NH}_3$  at working temperature 120 °C. A summary of gas sensing properties of screen-printed ZnO sensors are shown in Table 2.11

Table 2.11 A brief summary of the optimum gas response of screen printed ZnO gas sensors at various operating temperature towards exposed to different gases.

<b>ZnO powder synthesis</b>	<b>Analyte gas</b>	<b>Gas conc. (ppm)</b>	<b>Operating temp. T<sub>opt</sub> (°C)</b>	<b>Response (Approx.)</b>	<b>Ref.</b>
Commercial	NH <sub>3</sub>	1000	350	6	Wagh et al. 2006
Ball milling	H <sub>2</sub>	1000	400	28.05	Patil and Patil 2009
	LPG	1000	350	8.07	
Commercial	Ethanol	1000	350	12	Patil et al. 2007
Chemical Co - precipitation	NH <sub>3</sub>	90	Ambient	0.8	Rao and Rao 1999
Commercial	Cl <sub>2</sub>	300	400	21	Patil and Patil 2007
Sol-gel	Ozone	0.1	250	2.1	Carotta et al. 2009
	NO <sub>2</sub>	0.1	200	3.5	
	CO	50	450	2.1	
Vapour transport process and controlled oxidation	Ozone	0.1	300	2.8	Carotta et al. 2009
	NO <sub>2</sub>	0.1	300	2.5	
	CO	50	400	1.4	
Vapour –phase oxidation	Benzene	100	475	4.5	Z. Bai et al. 2010
	Toluene	100	475	9	
	Methanol	100	475	5.5	

## **2.8 Scope and objectives of the research work**

### **2.8.1 Scope**

Among the existing printing techniques, the screen-printing technique is a cost-effective and reliable method which can be used to print on substrate of interest in large-volume without the requirement of the sophisticated printing environment, such as high vacuum, inert gas-flow, high-grade clean rooms and so on. By considering these, conductive electrodes for the various devices, specifically TFTs can be fabricated through screen printing in large volumes with shorter time, but this also offers some challenges such as high thickness and high roughness which are not favourable. There is an attempt made to reduce the thickness and roughness of the films, thereby the TFTs devices can be worked efficiently. Screen printed films can also be employed to fabricate the active layer for the gas sensors because of the high porosity, which enables the analyte gases to have an optimum interaction with materials, hence the effective response can be obtained.

One of the frequent challenges in the screen-printing technique is clogging of pores in the screen mesh during screen printing. Here, the particles of size varying from nano to microns get stucked in the pores of screen mesh and block the ink to pass through these pores, which results in the fabrication of distorted patterns in the subsequent printing. To overcome this problem, particle free approach is employed in which screen-printing inks are made of precursor solution of the functional materials.

Presently, the screen-printed films are obtained from the particle-based approach, consisting of steps as follows (i) mixing of precursors, (ii) synthesis of functional material particles, (iii) calcination of functional material particles, (iv) preparation of organic vehicle, (v) mixing of functional material particles with organic vehicle, (vi) printing on substrates and (vii) followed by annealing of the printed patterns. But, novel particle-free approach, consisting of steps (i) direct mixing of metal salt into the organic vehicle, (ii) printing on the substrates and (iii) in-situ formation of ZnO films by annealing. Hence, particle-free approach bypasses the steps such synthesis and calcination of functional material like ZnO powder, thereby it consumes less-time than the previously reported works.

### 2.8.2 Objectives

The objectives of the present study encompass the fabrication of well adhered metal and metal oxide films for the applications such as gate electrode in TFTs and the sensing layer of the gas sensors via screen printing technique.

- ❖ To synthesize and characterize conducting (Ag, Ag-Cu) and semiconducting ( $\text{CaVO}_3$ , pristine and Sr-doped ZnO) functional materials for the formulation of screen-printable inks.
- ❖ To formulate particle-free (Ag, ZnO) and particle-based (ZnO,  $\text{BaSnO}_3$ ) screen printable inks to develop films on flexible and rigid substrates.
- ❖ To fabricate screen-printed silver patterns with a minimum thickness ( $< 3 \mu\text{m}$ ) and acceptable roughness.
- ❖ To develop and characterize the screen-printed silver gate electrodes for the TFTs.
- ❖ To fabricate and characterize screen printed semiconducting ZnO, Sr-doped ZnO,  $\text{BaSnO}_3$  and La-doped  $\text{BaSnO}_3$  films for sensing of hazardous gases.

## CHAPTER 3

# SYNTHESIS OF METAL, METAL ALLOY, METAL - OXIDE AND DOPED METAL-OXIDE FUNCTIONAL MATERIAL FOR THE FORMULATION OF SCREEN-PRINTING INKS

### 3.1 Introduction

This Chapter encompasses the preparation and characterization of functional materials namely Ag, Ag-Cu alloy,  $\text{CaVO}_3$ , pristine and Sr-doped ZnO particles of size varying from nano-to micro size which are compatible for the formulation of screen-printing inks. F.Fievet, and his researchers established a nanoparticles synthesis technique termed -polyol process was adopted to synthesis Ag and Ag-Cu nanoparticles in ethylene glycol medium. Whereas,  $\text{CaVO}_3$ , pristine and Sr-doped ZnO particles were synthesized via time and energy-saving method developed in mid-80's named solution combustion synthesis.

### 3.2 Experimental procedure

#### 3.2.1 Materials

All the chemical reagents used in the experiments were of analytical grade and used without further purification, which were silver nitrate ( $\text{AgNO}_3$ ; CDH Pvt. Ltd, India, (99.8% purity)), Cupric nitrate trihydrate ( $\text{Cu}(\text{NO}_3)_2 \cdot 3\text{H}_2\text{O}$ ; Molychem India, (99.5% purity)), Sodium borohydride ( $\text{NaBH}_4$ ; Molychem India (97% purity)), Ethylene glycol ( $\text{C}_2\text{H}_6\text{O}_2$ ; Spectrum reagent & Chemical Pvt.Ltd, India, (98% purity)) Polyvinylpyrrolidone (PVP - K30, MW 40000; SRL Pvt. Ltd, India), Vanadyl acetylacetonate ( $(\text{C}_{10}\text{H}_{14}\text{O}_5\text{V})$ ; Tokyo Chemical Industry CO., LTD., (95% purity)), Calcium nitrate ( $(\text{Ca}(\text{NO}_3)_2 \cdot 4\text{H}_2\text{O})$ ; Molychem India, (99.5% purity)), Nitric acid ( $(\text{HNO}_3)$ ; NICE Chemicals Pvt. Ltd, Cochin, India, (70% purity)), Zinc Nitrate hexahydrate ( $\text{Zn}(\text{NO}_3)_2 \cdot 6\text{H}_2\text{O}$ ; SRL Pvt. Ltd India (99 % purity)), Urea ( $\text{CH}_4\text{NO}_2$ ; Spectrum Pvt. Ltd India (98% purity)), Citric acid ( $\text{C}_6\text{H}_8\text{O}_7$ ; Sigma Aldrich (Purity 99.5%)), Glycine ( $(\text{C}_2\text{H}_5\text{NO}_2$ ; SRL Pvt. Ltd India (99% purity)), and Strontium nitrate ( $\text{Sr}(\text{NO}_3)_2$ ; Molychem Pvt. Ltd India (99% purity)).

### 3.2.2 Synthesis of silver (Ag) and silver-copper (Ag-Cu) alloy nanoparticles

A 0.1 M solution of  $\text{AgNO}_3$  was prepared in ethylene glycol by dissolving 1.02 g of  $\text{AgNO}_3$  in 60 ml ethylene glycol using ultrasonication for 30 min. An amount of 10.2 g of PVP was dissolved in another 60 ml ethylene glycol in a three-neck round bottom flask by using a moderate stirring of 400 rpm and at a temperature of 100 °C in an oil bath. The temperature was kept same throughout the experiment. When this solution turned to light yellow colour  $\text{AgNO}_3$  solution was injected drop by drop at a rate of 2 ml/min. The reaction was allowed for 4 h at the same temperature and stirring rate. A brown colloidal solution was formed which indicated the formation of the PVP capped silver nanoparticles. The colloidal solution was then cooled down to room temperature. To remove the excess PVP, solution was dispersed in ethanol in 1: 3 (colloidal Ag solution: ethanol) ratio and centrifuge at 8000 rpm for 10 min.

During the synthesis of Ag-Cu alloys nanoparticles,  $\text{AgNO}_3$  and  $\text{Cu}(\text{NO}_3)_2 \cdot 3\text{H}_2\text{O}$  were dissolved in 50 ml of ethylene glycol separately. Ethylene glycol, sodium borohydride ( $\text{NaBH}_4$ ) and polyvinylpyrrolidone (PVP) served as the solvent, reducing agent and stabilizer, respectively. 4.2 gm of PVP was added in 100 ml of ethylene glycol and sonicated until it completely dissolved in ethylene glycol. Both the metal precursors and PVP solutions were transferred into three-necked round bottom flasks, which was kept in an oil bath at a reaction temperature of 150 °C with a rotation of 450 rpm for 4 h in an inert atmosphere inside the flask. Simultaneously, a solution made of 0.42 gm of  $\text{NaBH}_4$  and 50 ml ethylene glycol which is placed in an ice bath, injected into the former solution loaded in the flask at a rate of 2 ml/min. Fig. 3.1 illustrates the set-up for the synthesis of Ag and Ag-Cu alloy nanoparticles by poly-ol method. After observing the color change from light blue to gray, the colloidal solution was cooled down to room temperature. To remove the excess PVP, it was dispersed in ethanol with a ratio of 1: 3 (colloidal Ag and Ag-Cu solution: ethanol) followed by centrifugation at 8000 rpm for 10 min and washing step was repeated for three times. Ag and Ag-Cu alloy nanoparticles were collected and dispersed in ethanol solvent. The chemical reactions may occur during synthesis of alloy nanoparticles are as shown in equations 3.1 and 3.2. The films were developed on the glass substrate using the



formulated conducting Ag-Cu ink by pad printing process which was followed by annealing at 450 °C for 20 min under different atmosphere such as O<sub>2</sub>, N<sub>2</sub> and H<sub>2</sub>.

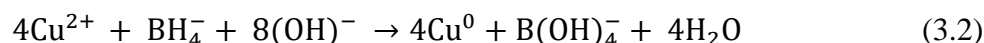
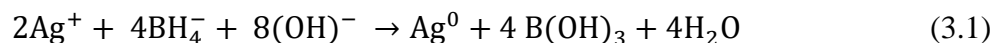


Fig. 3.1 Set-up for the synthesis of Ag and Ag-Cu alloy nanoparticles by poly-ol method.

### 3.2.2 Synthesis of calcium vanadium oxide (CaVO<sub>3</sub>)

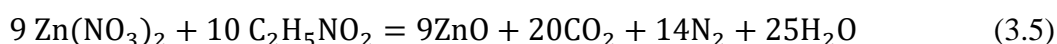
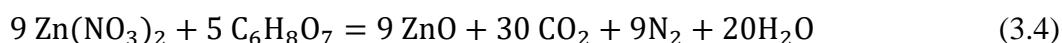
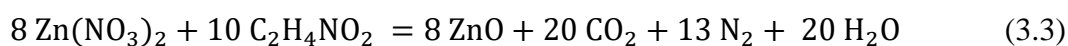
A stoichiometric amount of Ca(NO<sub>3</sub>)<sub>2</sub>·4H<sub>2</sub>O was dissolved in 8 M of de-ionized water in a beaker. Simultaneously, C<sub>10</sub>H<sub>14</sub>O<sub>5</sub>V was mixed with 635 μL of HNO<sub>3</sub>, and dissolved in 8 M of de-ionized water. Both the aqueous solutions were mixed together and stirred for 12 h. Films were deposited using drop cast technique onto different RCA-1 cleaned soda-lime-silica glass substrates and followed by annealing at different temperatures varying from 140 °C to 420 °C for 15 min.

### 3.2.3 Synthesis of pristine and strontium (Sr) doped zinc oxide (ZnO)

#### 3.2.3.1 ZnO particles using three fuels

ZnO particles were synthesised through solution combustion process using zinc nitrate (Zn(NO<sub>3</sub>)<sub>2</sub>) as oxidiser and three different fuels which are inexpensive and less

volatile due to their low calorific values; urea ( $-2.98$  Kcal/g), citric acid ( $-2.76$  Kcal/g) and glycine ( $-3.24$  Kcal/g). A stoichiometric quantity of all precursors used as per the balanced chemical equations 3.3, 3.4 and 3.5 are as follows;



Three separate transparent precursor solutions were obtained by dissolving the zinc nitrate (10 g) and individual fuel (urea: 5.28 g; citric acid: 5.63 g; glycine: 4.4 g) in DI water (20 ml). Homogeneous solution was heated at  $400$  °C to initiate the combustion reaction and resulted in the formation of voluminous, fluffy product and gases. Later, the ascombusted powder was ground using agate mortar and pestle to obtain fine powder and calcined at a temperature of  $600$  °C for 2 h.

### 3.2.3.2 Sr-doped ZnO particles using fuel-glycine

In this procedure, 10 g of zinc nitrate 0.1054 g of strontium nitrate and 4.4 g of glycine were dissolved in 15 ml of water and stirred for 40 min separately. Three separate precursor solutions were mixed and stirred for 15 min to obtain a stable and clear solution. Homogeneous solution was heated at  $300$  °C to carry out the combustion; as a result, voluminous, fluffy product and gases were produced. As-combusted powder was further crushed using an agate mortar and pestle and calcined at a temperature of  $600$  °C for 2 h.

### 3.2.4 Measurement and characterization

*Thermogravimetric analysis:* Thermal behavior of the combustible precursors were analyzed using thermogravimetric analyzer (TGA; Perkin Elmer, Thermo-gravimetric Analyzer TGA 4000) at heating rate of  $10$  °C/min in  $\text{N}_2$  atmosphere (30 ml/min).

*X-ray diffraction studies:* Phase formation and crystalline structure of the Ag, Ag-Cu alloy, pristine and Sr-doped ZnO particles and films of Ag-Cu alloy and  $\text{CaVO}_3$  obtained using pad printing and drop-casting were characterized using XRD (XRD; RIGAKU Miniflex 600) using Cu-K $\alpha$  radiation at a scanning rate of 1-2 °/min.

*Calculation of Lattice parameter:* Precise lattice parameter of the synthesized FCC Ag and Ag-Cu alloy NPs was extrapolated using Nelson-Relay function. Hexagonal closely packed structured ZnO particle's lattice parameter was calculated using Cohen's analysis method.

*Estimation of microstructural parameters:* The correction of the instrumental broadening  $\beta_{hkl}$  corresponding to the diffraction peaks was done using the following equation 3.6 (Mote et al. 2012):

$$\beta_{hkl} = [(\beta_{hkl}^2)_{measured} - (\beta_{hkl}^2)_{instrumental}]^{1/2} \quad (3.6)$$

The mean crystallite size of the Ag, Ag-Cu alloy and ZnO particles were estimated using Scherrer equation 3.7, as follows

$$D_v = \frac{k\lambda}{\beta_{hkl}\cos\theta_{hkl}} \quad (3.7)$$

where  $\beta$  defines FWHM of the peak (in rad) and value of k is 0.9 for spherical particles,  $\theta$  is the Bragg angle ( $^\circ$ ),  $\lambda$  is the wavelength of the Cu K<sub>a</sub> radiation X-rays (1.541 Å). Apart from the instrumental X-ray peak broadening, crystallite size and lattice strain are two components that contribute to the total peak broadening. Considering the two components, the total peak broadening can be written as an equation 3.8.

$$\beta_{hkl} = \beta_D + \beta_s \quad (3.8)$$

Equation 3.9 is obtained by substituting relations of broadening due to crystallite size  $\beta_D = \frac{k\lambda}{D_v\cos\theta}$  and lattice strain  $\beta_s = 4\epsilon\tan\theta$  in equation 3.8.

$$\beta_{hkl}\cos\theta_{hkl} = \frac{k\lambda}{D_v} + 4\epsilon\sin\theta_{hkl} \quad (3.9)$$

In Williamson-Hall Iso-Strain Model (W-H ISM), crystal is assumed to be isotropic in nature, in which strain induced in the particles are the same in all directions. Equation 3.9, which holds a straight line ( $y = mx + c$ ) behavior and a plot is drawn by considering  $\beta\cos\theta_{hkl}$  and  $4\sin\theta_{hkl}$  along the Y-axis and X-axis, respectively. Intercept and slope of the extrapolated line are used to estimate the crystallite size and lattice strain. According to Hooke's law, stress ( $\sigma$ ) has a linear relation with strain within the elastic limit and is given by  $\sigma = E\epsilon$ , and it is valid only for the smaller strain. In

Williamson-Hall Anisotropic Model (W-H ASM) deformation stress in all crystallographic directions are uniform, the strain ( $\varepsilon$ ) is replaced by  $\sigma/E_{hkl}$  in equation 3.9 and rewritten as equation 3.10. [23]:

$$\beta_{hkl} \cos \theta_{hkl} = \frac{k\lambda}{D_v} + \frac{4\sigma \sin \theta_{hkl}}{E_{hkl}} \quad (3.10)$$

Equation 3.10 follows a linear trajectory ( $y = mx + c$ ), a plot of  $y = \beta \cos \theta_{hkl}$  against  $x = 4 \sin \theta_{hkl} / E_{hkl}$ . Intercept and slope of the extrapolated line are used to estimate the crystallite size and deformed stress in the ZnO phase.

For the hexagonal crystal, Young's modulus relies on the crystallographic direction is given by equation 3.11,

$$E_{hkl} = \frac{\left[ h^2 + \left( \frac{h+2k}{3} \right)^2 + (al/c)^2 \right]^2}{s_{11} \left[ h^2 + \left( \frac{h+2k}{3} \right)^2 + (al/c)^2 \right]^2 + s_{33} (al/c)^4 + (2s_{13} + s_{44}) \left( h^2 + \left( \frac{h+2k}{3} \right)^2 \right) (al/c)^2} \quad (3.11)$$

where  $S_{11}$ ,  $S_{13}$ ,  $S_{33}$ ,  $S_{44}$ , and  $s_{11}$ , are the elastic compliances of ZnO and Sr doped ZnO with values of  $7.858 \times 10^{-12}$ ,  $-2.206 \times 10^{-12}$ ,  $6.940 \times 10^{-12}$ , and  $23.57 \times 10^{-12} \text{ m}^2 \text{ N}^{-1}$ , respectively.

In the Williamson-Hall Energy Density Model (W-H-EDM), ZnO and Sr doped ZnO crystals are assumed to be isotropic in nature. Lattice strain energy 'u' influences the constants of proportionality associated with stress-strain relation. According to Hooke's law,  $u = (\varepsilon^2 E_{hkl})/2$  and equation 3.9 can be modified as follows (3.12):

$$\beta_{hkl} \cos \theta_{hkl} = \frac{k\lambda}{D_v} + 4 \sin \theta_{hkl} \left( \frac{2u}{E_{hkl}} \right)^{1/2} \quad (3.12)$$

A plot is obtained by taking  $\beta_{hkl} \cos \theta_{hkl}$  and  $4 \sin \theta_{hkl} \left( \frac{2}{E_{hkl}} \right)^{1/2}$  along the Y-axis and X-axis. Slope and intercept of the extrapolated fitted lines are used to calculate the lattice strain energy density 'u' and crystallite size ' $D_v$ '.

The Halder-Wagner (HW) method is an alternative equation for the determination of  $D_v$  and  $\varepsilon$  more precisely, the total peak broadening from H-W equation (Izumi & Ikeda, 2015) is given by following equation 3.13:

$$\left( \frac{\beta_{hkl}}{\tan \theta} \right)^2 = \left( \frac{k\lambda}{D_v} \right) \cdot \frac{\beta_{hkl}}{\tan \theta \cdot \sin \theta} + 16\varepsilon^2 \quad (3.13)$$

Equation (3.13) follows a linear trajectory ( $y = mx + c$ ) in a same fashion as equation (3.7). A plot is drawn by taking  $(\beta_{hkl}/\tan\theta)^2$  and  $\beta_{hkl}/(\tan\theta \cdot \sin\theta)$  along Y-axis and X-axis, respectively. The slope and intercept of the extrapolated fitted lines are used to calculate the crystallite size ' $D_v$ ' and lattice strain ( $\epsilon$ ) respectively, where  $\beta_{hkl}$ ,  $\lambda$ ,  $\theta$  and  $D_v$  define the same as in equation (3.7), but the value of  $k$  is 0.9 and  $4/3$  for W-H and H-W methods respectively.

*Morphological studies:* Transmission electron microscopy (TEM; JEOL JEM-2010, Japan.) was used to understand the morphology and particle size of the Ag and Ag-Cu alloy nanoparticles dispersed in the ethanol. The surface morphologies with elemental analysis of the pad-printed Ag-Cu alloy and drop-casted  $\text{CaVO}_3$  films were discerned by using scanning electron microscope (JEOL model JSM 6380) with Energy-dispersive X-ray spectroscopy. To understand the composition and chemical state of elements present in the Ag-Cu alloy and  $\text{CaVO}_3$  films, X-ray photoelectron spectroscopy (XPS; PHI5000 Versa probe II) study was performed using Al  $K\alpha$  radiation ( $\sim 1486.6$  eV) as an excitation source.

*UV-vis Spectroscopy:* The optical properties of Ag, Ag-Cu nanoparticles,  $\text{CaVO}_3$  films were analyzed using UV-Vis Spectroscopy (USB4000-UV-VIS, Ocean Optics).

*Raman Spectroscopy:* Raman spectra was measured with a Micro-Raman spectrometer (Horiba Jobin Yvon) equipped with an integral microscope (Olympus BX 41) for better understanding of molecular structure.

*Fourier transform infrared spectroscopy:* The FTIR spectra of the  $\text{CaVO}_3$  drop-casted films were recorded by ATR mode in the wavenumber range of  $4000\text{--}650\text{ cm}^{-1}$  using FTIR (FT-IR, MAGNA 550, Nicolet Instrument Co.) to understand the different modes of element-element bonds.

*Particle size and count analysis:* The particle size distribution of ZnO and Sr-doped ZnO particles were measured by particle size analyzer (Horiba SZ-100).

*Thickness measurement:* The film thickness was estimated by a step profilometer (Ambios XP-2 Profilometer, SN 167).

*Resistance measurement:* The sheet resistance ( $R_s$ ) of the processed films was measured using a four-point probe instrument (SES Instruments Pvt. Ltd). Sheet resistances

(average of several measurements at different positions on the samples) were evaluated after considering proper correction factors based on sample geometries. The bulk resistivity ( $\rho$ ) of the films with thickness ( $t$ ) can be estimated using following relation (3.14):

$$\rho = R_s \times t \quad (3.14)$$

### 3.3 Results and discussion

#### 3.3.1 Characterization of synthesized silver (Ag) and silver-copper (Ag-Cu) alloy nanoparticles

The maximum surface plasmon resonance peak was found at 410 nm and 470 nm for synthesized Ag NPs and Ag-Cu alloy NPs respectively and their values were compared with the spectrum peak of the bulk Ag (320 nm) as shown in fig. 3.2. The UV-Vis spectrum peak of bulk Ag was observed at 320 nm due to the inter-band  $4d \rightarrow 5sp$  transitions, but the redshift of the peak to around 410 nm may be due to the occurrence of the plasmonic resonance phenomenon in the nano-dispersion of silver metal (Henglein. 1993). The UV-Vis spectrum shows the characteristic plasmon absorption peak which is due to the oscillation of free electrons.

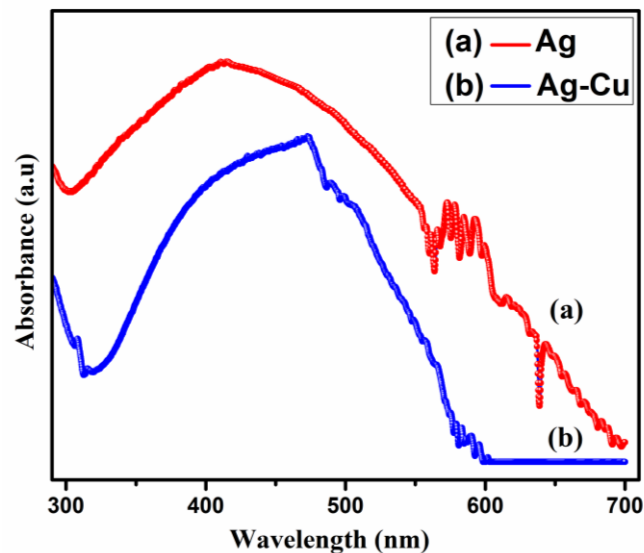


Fig. 3.2 UV-Visible absorption spectra of PVP capped nanoparticles of Ag and Ag-Cu alloy.

Position of surface plasmon resonance peak shifting towards the red or blue end of the optical absorption spectrum relies on many parameters such as nature of the metal

nanoparticle, its size, shape, state of aggregation, and the surrounding dielectric medium (Smitha et al. 2008). The peak of Ag-Cu lies in between the maximum absorption spectra of pure Ag (410 nm) and Cu (575 nm) which are available reported literature (Agnihotri et al. 2014; Rahman et al. 2015). The red shift of the surface plasmon resonance band of Ag-Cu alloy NPs in contrast with those of the pure Ag (410 nm) confirms the formation of Ag rich Ag-Cu alloy, not the heterogeneous monometallic particles of Ag and Cu metals (Huang et al. 2006). Broadening of the SPR may be arisen from the particle agglomeration and large particle size distribution. The position of the maximum SPR of the alloy NPs can be shifted by varying the molar ratio of elements.

In order to study the crystallinity of as-synthesized Ag and Ag-Cu alloy NPs and enumerate the crystallite size, X-ray diffraction measurements were carried out at room temperature and patterns were recorded as shown in fig. 3.3 (a). Four intense peaks of synthesised Ag nanoparticles were corresponding to the silver peaks and matched well with the ICDD pattern of Ag (ICDD: 00-004-0783). XRD pattern of synthesised Ag-Cu alloy nanoparticles showed intense peaks were positioned at  $2\theta$  equal to  $38.86^\circ$ ,  $45.15^\circ$ ,  $65.19^\circ$  and  $78.24^\circ$ ; these patterns did not match either with pure silver or pure copper literature reported values. The intensity of the diffraction peaks of Ag-Cu is relatively lower than the intensity of the diffraction peaks of Ag. The intensity of the peaks depends on the direction and degree of alignment of particles, types of atoms and also the kind of radiation used. During alloying, the Cu atoms substitute the Ag atoms in the Ag matrix, which is caused to the decrement of crystallinity and in parallel strain will be induced. Both, the crystallinity decrement and induced strain, may be the reasons for intensity reduction of diffraction peaks. The usage of Cu-K $\alpha$  radiation in lab-scale XRD instrument also could be another reason of intensity reduction. XRD patterns were compared with reported standard ICDD pattern of Ag (ICDD: 00-004-0783), there was a tiny shift of the peaks towards the smaller diffraction angle, which confirmed the formation of solid solution of silver and copper. It was indexed as (111), (200), (220) and (311) of FCC structure of the Ag rich Ag-Cu alloy (Choi et al. 2015). Ag-Cu alloy nanoparticles synthesized by the polyol method possess Ag rich phase. In the Ag rich phase Ag-Cu alloy nanoparticles, the peaks of the face-centred cubic (FCC) copper are not detected as is expected for a very small volume fraction. The reported

literatures revealed that peaks of Ag and Cu were not found in the Cu rich phase and Ag rich phase of bimetallic Ag-Cu alloy nanoparticles respectively. The intensity of the Ag and Cu peaks are pronounced in the Ag-Cu alloys XRD graph, when the Ag:Cu feed ratio is increases and decreases respectively (Ang and chin, 2005). The lattice parameter ‘a’ of each peak was calculated using the equations 3.15 and 3.16. h, k and l are the miller indices of the crystal plane (Cullity and Stock 2014). The lattice parameter of the Ag and Ag-Cu alloy nanoparticles obtained using equation 3.15 were extrapolated from the graph of Nelson-Relay function versus lattice constant shown in fig. 3.3(b).

$$a = \frac{\lambda(h^2+l^2+k^2)^{1/2}}{2\sin(\theta)} \quad (3.15)$$

$$F(\theta) = \left[ \frac{\cos^2\theta}{\sin\theta} + \frac{\cos^2\theta}{\theta} \right] \quad (3.16)$$

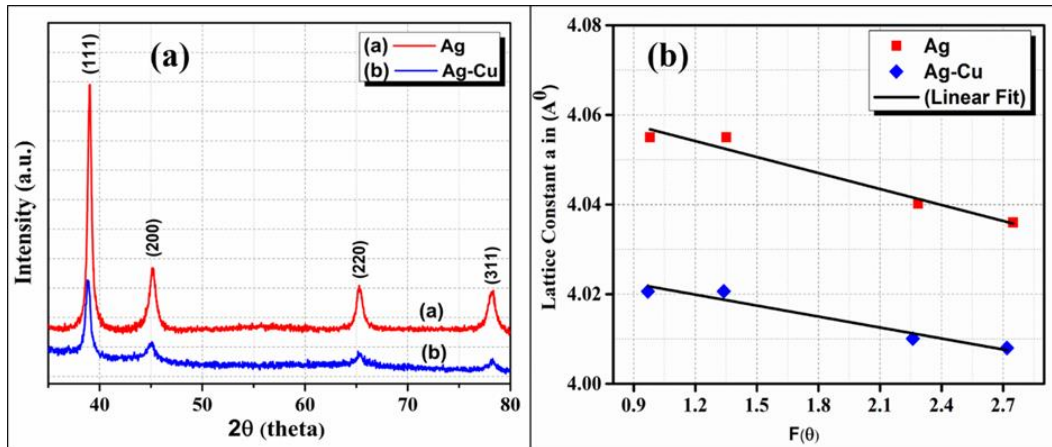


Fig. 3.3 (a) XRD pattern of Ag and Ag-Cu alloy NPs, (b) graph of Nelson-Relay function as a function of lattice constant.

The values of ‘a’ and  $F(\theta)$  of all indexed peaks were plotted along the Y-axis and X-axis respectively, the intercept of the linear fit straight line at y-axis was taken as lattice parameter. Lattice parameter of Ag and Ag-Cu alloy NPs are found to be 4.077 Å and 4.034 Å respectively. Lattice parameter values of the Ag-Cu lies in between the lattice parameter of elemental Ag and Cu are 4.089 Å and 3.615 Å respectively (Linde, 1966). Table. 3.1 shows the phases present and corresponding lattice parameters of Ag and Ag-Cu samples. The marginal reduction of the lattice parameter attributed to the formation Ag-Cu alloy NPs (Rahman et al. 2012), due to incorporation of Cu in FCC Ag phase, is a good agreement with other experimental results (Singh et al. 2009).



Table 3.1 Characteristics of Ag and Ag-Cu alloy nanoparticles with phases present, their corresponding lattice parameters and absorption peak position.

Sample	Phase observed	Lattice parameter ( $\text{\AA}$ )	$\lambda_{max}$ (nm)
Ag	Ag	4.077	415
Ag-Cu	Ag-Cu (Ag rich phase)	4.034	470

Crystallite size was estimated using Scherrer equation and these values were compared with W-H Iso-strain model (Venkateswarlu et al. 2010), H-W method and TEM analysis results. A W-H and H-W plot were drawn as depicted in fig. 3.4 (a) and (b). In W-H method, crystallite Size ( $D_v$ ) and Strain ( $\epsilon$ ) for Ag estimated to be 32 nm and  $3.15 \times 10^{-3}$  and for Ag-Cu alloy NPs to be 45nm and  $4.22 \times 10^{-3}$ . Whereas in H-W method, crystallite size of Ag and Ag-Cu alloy NPs were calculated to be 27 nm and 38 nm, while strain was  $7.04 \times 10^{-3}$  and  $4.28 \times 10^{-3}$ , respectively.

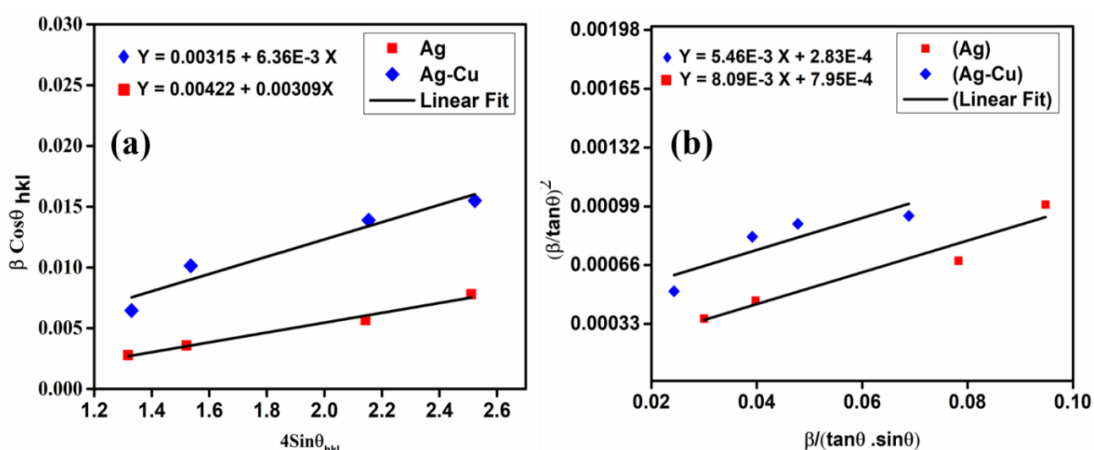


Fig. 3.4 (a) Williamson Hall-ISM plot and (b) Halder–Wagner plot of Ag, Ag-Cu alloy nanoparticles.

Fig. 3.5 (a) depicts the TEM images of Ag NPs reveals the particles owned distorted spherical morphology. The particles of Ag were broadly distributed in the range of 10 to 70 nm with an average particles size of  $33 \pm 19$  nm as shown in fig. 3.5 (b). Fig. 3.5 (c) shows the synthesised Ag particles, which are capped with PVP, hence uniform and stable dispersion of Ag NPs in the solvent is possible. The SAED pattern of Ag NPs (fig. 3.5 (d)) suggests that particles are polycrystalline in nature which is in good agreement with the X-ray diffraction studies. TEM images of Ag-Cu alloys NPs (fig. 3.6(a)) show the distorted spherical morphology of the particles. Ag-Cu particles were

narrowly distributed in the range of 30 to 55 nm with a particle size of  $48 \pm 15$  nm as observed in 3.6 (b). The synthesised Ag-Cu particles are capped with PVP as shown in fig. 3.6 (c), which enables the uniform and stable dispersion of Ag-Cu NPs in the solvent. The SAED pattern of Ag-Cu NPs (fig. 3.6 (d)) suggests that particles are polycrystalline in nature which is in good agreement with the X-ray diffraction studies (Choi et al. 2015). The computed micro-structural parameters of polyol synthesised Ag and Ag-Cu nanoparticles are tabulated in the Table 3.2.

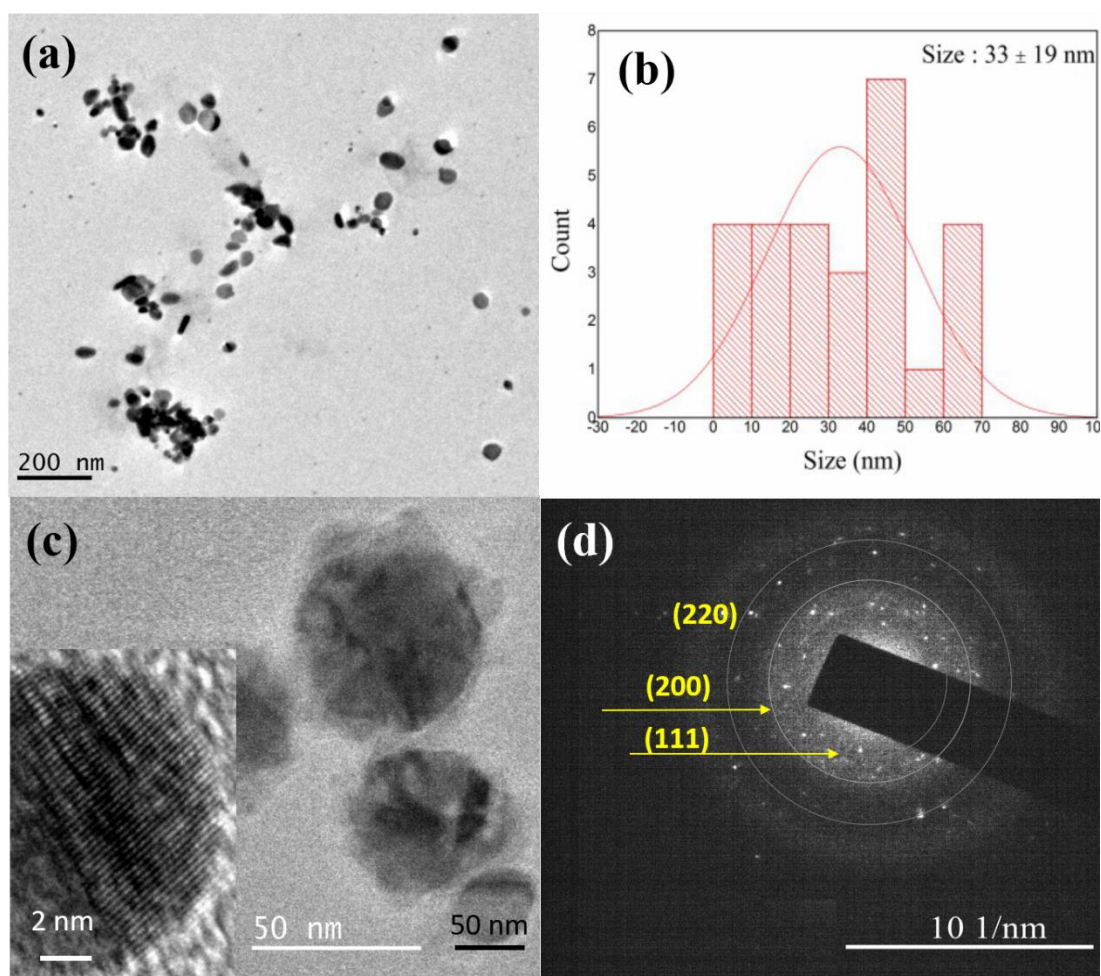


Fig. 3.5 TEM images of (a) synthesized Ag nanoparticles after washing with ethanol, (b) corresponding size distribution, (c) magnified view of nanoparticles and (d) SAED pattern.

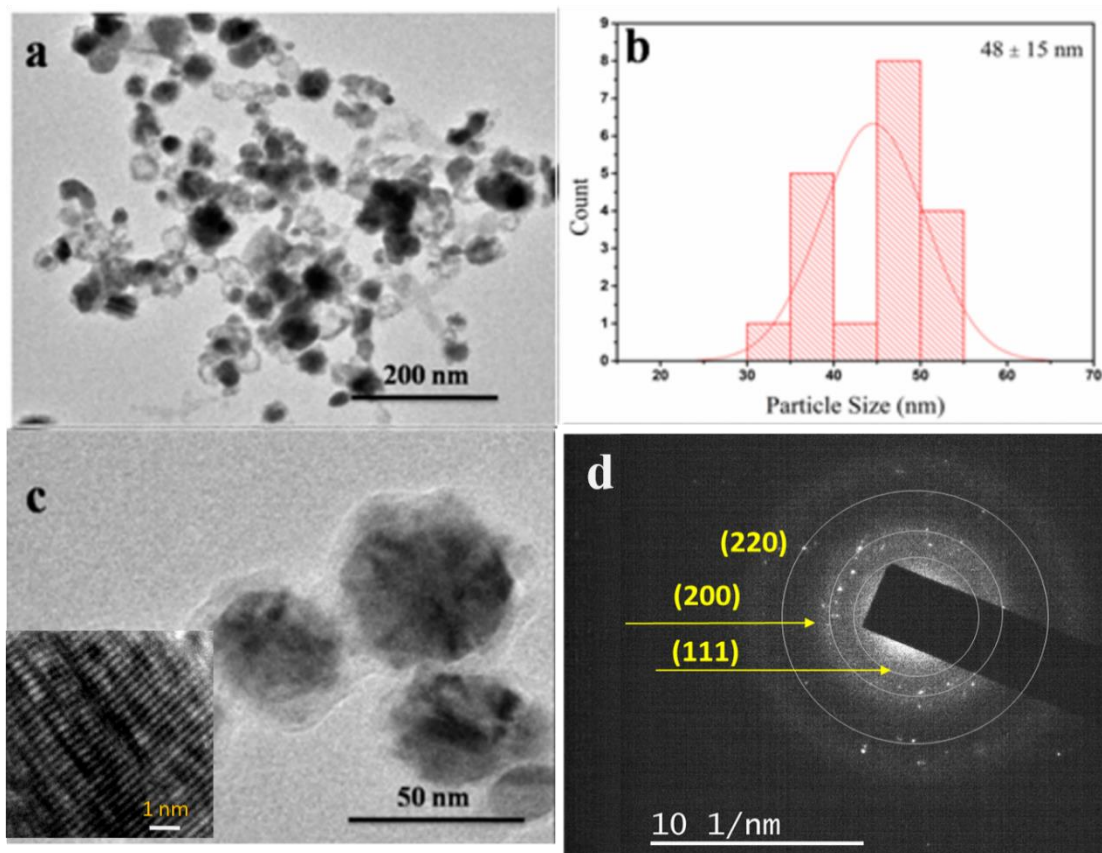


Fig. 3.6 TEM images of (a) synthesized Ag-Cu alloy nanoparticles after washing with ethanol, (b) corresponding size distribution, (c) magnified view of nanoparticles and (d) SAED pattern.

Table 3.2 The estimated micro structural parameters of synthesized Ag and Ag-Cu nanoparticles.

Sample	Scherrer analysis $D_v(\text{nm})$	W-H ISM analysis		H-W analysis		TEM analysis $D_v(\text{nm})$
		$D_v(\text{nm})$	$\epsilon \times 10^{-3}$	$D_v(\text{nm})$	$\epsilon \times 10^{-3}$	
Ag	16	32	4.22	27	7.04	33±19
Ag-Cu	22	45	3.15	38	4.28	48 ±15

In the Debye-Scherrer equation, peak broadening is only due to crystallite size. But in case of W-H and H-W methods, peak broadening includes not only crystallite size but also the lattice strain. This variation in crystallite size is largely attributed to the considering the lattice strain in the samples. The values obtained from the W-H method are more realistic than the H-W method (D Nath et al. 2020).

To confirm the capping of synthesized Ag-Cu alloy NPs with PVP, FT-IR characterization was done. FT-IR spectrum (fig. 3.7) was recorded in the range from  $4000\text{ cm}^{-1}$  to  $400\text{ cm}^{-1}$ , in which structural properties of the PVP capped Ag-Cu alloy NPs in ethanol was compared with PVP in ethanol. The broad band at  $3374.86\text{ cm}^{-1}$  and peak at  $1045\text{ cm}^{-1}$  signifies the O-H and C-O symmetric stretching of covalent bond in ethanol respectively (Doroshenko et al. 2013; Vahur et al. 2016). PVP exhibits characteristic absorption peaks in the FTIR spectrum at the frequencies  $2975\text{ cm}^{-1}$  and  $2925\text{ cm}^{-1}$ , is attributed to the asymmetric and symmetric stretching of C-H respectively. Further peaks at  $1287\text{ cm}^{-1}$  and  $879\text{ cm}^{-1}$  were due to the C-N stretching mode and C-C aromatic vibration mode respectively (Bernabò et al. 2017). Absorption peaks at  $1657\text{ cm}^{-1}$  and  $1078\text{ cm}^{-1}$  represent the C=O and C-N stretching vibration in PVP respectively. Due to the formation of bond and strong mutual interaction of PVP chain with Ag-Cu alloy surface atoms, the peak at  $1657\text{ cm}^{-1}$  attributed to C=O stretching was shifted to lower wave number  $1638\text{ cm}^{-1}$ . Due to chemical coordination with alloy atoms and C-N bond, the peak at  $1078\text{ cm}^{-1}$  was shifted higher wave number  $1085\text{ cm}^{-1}$  (Chahal et al. 2010; Sumit Sarkar and Das, 2017).

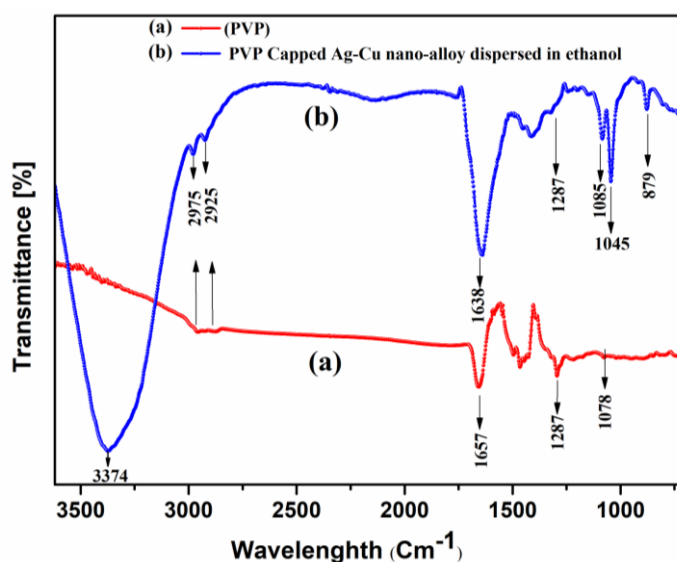


Fig. 3.7 FTIR Spectrum of (a) PVP and (b) PVP capped Ag-Cu alloys NPs dispersed in ethanol.

### Characterization of Ag-Cu alloy films

The conductivity of pad-printed Ag-Cu alloy films annealed at  $450\text{ }^{\circ}\text{C}$  for 20 min under different atmosphere such as  $\text{N}_2$ ,  $\text{H}_2$  and  $\text{O}_2$  was found to be  $6.6\pm 0.1\times 10^5$ ,  $2.5\pm 0.1\times 10^5$

and  $1.33 \pm 0.3 \times 10^5 \text{ Sm}^{-1}$  respectively. The reported highest conductivity of silver is in the order of  $10^7 \text{ Sm}^{-1}$  (Liu et al. 2013). Observing the conductivity of the Ag-Cu alloy thin films annealed under different atmosphere were two orders less as compared to the reported values of pure Ag. The reason behind the inferior conductivity may be due to oxidation of Cu element into its oxide form. In order to investigate the cause for lower conductivity, compared to pure Ag films were analysed through different characterization techniques.

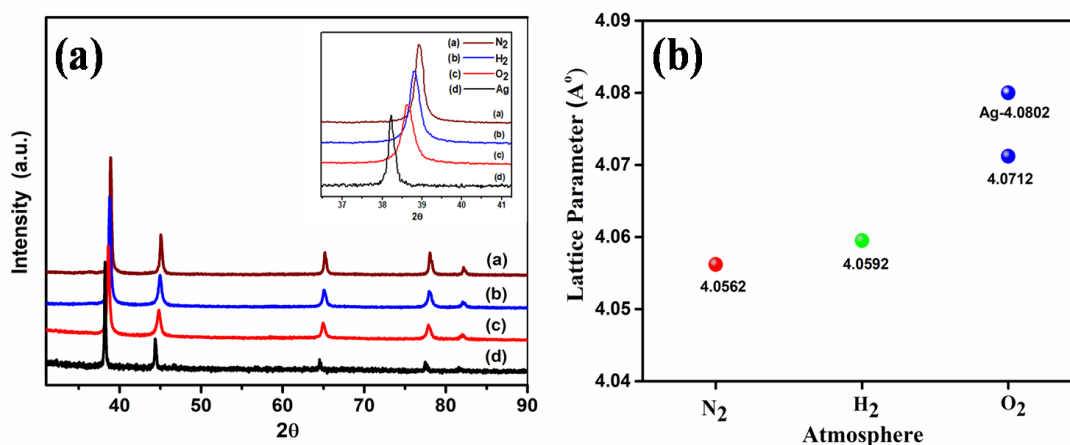


Fig. 3.8 (a). XRD pattern of Ag-Cu alloy thin films annealed under different atmosphere and Ag thin film annealed under O<sub>2</sub> atmosphere (b). The lattice parameter of Ag, Ag-Cu alloy film annealed under different atmosphere.

The XRD pattern of Ag-Cu thin films annealed under different atmosphere such as O<sub>2</sub>, N<sub>2</sub> and H<sub>2</sub> are reported in fig. 3.8 (a). In Ag-Cu thin films XRD patterns, only reflections of silver solid solution are identified by an offset in comparison with pure Ag peaks; is called as an Ag rich phase. The lattice parameter for the Ag-Cu alloy is least for films annealed in N<sub>2</sub> atmosphere (4.05 Å) and maximum at O<sub>2</sub> atmosphere (4.07 Å) as observed in fig. 3.8 (b). This may be due to oxidation of copper, in which oxygen may be reacted with copper to form copper oxides and leached from Ag-Cu alloy. Formed CuO is segregated from the alloy and retained with Ag rich parent structure (Hirsimäki et al. 2005). The synthesised Ag-Cu alloy nanoparticles dispersed in the ethanol to form ink and formulated ink was pad printed on the glass substrates. During the annealing of the film in the H<sub>2</sub> atmosphere, the green pad printed pattern consists of ethanol is oxidised into CO<sub>2</sub> and H<sub>2</sub>O. In Ag-Cu films XRD, the presence of oxidized CuO was not detected. The reason behind this could be that if any secondary

phase in the parent system has smaller volume fraction, then the detection of secondary phase is difficult using Cu-K $\alpha$  radiation as an incident x-ray. Similar observations have been found in the various systems such as rGO-ZnO nanocomposites (Meti et al. 2018).

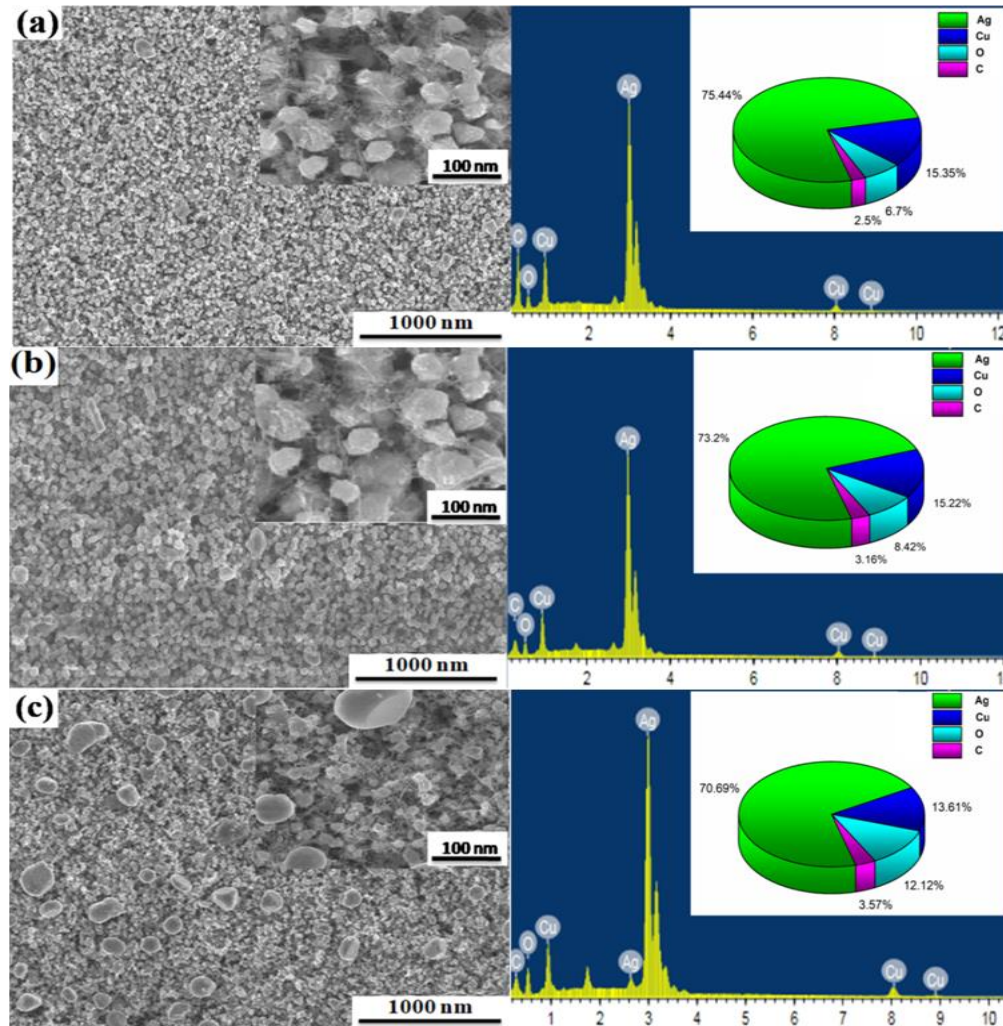


Fig. 3.9 FE-SEM images (left side) and their corresponding EDX spectrum (right side) of Ag-Cu films annealed at 450° C in (a) N<sub>2</sub>, (b) H<sub>2</sub>, and (c) O<sub>2</sub> atmosphere.

The morphological feature and elemental composition of pad printed Ag-Cu films annealed at 450 °C under H<sub>2</sub>, N<sub>2</sub> and O<sub>2</sub> atmosphere were determined as shown in fig. 3.9. It exhibits a dense microstructure along with many micro droplets. Some spherical structured morphology came out of the film as globules upon annealed in N<sub>2</sub> atmosphere. Further, the size of the globules increased in the films which are annealed in H<sub>2</sub> and O<sub>2</sub> atmosphere. In parallel, the relative composition of the oxygen element was increased in the films annealed in H<sub>2</sub> and O<sub>2</sub> atmosphere, but it was less in the film annealed in N<sub>2</sub> atmosphere. The copper element in the Ag-Cu alloy system transformed

to copper oxide upon reaction with atmospheric oxygen and segregated as different morphology with noticeable size at the surfaces (Li et al. 1991). Increased amount of oxygen and appearance of globules gave clues about the chance of oxidation of copper. These copper oxides acted as undoped semiconductor, affected the electrical conductivity of the film considerably (Sharma et al. 2013). Formation of globules could be responsible for lowest conductivity of film annealed in O<sub>2</sub> atmosphere, as the globules leads to the formation of hillock. This abnormal growth could be due to the formation of copper oxide as secondary phase embedded on the alloy films. These problems can be minimized when the films are annealed in an inert environment such as argon, helium or vacuum atmosphere (Sharma and Spitz 1980).

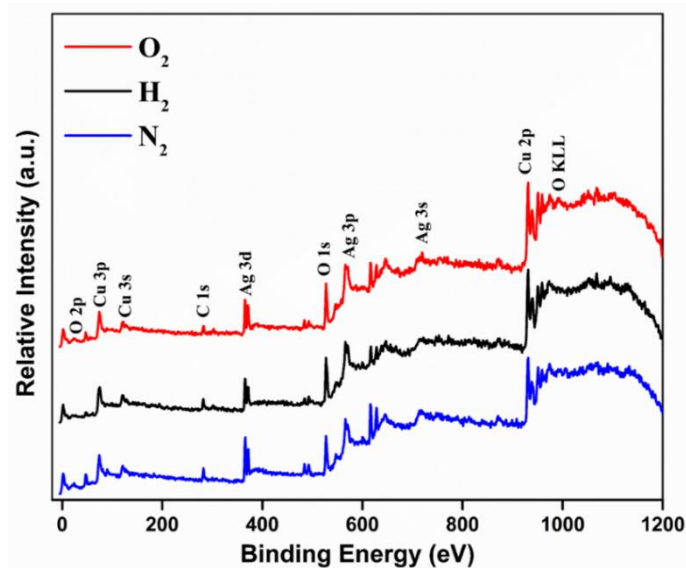


Fig. 3.10 XPS Survey spectrum of Ag-Cu film annealed in different atmosphere.

XPS survey scan of the Ag-Cu pad printed film annealed in N<sub>2</sub>, H<sub>2</sub> and O<sub>2</sub> atmosphere confirms the presence of Ag, Cu, O and C elements in the films by depicting the binding energies appeared at around 24.1eV, 74.2 eV, 121.9 eV, 284 eV, 370.1 eV, 531 eV, 570 eV, 717 eV, and 931.3 eV represents O 2p, Cu 3p, Cu 3s, C 1s, Ag 3d, O 1s, Ag 3p, Ag 3s, and Cu 2p respectively, as shown in fig. 3.10. Further, to examine the different chemical states of Cu atom in the films, Cu 2p spectra is deconvoluted into two principal peaks centred at 931 eV and 932.4 eV, are correlated to the formation of Cu<sup>0</sup> and Cu<sup>2+</sup>, respectively (Choi et al. 2015; Fortunato et al. 2001) as seen in fig. 3.11 (a), (b) and (c). However, the peak intensity of Cu<sup>0</sup> at 931 eV is same as that of Cu<sup>2+</sup> at 932.4 eV. The area (eV.cps) under the curves represents the concentration of Cu<sup>0</sup>

present in the films annealed under N<sub>2</sub>, H<sub>2</sub> and O<sub>2</sub> atmosphere are 6940, 6844 and 4365. Concentration of Cu<sup>2+</sup> (eV.cps) in the films annealed under N<sub>2</sub>, H<sub>2</sub> and O<sub>2</sub> are 5596, 6124 and 4116. But the trend in the intensity ratio of Cu<sup>0</sup>/Cu<sup>2+</sup> increased in N<sub>2</sub> atmosphere as compared to H<sub>2</sub> and O<sub>2</sub> atmosphere shown in fig. 3.11 (d).

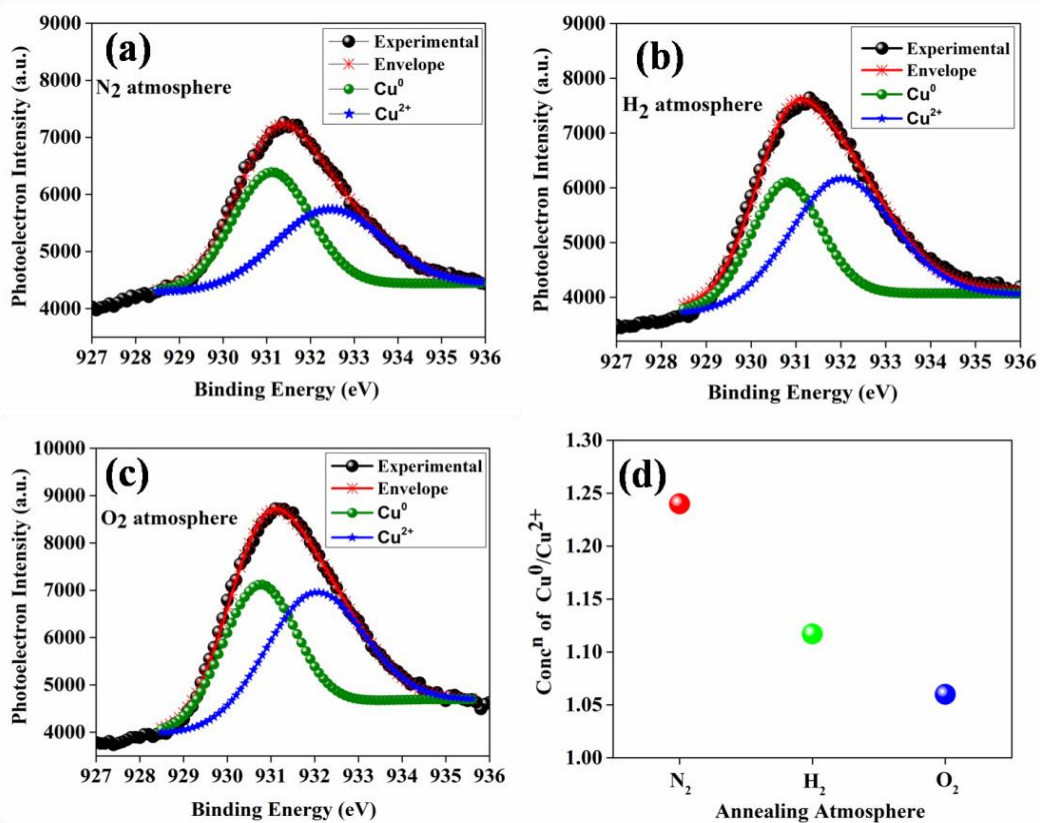


Fig.3.11 Deconvoluted Cu<sub>2p<sub>3/2</sub></sub> peaks of Ag-Cu alloy film annealed (a) in N<sub>2</sub> atmosphere, (b) in H<sub>2</sub> atmosphere, (c) in O<sub>2</sub> atmosphere; (d) concentration of Cu<sup>0</sup>/Cu<sup>2+</sup> as a function of annealing atmosphere.

In fig. 3.12 (a), (b) and (c), O 1s deconvoluted spectra, two peaks are observed at 529.4 eV and 531.1 eV in all three films. The first peak at 529.4 eV corresponds to O<sup>2-</sup> in CuO and second peak at 531.1 eV can be attributed to the adsorbed oxygen (Ibupoto et al. 2013). The area (eV. cPs) under curves represent the concentration of O<sup>2-</sup> in CuO in N<sub>2</sub>, H<sub>2</sub> and O<sub>2</sub> and values are 3607.7, 3949.2 and 4029 respectively. The concentration of O<sup>2-</sup> in CuO can be observed a maximum in O<sub>2</sub> atmosphere. It is quite obvious that the presence of oxygen facilitates conversion of metals to metal oxides as seen in fig. 3.12(d). Both factors (i) increased intensity ratio of Cu<sup>0</sup>/Cu<sup>2+</sup> and (ii) lesser concentration of O<sup>2-</sup> in CuO, lead to a higher conductivity in Ag-Cu films annealed in



N<sub>2</sub> atmosphere in contrast to other atmospheres. The ratio of Cu<sup>0</sup>/Cu<sup>2+</sup> in the Ag-Cu films annealed under N<sub>2</sub>, H<sub>2</sub> and O<sub>2</sub> atmosphere is found to be 1.24, 1.17 and 1.06 respectively (Fig. 3.12 (d)). On the other side, the ratio of Cu<sup>2+</sup>/Cu<sup>0</sup> in the film annealed under O<sub>2</sub> atmosphere is higher than the film annealed under N<sub>2</sub> and H<sub>2</sub> atmospheres. It notifies that the more oxidation of Cu element has occurred in the film annealed under O<sub>2</sub> atmosphere than the film annealed under N<sub>2</sub> and H<sub>2</sub> atmospheres. Hence, it is a strong evidence in support of the higher conductivity of Ag-Cu film annealed in N<sub>2</sub> atmosphere.

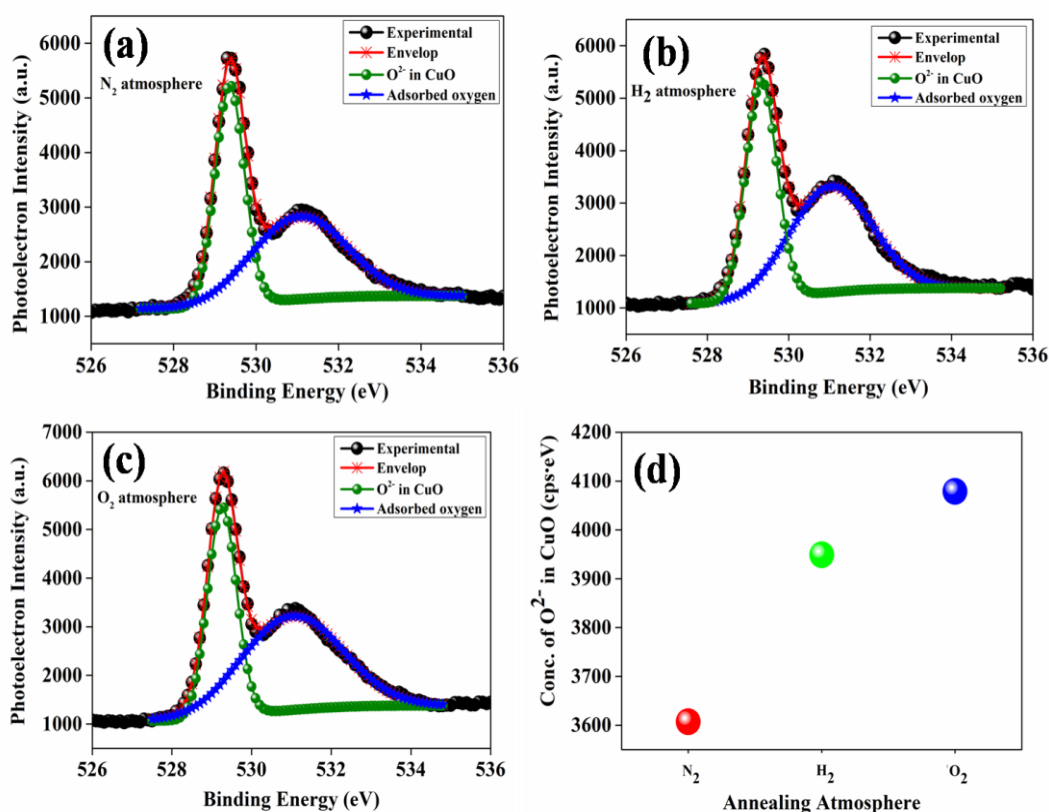


Fig. 3.12 Deconvoluted O 1s peaks of Ag-Cu alloy film annealed (a) in N<sub>2</sub> atmosphere, (b) in H<sub>2</sub> atmosphere, (c) in O<sub>2</sub> atmosphere; (d) Concentration of O<sup>2-</sup> as a function of annealing atmosphere.

In addition to this, the conductivity of pad-printed Ag-Cu alloy films annealed under H<sub>2</sub> atmosphere is relatively higher than the conductivity of Ag-Cu alloy films annealed under O<sub>2</sub> atmosphere, but not in appreciable manner. The reason behind this could be that during the annealing of the film in the H<sub>2</sub> atmosphere, the green pad printed pattern consisting of ethanol is oxidized into CO<sub>2</sub> and H<sub>2</sub>O. The moisture caused to

promote the oxidisation of Cu to copper oxides (CuO). The formed CuO gets reduced to again to Cu using the H<sub>2</sub> present in the surrounding. Since the annealing time was shorter, the reduction of CuO to Cu in H<sub>2</sub> atmosphere might not have done efficiently (Yabuki et al., 2010). Fig. 3.12(d) revealed that presence of copper oxide in films annealed under O<sub>2</sub> is more than in the films annealed under H<sub>2</sub> atmosphere and clearly stating that some percentage of CuO is reduced to Cu under H<sub>2</sub> atmosphere.

### 3.3.2 Characterization of calcium vanadium oxide (CaVO<sub>3</sub>)

The probable solution combustion synthesis reaction may be happened during the formation of CaVO<sub>3</sub> is presented as equation, 3.17.



Redox reaction between oxidizer and reducer evolves enormous amount of heat energy which incurs the conversion of metal precursors into metal oxide (calcium vanadium oxide); it is not only restricted to the formation of the CaVO<sub>3</sub>, also forms CaV<sub>2</sub>O<sub>5</sub> and Ca<sub>2</sub>V<sub>2</sub>O<sub>7</sub> as secondary phases. Intensity of the redox reaction depends on the number of electrons of the two compounds taking part in the reaction. More complexation of metal ions in the form of ligand prevents electrons of metal precursors to take part in the redox reaction, hence the intensity of the combustion reaction is minimized (Gupta et al. 2018).

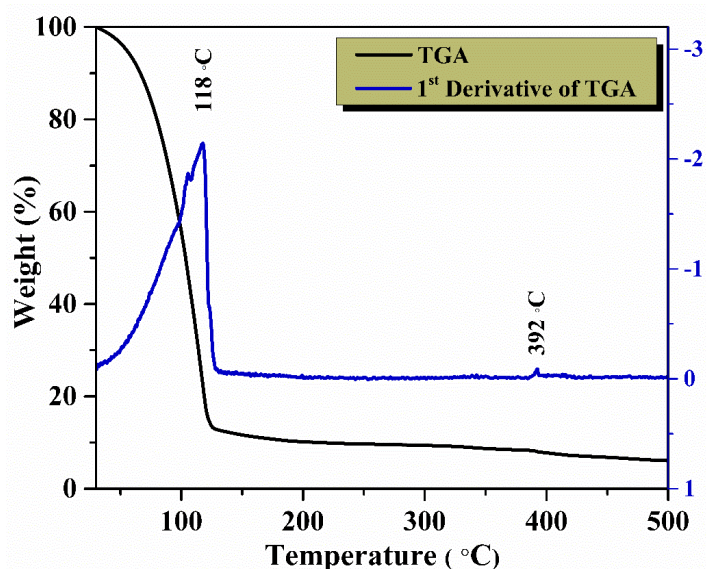


Fig. 3.13 TGA of dried gel prepared by vanadyl acetyl acetonate and calcium nitrate as fuel and oxidizer.

The TGA and its 1<sup>st</sup> derivative are shown in fig. 3.13. About 90 % of weight loss is found at temperature 118 °C, which is attributed to the occurrence of the combustion process. Further, a small amount of weight loss at 392 °C, indicates the oxidation of unstable calcium vanadium oxide to stable oxides namely calcium vanadates ( $\text{Ca}_2\text{V}_2\text{O}_7$ ) (Fukushima et al. 1998). Fig. 3.14 (a), shows the influence of annealing temperature on conductivity of the calcium vanadium oxide (CVO) films, annealed at different temperatures ranging from 140 °C to 420 °C with an equal interval of 20 °C for 15 min under ambient conditions.

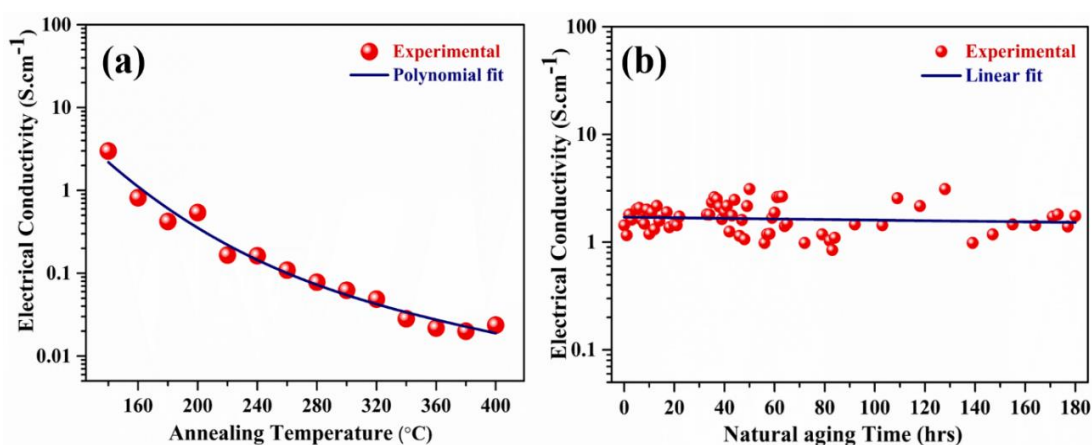


Fig. 3.14 (a) Conductivity of CVO films as a function of annealing temperature. (b) Conductivity of CVO film annealed at 140 °C in natural aging test.

The conductivity of CVO  $\sim 3 \text{ S.cm}^{-1}$ , is found with an annealing temperature of 140 °C. Further, it is decreased gradually with increase in annealing temperature up to 400 °C, whereas CVO film annealed at 420 °C is insulating in nature. The conductivity of CVO films is temperature dependent, showed a decreasing trend as the annealed temperature increases and became insulating at a temperature above 400 °C (Beck et al. 2018). The reason behind the transition from metal to insulator may be due to the appearance of insulating phases of CVO, as explained in the X-ray diffraction analysis (Garcia-Jaca et al. 1995). Higher annealing temperature promotes oxidation; induces additional scattering which transform conducting CVO films to insulating one, contradictory to the case of  $\text{LaTiO}_3$  and other TCOs (Fukushima et al. 1994). The stability of the electrical conductivity of CVO film annealed at 140 °C was studied in natural aging test with respect to time (hrs), as shown in fig. 3.14 (b). The electrical conductivity of CVO film is in the range of 1  $\text{S.cm}^{-1}$  to 3  $\text{S.cm}^{-1}$ , when aging was

performed at ambient for 180 hrs. The factors such as residual stress, micro structural defects recovery, oxygen adsorption and desorption, affect the conductivity of the films (Chen et al. 2005).

The XRD patterns of the solution combustion processed CVO films annealed at different temperatures, are shown in fig. 3.15. XRD revealed the CVO films annealed at lower temperatures (140 °C -160 °C) possess less crystalline in nature; it might be due to heat released in exothermic reaction was insufficient for complete conversion of complex metal precursor to metal oxides and incomplete decomposition of the organic constituents. The films annealed beyond the 160 °C temperature, the intensity of XRD patterns started increasing and at higher annealing temperatures (220 °C - 420 °C) the films showed high crystallinity. Here, three phases were evolved namely  $\text{CaVO}_3$  (conducting phase),  $\text{CaV}_2\text{O}_5$  and  $\text{Ca}_2\text{V}_2\text{O}_7$  (insulating phase). Presence of phase  $\text{Ca}_2\text{V}_2\text{O}_7$  hindered the conductivity of the films because of its dielectric property. But, phase  $\text{CaV}_2\text{O}_5$  was conducting to a smaller extent, because  $\text{CaV}_n\text{O}_{2n+1}$  oxides were strongly correlated materials (Anisimov 2010). All the peaks of three phases  $\text{CaVO}_3$ ,  $\text{CaV}_2\text{O}_5$ , and  $\text{Ca}_2\text{V}_2\text{O}_7$  in the figure were exactly matching with their respective ICDD card numbers 00-014-0127, 01-087-0953, 01-072-2312.

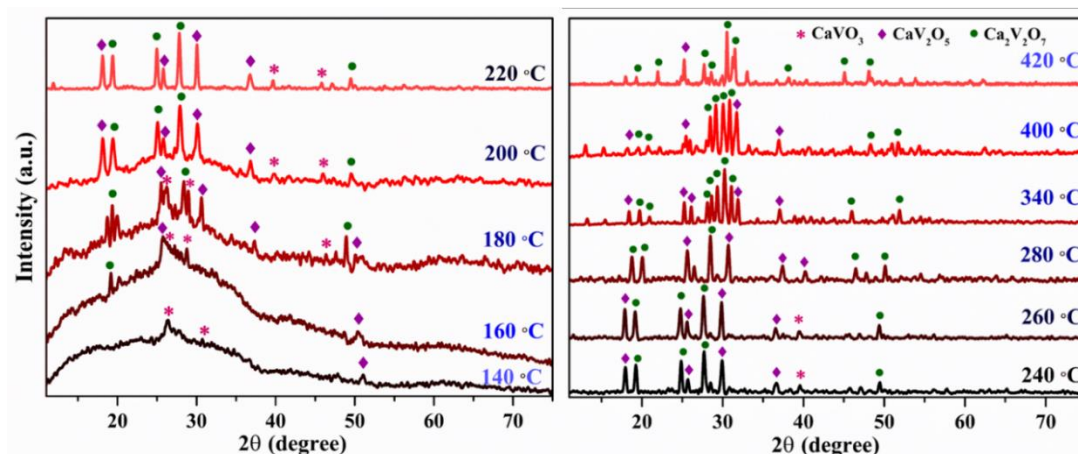


Fig. 3.15 XRD patterns of solution combustion processed CVO films as function of annealing temperature;  $\text{CaVO}_3$  (\*);  $\text{CaV}_2\text{O}_5$  (♦);  $\text{Ca}_2\text{V}_2\text{O}_7$  (●).

In the XRD pattern of film annealed at 140 °C, peaks appeared at  $2\theta = 26.46^\circ$  and  $30.7^\circ$  confirmed the formation of  $\text{CaVO}_3$  phase and peak appeared at  $2\theta = 51.06^\circ$  confirmed the formation of  $\text{CaV}_2\text{O}_5$  phase. Due to the presence of  $\text{CaVO}_3$  phase along with  $\text{CaV}_2\text{O}_5$  phase, the film exhibited high conductivity at the low annealing temperature.

As the annealing temperature of the film crosses 160 °C, insulating  $\text{Ca}_2\text{V}_2\text{O}_7$  phase appears. The intensity of peak related to  $\text{Ca}_2\text{V}_2\text{O}_7$  phase was increased as the annealing temperature (180 - 420 °C) increases. As the annealing temperature is increased, peaks of  $\text{CaVO}_3$  phase were reduced. At high annealing temperatures (280-420 °C), peaks signify the  $\text{CaVO}_3$  phase were completely disappeared. The formation of insulating  $\text{Ca}_2\text{V}_2\text{O}_7$  phase and also disappearance of conducting  $\text{CaVO}_3$  phase at higher annealing temperature, reduces the conductivity. At high annealing temperature 420 °C, a predominant formation of insulating  $\text{Ca}_2\text{V}_2\text{O}_7$  phase made the film an insulator.

Raman spectra of CVO films annealed at different temperatures are shown in fig. 3.16 (a). The noticeable vibration region of the vanadium oxide lies in the region of 1200-100  $\text{cm}^{-1}$  range. Depending on the behaviour of molecular vibrations, Raman spectra of vanadium oxides split into three segments, stretching of V-O lies at 1050-770  $\text{cm}^{-1}$ , the V-O-V stretching lies at 800-400  $\text{cm}^{-1}$  region (symmetric at 500-400  $\text{cm}^{-1}$  and asymmetric at 800-600  $\text{cm}^{-1}$ ) and bending mode at 400-150  $\text{cm}^{-1}$  respectively (Deo et al. 1990). The vanadyl (V-O) stretching mode is shifted to left i.e., towards lower frequencies, with an increase in annealing temperature. The empirical formula relates Raman stretching frequencies of V-O bonds to the bond length in vanadium oxide compounds as shown in equation (3.18) (Deo et al. 1990):

$$v = 21349 \exp(-1.9176R) \quad (3.18)$$

where  $v$  and  $R$  are the Raman stretching frequency in  $\text{cm}^{-1}$  and bond length in Å respectively. The vanadyl V-O stretching mode appears at lower frequencies for shorter bond length with high annealing temperature, whereas it shifted to a higher frequency for longer bond length with low annealing temperature. Shifting of V-O stretching mode to lower frequencies confirmed the evolution of insulating phase ( $\text{Ca}_2\text{V}_2\text{O}_7$ ) at a higher temperature. The stretching mode of V-O in the CVO films annealed in the temperature range 140 °C -180 °C is found at higher frequencies, which indicates the presence of conducting phase ( $\text{CaVO}_3$ ). Two modes appeared at 320-340  $\text{cm}^{-1}$  and 810  $\text{cm}^{-1}$  stipulated the transition of  $\text{CaV}_2\text{O}_5$  phase (Popovic et al., 2002). In addition, peaks due to the bending mode of V-O-V shift to higher frequencies. Formation of stable vanadium oxide  $\text{V}_2\text{O}_5$  from metastable  $\text{VO}_2$ , due to oxidation makes two major peaks

nearby (Ureña-Begara et al. 2017). Peaks shifted to lower frequencies confirmed the evolution of insulating phases.

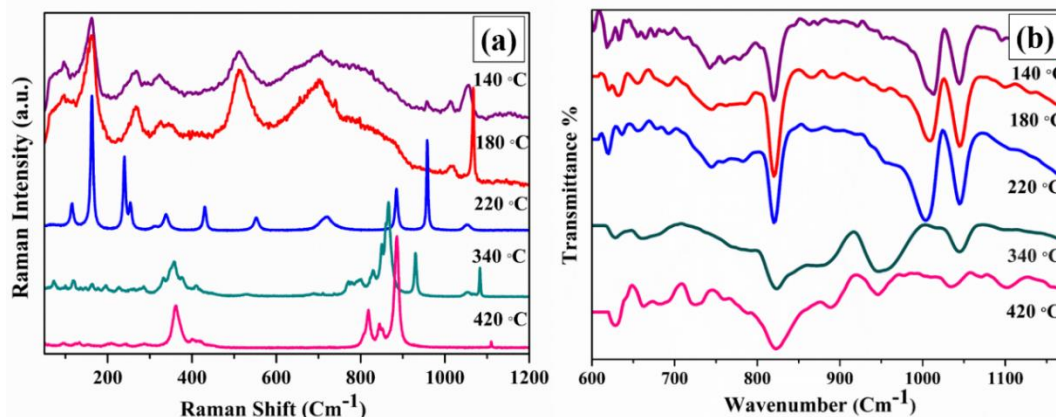


Fig. 3.16 (a) Raman spectra and (b) FTIR spectra of CVO films as function of annealing temperature.

CVO films are further analysed by FTIR spectra as shown in fig. 3.16 (b). The stretching and bending vibrational IR active modes of vanadium –oxygen appear in the range of 600-1100  $\text{cm}^{-1}$ . A distinct sharp medium band is observed from 600-800  $\text{cm}^{-1}$ , where the peaks at  $\sim 620 \text{ cm}^{-1}$  and  $\sim 740 \text{ cm}^{-1}$  are attributed to bending vibration of V-O and asymmetric stretching mode of V-O-V respectively (Ardelean et al. 2004; S Sarkar et al. 2014). Strong broadband is observed in the range of 800-1060  $\text{cm}^{-1}$  and the peaks at  $\sim 820 \text{ cm}^{-1}$  and  $\sim 1005 \text{ cm}^{-1}$  are attributed to symmetric stretching of V-O-V and V-O. IR spectra of the films annealed at higher temperature 340 °C and 420 °C showed strong stretching modes of V-O bond which is shifted to  $\sim 956 \text{ cm}^{-1}$  due to presence of pyrovanadates, particularly the insulating phase  $\text{Ca}_2\text{V}_2\text{O}_7$  (Frederickson and Hausen 1963; Gu & Yan 2009).

The morphologies of the films annealed at different temperatures were analysed by SEM as shown in fig. 3.17. Films possess highly porous granular structure with nanosized feature, but percolation path in between grains are responsible for conductivity. The presence of pores in the films is mainly caused by the release of different types of gases such as  $\text{CO}_2$ ,  $\text{N}_2$  and  $\text{H}_2\text{O}$ . The compositional analysis of the CVO films at annealed at 180 and 340 °C temperature was studied using EDS as shown in fig. 3.18. The spectrum confirms the presence of calcium (Ca), vanadium (V), oxygen (O), carbon (C) and nitrogen (N) as major elements. The weight percentage of

elements C and N is diminished in the film annealed at 340 °C, this could be due to the decomposition of unburnt carbon and nitrate precursor.

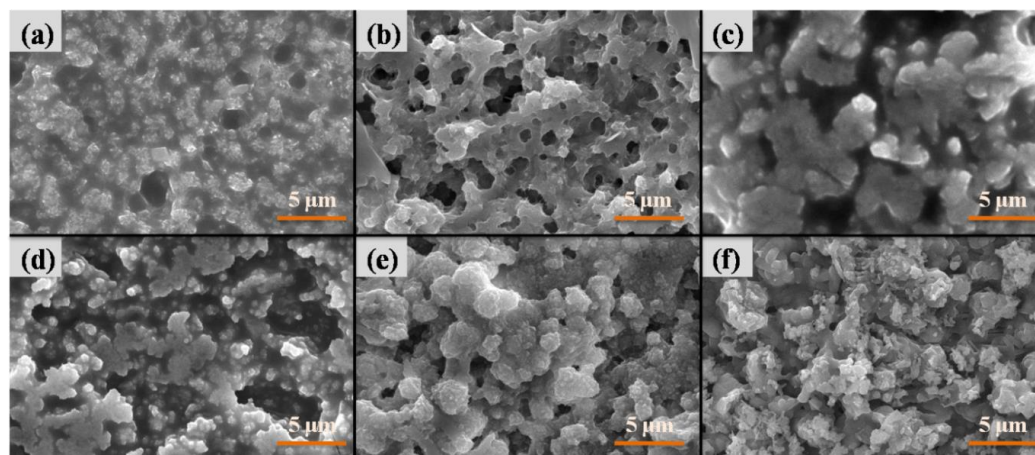


Fig. 3.17 SEM of CVO films annealed at different temperatures (a) 140 °C, (b) 180 °C, (c) 220 °C, (d) 280 °C, (e) 340 °C and (f) 420 °C.

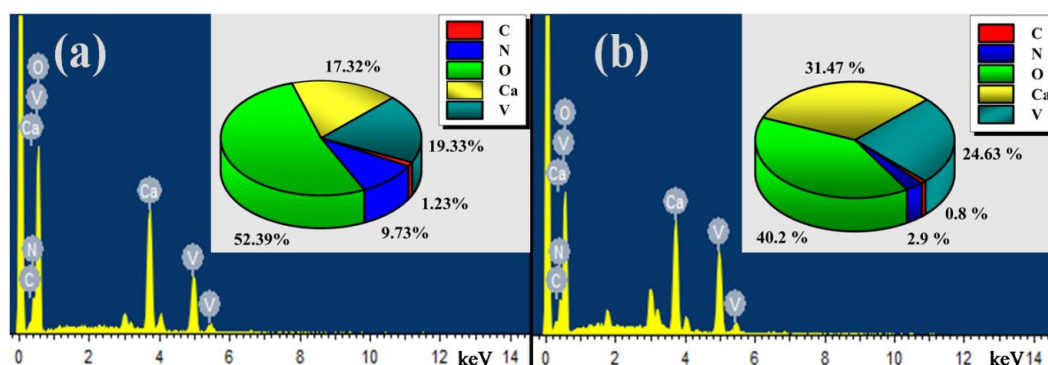


Fig. 3.18 EDS spectra of CVO films annealed at (a) 180 °C and (b) 340 °C.

In order to understand the augmentation in resistivity of the films in response to annealing temperature are analysed by XPS. The XPS wide scan and Ca 2p core level spectra of the CVO films annealed at 180 °C and 340 °C are shown in fig. 3.19 (a). Presence of carbon, calcium, vanadium, oxygen elements are confirmed from XPS peaks centred at 283 eV, 345 eV, 515 eV, and 531 eV respectively and represents the C 1s, Ca 2p, V 2p, N 1s and O 1s core level in both the CVO films, are well matched with reported literature (Y. Liu et al. 2016; X. Pan et al. 2014). The Ca 2p core level XPS spectra is shown in fig. 3.19 (b) where the presence of single doublets, reveal the same chemical environments present in all perovskites (Dudric et al., 2014).

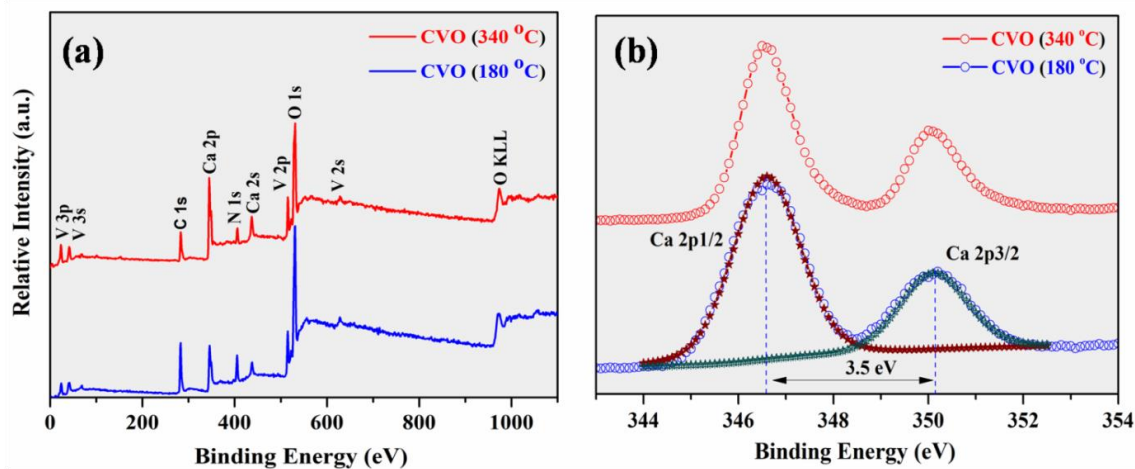


Fig. 3.19 (a) XPS wide scan and (b) Ca 2p core level spectrum of calcium vanadium oxide annealed at 180 °C and 340 °C.

The peaks at 346.7 and 350.2 eV corresponds to Ca 2p<sub>1/2</sub> and Ca 2p<sub>3/2</sub>, with an intensity ratio of 2:1 and a difference in their binding energies of 3.5 eV, indicating the presence of Ca<sup>2+</sup> (Chu et al. 2013; Zhang et al. 2012). In order to find the valence state of vanadium such as V<sup>3+</sup>, V<sup>4+</sup> and V<sup>5+</sup> in the CVO films (annealed at 180 °C & 340 °C), the V 2p peak was deconvoluted as shown in fig. 3.20 (a) and (b). Details of the V 2p<sub>3/2</sub> core level curve fitting are given in Table 3.3. The V 2p<sub>3/2</sub> peak was deconvoluted into two peaks at binding energies of 516.4 eV and 516.9 eV, assigned to V<sup>4+</sup> and V<sup>5+</sup> in the CVO film annealed at 180 °C; whereas in the CVO film annealed at 340 °C, V<sup>4+</sup> and V<sup>5+</sup> were centred at binding energies of 516.3 eV and 516.8 eV, respectively. XPS data of both V<sup>4+</sup> and V<sup>5+</sup> are in good agreement with reported literature (Silversmit et al. 2004).

Table 3.3 XPS fit parameters for the V 2p annealed at 180 °C and 340 °C.

Annealing temperature	Core level	Binding energy (eV)	FWHM	Area (cps·eV)
180 °C	V <sup>5+</sup> 2p <sub>3/2</sub>	516.9	0.82	1935.5
	V <sup>4+</sup> 2p <sub>3/2</sub>	516.4	0.66	2100.6
340 °C	V <sup>5+</sup> 2p <sub>3/2</sub>	516.8	0.96	2627.0
	V <sup>4+</sup> 2p <sub>3/2</sub>	516.3	0.77	1670.0



The vanadium system is very rich due to many valence states of vanadium ranging from  $V^{3+}$  to  $V^{5+}$ . In vanadium oxide films conducting oxide  $VO_2$  ( $V^{4+}$ ) transforms to insulator oxide  $V_2O_5$  ( $V^{5+}$ ) with increase in temperature due to oxidation of  $V^{4+}$  to  $V^{5+}$  (Y. Liu et al. 2016). Elemental state of vanadium in  $CaVO_3$  and  $Ca_2V_2O_7$  are 4+ and 5+ respectively. Area enclosed by  $V^{4+}$  and  $V^{5+}$  in V 2p<sub>3/2</sub> XPS spectra were almost the same in CVO film annealed at 180 °C; whereas in CVO film annealed at 340 °C, area encompassed by 4+ valence state became smaller and area enclosed by 5+ valence state was enlarged. Substantial presence  $Ca_2V_2O_7$  phase compared to  $CaVO_3$  makes the resistivity to a higher value in CVO films annealed at elevated temperature. Presence of carbon in the films annealed at 180 °C and 340 °C is examined in fig. 3.20 (c) and carbon content is diminished with increasing temperature. Though, the impurity composition is decreased in the films annealed at higher temperature, but the conductivity is not improved because of the non-conducting phase.

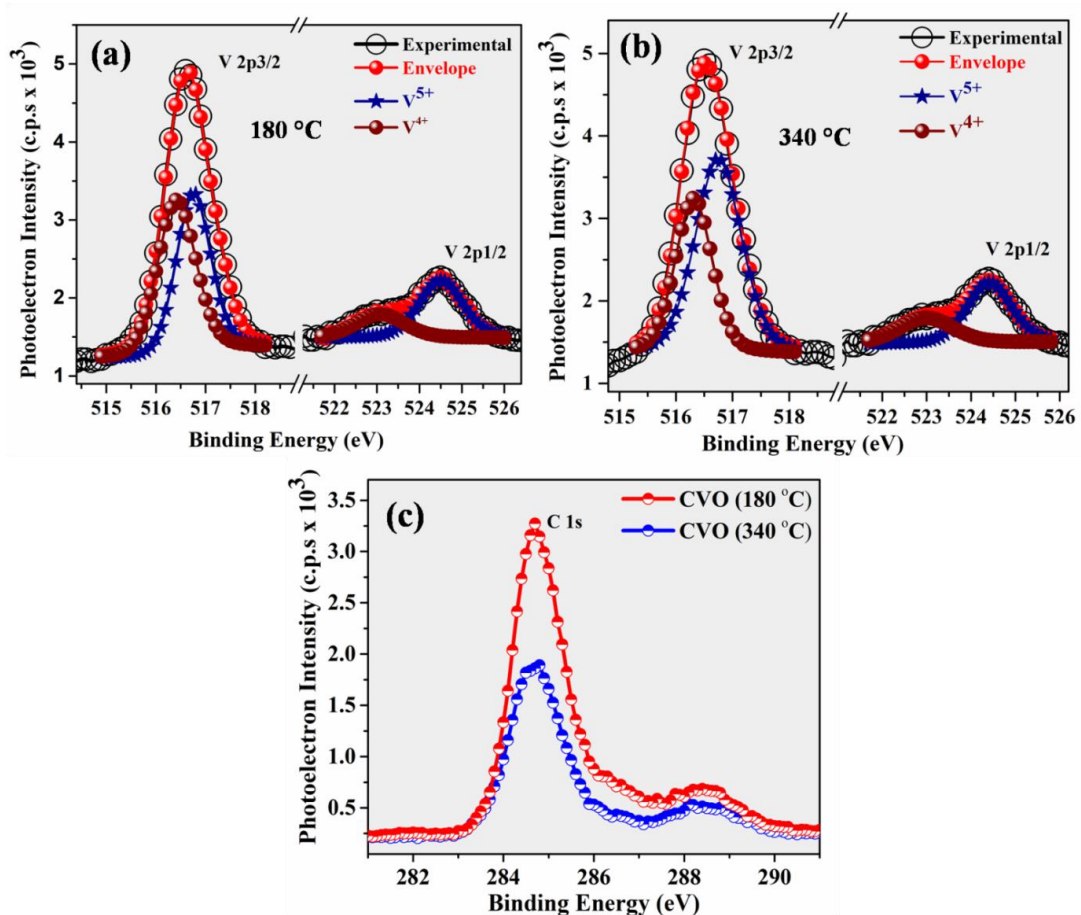


Fig. 3.20 V 2p spectra of CVO films annealed at (a) 180 °C (b) 340 °C and (c) C 1s spectra of CVO films annealed at 180 °C and 340 °C.

### 3.3.3 Characterization of undoped and strontium doped zinc oxide particles

#### 3.3.3.1 ZnO particles using three fuels

TGA helps to understand the pathways of combustion synthesis. Fig. 3.21 shows the TG thermographs and its derivative of a precursor gel of each fuel system. TG thermographs depicted the mass loss occurred in multi-steps in the urea and citric acid fuel-system, whereas in glycine fuel-system mass loss was found in a single step. In SCS, a volume of the precursor solution was preheated near to the boiling point of the solvent, where evaporation of free and bound water was taken place (phase I). The persistent weight loss in all fuel system up to 130 °C is observed, it may be due to evaporation of free and desorption of chemically absorbed water molecules.

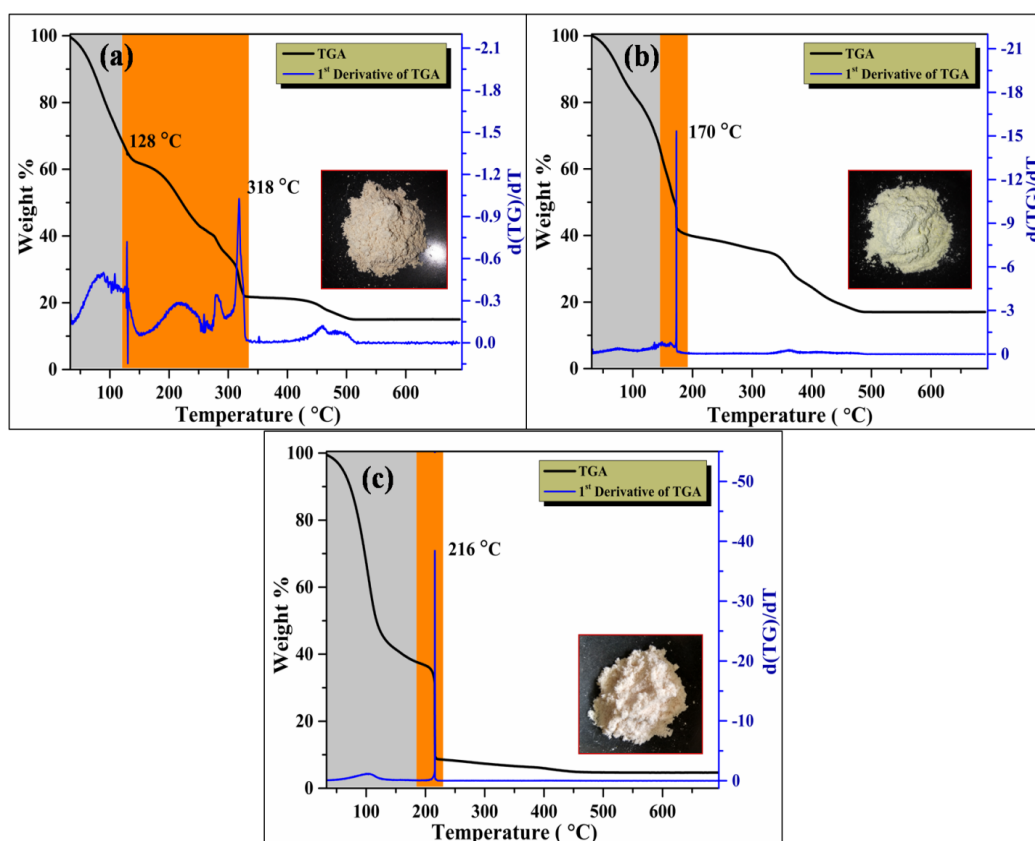


Fig. 3.21 Thermogravimetric analysis of dried gel, (a) urea, (b) citric acid and (c) glycine. Phase I, Phase-II and Phase-III of the weight loss are represented by grey, orange and white color. The inset shows the colour of powder after the calcination at 600 °C.

In phase II, at a particular temperature, weight loss takes place due to combustion, accompanied by liberation of heat and gases is called ignition temperature.

Considerable weight loss was found at 170 °C & 216 °C in citric acid and glycine fuel-system respectively, whereas in urea fuel-system, mass loss took place at temperatures 128 °C and 318 °C. The sudden weight loss attributed to the escape of an enormous amount of by-product gases evolved during combustion. In urea fuel-system, weight loss of 35 % was occurred between 128 °C and 318 °C. Removal of excess carbonaceous impurity was done in phase III; as the weight loss of approximately 6 %, 15 % and 3 %, respectively in the temperature range 450 °C to 600 °C was due to the incineration of carbonaceous residue led to the evolution of CO<sub>2</sub> gases. In citric acid fuel-system, weight loss in distinct stages could be attributed to the formation of intermediate compound namely citraconic or aconitic acid, which are pyrolytic by-product of citric acid. TG thermographs (fig. 3.21 (b)) depicts the weight loss of ~16 % up to a temperature of 400 °C, which may be due to the decomposition of aconitic acid or citraconic acid.

The XRD patterns of solution combustion synthesized as-combusted and calcined at 600 °C for 2 h of ZnO as shown in fig. 3.22, confirmed the formation of ZnO with wurtzite structure in all three cases. The reflections are found at an angle ( $2\theta$ ) of 31.7°, 34.4°, 36.3°, 56.6° and 62.9°, which are indexed as (1 0 0), (0 0 2), (1 0 1), (1 1 0) and (1 0 3) planes (ICDD-01-079-0205). The peaks at an angle ( $2\theta$ ) of 47.6°, 67.9° and 69.2° correspond to (1 0 2), (1 1 2) and (2 0 1) planes. Fig. 3.22 (b) XRD pattern of the calcined ZnO particles reveals that the carbonaceous impurity in the calcined ZnO particles is reduced and the reflections of calcined ZnO nanocrystalline powder are become sharper.

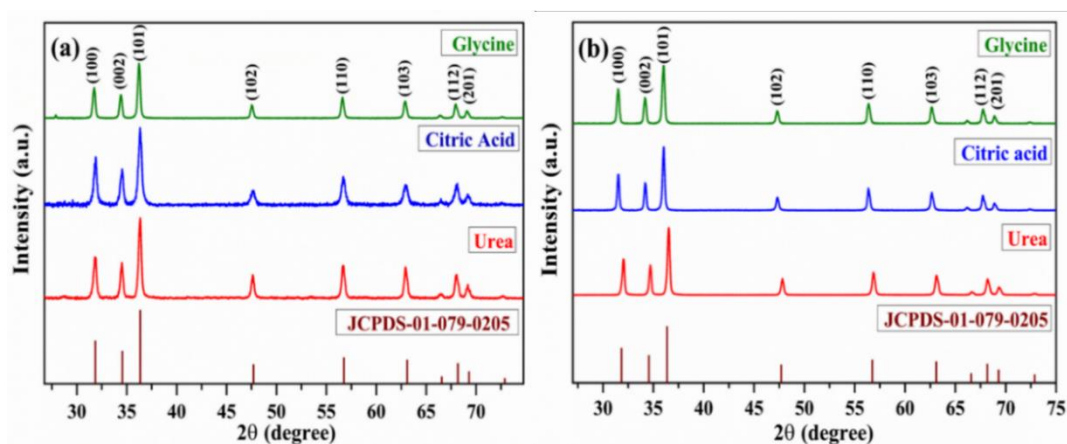


Fig. 3.22 XRD patterns of solution combustion synthesized (a) as-combusted and (b) calcined ZnO particles.

The precise lattice parameters of the as-combusted and calcined ZnO of wurtzite structure were calculated by using Cohen's method. The steps involved in the calculation of precise lattice parameter of as-combusted ZnO particles synthesized using fuel-urea is shown in Table 3.4. The estimated precise lattice parameters 'a' and 'c' using Cohen's analysis is shown in fig. 3.23 (a). Unit cell volume (V) and bond length (l) of the Zn-O are calculated using the following relations (3.19 and 3.20) and results are summarized in fig. 3.23 (b).

$$V = \frac{\sqrt{3} a^2 c}{2} = 0.866a^2c \quad (3.19)$$

$$l = \left[ \frac{a^2}{3} + c^2 \left( \frac{1}{2} - u \right)^2 \right]^{1/2} \quad (3.20)$$

Where parameter 'u' is defined as  $u = \frac{a^2}{3c^2} + 0.25$ .

Table 3.4 Spread sheet of cohen's analysis for the calculation of precise lattice parameter 'a' and 'c' of ZnO powder (combusted using fuel-urea).

<b>2θ (deg)</b>	<b>θ (rad)</b>	<b>h k l</b>	<b>α</b>	<b>γ</b>	<b>δ</b>	<b>Sinθ</b>
31.280	0.2731	1 0 0	1	0	0.269	0.2695
34.493	0.3012	0 0 2	0	4	0.320	0.2964
36.325	0.3172	1 0 1	1	1	0.350	0.3117
47.625	0.4158	1 0 2	1	4	0.545	0.4037
56.687	0.4950	1 1 0	3	0	0.698	0.4747
62.956	0.5497	1 0 3	1	9	0.793	0.5221
68.043	0.5941	1 1 2	3	4	0.865	0.5595
69.177	0.6040	2 0 1	4	1	0.873	0.5676

Employing the cohen's method

$$3.5089 = 38A + 30B + 10.1449C$$

$$5.1282 = 30A + 131B + 15.2905C$$

$$1.0966 = 10.1449A + 15.2905B + 3.2253C$$

$$a = \frac{\lambda}{(3A)^{1/2}} = 3.2362 \text{ \AA}, \quad c = \frac{\lambda}{(4B)^{1/2}} = 5.18 \text{ \AA}$$

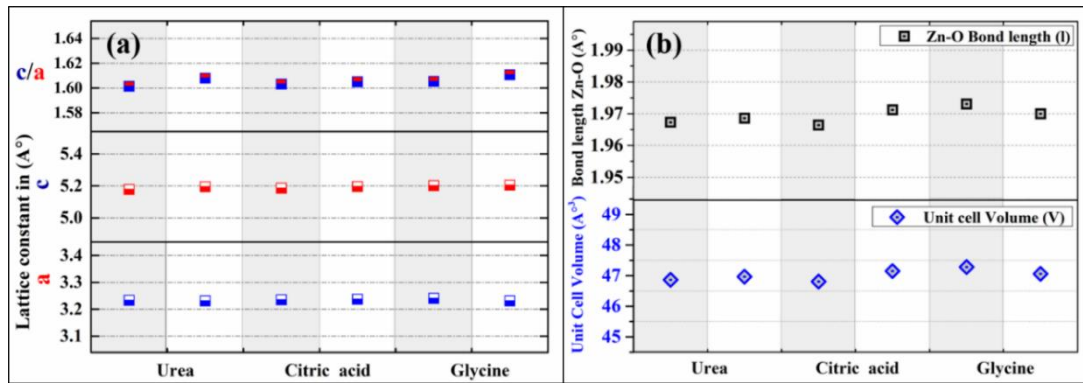


Fig. 3.23 (a) Lattice parameter a, c and ratio c/a and (b) unit-cell volume and bond length of Zn-O in [  $\square$  ] as-combusted and [  $\blacksquare$  ] calcined ZnO powder.

The results attained from the Scherrer equation, W-H ISM, W-H ASM and W-H EDM are tabulated in Table 3.5. Plots of W-H ISM, W-H ASM and W-H EDM for the calculation of crystallite size are shown in Appendix I. The average crystallite size of the as-combusted and calcined ZnO particles obtained from various models are almost similar; it implies that effect of the strain inclusion on the average crystallite size of ZnO particles has a negligible impact. Crystallite size of calcined ZnO particles is larger in comparison with as-combusted ZnO particles obtained from the same fuel system; the sufficient energy may have supplied to growth of the crystallites and caused to the formation of large crystallites.

Table 3.5 The estimated microstructural parameters of synthesized ZnO powder.

ZnO from the different fuel system	Crystallite size using different methods						
	Scherrer $D_v$ (nm)	W-H ISM		W-H ASM		W-H EDM	
		$D_v$ (nm)	$\epsilon \times 10^{-3}$	$D_v$ (nm)	$\sigma$ (MPa)	$D_v$ (nm)	$u$ ( $\text{kJ}\cdot\text{m}^{-3}$ )
Urea (before calcination)	24	25	0.649	25	28	27	3.2
Urea (after calcination)	31	40	0.941	41	111	42	54.6
Citric Acid (before calcination)	20	22	0.025	23	49.4	22	8.85
Citric Acid (after calcination)	29	31	0.46	31	31.3	31	3.93
Glycine (before calcination)	27	28	0.132	28	10.8	28	4.35
Glycine (after calcination)	34	42	0.678	43	86.1	43	31.7

The surface morphology and particle size distribution of the calcined ZnO particles are presented in fig. 3.24. ZnO particles obtained from the urea-fuel system possessed an irregular shape. Around 45% of powder are of sub-microns with mean particle size of

0.4  $\mu\text{m}$  and remaining particles are ranging from 5 to 8 microns with mean particle size of 7.5  $\mu\text{m}$ . Spherical and short rod shape morphology is observed in the ZnO particles processed with citric acid as fuel. The size of 50 % particles lies in between the 0.5 to 2.5 microns with mean particle size of 0.94 microns. Another 50 % particles, whose size are varying from 4 to 7.5 microns uniformly with a mean particle size of 5.7 microns. Unlike the two cases, ZnO powder prepared from the glycine has fine-spherical shape with mean particle size of 0.84 microns. The ZnO particles obtained using glycine fuel exhibited uniform morphology. This uniform morphology of the particles helps in the formation of more chemisorbed oxygen species on the surface. Hence, the detection of gases can be performed effectively using ZnO particles prepared from the glycine fuel.

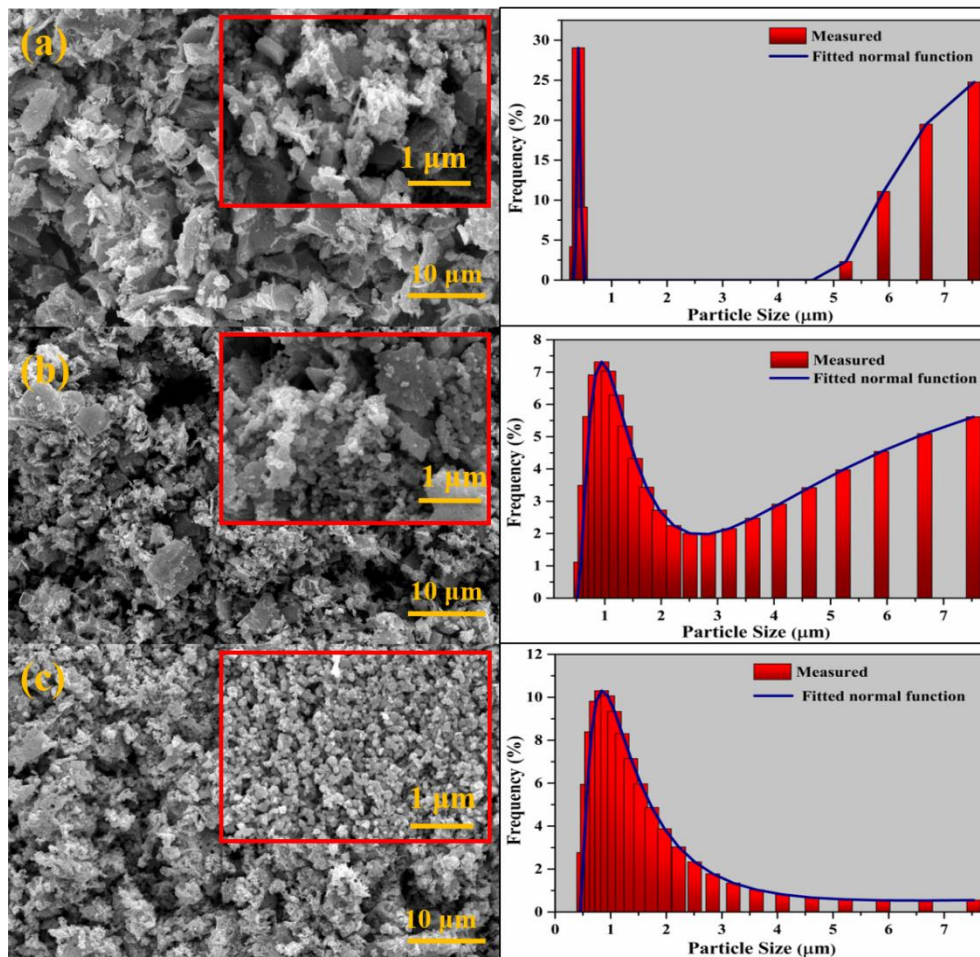


Fig. 3.24 SEM images of calcined ZnO powders and particle size distribution using fuel (a) urea, (b) citric acid and (c) glycine.

### 3.3.3.2 Sr-doped ZnO particles using fuel-glycine

Fig. 3.25 (a) depicts the TG thermographs and its derivative of a precursor gel of zinc nitrate, strontium nitrate and glycine. Continuous weight loss up to 140 °C is due to the evaporation of free and bound water. In SCS, removal of solvent takes place in the phase I, thereby persistent mass loss is found up to the boiling point of water. In phase II, a sudden weight loss is observed at a temperature  $\sim 196$  °C, this is due to a redox reaction between both the oxidizers ( $\text{Sr}(\text{NO}_3)_2$  and  $\text{Zn}(\text{NO}_3)_2$ ) and reducer ( $\text{C}_2\text{H}_5\text{NO}_2$ ), which is accompanied by the liberation of heat and by-product gases. The similar combustion reaction was noticed at 216 °C to obtain undoped ZnO from zinc nitrate- glycine, reported in the previous section. Removal of excess carbonaceous impurity is accomplished in phase III; weight loss of about 20-25 % is found in the temperature range from 450 °C to 600 °C, is due to the decomposition of by-products such as HCNO and CO leads to the evolution of  $\text{CO}_2$  and  $\text{N}_2$  gases. Further, no loss of mass is found above 500 °C, it confirms the stability of Sr doped ZnO at a higher temperature. Synthesized Sr-doped ZnO particles have a mean particle size of  $0.45 \pm 0.13$  microns and is shown in fig. 3.25 (b).

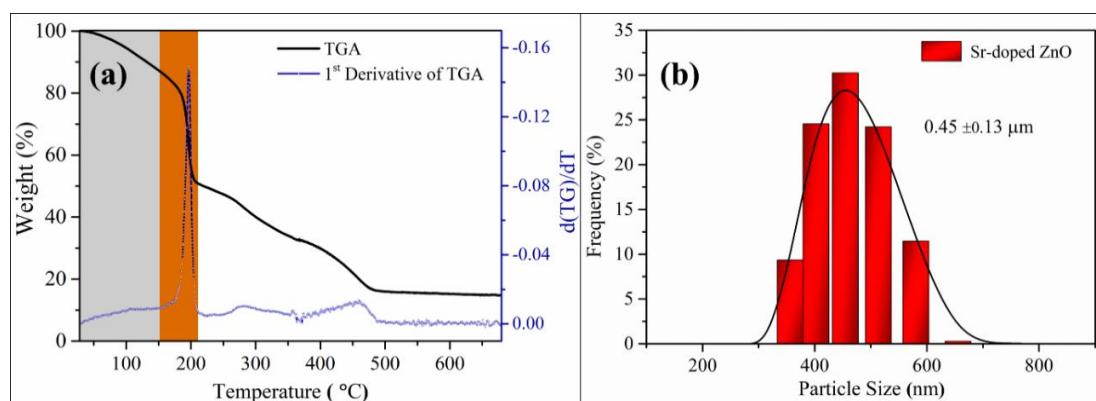


Fig. 3.25 (a) TG and DTG spectrum of precursor gel of zinc nitrate-strontium nitrate-glycine system and (b) particle size distribution of Sr-doped ZnO.

### 3.4 Conclusions

Ag and Ag-Cu alloy NPs capped with PVP were synthesized by two step reduction polyol method with an average size of  $33 \pm 19$  and  $48 \pm 15$  nm respectively. In UV-visible spectroscopy, absorption maxima of Ag and Ag-Cu alloy NPs dispersed in

ethanol appeared at 410 nm and 470 nm respectively. The calculated lattice parameter of Ag and Ag-Cu alloy NPs were  $\sim 4.077 \text{ \AA}$  and  $\sim 4.034 \text{ \AA}$  respectively.

Calcium vanadium oxide films were fabricated through solution combustion synthesis technique and annealed at different temperature from  $140 \text{ }^\circ\text{C}$  to  $420 \text{ }^\circ\text{C}$ . The conductivity of the CVO films annealed at  $140 \text{ }^\circ\text{C}$  possessed conductivity  $\sim 3 \text{ S.cm}^{-1}$  was observed in ambient. Evolution of conducting phases ( $\text{CaVO}_3$ ,  $\text{CaV}_2\text{O}_5$ ) and insulating phase ( $\text{Ca}_2\text{V}_2\text{O}_7$ ) at low and high annealing temperature respectively, influence the conductivity of the films. Transformation of conducting phase to insulating was predominant at annealing temperature of  $> 400 \text{ }^\circ\text{C}$ .

Phase pure, non-stoichiometric, highly reactive, nanocrystalline pristine and Sr-doped ZnO with wurtzite structure was synthesized by SCS route and calcined at  $600 \text{ }^\circ\text{C}$  for 2 h. The microstructural parameters such as crystallite size, lattice distortion  $\epsilon$ , stress  $\sigma$  and lattice strain energy density  $u$  of pristine and Sr-doped ZnO were estimated using W–H ISM, W–H ASM and W–H EDM models. Synthesized ZnO particle exhibited spherical morphology with a binomial distribution for urea and citric acid, where as a monomial distribution was observed in pristine and Sr-doped ZnO with glycine as a fuel.



## CHAPTER 4

### FORMULATION OF PARTICLE-FREE AND PARTICLE BASED SCREEN PRINTING INKS

#### 4.1 Introduction

This chapter deals the formulation of screen printable particle free and particle-based metal and metal oxide inks. The combustible molecular precursor-based particle free metal (Ag) and metal oxide (ZnO) screen-printing inks were formulated, which help in overcome the frequent practical problems associated with particle-based screen-printing inks such as clogging of pores in the screen mesh, which caused to the distorted printed patterns in the further printing. In addition, the formulation of this, ink is cost-effective and can be prepared in less-time than the conventional particle-based screen-printing inks. The conventional particle-based metal oxide (ZnO and BaSnO<sub>3</sub>) screen printing inks were also formulated using eco-friendly binder and solvents. Rheological properties such as viscosity, viscoelastic region, and change over point of the formulated particle-free screen-printing inks were studied. Thermal behaviour of the particle free silver inks, and individual organic vehicle for the particle based of screen-printing inks were carried out, which gave an exact idea about the required annealing temperature for the fabrication of screen-printed films with minimal carbon content.

#### 4.2. Experimental procedure

##### 4.2.1 Materials

All reagents were of analytical grade and used without further purification. Silver nitrate (AgNO<sub>3</sub>; Sigma-Aldrich, purity ≥ 99.0%), citric acid (C<sub>6</sub>H<sub>8</sub>O<sub>7</sub>; Sigma, purity ≥ 99.5%), zinc nitrate hexahydrate (Zn(NO<sub>3</sub>)<sub>2</sub>·6H<sub>2</sub>O; SRL Pvt. Ltd India (99 % purity)), glycine (C<sub>2</sub>H<sub>5</sub>NO<sub>2</sub>; SRL Pvt. Ltd. India (99% purity)), sodium-carboxymethyl cellulose (Na-CMC; Loba Chemie Pvt. Ltd. India), hydroxyethyl-cellulose (HEC; Sigma-Aldrich), and de-ionised (DI) water were used.

## 4.2.2 Formulation of particle-free screen-printing inks

### 4.2.2.1 Formulation of particle free silver screen printing inks.

The steps involved in the formulation of particle free screen-printable inks using  $\text{AgNO}_3$ ,  $\text{C}_6\text{H}_8\text{O}_7$ , Na-CMC and water are shown in fig. 4.1. A stoichiometric quantity of  $\text{AgNO}_3$  and  $\text{C}_6\text{H}_8\text{O}_7$  were taken according to the balanced equation 4.1 (Salian et al. 2019) and dissolved in the DI water separately. Both solutions were mixed and stirred at 350 rpm for 1 h and the formed precipitates were filtered out to get clear solution. 5 wt. % Na-CMC was added into the filtered solution and stirred at 150 rpm for 12 h.

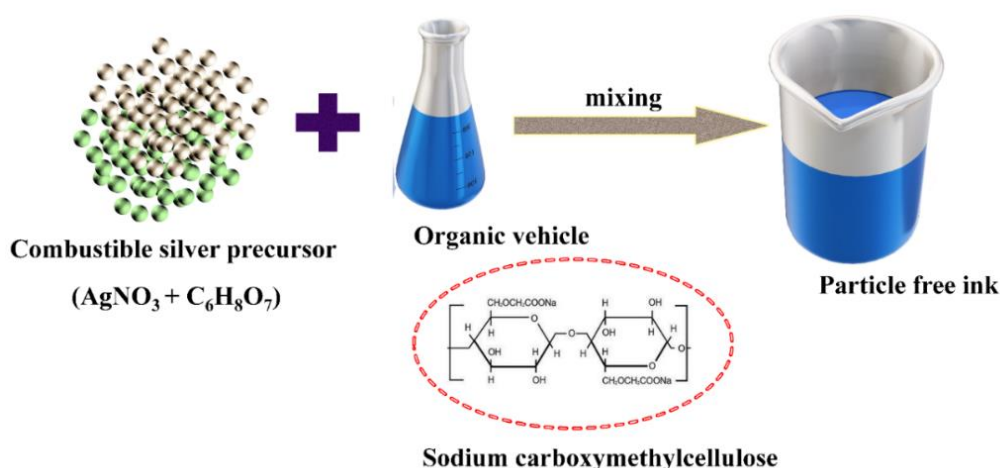
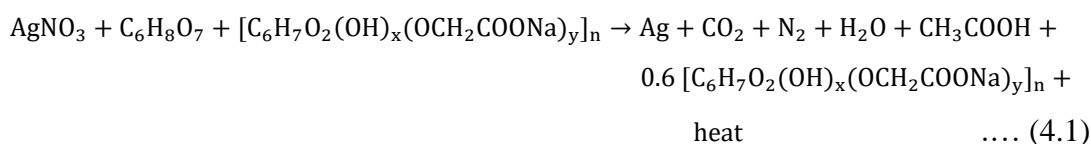


Fig. 4.1 Schematic representation of the formulation of screen-printable particle-free silver ink.

### 4.2.2.2 Formulation of particle free ZnO screen printing inks.

Aqueous combustible molecular precursor-based particle free screen printable ink was prepared by dissolving 10 g  $\text{Zn}(\text{NO}_3)_2$  and 8 g  $\text{C}_2\text{H}_5\text{NO}_2$  into 20 ml of DI water using a magnetic stirrer. 2g of biodegradable binder Na-CMC was added into the precursor solution and stirred at 50 rpm for 4 h. The steps involved in the formulation of screen-printable particle free ZnO inks using earlier mentioned precursors are shown in fig. 4.2.

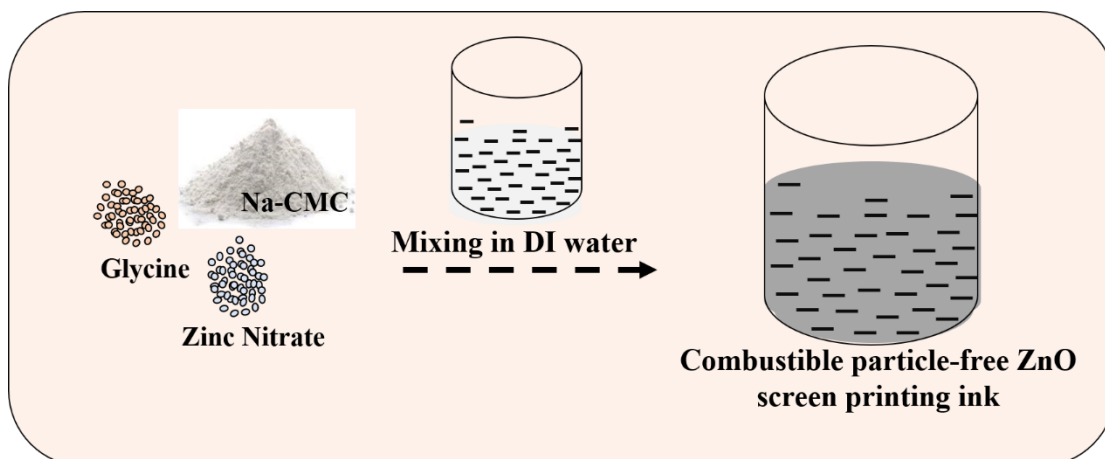


Fig. 4.2 Schematic representation of the formulation of screen-printable particle-free ZnO ink

### 4.2.3 Formulation of particle-based screen-printing inks

#### 4.2.3.1 Particle-based pristine and Sr-doped ZnO screen printing inks

The screen-printing inks of undoped and Sr-doped ZnO were prepared by mixing synthesized ZnO and Sr-doped ZnO powder as a functional material with viscous organic vehicle consist of 5 wt. % of Na-CMC binder and 10 ml of DI water. Hence, the formulated ink was made of functional material and an organic vehicle in a weight ratio of 60:40.

#### 4.2.3.2 Particle-based pristine and La-doped BaSnO<sub>3</sub> screen printing inks

The synthesised BaSnO<sub>3</sub> and La-doped BaSnO<sub>3</sub> powders as functional material were rigorously mixed with an organic vehicle; where organic vehicle was prepared by dissolving the 5 wt. % of hydroxy ethyl cellulose binder in 10 ml of DI water. Thixotropic pastes were made by mixing functional material and organic vehicle in a weight ratio of 60:40.

### 4.2.4 Characterization

*Rheological properties:* Rheological behavior of the formulated particle-free silver inks was investigated using plate-plate rheometer (REOPLUS, Anton Paar) at room temperature (25 °C). The viscosity of inks at different shear rate varying from 1 s<sup>-1</sup> to 1000 s<sup>-1</sup> were measured by the steady-state flow step (SSFS) test. Formulated inks were subjected to peak hold step (PHS) test in order to elucidate the rheology during printing

at specified shear rates in three intervals. Oscillatory shear measurements were conducted in a stress sweep step (SSS) test at a constant frequency of 1 Hz to understand the changes in ink structure and determine the linear viscoelastic region (LVR).

*Thermogravimetric analysis:* Thermal behaviour of particle-free screen-printing inks and organic vehicle of the particle-based screen-printing inks were analyzed using Thermo-gravimetric Analyzer (TGA 4000; PerkinElmer), at a heating rate of 10 °C/min in dynamic N<sub>2</sub> atmosphere.

*Structural analysis:* Functional groups of particle-free screen-printing inks and organic vehicle of the pristine and Sr-doped ZnO screen printing inks containing organic binder and solvent were characterized by FTIR (FTIR, MAGNA 550, Nico-142 let Instrument Co.).

## **4.3 Results and Discussion**

### **4.3.1 Particle-free screen-printing inks**

The present novel combustible molecular precursor-based particle free screen-printing ink may overcome frequent practical problems associated with particle-based screen-printing inks such as clogging of pores in the screen mesh, which caused to the distorted printed patterns in the further printing. In addition, the formulation of this ink is cost-effective and can be prepared in less-time than the conventional particle-based screen-printing inks.

#### **4.3.1.1 Particle-free silver screen printing inks**

Screen-printable particle-free inks, consisted of silver nitrate, citric acid, and organic vehicle (Na-CMC and water), are formulated. In the solution combustion process, redox reaction occurs between silver nitrate and citric acid, which leads to the formation of metallic silver from its precursor, simultaneously there is an evolution of heat due to combustion. The amount of heat which is liberated helps in burn-out the organic vehicle present in the screen-printable ink. Three different screen-printable inks were formulated by varying the concentrations (wt.%) of water and the silver nitrate loading in the inks was estimated as 14 % (Ink-1), 18 % (Ink-2), and 22 % (Ink-3). The weight of the constituents present in the three formulated inks are tabulated in Table 4.1.

Table 4.1 The weight of compositions of the screen-printable inks.

	Wt. of AgNO <sub>3</sub> (gms)	Wt. of citric acid (gms)	Wt. of Na-CMC (gms)	Wt. of water (gms)
<b>Ink-1</b>	2	0.75	0.45	12
<b>Ink-2</b>	2	0.75	0.45	8
<b>Ink-3</b>	2	0.75	0.45	6

Viscosity, percentage of viscosity recovery and its time during printing at the different shear rate were determined. Elastic/storage ( $G'$ ) and viscous/loss ( $G''$ ) moduli were calculated as a function of shear stress. All formulated inks exhibit shear thinning thixotropic behavior in which viscosity decreases with an increase of shear rate, as shown in fig.4.3 (a). The viscosity of formulated inks increase as the precursor loading is increased; the reason behind this may be the enhanced interaction between the precursors and organic vehicle. The viscosity of Ink-1, Ink-2, and Ink-3 at a shear rate of  $1 \text{ s}^{-1}$  was 210, 328, and 454 Pa.s, respectively. The higher solvent content Ink-1 exhibited the lower viscosity than the Ink-2 at shear rate  $< 322 \text{ s}^{-1}$ . At higher shear rate, the Ink-1 exhibited comparable viscosity with the Ink-2 and slightly higher than Ink-3. The reasons behind the increment in viscosity of Ink-1 at higher shear rate could be because of higher solvent content in Ink-1 creates poor network between the binder and solvent, results into the low viscosity at low shear rates. As the shear rate increases, due to poor compatibility between binder and solvent the stress clusters are introduced. These stress clusters cause to the extensive friction in the ink; hence the viscosity is increased (Wen lin et al. 2008). On the other side, spill or ejection of ink-2 at higher shear rates during the experiment may be caused to the decrement of the viscosity (Liu et al. 2021).

Considering the printing speed of  $50 \text{ mm s}^{-1}$ , the gap between the squeegee and mesh was  $\sim 250 \text{ }\mu\text{m}$ , and shear rate applied is  $200 \text{ s}^{-1}$  during the printing. Peak hold step test helps to understand the rheology of the inks during printing in which inks are subjected to different shear rate ( $0.1, 200$  and  $0.1 \text{ s}^{-1}$ ) in three intervals 0 to 30 s, 30-60 s, and 60-180 s, respectively and is shown in fig. 4.3 (b). Obviously, due to higher solvent content ( $\sim 77 \%$ ), Ink-1 possess low viscosity, which is nearly 297 Pa.s at first interval (ink on the mesh before printing) and reduces to 2.73 Pa.s in interval II (during

printing). After the printing, recovered viscosity is about 82 % at 80 s and 88 % at 110 s. The viscosity recovery of the formulated inks after the printing is shown in Table 4.2.

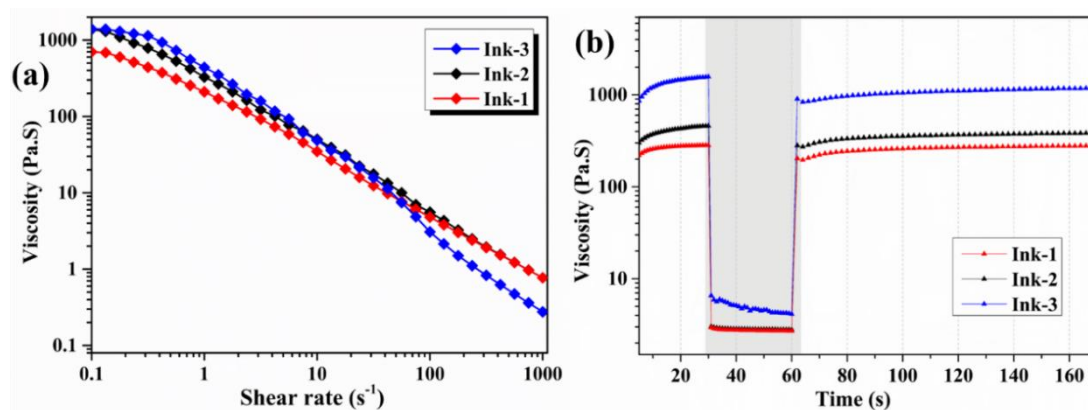


Fig.4.3 (a) Viscosity as a function of shear rate. (b) Rheological behavior during screen printing. Indigo colour shows the printing process.

Table 4.2 Variation of viscosity (Pa.s) of the different formulated inks during printing process at ambient condition.

	<b>0.1 s<sup>-1</sup> @</b>	<b>200 s<sup>-1</sup>@</b>	<b>0.1 s<sup>-1</sup> @</b>	<b>Recovery @</b>	<b>0.1 s<sup>-1</sup> @</b>	<b>Recovery @</b>
	<b>20 s</b>	<b>50 s</b>	<b>80 s</b>	<b>80 s</b>	<b>110 s</b>	<b>110 s</b>
Ink-1	297	2.73	244	82%	263	88%
Ink-2	430	2.81	344	80%	361	84%
Ink-3	1460	4.56	971	67%	1080	74%

For printing narrower line definition, higher viscosities are preferred, whereas, ink with lower viscosity and higher recovery may lead to blistering in printed patterns (Faddoul et al. 2012). With lower solvent content (~ 67 %) i.e., Ink-3, recovery of viscosity after printing (in Interval III) at 80 s and 110 s were 67 % and 74 % respectively is lower compared to Ink-1 and Ink-2. Inks which exhibit the slow viscosity recovery have an impact on the levelling during printing. Ink-2 with a viscosity of 430 Pa.s before printing, is reduced to 2.81 Pa.s during squeegee movement. Nearly 80 % and 84 % of viscosity were recovered after printing in 80 s and 110 s, respectively. Ink-2 possessed moderate rate of viscosity recovery at 80 s and 110 s. Ink-2 may not be associated with problems such as blistering, bleeding, improper levelling etc., thereby supports in the fabrication of high-quality films. Rheology properties of the inks estimated during

printing at different printing speeds of 12.5, 25, 37.5 mm s<sup>-1</sup> and their corresponding shear rates were 50, 100, 150 s<sup>-1</sup> as shown in fig. 4.4.

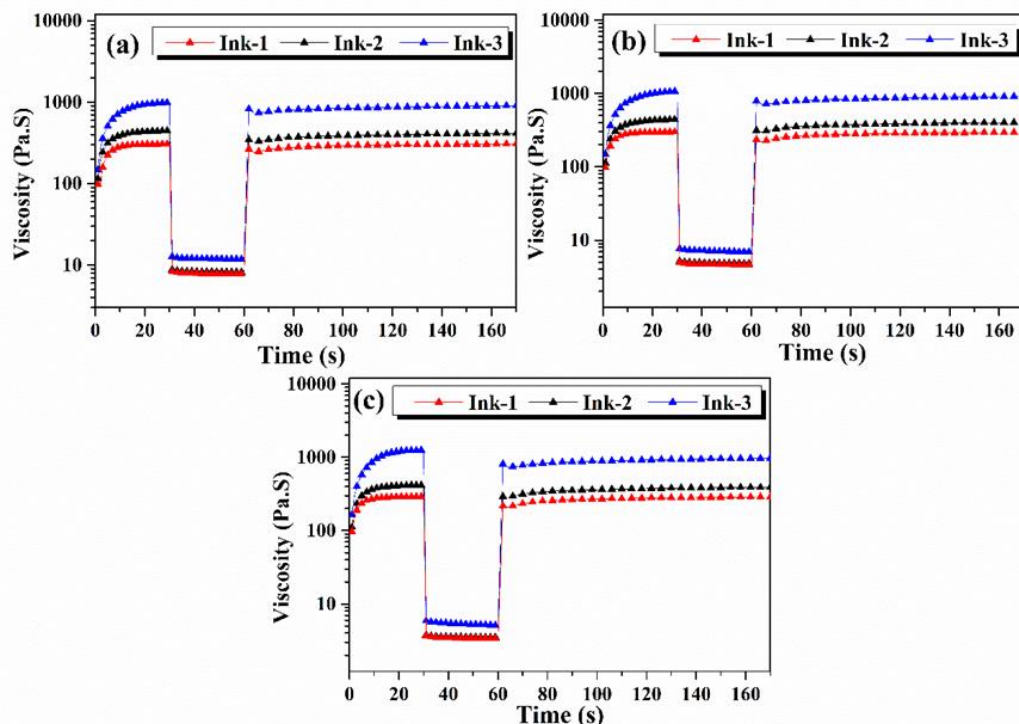


Fig. 4.4. Rheological behaviour during screen printing at different printing speeds of (a) 12.5 mm s<sup>-1</sup>, (b) 25 mm s<sup>-1</sup>, and (c) 37.5 mm s<sup>-1</sup>.

Percentage of viscosity recovered at 80 s and 110 s during printing at different printing speed 12.5, 25, 37.5 mm s<sup>-1</sup> is tabulated in Tables 4.3, 4.4, and 4.5 respectively. The Ink-1 recovered nearly 97 % of its initial viscosity after 110 s under printing speed 12.5 m/s, whereas Ink-3 recovered only 59 % of its initial viscosity after 110 s under the same printing conditions.

Table 4.3 Variation of viscosity (Pa.s) of different formulated inks at printing speed of 12.5 mm s<sup>-1</sup>.

	<b>0.1 s<sup>-1</sup> @</b>	<b>50 s<sup>-1</sup>@</b>	<b>0.1 s<sup>-1</sup> @</b>	<b>Recovery @</b>	<b>0.1 s<sup>-1</sup> @</b>	<b>Recovery @</b>
	<b>20 s</b>	<b>50 s</b>	<b>80 s</b>	<b>80 s</b>	<b>110 s</b>	<b>110 s</b>
Ink-1	297	7.8	279	94 %	289	97 %
Ink-2	430	8.2	372	86 %	394	91 %
Ink-3	1460	11.8	810	55 %	857	59 %

It was observed that Ink-1 recovered nearly 97-92 % of its initial viscosity after 110 s under printing speed in the range of 12.5-37.5 m/s. Ink-2 and Ink-3 recovered nearly 91- 86 % and 62- 59% of their initial viscosity respectively, under printing speed in the range of 12.5-37.5 m/s.

Table 4.4 Variation of viscosity (Pa.s) of different formulated inks at printing speed of 25 mm s<sup>-1</sup>.

	<b>0.1 s<sup>-1</sup> @ 20 s</b>	<b>150 s<sup>-1</sup>@ 50 s</b>	<b>0.1 s<sup>-1</sup> @ 80 s</b>	<b>Recovery @ 80 s</b>	<b>0.1 s<sup>-1</sup> @ 110 s</b>	<b>Recovery @ 110 s</b>
Ink-1	297	4.6	264	89 %	284	95 %
Ink-2	430	4.8	356	83 %	382	89 %
Ink-3	1460	6.9	798	55 %	855	59%

Table 4.5 Variation of viscosity (Pa.s) of different formulated inks at printing speed of 37.5 mm s<sup>-1</sup>.

	<b>0.1 s<sup>-1</sup> @ 20 s</b>	<b>150 s<sup>-1</sup>@ 50 s</b>	<b>0.1 s<sup>-1</sup> @ 80 s</b>	<b>Recovery @ 80 s</b>	<b>0.1 s<sup>-1</sup> @ 110 s</b>	<b>Recovery @ 110 s</b>
Ink-1	297	3.4	254	85 %	274	92 %
Ink-2	430	3.5	341	79 %	369	86 %
Ink-3	1460	5.2	835	57 %	904	62%

Oscillatory rheological measurements were performed to study the modification of ink structure during printing. Both the moduli (G' and G'') of three inks decreases with an increase in shear stress, as shown in fig. 4.5 (a).

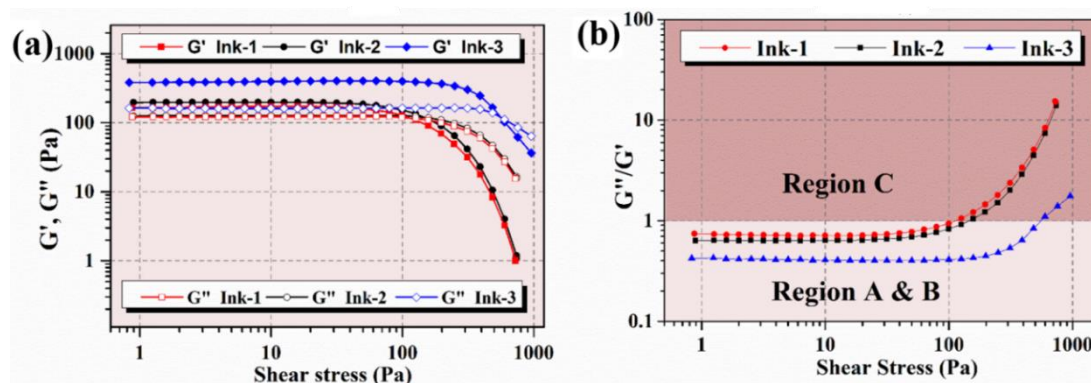


Fig. 4.5 (a) Oscillatory rheological test, and (b) Variation of G' and G'' and d) G''/G' ratio as a function of shear stress of formulated inks.



It reveals that linear visco-elastic region (Region A) lies within the 25 Pa, 31 Pa and 75 Pa for the Ink-1, Ink-2 and Ink-3 respectively. The linear-elastic region indicates the maximum deformation stress that can be hold by inks without losing its liquid-like and solid-like structure. In addition, all the inks show a solid-like structure dominant at lower shear stresses as shown in fig 4.5 (b) and ratio of liquid-like to solid-like structure ( $G''/ G'$ ) for the Ink-1, Ink-2 and Ink-3 are found to be 0.75, 0.61 and 0.40 respectively in Region A. Further, in Region B, complex modulus components  $G'$  and  $G''$  decreased continuously with increasing shear stress and the value of  $G''$  continued to be lower than  $G'$ . Even though inks show an elastic dominated behaviour ( $G'' < G'$ ), but as shear stress increases the ink structure gets weaken and continue breakdown (Durairaj et al. 2009). Region C starts from the point, where the modulus ratio ( $G''/ G'$ ) is unity, and extends to a higher shear stress with the value of  $G''$  maintained higher than the  $G'$ . Shear stress at  $G' = G''$  is called change-over point, which is used to assess the cohesiveness of the ink, after which liquid-like behaviour dominates the solid-like behaviour (Durairaj et al. 2009). The change-over point of Ink-1, Ink-2, and Ink-3 are found to be 110, 150, 538 Pa, respectively. Ink with lower change-over point offers fracture and tends to increase the skipping defects after the printing process (Bao et al. 1998).

TG analysis was performed to study the thermal behaviour of prepared inks and is shown in fig. 4.6 (a). TG-DTG analysis shows thermal behaviour of the inks, which is composed of silver nitrate and citric acid in the aqueous medium.

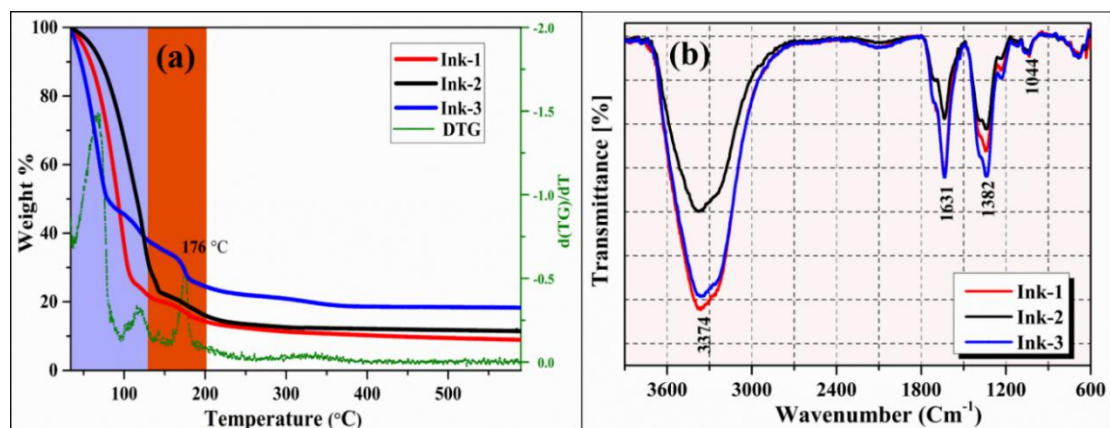


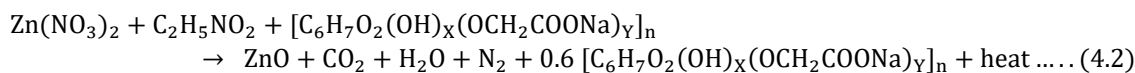
Fig. 4.6 (a) Thermogravimetric analysis and (b) FTIR spectra of formulated particle-free screen-printing inks containing the organic vehicle. Indigo color denotes evaporation of the solvent and red colored zone indicates the combustion process.

DTG reveals the weight loss of about 78%, 68% and 62% at 70 °C in the Ink -1, Ink-2 and Ink-3 respectively, which may be due to the evaporation of water content in the inks. Furthermore, small weight loss was found at 118 °C are attributed to evaporation of bound water (Salian et al. 2019), which are highlighted by indigo color in fig. 4.6 (a). A significant weight loss at 176 °C is due to the redox reaction between silver nitrate and citric acid (red colored zone in fig. 4.6 (a)). At this temperature, citric acid helps in reduction of silver nitrate to silver, hence is called self-reducible; simultaneously it liberates an enormous amount of heat (enthalpy) along with the evolution of gases. Released heat due to combustion could help in burning out the Na-CMC, which was added as a binder. Thermogravimetry revealed that 200 °C is the minimum temperature required to cure the silver precursor-based screen-printable inks. Afterward, about 3 % of weight loss is found between 200-400 °C in all inks, which may be due to the decomposition of Na-CMC. Since, the initial decomposition temperature ( $T_d$ ), and final decomposition temperature ( $T_f$ ) of Na-CMC are 278 °C and 410 °C, respectively (Li et al. 1999). Fig. 4.6 (b) shows the FT-IR spectrum of formulated silver screen printable inks comprised of Na-CMC and water as a binder and solvent respectively. The broadband at the  $\sim 3374\text{ cm}^{-1}$  is due to O-H symmetric stretching of covalent bond in water. The variation in the intensity of water stretching bond could be due to the moisture variation on the sample holder of the equipment during the characterization performed (Alharbi and Guirguis, 2019). Presence of Na-CMC is confirmed by characteristic absorption at  $\sim 1631\text{ cm}^{-1}$  and  $\sim 1044\text{ cm}^{-1}$ . The peak at  $\sim 1631\text{ cm}^{-1}$  is attributed to the carboxymethyl ether group ( $\text{COO}^-$ ) asymmetrical stretching in Na-CMC (Heinze and Pfeiffer 1999). The small band at  $\sim 1044\text{ cm}^{-1}$  indicates the stretching of C–O–C of the polysaccharide skeleton (Rani et al. 2014). A small peak at about  $1382\text{ cm}^{-1}$  in the inks, may be attributed to the  $\text{NO}_3^-$  vibrations of silver nitrate (Trchová and Stejskal 2010).

#### **4.3.1.2 Particle-free ZnO screen printing inks**

Aqueous combustible particle free ZnO screen-printing ink comprised of  $\text{Zn}(\text{NO}_3)_2$ ,  $\text{C}_2\text{H}_5\text{NO}_2$ , Na-CMC and water as a oxidizer, reducer, binder and solvent, respectively was formulated. In the SCS process, redox reaction occurs between oxidizer and reducer and resulted to the formation of ZnO phase accompanied with heat

liberation. A possible redox reaction to be carried out is shown in equation 4.2. Liberated heat helps to decompose the small amount of sodium carboxymethylcellulose (Na-CMC).



The present novel combustible molecular precursor-based screen-printing ink may overcome practical problems associated with clogging of pores in the patterned mesh and agglomeration of nanoparticles often observed in the particle-based screen-printing inks. Further, the steps involved in the formulation of particle-free ink is cost-effective than conventional particle based screen-printing inks.

Thermal behaviour of formulated clogging free combustible molecular precursor-based screen printable ink was characterized by thermogravimetric (TG) analysis in the temperature range from 32 °C to 660 °C (fig. 4.7 (a)). The TG-DTG of the particle-free screen-printing inks showed that the mass loss took place in the five steps. The first mass loss of about 45 % was noticed between the 32 °C and 130 °C, corresponded to the evaporation of water molecules. A small mass loss observed in the temperature range 130 °C- 170 °C, attributed to the conversion of hexahydrate of zinc salt to the monohydrate nitrate (Waqas et al. 2015). Nearly, 25 % mass loss occurred from 170 °C to 280 °C could be associated with combustion of the precursor solution. The temperature 232 °C was considered as combustion temperature, where the considerable mass loss was observed.

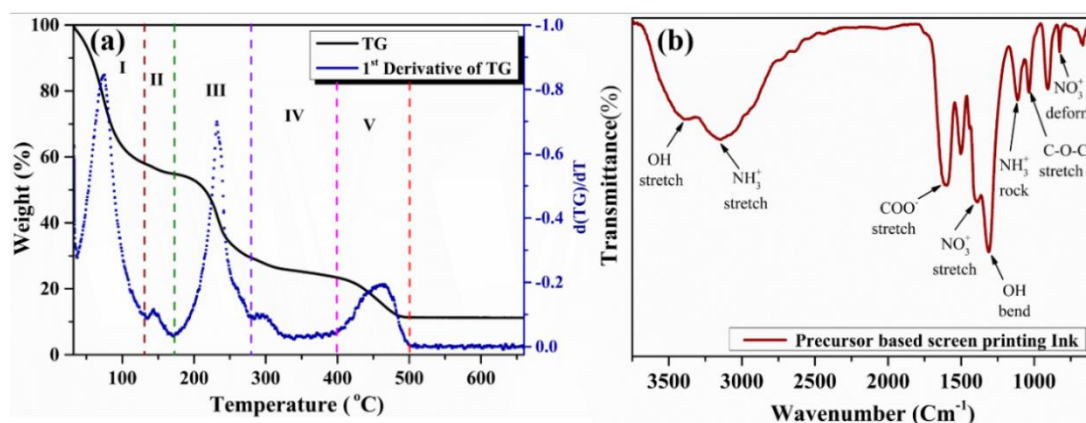


Fig.4.7 (a) Thermogravimetric analysis and (b) FTIR spectra of aqueous-based clogging free combustible molecular precursor ZnO screen printing ink.

A small peak in the DTG curve is observed from 280 °C to 320 °C corresponds to the considerable mass loss, due to removal of carbonaceous impurity generated during combustion and also the minute decomposition of Na-CMC, since the initial decomposition temperature of Na-CMC is almost near to the 280 °C. In the fifth stage, mass loss of 10 % was observed between the 400 °C and 500 °C, due to the further thermolysis of Na-CMC (final decomposition temperature 410 °C) and combustion by-products such as HCNO and CO. No mass loss was found above 500 °C, which indicated the formation of stable ZnO (Xing et al. 2011). FT-IR spectrum of the aqueous combustible molecular precursors for ZnO screen printing ink provides the molecular structure of its constituents (fig. 4.7 (b)). The small intense band in the higher energy region at 3390  $\text{cm}^{-1}$ , indicates the O–H symmetric stretching of the water molecules. The peaks at 1610, 1315 and 1042  $\text{cm}^{-1}$  attributed to the  $\text{COO}^-$  asymmetric stretching of carboxymethyl ether group and –OH bending, C-O-C stretching vibration of Na-CMC respectively (Pushpamalar et al. 2006). The bands at 3165 and 1105  $\text{cm}^{-1}$ , assigned to the stretching and rocking vibration of the ammonium ( $\text{NH}_3^+$ ) group in the glycine respectively (Kumar et al. 2012). The bands at 1385 and 830  $\text{cm}^{-1}$ , are assigned to the asymmetrical stretching and deformation modes of the nitrate ions ( $\text{NO}_3^-$ ) (Machado et al. 2010).

### **4.3.2 Particle-based metal oxide screen-printing inks**

Screen-printing ink has two-parts; functional materials and an organic vehicle. Properties and printability of screen-printing ink depend on the solid loading, particles size and its distribution and rheology.

#### **4.3.2.1 Pristine and Sr-doped ZnO screen printing inks**

Water-based environmental-friendly screen-printing ink consisted of 60 wt. % of pristine/Sr-doped ZnO as functional material and remaining 40 wt. % organic vehicle (Na-CMC and DI water) was formulated. Fig. 4.8 depicts the (a) thermal and (b) structural analysis of the organic vehicle consists of 4 wt.% of Na-CMC in 10 ml of DI water. In thermogram, weight loss of vehicle was recorded up to 500 °C. About 94 % weight loss is found in between 30-90 °C, because of the evaporation of water molecules present in an organic vehicle as a solvent. Again, a small weight loss is found in between 200 – 400 °C, this attribute to the decomposition of Na-CMC.

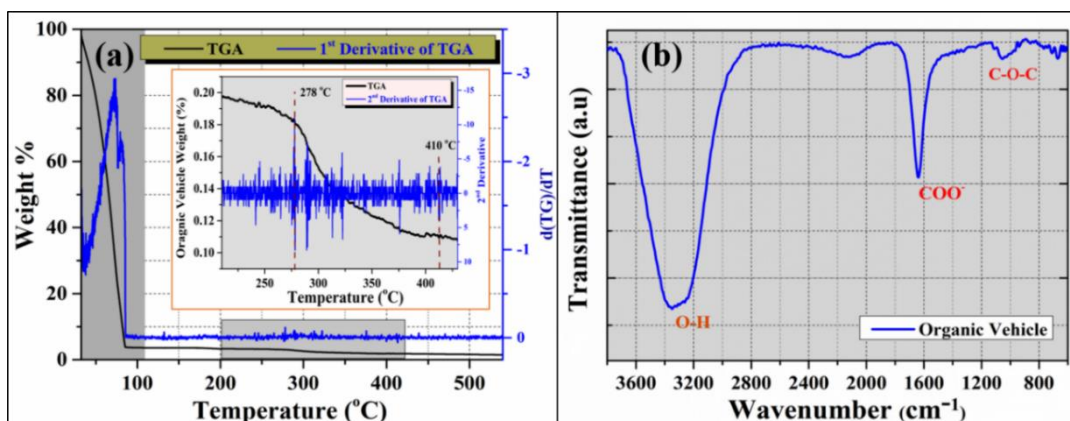


Fig. 4.8 (a) TGA curve and (b) FTIR spectra of organic vehicle (Na-CMC and DI water).

The inset of fig. 4.8 (a) curve reveals that the initial decomposition temperature ( $T_d$ ) and final decomposition temperature ( $T_f$ ) of Na-CMC are 278 °C and 410 °C, respectively (Li et al. 1999). FTIR spectrum of organic vehicle is recorded in the wavelength range of 3800 – 600  $\text{cm}^{-1}$  in fig. 4.8 (b). The broad band at  $\sim 3374 \text{ cm}^{-1}$  is attributed to the O-H symmetric stretching of covalent bond in water. Characteristic absorption at  $\sim 1610 \text{ cm}^{-1}$  confirms the asymmetrical stretching of a carboxymethyl ether group ( $\text{COO}^-$ ) in Na-CMC (Heinze and Pfeiffer 1999). The intense band at  $\sim 1050 \text{ cm}^{-1}$  is related to the C–O–C stretch, which shift to a lower wavenumber indicates the characteristics of the polysaccharide skeleton (Rani et al. 2014).

#### 4.3.2.2 Pristine and La-doped BaSnO<sub>3</sub> screen printing inks

Water-based environmental-friendly pristine and La-doped BaSnO<sub>3</sub> screen-printing inks were formulated. Formulated inks were made up of 60 wt. % of pristine/La-doped BaSnO<sub>3</sub> as functional material and 40 wt. % as organic vehicle. Organic vehicle was processed by adding 5 wt. % of HEC into the 10 ml of water and followed by stirring at rate of 200 rpm for 12 h. Fig. 4.9 shows the thermogravimetric and structural analysis of the prepared water based organic vehicle. In thermogram, the weight loss was occurred in four stages: firstly, small loss was observed in the temperature range from 38-108 °C due to desorption of water from the hydrogel surface. Secondly, nearly 89 % of weight loss was observed in the temperature range 108-268.4 °C attributed to the decomposition of HEC molecules. Small weight loss nearly, about 4 % of weight loss was occurred in the temperature range 268.4 °C- 344.4 °C due to

the degradation of undecomposed HEC molecules. Lastly, a remaining 5 % of weight loss was in the temperature range between 334.4 and 408 °C due to the decomposition of HEC molecules at the final stage (Fawal et al. 2018).

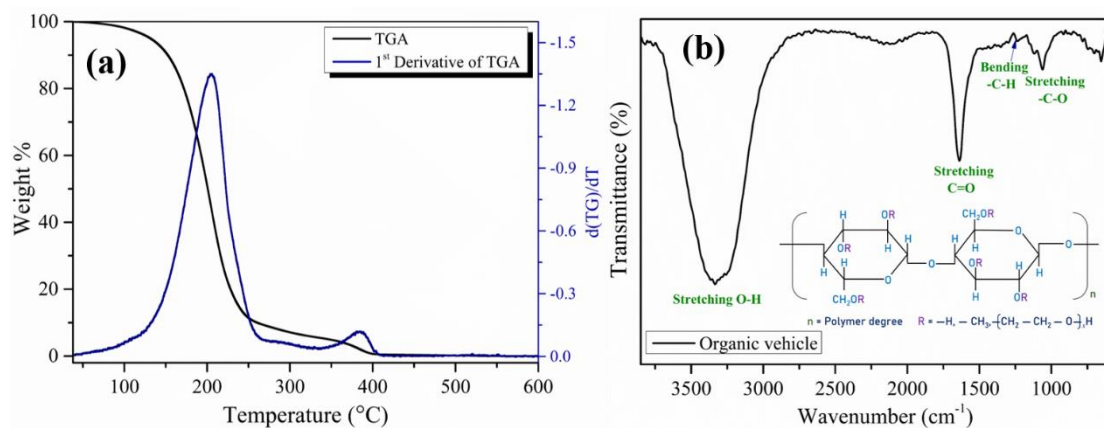


Fig. 4.9 (a) TGA curve and (b) FTIR spectra of organic vehicle (HEC and DI water).

FTIR spectrum of organic vehicle was recorded in the wavelength range of 3800 – 600 cm<sup>-1</sup>, the broad band at ~3334 cm<sup>-1</sup> attributed to the O-H symmetric stretching of covalent bond in water. Characteristic absorption at ~1610 cm<sup>-1</sup> confirms the asymmetrical stretching of a double bond of carbonyl, carboxyl and carboxyl salt (C=O) in HEC (Sheikh et al. 2013). The intense band at ~1246 and ~1050 cm<sup>-1</sup> is related to the stretching vibration of C-H and C–O bonds present in the HEC molecules (Fawal et al. 2018).

#### 4.4 Conclusions

In summary, water-based reducible particle-free silver precursor screen-printable inks comprised of silver nitrate (< 25%), citric acid, Na-CMC, and water were formulated. Formulated inks with silver precursor loading of 14%, 18%, and 22% exhibit shear thinning and rheological properties decent for screen printing. Rheology of developed inks during printing was studied, and about 74–88% of viscosity recovered in 110 s. The curing temperature of formulated inks to obtain the conductive films is 176 °C. The FTIR Peaks at ~1631 cm<sup>-1</sup> and ~1044 cm<sup>-1</sup> confirms the presence of Na-CMC, while a small peak at about 1382 cm<sup>-1</sup> attributes to the NO<sub>3</sub><sup>-</sup> vibrations of silver nitrate.

An aqueous combustible particle- free ZnO screen printing ink made of zinc nitrate, glycine, Na-CMC, and water was formulated. The minimum curing temperature

of the formulated ZnO screen printing inks is 400 °C. Presence of Na-CMC in ZnO screen printing ink is confirmed by the FTIR peaks at 1610, 1315 and 1042  $\text{cm}^{-1}$ . The bands at 3165 and 1105  $\text{cm}^{-1}$ , reveals the presence of glycine, while small protrude at 1385 and 830  $\text{cm}^{-1}$  belongs to the nitrate ions ( $\text{NO}_3^-$ ) of zinc nitrate.

An environmental-friendly particle-based pristine and Sr-doped ZnO screen-printing inks were formulated, which comprised of 60 wt. % of pristine/Sr-doped ZnO as functional material respectively and remaining 40 wt. % as organic vehicle. The minimum annealing temperature required to form the porous pristine and Sr-doped ZnO films is 400 °C.

An environmental-friendly particle-based pristine and La-doped  $\text{BaSnO}_3$  screen-printing inks were formulated. The formulated inks were made up of 60 wt. % of pristine/La-doped  $\text{BaSnO}_3$  as a functional material and remaining 40 wt. % with an organic vehicle (HEC and DI water).





## CHAPTER 5

### SCREEN PRINTED FILMS OF METAL, PRISTINE AND DOPED METAL OXIDE – THEIR APPLICATIONS

#### 5.1. Introduction

Here, the fabrication and characterization of metal (Ag) and metal oxide (ZnO, Sr-doped ZnO, BaSnO<sub>3</sub> and La-doped BaSnO<sub>3</sub>) screen printed films are discussed. In this chapter, Ag films were printed on the rigid and flexible substrates using particle-free Ag screen printing inks and optimized Ag screen printed films were incorporated as gate electrode in a BGTC TFTs. Gas sensing performance of the screen printed ZnO, Sr-doped ZnO, BaSnO<sub>3</sub> and La-doped BaSnO<sub>3</sub> thick films being used as a sensing layer were evaluated towards the various analyte gases such as NH<sub>3</sub>, C<sub>2</sub>H<sub>5</sub>OH, H<sub>2</sub>S etc.

#### 5.2. Experimental Procedure

The pattern was printed using stainless-steel frame in which the nylon screen mesh (500 counts) stretched under the tension of 20 N/m. Coater and polymer squeegee blade (shore-B) were kept at an angle of 90° and 45° with the screen mesh, respectively. Snap-off distance, printing speed and printing force was maintained 1.5 mm, 50 mm s<sup>-1</sup> and ~ 30 N, respectively.

##### 5.2.1 Fabrication of screen-printed silver patterns as bottom gate electrode in TFTs

Formulated particle-free silver screen printing inks were transferred on to the glass and polyamide substrates by screen printing technique. Further, the as-printed films were annealed at 200 °C for 20 min. Multiple layers of screen-printed films were prepared by using optimized formulated particle-free silver ink. To realize the application of screen-printed silver films as an electrode, a bottom gate top contact (BGTC) thin film transistor (TFT) with low-temperature solution combustion derived indium zinc tin oxide (IZTO)-semiconductor, and the sodium β-alumina high-k dielectric were fabricated. The formulation of the solution and the fabrication of both the semiconductor and dielectric films were explained elsewhere (Pujar et al. 2019).

### **5.2.2 Fabrication of ZnO based screen printed films - gas sensing applications**

An aqueous combustible particle free ZnO ink was deposited onto the corning glass substrates to fabricate patterns of  $2 \times 2 \text{ cm}^2$  via screen printing. These screen-printed patterns were annealed for an hour at  $400 \text{ }^\circ\text{C}$  and  $500 \text{ }^\circ\text{C}$ . A pair of metallic electrodes of dimension  $0.3 \times 2 \text{ cm}^2$  deposited at a distance 1.5 cm apart from each other.

Screen printing of the particle based pristine and Sr-doped ZnO ink was performed on the corning glass substrate and later annealed at  $500 \text{ }^\circ\text{C}$  for 2 h in ambient. The RuO<sub>2</sub> activated Sr-doped ZnO heterostructure film were fabricated by immersing the Sr-doped ZnO screen printed thick film into 0.02 M aqueous solution of RuCl<sub>3</sub> for 5 min, followed by exposure under infra-red light for 1 h and annealed at  $500 \text{ }^\circ\text{C}$  for 30 min in a muffle furnace.

Chemiresistive planar type configuration sensors of undoped, Sr-doped and RuO<sub>2</sub> activated Sr-doped ZnO were fabricated by depositing a pair of metallic electrodes of dimension  $0.3 \times 2 \text{ cm}^2$  deposited at a distance 1.5 cm apart from each other on an active area of  $2 \times 2 \text{ cm}^2$  screen-printed sensing layer. Silver-electrodes were dried at  $120 \text{ }^\circ\text{C}$  for 1 h in hot air oven.

### **5.2.3 Fabrication of BaSnO<sub>3</sub> based screen printed films - gas sensing applications**

The formulated particle-based pristine and La-doped BaSnO<sub>3</sub> screen printing inks were screen printed on the corning glass. As printed films were annealed in ambient conditions at  $500 \text{ }^\circ\text{C}$  for 2 h.

To develop surface activated CLBSO and RLBSO films, two different screen-printed La-doped BaSnO<sub>3</sub> films were dipped for 10 min in 0.03 M aqueous solution of CeCl<sub>3</sub> and RuCl<sub>3</sub>, respectively. Later, the films were exposed by infra-red light for 1 h followed by annealing in a muffle furnace at  $500 \text{ }^\circ\text{C}$  for 30 min. Chemiresistive planar type configuration sensors of metal oxide were fabricated as mentioned earlier and their gas sensing characteristics were estimated and analysed.

### **5.2.3 Measurements and characterization**

*XRD analysis:* Crystal structure of screen-printed films (Ag, ZnO, Sr-doped ZnO, BaSnO<sub>3</sub> and La-doped BaSnO<sub>3</sub>) were characterized by X-ray diffraction (XRD; RIGAKU Miniflex 600) using Cu-K $\alpha$  radiation at a scanning rate of  $1 \text{ }^\circ/\text{min}$ .

*Calculation of lattice parameter:* Hexagonal closely packed structured ZnO particle's lattice parameter was calculated using Cohen's method.

*Morphological and Elemental composition studies:* The surface morphology and elemental composition of screen-printed films were assessed using scanning electron microscopy (JEOL model JSM 6380 system) with energy-dispersive X-ray spectroscopy. To understand the chemical state of elements, present in the pristine, doped and surface activated screen-printed films X-ray photoelectron spectroscopy (XPS; PHI5000 Versa probe II) study was performed using Al K $\alpha$  radiation (~1486.6 eV) as an excitation source.

*Atomic Force Microscopy:* The roughness of single and multi-layered screen-printed Ag films was characterized by atomic force microscopy (AFM, Park XE-100).

*Adhesion Test:* Adhesion of the screen-printed films on the glass substrates were assessed according to ASTM D3359-09 (Paint, Related Coatings, & Applications, 2009).

*Resistance measurement:* The sheet resistance ( $R_s$ ) of the Ag screen printed films was measured using a four-point probe instrument (SES Instruments Pvt. Ltd). Sheet resistances (average of several measurements at different positions) were computed after considering proper correction factors based on sample geometries. Conductivity was calculated using the formula shown in equation 5.1.

$$\sigma = \frac{1}{R_s \times t} \quad (5.1)$$

*Thickness measurement:* Thickness of the Ag and ZnO based screen-printed films were measured using scanning electron microscopy (JEOL model JSM 6380 system) and step profilometer (Ambios XP-2 Profilometer, SN 167) respectively.

*TFTs performance test:* The fabricated TFTs were characterized using parameter analyzer with KITHELY source meter. Further, the static performance parameters such as saturation mobility ( $\mu_{sat}$ , eqn. 5.2), on: off ratio ( $I_{on}/I_{off}$ ), and the threshold voltage ( $V_{th}$ ) were estimated.

$$I_{D(sat)} = \frac{W}{2L} \times \mu_{sat} \times C_i \times (V_G - V_{th})^2 \quad (5.2)$$

Where,  $I_{D(sat)}$ ,  $W/L$ , and  $C_i$  are saturation drain current, channel dimensions, and the capacitance per unit area of sodium  $\beta$  alumina.

*Edge sharpness and resolution:* Edge sharpness and resolution of the Ag, undoped and Sr-doped screen-printed films were characterized by optical microscope (Zeiss microscopy Pvt. Ltd.).

*UV-vis Spectroscopy:* The optical properties of undoped and Sr-doped films were analyzed using UV-Vis Spectroscopy (USB4000-UV-VIS, Ocean Optics).

*UV sensing measurement:* UV sensing properties were examined at ambient condition in a ceased black-box containing the UV lamp with intensity of 2.3 mW/cm<sup>2</sup>.

*Gas sensing measurement:* Gas sensing characterization was carried out in the custom-made air-sealed gas chamber unit with a heater, probes and thermocouples. Schematic illustration of gas sensing measurement set-up is depicted in fig. 5.1.

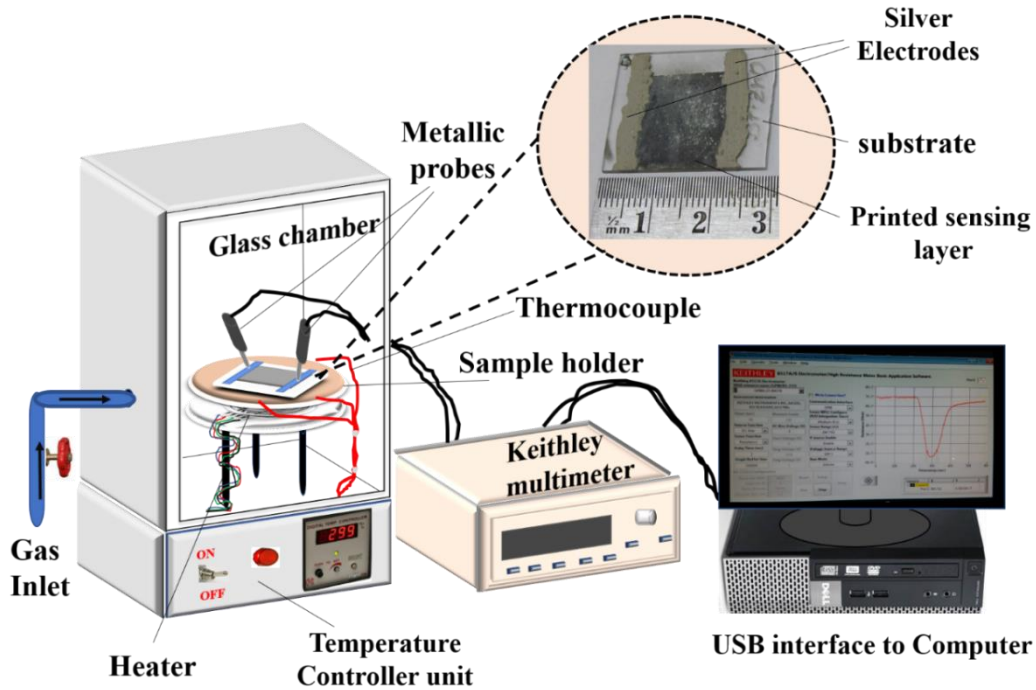


Fig. 5.1. Schematic diagram of set-up for the gas sensing measurement system

Static liquid gas distribution method was employed to calculate the desired concentration (C) of the target gas in ppm by using the equation 5.3 (Poloju et al. 2018).

$$C = \frac{22.4 \times \phi \times \rho \times V_1}{M \times V_2} \times 1000 \quad (5.3)$$

Where C (ppm) is the concentration of target gas,  $\phi$  is the gas volume fraction or purity,  $V_1$  ( $\mu$ l) and  $V_2$  (l) are volumes of liquid and chamber.  $\rho$  ( $g\ ml^{-1}$ ) and  $M$  ( $g\ mol^{-1}$ ) are

density and molecular weight of the liquid respectively. Since, small amount of vapours was loaded, therefore the variation in pressure characteristics inside the chamber was not observed. Gas sensing characteristics such as sensitivity, response and recovery time towards the ammonia and formaldehyde of ZnO sensors obtained from particle free inks were evaluated. Gas sensing properties of the particle based screen-printed ZnO sensors obtained from the three fuel- systems towards the 100 ppm of ammonia, ethanol, LPG, chlorine and 50 ppm of hydrogen sulfide gases were estimated. Pristine, Sr-doped ZnO and RuO<sub>2</sub> activated ZnO sensors were characterized for the gas sensing properties, when exposed to different concentrations of ammonia at room temperature. The room temperature ammonia and formaldehyde sensing properties of BaSnO<sub>3</sub> based sensors were evaluated and analysed. Gas response or sensitivity (*S*) is defined as the ratio of change in resistance of the sensor in presence and absence of the target gas to initial resistance of the sensor. The relation for *S* is as follows (equation 5.4):

$$S = \frac{(R_g - R_a)}{R_a} \quad (5.4)$$

Resistance of the sensor was measured using an electrometer (6517B, Keithley, Germany) with computer interface. The *R<sub>a</sub>* and *R<sub>gas</sub>* are defined as the electrical resistances of the sensor upon exposure to air and analyte gases respectively. Response and recovery times were defined as the time taken to achieve 90 % of electrical resistance change during adsorption and desorption, respectively. The gas response of the sensor was measured at constant pressure. DC bias voltage applied was -3V and relative humidity in the gas chamber was maintained at 60% using a digital humidity controller (Humitherm, India) during gas sensing measurements.

### 5.3. Results and Discussion

#### 5.3.1 Characterization of Ag screen printed films and its applications

The X-ray diffraction of screen-printed films obtained from the different Ag formulated inks annealed at 200 °C for 20 min is shown in fig. 5.2 (a). XRD reveals the films to be highly crystalline with the distinct sharp peaks at 38.8°, 44.9°, 64.9°, 77.9° and 81.9° for the planar reflections of (111), (200), (220), (311) and (222) respectively (ICDD: 01-087-0720). Also, it confirms that no other phases are formed after the reduction of silver nitrate to silver. The conductivity of the screen-printed silver films

on glass substrates using aqueous combustible precursor-based inks is shown in fig. 5.2 (b). The conductivity values of the films are found to be  $2.6 \times 10^6$ ,  $4.0 \times 10^6$  and  $8.2 \times 10^6$  S.m<sup>-1</sup> from Ink-1, Ink-2, and Ink-3, respectively. Obviously, as the concentration of silver nitrate in ink increases the conductivity is also increased. On the other side, the recovery rate of viscosity during printing at 80 s decreases with increases in wt.% of silver nitrate. The conductivity of printed films on the polyamide substrate developed using ink-2 is found to be  $2.6 \times 10^6$  S.m<sup>-1</sup>.

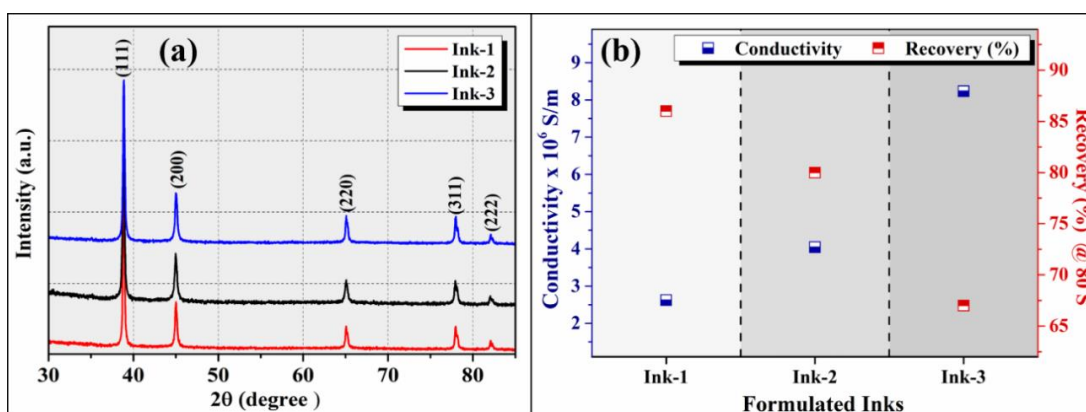
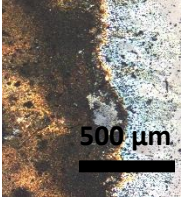
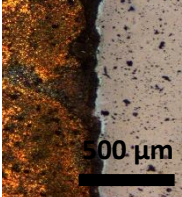
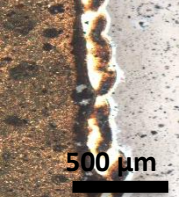


Fig. 5.2 (a) XRD pattern and (b) electrical conductivity of the silver screen printed films prepared from Ink-1, Ink-2, and Ink-3.

The Ink-2 possessed the high viscosity than the Ink-1 and also exhibited the fast recovery rate of viscosity and higher value of modulus ratio ( $G''/G'$ ) compared to Ink-3. Ink-2 offered not only the high conductivity with narrow line definition and sharper edges, but also avoids paste to fracture and blistering defects as shown in Table 5.1. A peel-off or scotch tape test was conducted to assess the adhesion of silver films obtained from Ink-2 on the glass substrates as shown in fig. 5.3. The peeling test confirms the adhesion of silver film over substrates lies in the 3B category, according to ASTM-3359B.

Table 5.1 Comparison of formulated inks with rheological, electrical properties.

Inks	Viscosity (Pa.s)	Recovery @ 80 s (%)	Modulus ratio (G''/ G')	Change-over point (Pa.s)	Conductivity ( $\times 10^6 \text{ Sm}^{-1}$ )	Edge of the film
<b>Ink-1</b>	210	82	0.75	110	2.6	
<b>Ink-2</b>	328	80	0.61	150	4.0	
<b>Ink-3</b>	454	67	0.40	538	8.2	

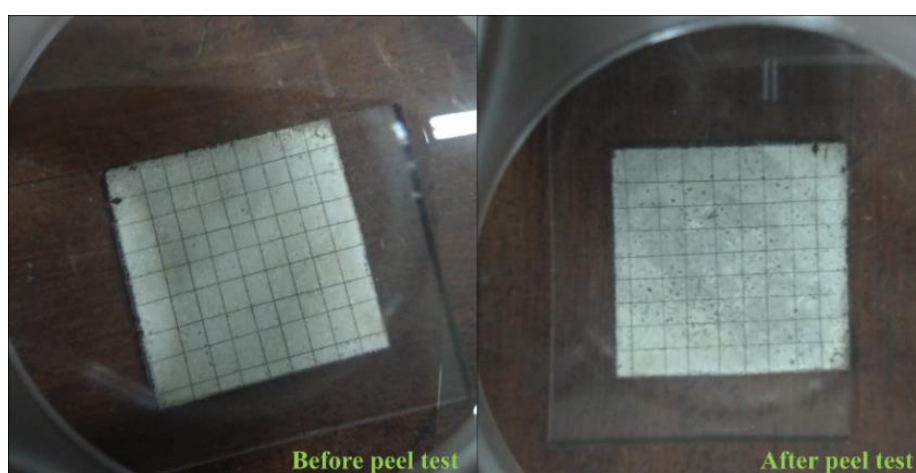


Fig. 5.3 Cross-cut tape test for the screen-printed silver films.

Optical images of printed patterns on glass substrates using Ink-2 are shown in fig. 5.4 (a). Irrespective of the direction of printing (is shown by black colored arrow), edges of the printed pattern are smooth and sharp (fig 5.4 b-d). The bright LED (under the externally applied voltage) as shown in fig. 5.4 (e), were connected to silver films processed on polyamide substrates to validate its continuity and applicability.

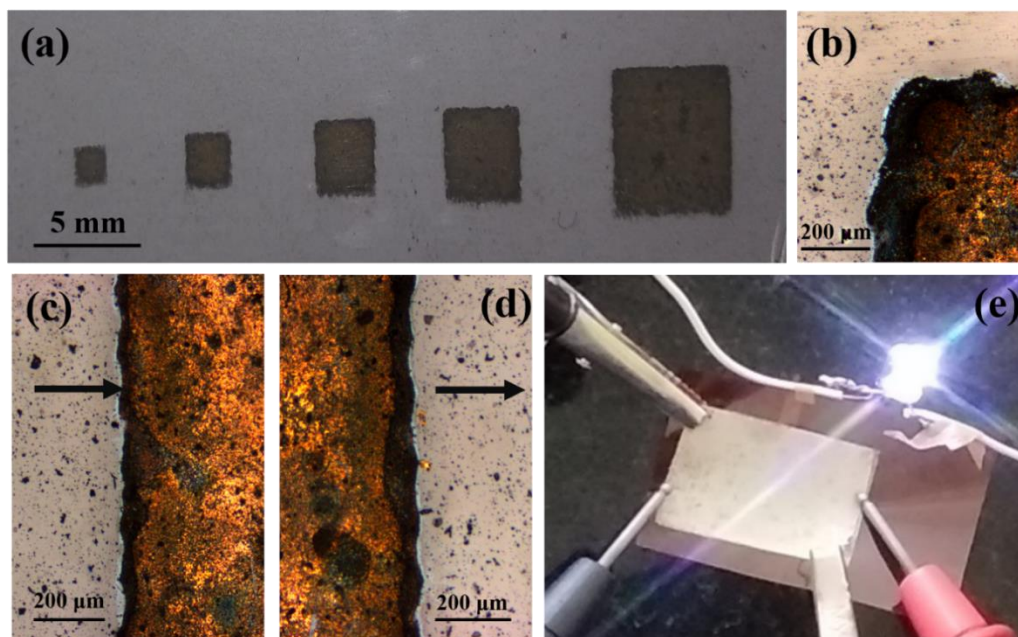


Fig. 5.4 (a) Optical images Ag films and tracks from Ink-2, (b), (c), (d) Optical microscopy images of the edge of the silver printed lines on glass substrates. Black arrow indicates the direction of printing. (e) Operation of LED's connected to the silver films printed on the flexible polyamide substrate.

A particle-free ink exhibits the lowest resistivity of  $24 \mu\Omega\text{-cm}$  with the thickness of  $3 \mu\text{m}$ , is found to be a promising competitor to the commercially available inks consist of more than 45-55 % of silver loading. Hence, chances of agglomeration and clogging of the pores in the screen mesh during printing can be completely avoided with particle free ink. As a result, Ink-2 is used for further study of multiple layer printing due to its excellent rheological properties, superior performance, and good printing resolution. The conductivity of the single and multi-layered films is comparable, though anticipation is that conductivity should be the same. Resistivity values are in the range of  $2\text{-}4 \times 10^{-5} \Omega\text{-cm}$ . The elemental composition of the single and multi-layered films are shown in fig. 5.5.



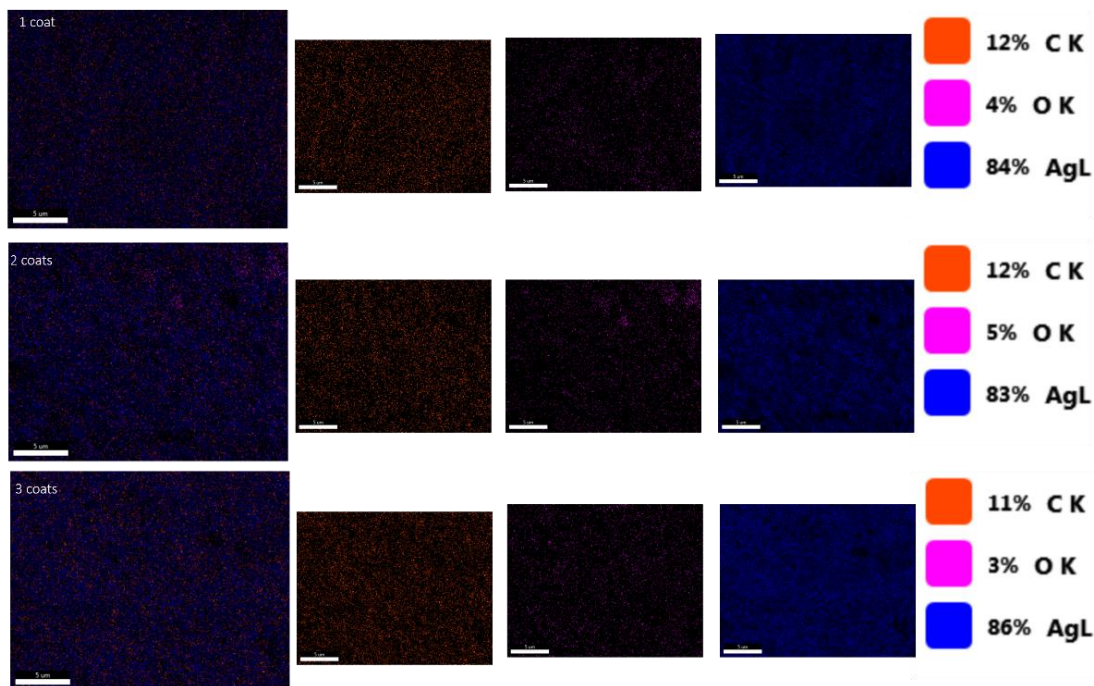


Fig. 5.5 EDS mapping of silver (Ag), carbon (C) and oxygen (O) elemental distribution on the surface of the film with multiple layers: (a) one, (b) two and (c) three coats.

Morphology, roughness, and thickness of the single, double, and triple layered films are shown in fig. 5.6. The SEM micrograph suggests that the printed films are composed of well-connected networks of the silver. Furthermore, the AFM analysis shows the films are smooth with minimal roughness of about 43.1 nm in a single pass of squeeze during screen printing. The film thickness is found to be increased with the increase in a number of squeeze movement in the printing process. The minimum thickness obtained of about 3  $\mu\text{m}$  in a single pass of squeeze. The film thickness achieved using particle-free screen-printing inks is extremely lower than the thickness of the screen-printed films obtained by particle-based inks.

Due to its superior performance and good printing resolution, Ink-2 is further used to develop a printed gate electrode of the oxide-TFT. To reveal the efficacy of the present screen-printed silver film, a BGTC TFTs with screen printed silver as a gate electrode is fabricated using solution combustion derived IZTO as semiconductor and the solution processed sodium  $\beta$ -alumina as dielectric (fig. 5.7 (a)). The output and transfer characteristics of TFTs is presented in fig. 5.7 (a) and (b). The static

performance parameters such as  $\mu_{\text{sat}}$ ,  $I_{\text{on}}/I_{\text{off}}$ , and  $V_{\text{th}}$  are estimated to be  $0.88 \text{ cm}^2\text{V}^{-1}\text{s}^{-1}$ ,  $10^2$ , and  $\sim 0.3 \text{ V}$ , respectively.

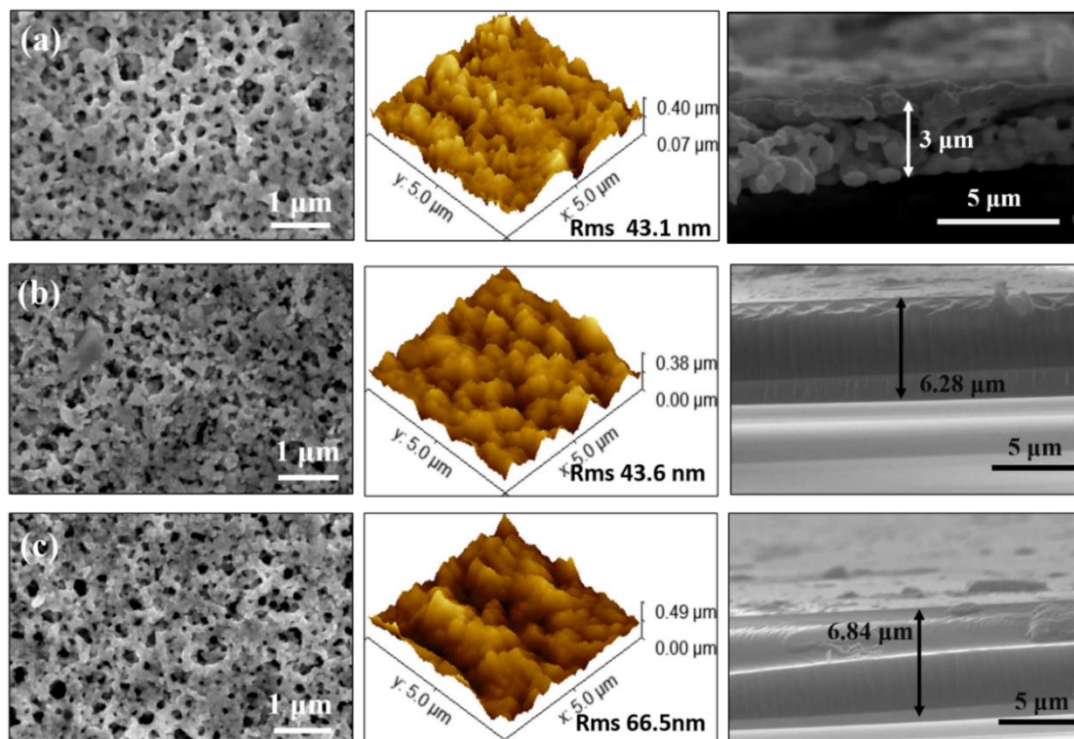


Fig. 5.6 SEM, AFM, and thickness of the screen-printed films of different layers (a) one (b) two and (c) three layers obtained using Ink-2.

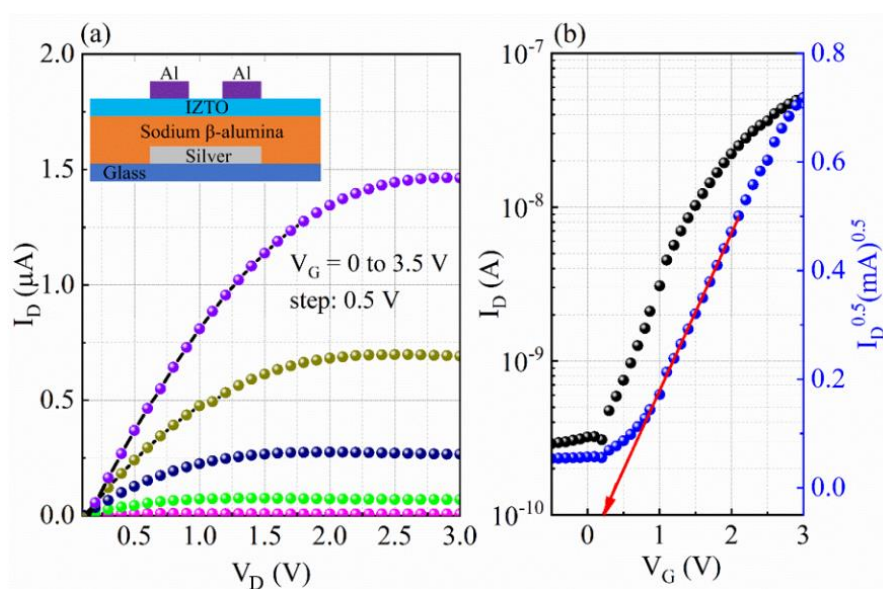


Fig. 5.7 (a) Output and (b) transfer characteristics of the TFT.

### 5.3.2 Combustion derived ZnO based screen printed films – A UV and Gas Sensor

#### 5.3.2.1 Undoped particle-free screen printed ZnO films

The XRD diffraction patterns of the screen printed ZnO films processed from the combustible molecular precursor-based screen-printing ink annealed at temperature 400 °C and 500 °C are depicted in fig. 5.8 (a). Diffraction peaks at 31.92°, 34.74°, 36.56°, 47.86°, 56.9°, 63.16° and 68.16° correspond to the deflection planes (100), (002), (101), (102), (110), (103) and (112) respectively, are in good agreement with ICDD (00-01-1136). Furthermore, no other peak related to any secondary phase indicates the formation of the pure phase of polycrystalline wurtzite structured ZnO from clogging free combustible molecular precursor. The intensity of predominant diffraction peaks assigned to the planes ((100), (002) and (101)) of the ZnO phase in the film processed at temperature 500 °C was found higher than the intensity of the peaks of the respective planes in the ZnO film annealed at 400 °C as shown in fig. 5.8 (b), which revealed the enhancement of crystallinity. The elevated annealing temperature may be yielded sufficient energy to recrystallize the particles, thereby the degree of crystal perfection is increased (Katoch et al. 2013).

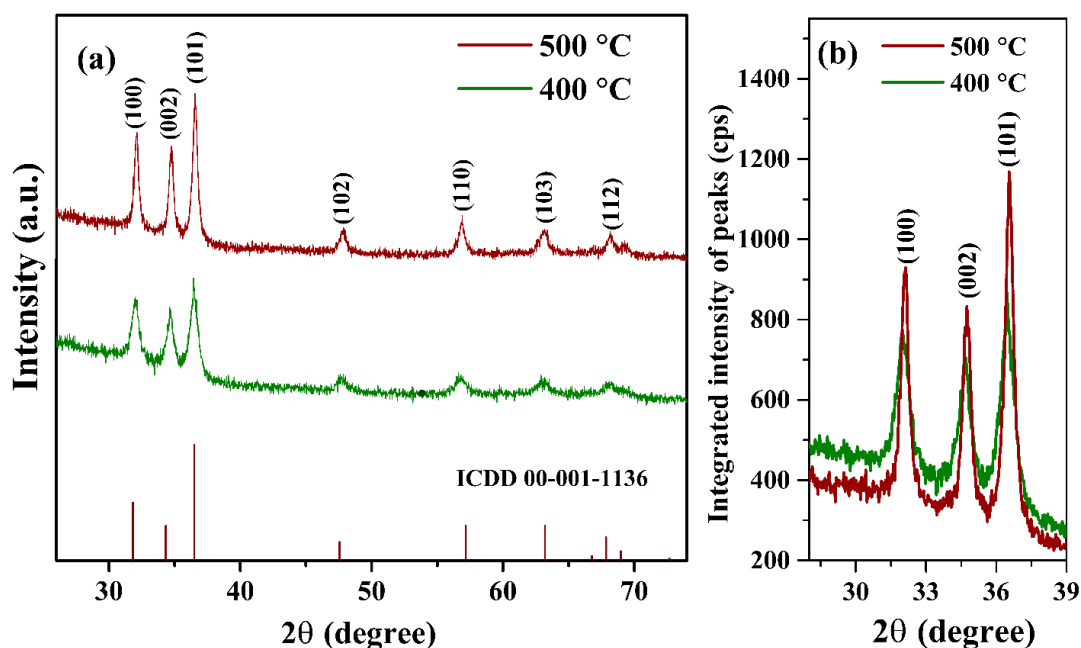


Fig. 5.8 (a) XRD pattern of screen-printed ZnO films annealed at different temperatures and (b) integrated intensity of (100), (002) and (101) diffraction peaks.

Precise lattice constants ‘*a*’ and ‘*c*’ of the ZnO phase in the films were estimated using Cohen’s analysis method. The steps involved in the computation of lattice constants using Cohen’s method is given in the Appendix II. Unit cell volume ( $V_o$ ) and bond length (*l*) of Zn-O were estimated using the equations 3.19 and 3.20 respectively. Lattice constants of the screen printed ZnO films processed at 400°C and 500°C are  $a = 3.25 \text{ \AA}, c = 5.21 \text{ \AA}$  and  $a = 3.27 \text{ \AA}, c = 5.24 \text{ \AA}$  respectively. *c/a* ratio of the ZnO hexagonal crystal structure present in both films is estimated as 1.6. Unit volume and bond length (Zn-O) of the ZnO film annealed at 400 °C are found to be  $47.84 \text{ \AA}^3$  and  $1.98 \text{ \AA}$  respectively, whereas for ZnO film annealed at 500 °C are observed to be  $48.76 \text{ \AA}^3$  and  $1.99 \text{ \AA}$  respectively.

Crystallite size and lattice distortion were estimated for the ZnO phase in the films processed at 400 °C and 500°C. Crystallite size ( $D_v$ ) of the ZnO phase was determined employing the Scherrer equation (3.7) and found to be 17 nm and 21 nm for the ZnO films processed at 400 °C and 500°C respectively. Crystallite size and induced lattice strain were also calculated using the W-H and H-W plots obtained from the following equations (3.9) and (3.13) respectively, (Plots of W-H and H-W for the calculation of crystallite size are found in Appendix III). Obtained results from the Scherrer, W-H and H-W equations are shown in Table 5.2.

Table 5.2 The microstructural parameters of combustible precursor-based screen-printed films annealed at different temperature.

<b>Microstructural parameters of ZnO using different methods</b>					
Annealing temperature	Scherrer	Williamson-Hall (W-H)		Halder-Wagner (H-W)	
	$D_v$ (nm)	$D_v$ (nm)	$\epsilon \times 10^{-3}$	$D_v$ (nm)	$\epsilon \times 10^{-3}$
400 °C	12	20	3.69	21	4.47
500 °C	17	31	2.29	33	3.06

It is noticed that the crystallite size of the ZnO phase in the films annealed at 500 °C increases from ~ 20 nm to ~ 31 nm, but lattice strain decreases. Higher annealing temperatures might have provided adequate activation energy for the migration of crystallites towards the equilibrium sites and coalesce together to form larger crystallites. Increase in grain size with increasing annealing temperature, caused to the

minimization of the stress field present on the grain boundaries, therefore the lattice strain also reduces consequently and as result the crystallinity is enhanced (Choudhury et al. 2015).

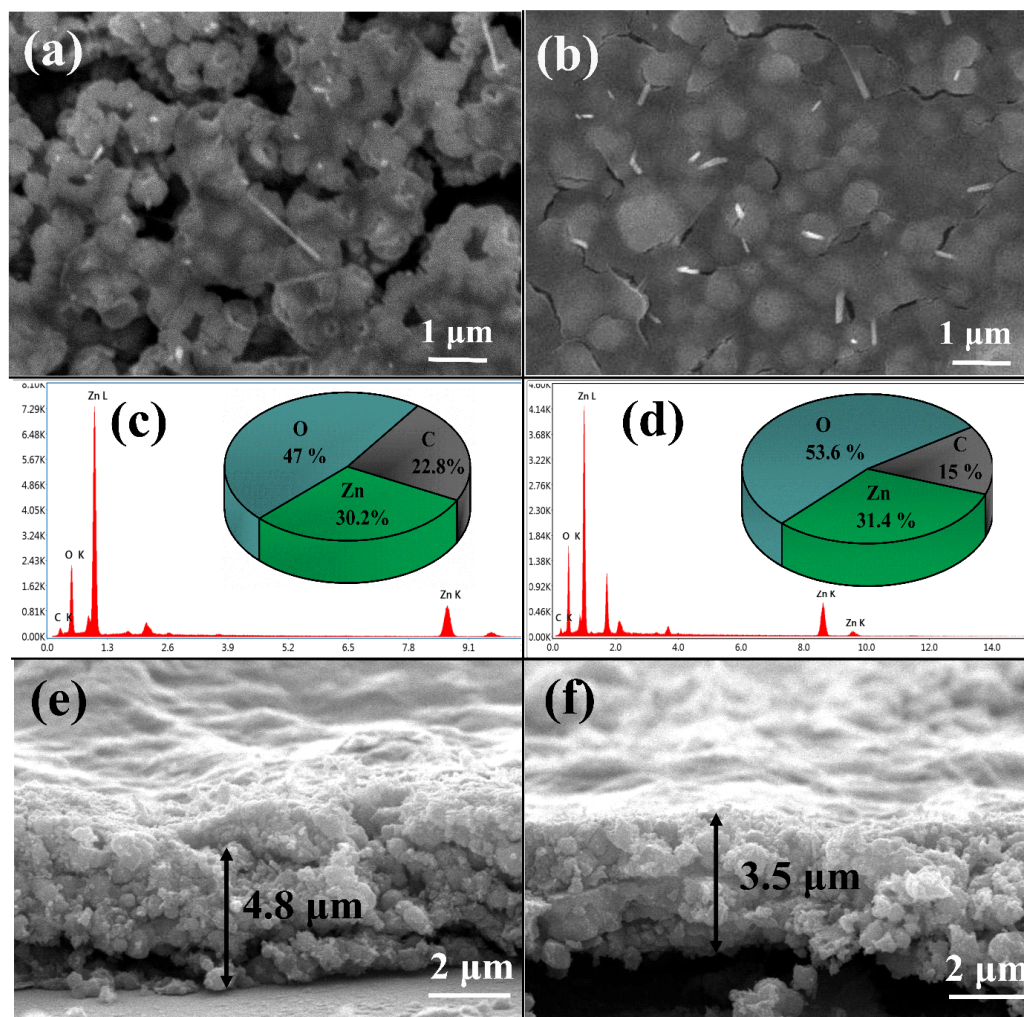


Fig. 5.9 SEM images of screen printed ZnO films annealed at (a) 400 °C and (b) 500 °C, Composition of elements present in the films annealed at (c) 400 °C and (d) 500 °C, Thickness of screen-printed films annealed at (e) 400 °C and (f) 500 °C.

The SEM images of screen printed ZnO films processed at 400 °C (fig. 5.9 (a)) indicates the grouped austromegabalanuspsittacus-sea species shaped morphology, with the small protruded needle-like structure from the surface. Protruded globules with the enlarged needle-like nanostructure were observed in the screen-printed ZnO films processed at 500 °C as shown in fig. 5.9 (b). The surface was more smoothed in the film processed at 500 °C than the film annealed at 400 °C. EDS spectra of screen printed

ZnO films processed at 400 °C and 500 °C is depicted in fig. 5.9 (c) and (d) respectively. EDS reveals the presence of Zn, O, and C elements in both films and the presence of carbon may be due to the unburnt residue of Na-CMC binder at the particular annealing temperature. Gradual decrease in carbon (elemental) concentration from about 22.8 % to 15 % in ZnO film processed at 500 °C, because of the profound thermal decomposition at the higher annealing temperature. TG analysis also indicated nearly 11 % mass loss in the temperature range between 400 °C and 480 °C. The thickness of the screen printed ZnO films processed at 400 °C and 500 °C were estimated using cross-section image (fig. 5.9 (e) and (f)) and found to be 4.8 μm and 3.5 μm, respectively.

The measured UV-visible diffuse reflectance spectra of combustible precursor based screen-printed ZnO films processed at different annealing temperatures is shown in Fig. 5.10 (a). Film processed at 400 °C exhibited higher reflectance (> 55%) than the film processed at 500 °C, which indicates changes in carrier concentration, surface microstructure, oxygen content, defects, etc. The optical bandgap of the screen-printed ZnO films processed at different annealing temperatures was derived by extrapolation of the linear fit of the curve  $(ahv)^2$  against  $hv$  up to a point,  $\alpha = 0$  as depicted in the inset of fig. 5.10 (a). The plot was obtained using the following equation 5.5 (Raj et al. 2016);

$$anhv = C(hv - E_g)^{1/2} \quad (5.5)$$

Where  $\alpha$ ,  $n$ ,  $hv$ ,  $E_g$  and  $C$  are absorbance coefficient, refractive index, photon energy, bandgap and velocity of light respectively. The bandgap was found to be 3.09 and 3.02 eV for the screen-printed ZnO films annealed at 400°C and 500°C respectively. The growth of grains into larger size in the films annealed at higher temperature may be caused to the decrement of bandgap (Parra and Haque 2014). It is also found that bandgap of the obtained ZnO nanostructures is lower than the bulk ZnO, indicates the presence of a high concentration of donor levels due to impurities or defects (Bayan and Mohanta 2013). The PL spectra of combustible precursor based screen-printed films annealed at 400 °C and 500 °C under an excitation wavelength of 380 nm are shown in fig. 5.10 (b). The intensity of defect-related emissions gets enhanced as the

processing temperature is increased. The emission peaks found at nearly 410 and 464 nm are signifying the neutral ( $V_{Zn}$ ) and ionized zinc vacancy ( $V_{Zn}'$ ) related defects.

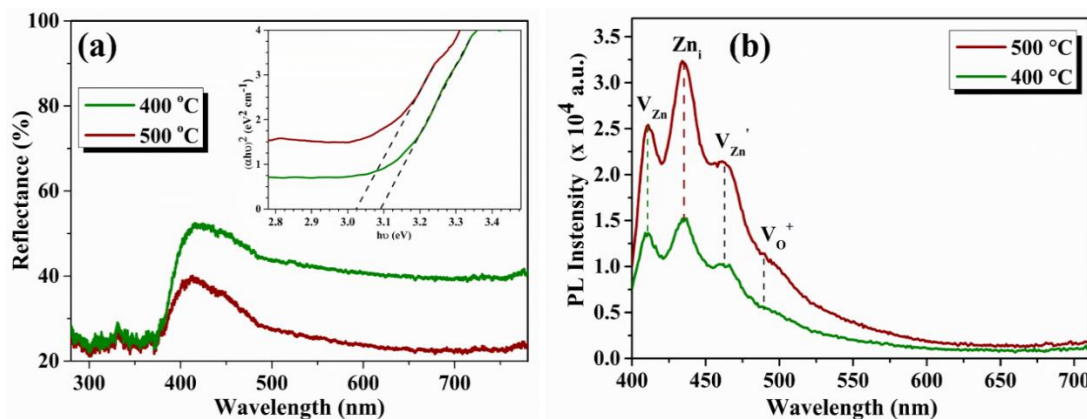


Fig. 5.10 (a) UV-vis reflectance spectra, inset is the Tauc's plot; (b) Photoluminescence spectra of screen printed ZnO films processed at 400 °C and 500 °C.

Further, emission peaks at 434 and 490 nm are ascribed to the donor-related defects zinc interstitial ( $Zn_i$ ) and oxygen vacancy ( $V_o^+$ ) respectively (Bayan and Chakraborty 2014; Yu et al. 2016). The enhancement of defect-related emission with an increase in the annealing temperature is observed. Higher annealing temperature promotes the perturbation of atomic arrangements in the crystal system which has resulted in the generation of more point defects such as interstitials, vacancies, etc. The concentration of  $Zn_i$  and  $V_o^+$  defects is observed more in the ZnO film annealed at 500 °C, reason behind this may be the substantial removal of oxygen from the ZnO crystal structure (Bayan and Chakraborty 2014). By comparing the intensity of  $Zn_i$  defect-related emission peak of both the films, it is concluded that the concentration of donor type of defect (Zinc interstitial ( $Zn_i$ )) is more in the film processed at 500 °C than the processed at 400 °C. Hence the donor band within the bandgap of the film annealed at 500 °C extends to a larger extent (Bayan and Mohanta 2013).

The gas-sensing performance of aqueous combustible precursor-based screen printed ZnO sensors processed at 400 °C and 500 °C were symmetrically investigated and compared. The gas response of the screen-printed sensors towards the different concentrations of ammonia (0.75 ppm - 5 ppm) and formaldehyde (3 ppm - 10 ppm) are shown in fig. 5.11 (a) and (b) respectively. It is found that the gas response of both

screen-printed ZnO sensors increased as the concentration of two analyte gases is increased.

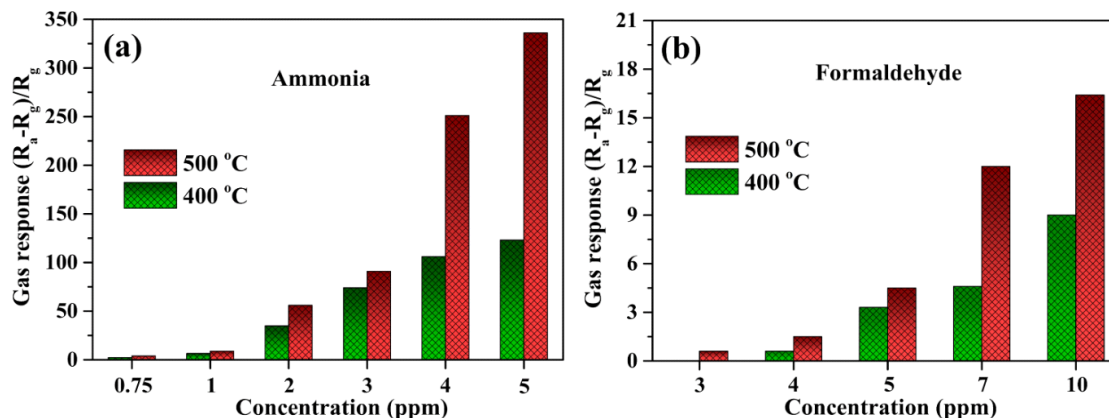


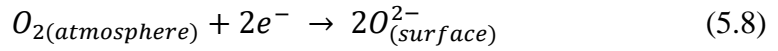
Fig. 5.11 Gas response of screen-printed ZnO sensors processed at different temperature towards the various concentration of gas (a) ammonia and (b) formaldehyde.

In fig. 5.11 (a), the gas response of the screen-printed ZnO sensor processed at 500 °C exhibited higher magnitude than the sensor processed at 400 °C upon exposure to various concentrations of NH<sub>3</sub>. The magnitude of response of the sensor processed at 500 °C was observed 3.98, 8.78, 55.9, 90.8, 251 and 336 towards the 0.75, 1, 2, 3, 4 and 5 ppm of NH<sub>3</sub> respectively. The highest gas response of the sensor processed at 500 °C was recorded 336 upon exposure to 5 ppm, which is nearly 2.73 times the gas response of the sensor processed at 400 °C. Fig. 5.11 (b) revealed that gas response of screen printed ZnO sensor processed at 500 °C enhanced by 2.5, 1.3, 2.6 and 1.8 times the ZnO sensor processed at 400 °C towards 4, 5, 7, and 10 ppm of HCHO. The screen-printed sensor processed at 400 °C was unable to detect 3 ppm of HCHO, but the sensor processed at 500 °C traced the same concentration of HCHO with a response value 0.6.

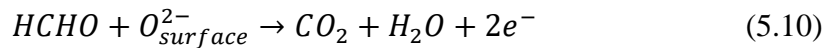
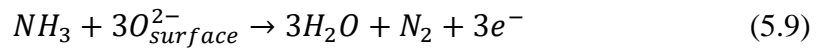
The gas sensing mechanism of ZnO relies on the modulation of electrical resistance in the presence and absence of the analyte gas. According to electron depletion region theory, pre-adsorbed oxygen gas molecules get chemisorbed on the ZnO film surface in the various forms like  $O_2^-$ ,  $O^-$ ,  $O^{2-}$  after the extraction of electrons out, as shown in equations (5.6), (5.7) and (5.8); as a result, the formation of electron depletion layer thereby electrical resistance of the sensor increases.







Lower bandgap stimulates the formation of chemisorbed oxygen molecules, but the concentration of chemisorbed oxygen species can be increased by smaller particle size, enhancing donor defects, and decreasing the desorption of oxygen molecules. At lower temperature, high concentration of  $O^{2-}$  molecules are formed. When the analyte gases (ammonia and formaldehyde) come in contact with the ZnO surface, chemisorbed oxygen species oxidize the analyte gas molecules, thereby electrons are returned to the conduction band as in equations (5.9) and (5.10). Hence, the electron depletion layer shrinks, thereby electrical resistance decreases.



The gas response of screen printed ZnO sensors annealed at 400 °C and 500 °C enhanced as the analyte gas concentration is increased. It may be due to the involvement of analyte gas molecules to react with chemisorbed species increases, which causes the release of electrons to the conduction band in large number, thereby electrical resistance decreases considerably. The reasons behind the enhanced gas-sensing performance of the screen-printed ZnO sensor annealed at 500 °C are high crystallinity, lesser lattice distortion, lower bandgap and high concentration of donor defects  $Zn_i$  and  $V_o$  in comparison with screen printed ZnO sensor annealed at 400 °C as shown in Table 5.3.

Table 5.3 Crystallinity, crystallite size, lattice distortion, band-gap and concentration of donor defects of screen printed ZnO sensors annealed at 400 °C and 500 °C.

Combustible precursor screen printed films annealed at	Crystallinity	Crystallite Size (nm)	Lattice Strain $\times 10^{-3}$	Bandgap (eV)	Concentration of donor defects
400 °C	Low	21	4.47	3.09	Low
500 °C	High	33	3.06	3.02	High

Oxides with high crystallinity possess periodic arrangements of cations and anions. By virtue of periodicity, the crystal has a smaller number of defects, due to completely

satisfied charge neutrality. On the other hand, amorphous or less crystalline materials don't have a periodic arrangement, the probability of defects (namely cation and/or anion vacancies) is high, this may lead to an increase in charge concentrations (Liu et al, 2018). Fig. 5.12 (a) illustrates the participation of chemisorbed species and ammonia molecules during the gas sensing mechanism. ZnO with inferior crystallinity contains a high number of electrons due to more structural imperfections (Katoch et al. 2013), which leads to the formation of a smaller electron depletion layer (EDL), as a result a small increase in the resistance during chemisorption process. Hence the modulation of resistance becomes smaller during anchoring and liberation of electrons when gaseous species come in contact, as shown in fig. 5.12 (b).

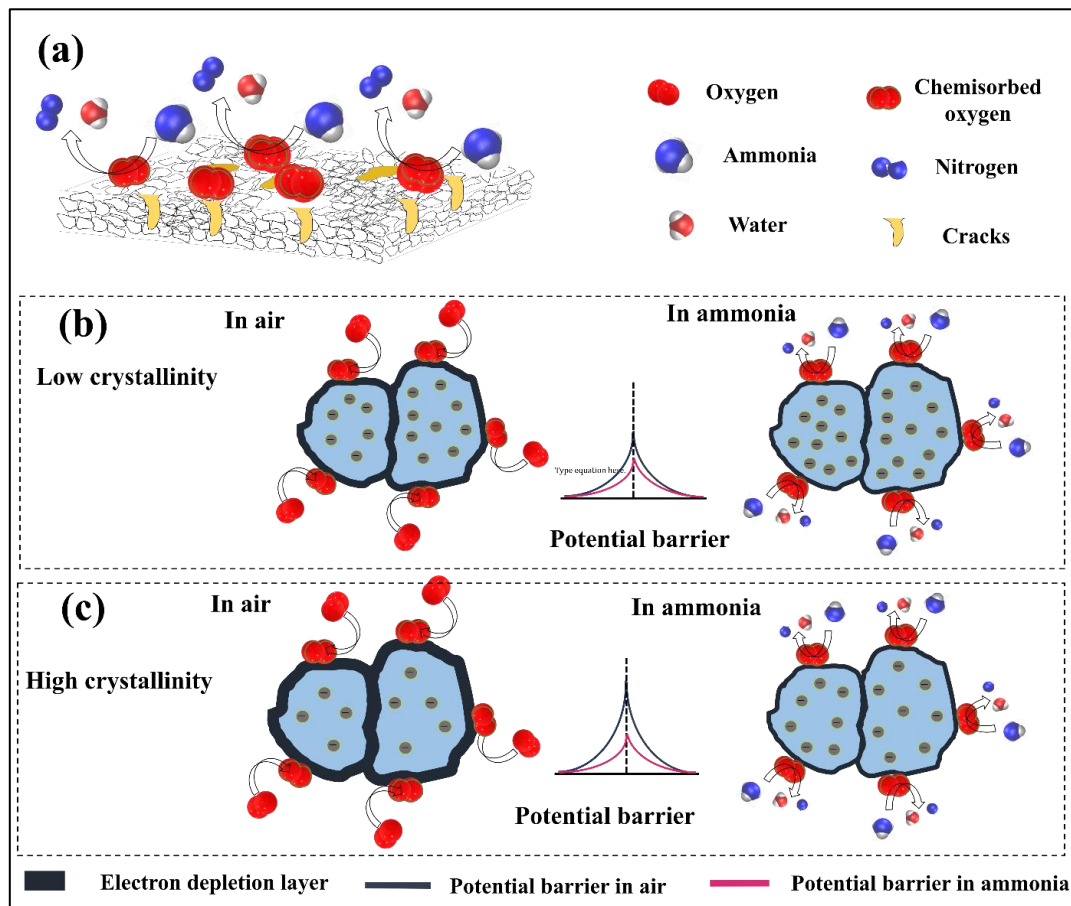


Fig. 5.12 Schematic illustration of the gas (ammonia) sensing mechanisms in the screen-printed ZnO sensors of different crystallinities.

On the other side, ZnO with better crystallinity, contains a smaller number of charge carriers encourage to form larger EDL, thereby the resistance of the sensor increases

significantly during the oxygen chemisorption process. It further leads to the pronounced resistance modulation during adsorption and desorption, thus exhibits superior gas responses as shown in fig. 5.12 (c). Hence, resistance modulation in high crystalline ZnO is higher than the low crystalline ZnO during anchoring and liberation of electrons upon exposure to the analyte gas as shown in equation (5.11).

$$\left(\frac{R_a}{R_g}\right)_{High\ crystallinity} > \left(\frac{R_a}{R_g}\right)_{Low\ crystallinity} \quad (5.11)$$

So, better crystallinity by densification may overcome the adverse effect of grain growth, and causes pronounced gas sensing ability in the screen-printed ZnO sensor annealed at 500 °C. Further, less lattice distortion (0.00229) in the screen printed ZnO sensor annealed at 500 °C assured the less scattering of electrons. Hence higher modulation in electrical resistance upon exposure to analyte gases (ammonia and formaldehyde) results in a higher gas response (Sahay and Nath 2008). In addition to this, donor-related defects ( $Zn_i$  and  $V_o$ ) increases the electrostatic interaction between the analyte gas molecules and ZnO nanostructure (Yu et al. 2016). Moreover, the presence of cracks on the surface makes the film permeable to the analyte gases, thereby gases comes in contact with underneath the grains, and increases the active sites for the chemisorption (Korotcenkov 2008). It is obvious that higher annealing temperature results in better crystallinity by densification, better crystallinity may overcome the adverse effect of the grain growth and causes a pronounced ability to detect the analyte gases.

Fig. 5.13 (a) and (b) depicts the real-time response of the screen printed ZnO sensors towards the various concentration of  $NH_3$  and HCHO respectively. The response of the gas sensors not only depends on the concentration of the analyte gases, but also on the adsorption and desorption process of oxygen molecules over the active site of the sensors. When the analyte gases are passed over both sensor surfaces, the resistance of the sensors decreases, which confirms the sensing behaviour. The resistance of the sensors reaches to its baseline resistance upon removal of analyte gas, which reveals the completion of the desorption process.

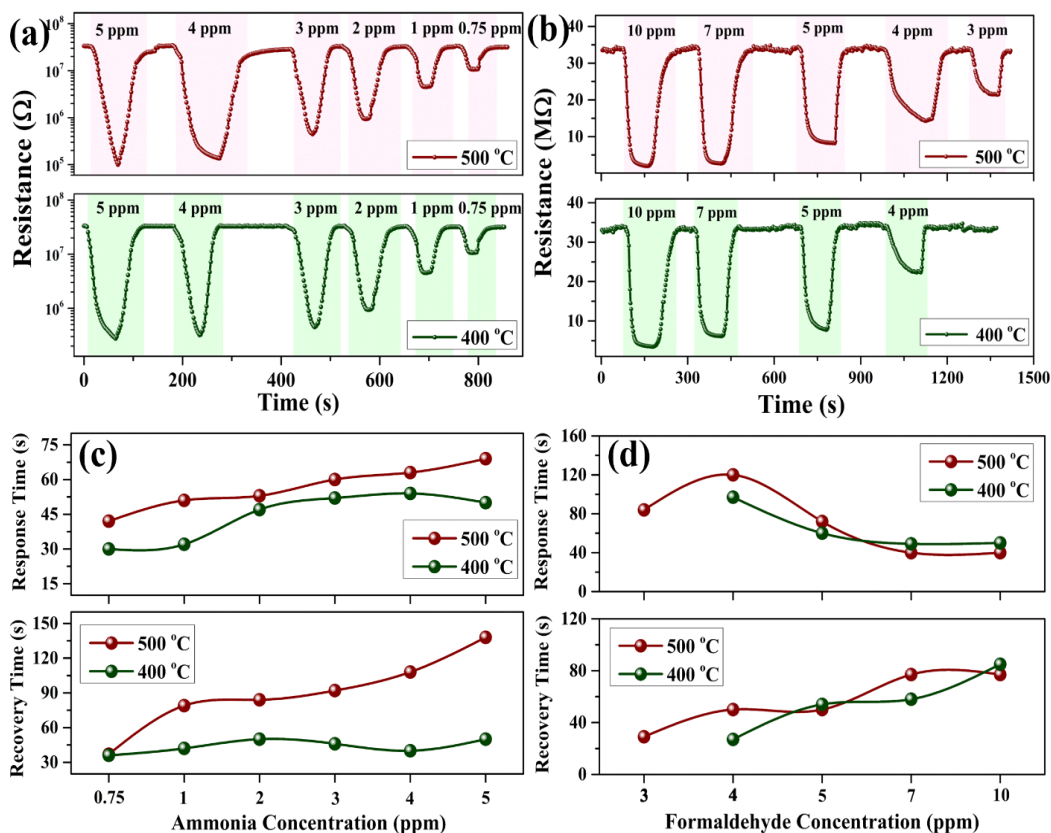


Fig. 5.13 Transient response of screen-printed ZnO sensors processed at 500 °C and 400 °C towards different gas concentrations of (a) ammonia and (b) formaldehyde, Response and recovery times of sensors annealed at 500 °C and 400 °C against different gas concentrations of (c) ammonia and (d) formaldehyde.

The response and recovery time of the screen-printed ZnO sensors processed at 400 °C and 500 °C towards the different concentrations of ammonia and formaldehyde were evaluated as shown in fig. 5.13 (c) and (d). Fig. 5.13 (c) revealed that the response time of screen-printed sensors processed at 400 °C and 500 °C upon exposure to 0.75 - 5 ppm of NH<sub>3</sub> were in the range from 30 to 50 s and 42 to 69 s respectively. While the recovery time of sensor processed at 500 °C was extended from 37 to 138 s, which is slower than the sensor processed at 400 °C (36-50 s) to the aforementioned concentration of ammonia. Response time of screen-printed sensor processed at 500 °C was decreased from 120 to 40 s against the HCHO concentration increased from 3 to 10 ppm. Whereas the sensor processed at 400 °C showed a response time in the range of 97-50 s upon exposure of HCHO concentration varied from 3 to 10 ppm. Recovery

time was in the range from 50-77 s and 27-85 s for the sensor processed at 500 °C and 400 °C respectively.

Sensor kinetics includes response and recovery time solely depends on the rate at which the series of reactions and diffusion of oxygen vacancies ( $V_O^{\bullet\bullet}$ )<sub>s</sub> occurs during adsorption-desorption of analyte gases; (i) surface reaction ( $O_2^X = (V_O^{\bullet\bullet})_s + 2e^- + \frac{1}{2} O_2$ ), (ii) surface diffusion of oxygen vacancy ( $V_O^{\bullet\bullet}$ )<sub>s</sub>, (iii) the reaction between surface ( $V_O^{\bullet\bullet}$ )<sub>s</sub> and grain boundary vacancies ( $V_O^{\bullet\bullet}$ )<sub>gb</sub>, (iv) grain boundary diffusion of vacancies ( $V_O^{\bullet\bullet}$ )<sub>gb</sub>, (v) the reaction between grain boundary ( $V_O^{\bullet\bullet}$ )<sub>gb</sub> and volume vacancies ( $V_O^{\bullet\bullet}$ )<sub>v</sub>, (vi) volume diffusion of vacancies ( $V_O^{\bullet\bullet}$ )<sub>v</sub> (Izu et al. 2003). When the diffusion mechanism (ii), (iv) and (vi) is the rate-limiting step, sensor kinetics depends on the size of crystallite. Smaller crystallites provide a shorter distance; hence the sensor kinetics becomes faster. When the reaction steps (iii) and (v) are rate-limiting step, then smaller crystallites make the response time quicker by facilitating the large reaction area (Izu et al. 2003). Screen printed sensor processed at 400 °C has smaller crystallites (20 nm) which may be helpful in the faster sensor kinetics, makes the faster response and recovery compared to the screen-printed ZnO sensor processed at 500 °C.

As shown in fig. 5.14 (a), sensing selectivity of the screen-printed ZnO sensor processed at 500 °C was examined, when exposed towards 5 ppm of ammonia, methanol, ethanol, formaldehyde, toluene, and xylene gases. It was found that high selectivity towards the ammonia (336) which was 75 and 168 times more than towards the HCHO (4.5) and ethanol (2) respectively at room temperature. Negligence response was found to methanol, toluene, and xylene gases. Two important reasons could be behind the high selectivity towards ammonia compared to other gases. Primarily, the presence of a single electron pair in NH<sub>3</sub> with pronounced electron-donating capability, which enables the NH<sub>3</sub> to pass over the active area of the sensing material effectively. Second, the smaller kinetic diameter of ammonia (0.36 nm) compared to the other gases smoothens the diffusion of gas throughout the sensing layer (Kulandaisamy et al. 2016).

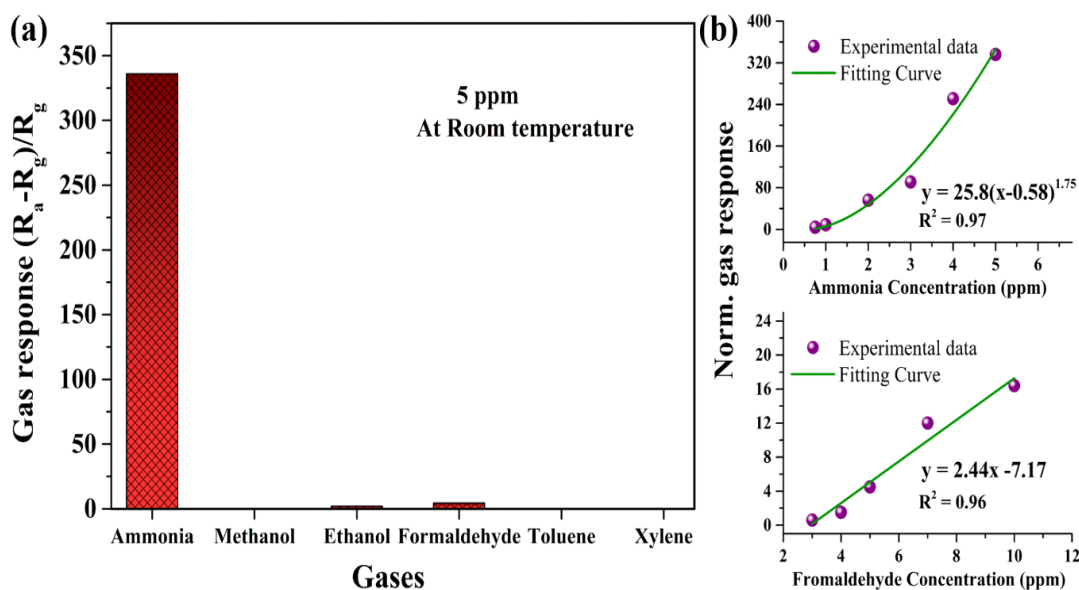



Fig. 5.14 (a) Response of screen-printed ZnO sensors processed at 500 °C when exposed to 5 ppm of different gases at room temperature and (b) fitting curves of the response of the sensor against ammonia and formaldehyde.

Limit of detection (LOD) of the screen-printed sensor processed at 500 °C was estimated using equations obtained from fitted curve as shown in fig. 5.14 (b). The relation between gas response towards various concentrations of  $\text{NH}_3$  and  $\text{HCHO}$  was fitted by a power function  $y = 25.8(x - 0.58)^{1.75}$  (with  $R^2 = 0.97$ ) and linear fitting function  $y = 2.44x - 7.17$  respectively, where  $y$  and  $x$  were gas response and concentration. LOD of the screen-printed sensor processed at 500 °C for the  $\text{NH}_3$  and  $\text{HCHO}$  were observed to be 0.6 and 2.9 respectively.

### 5.3.2.2 Undoped particle-based screen printed ZnO films

A scalable screen-printed single layer of ZnO films on the glass substrate was uniform. Adherence of printed ZnO thick films to the glass substrates was evaluated qualitatively by dribbling, shaking and handling the printed samples multiple times; no powdery depletion was observed from printed ZnO films. Further, screen printed ZnO films are still adhered to the substrate with minimal disarray of the film as shown in fig. 5.15 (a) and are compared with scale and designated as ‘4B’ according to Cross Cut Tape Test (ASTM D3359) classification implies that 95 % of printed material is retained due to strong adherence with the glass substrate.

(a) Screen printable Ink	Surface of the cross-cut area of the ZnO film	Area removed from surface with the tape (in %)	ASTM classification
Sodium carboxy-methyl cellulose in water + ZnO powder		Less than 5	4B

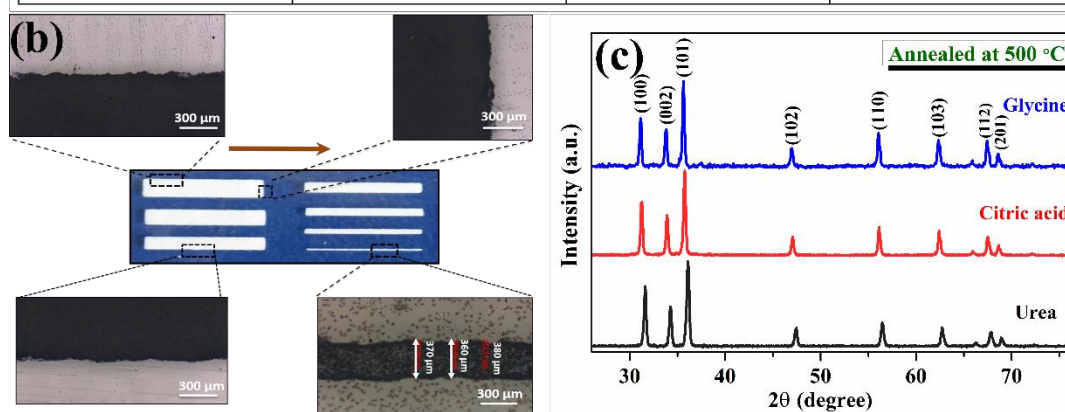


Fig. 5.15 Adhesion test of the screen printed ZnO films, (b) optical micrograph of printed features, and (c) XRD patterns of screen printed ZnO films annealed at 500 °C for 2 h.

The screen-printed pattern geometry is studied as shown in fig. 5.15 (b), no “sawtooth” effect at edges is observed, which implies there is no mismatch between mesh threads and pattern orientation. Screen printed film thickness was measured to be in the range of 13-18 μm. The purity and crystallinity of the ZnO screen-printed films were analysed using XRD and results of the films were plotted in the range of 20-77° (2θ) against intensity in fig. 5.15 (c); the strong intense peaks of ZnO films indexed as (100), (002), (102), (110), (103), (112) and (201), confirmed the pure phase of ZnO.

Surface morphology and elemental composition of the screen-printed films of ZnO are shown in fig. 5.16. SEM analysis revealed that the film surface was granular and highly porous in all three cases. Film surface morphology of the ZnO obtained from fuel-urea, looks lumpy due to large size particles and random connectivity between the particles.

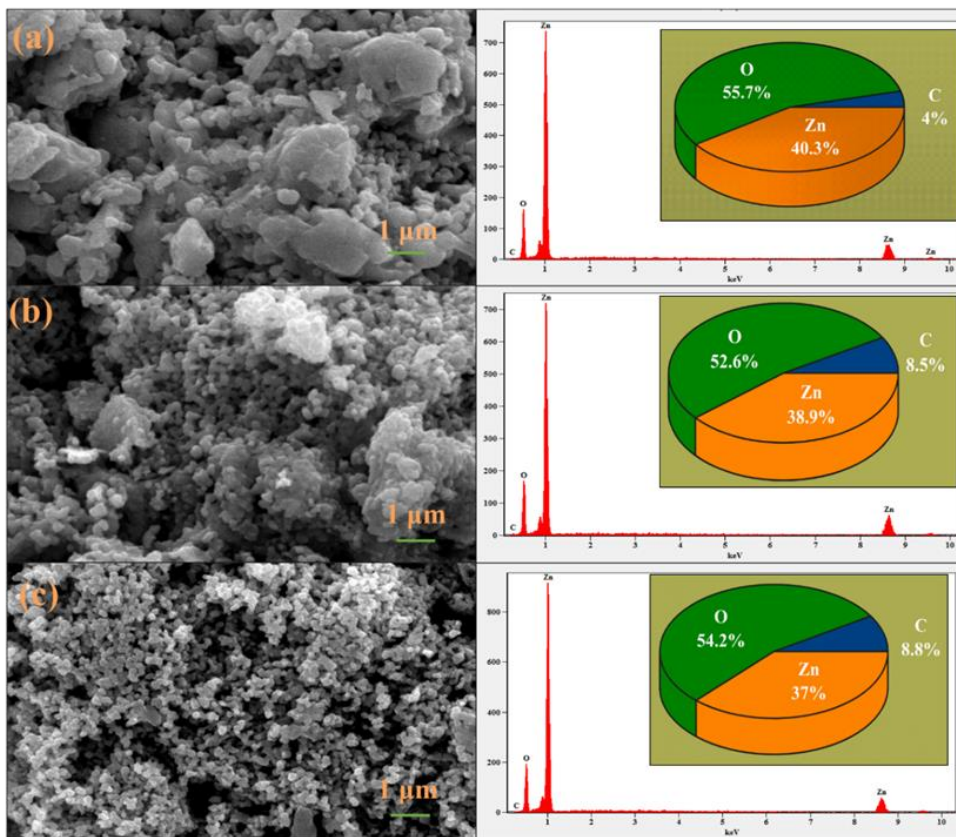


Fig. 5.16. SEM images and their corresponding EDS spectrum of the surface morphology of screen-printed films of ZnO synthesized by different fuel-system (a) urea, (b) citric Acid, (c) glycine.

Printed films of ZnO prepared from fuel- glycine are highly porous; could help in effective adsorption and desorption of atmospheric oxygen and analyte gases to pass over the underneath the particles. EDS spectrum depicts the presence of zinc (Zn), oxygen (O) and carbon (C) in all screen printed ZnO films. However, atomic % of Zn and O in each film were in non-stoichiometric proportion and excess in oxygen or deficient in Zn were found in all samples. An insulating ZnO stoichiometrically expected atomic % of Zn and O (in ZnO) are 50.5% and 49.5%, respectively. Whenever, surplus or shortfall of any type of atom in the crystal, distorts the band structure leads to increase in conductivity (Patil and Patil 2007). Each excess oxygen atom holds two more electrons makes the ZnO non-stoichiometric and n-type semiconductor. The carbon element traced in the printed films is attributed to the unburnt residue of the organic vehicle. The amount of carbon in the ZnO films from urea system slightly higher than in the films from other fuel systems.



The variation of absorbance in the UV-vis regions of the screen-printed films of ZnO synthesized by different fuel system is shown in the fig. 5.17 (a). UV-vis spectra reveal that screen printed ZnO films have an absorbance in the visible region, which is a characteristic of ZnO. Absorption edges are different from the films of ZnO processed by different fuel system due to the changes in their carrier concentration, particle size, surface microstructures and also, the amount of oxygen exists (Mohamed 2011; Pathak et al. 2016).

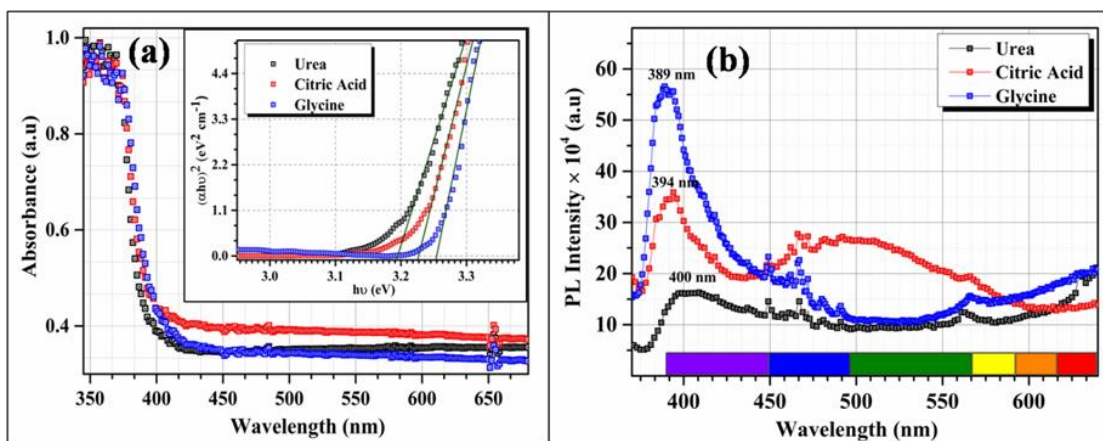


Fig. 5.17 (a) Absorbance spectra and Tauc's plot (Inset) (b) PL spectra of screen printed ZnO films.

Model for direct interband transitions gives a relationship between the absorbance coefficient ( $\alpha$ ) and band gap ( $E_g$ ) as equation 5.5. The optical bandgap is computed by extrapolation of a straight line of  $(ahv)^2$  against  $h\nu$  to the point,  $\alpha = 0$  is shown in the inset of fig. 5.17 (a). The optical bandgap is found to be 3.19 eV, 3.22 eV and 3.25 eV for the films of ZnO synthesized from urea, citric acid and glycine fuel-system respectively.

The PL spectra of synthesized ZnO from the different fuel- system is shown in fig. 5.17 (b). The photoluminescence (PL) emission spectrum is appropriate to understand the combination mechanisms of electron-hole pairs in semiconductor and effectiveness of charge carrier trapping, immigration and transfer. A strong UV near band edge emission (NBE) is observed at 389 nm, 394 nm and 400 nm in the screen printed films of ZnO obtained from the glycine, citric acid and urea fuels, respectively, is due to recombinations of excitons; whereas, high intensity of the peak signifies the crystallinity of the film. Both, high carrier concentration and reduction in band gap

contribute to the shift of the NBE emission in ZnO films (Sneha et al. 2017). Highest NBE emission intensity at 389 nm was found in the glycine fuel system, because of the higher recombination rate of charge carriers under irradiation of light. The PL free exciton peak intensity at 400 nm was significantly low in the urea fuel system, implied the effective recombinations of holes and electrons which caused to the separation of charge carriers. The weak blue emission at  $\sim 447$  nm mostly occurs to an acceptor energy level of Zn vacancy ( $Zn_o$ ). Again, the blue emission at around 470 nm attributes to the presence of oxygen vacancies ( $V_o$ ) in the ZnO films. The green emission at  $\sim 570$  nm may be due to an ionized oxygen vacancy of ZnO, as oxygen vacancies capture a hole from VB to form ionized oxygen vacancies ( $V_o^{++}$ ) (Ni et al. 2005). Oxygen vacancies take part a vital role in gas sensing by increasing the electrostatic interaction between ZnO surface and the reactive gas molecules (Yu et al. 2016).

Current density of the films is measured as a function of electric field as shown in fig. 5.18 (a), as the particles are interconnected to each other due to sintering. Variation of resistance under UV (325 nm) irradiation of screen-printed films of ZnO synthesised by the different fuel system is studied as a function of exposed duration, as shown in fig. 5.18 (b).

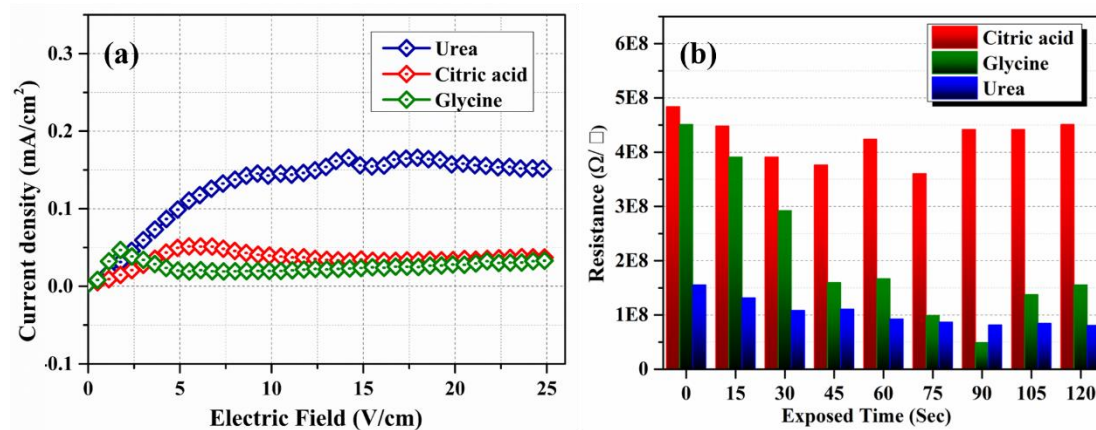


Fig. 5.18 (a) J-E characteristics curves of screen printed ZnO films (b) Resistance of screen printed ZnO films exposed to UV-light with different exposure time.

The resistance of screen printed ZnO films is decreased as the exposure time of the UV is increased. It's obvious that when the polycrystalline metal oxide irradiates to UV light, recombination of chemisorbed  $O_2^-$  ions with the photogenerated holes liberates  $O_2$  molecules:  $h^+ + O_2^- \rightarrow O_2$ . This process sluggish further chemisorption

of  $O_2^-$  ions as it reaches to saturation and maintains an original electron rich state of ZnO. Photo excitation reduces the inter-grain barrier height, as a result density of free carriers may be increased throughout the films (Zhang et al. 2003). Particularly, ZnO has slow photoconduction decay, which is controlled by surface defects (Takahashi et al. 1994). ZnO film from glycine fuel-system shows a significant decreasing trend with exposed time upto 45 sec with a maximum conductance of  $\sim 20$  nS, compared to other ZnO films. Since measurements are executed in the air, the effect of the ambient  $O_2$  molecules is present throughout the process.

The gas response of the screen-printed films of ZnO prepared by different fuel system were evaluated and compared at different operating temperature ranging from ambient to 450 °C with increment of 50 °C upon exposure to 100 ppm concentration of  $NH_3$ ,  $C_2H_5OH$ , LPG and  $Cl_2$  gases as shown in fig. 5.19.

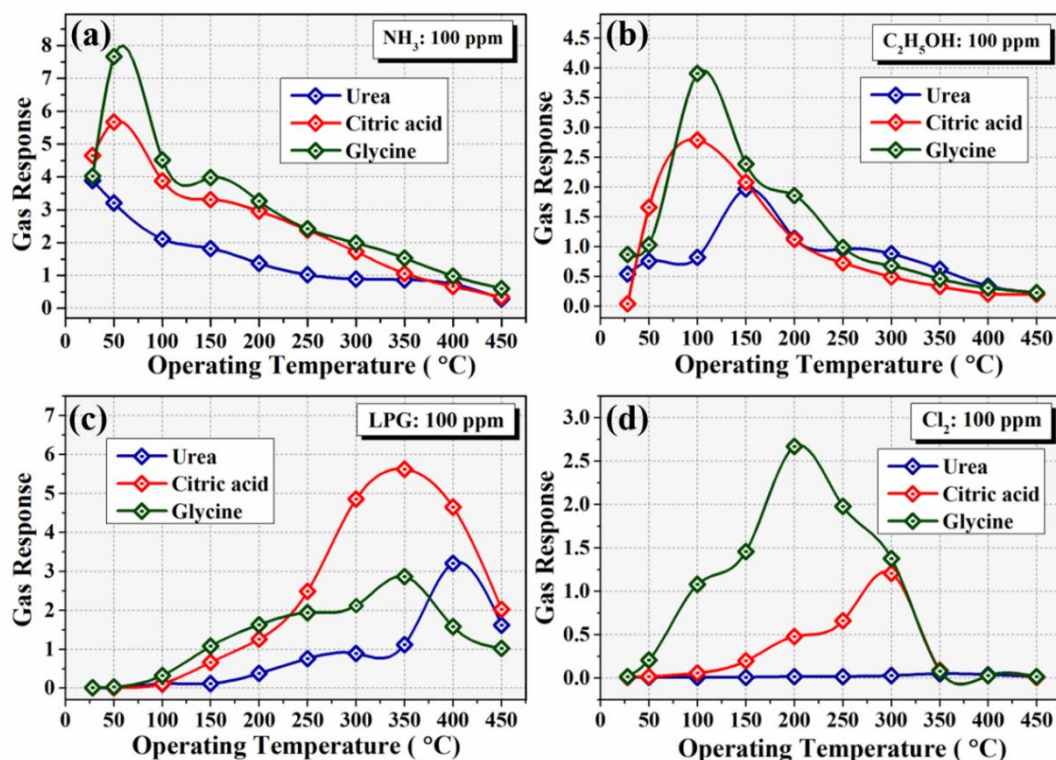
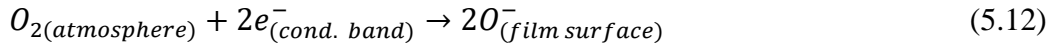


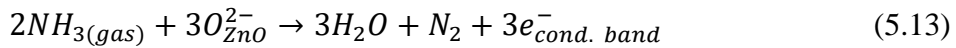
Fig. 5.19 Gas response as a function of the operating temperature of a screen-printed film of ZnO obtained from different fuel system exposed to 100 ppm of (a) ammonia, (b) ethanol, (c) LPG and (d) chlorine gases.

Gas sensing mechanism of metal oxide in the presence of analyte gases depends on the surface reactions (Lupan et al. 2018). First, atmospheric oxygen molecules are

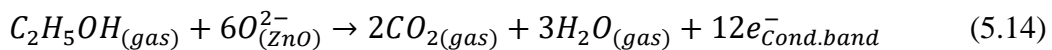
physiosorbed on the metal oxide surface sites. Molecular species can be chemisorbed at the surface by capturing electrons in the conduction band, concurrently an electron depletion region is formed (eq. 5.12); as a result, conductance of the metal oxides decreases.



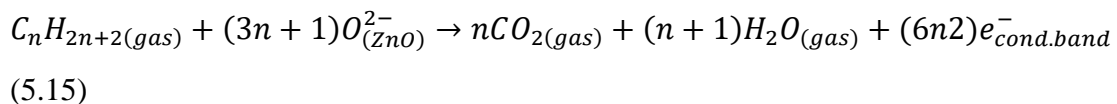
In the ZnO films, donor defects  $Zn_i^*$  (neutral), which act as an electron donor and electrons are extricated as  $Zn_i^* \leftrightarrow Zn_i + e^-$ . Secondly, the target gas reacts with chemisorbed oxygen species present on the surface and gets oxidised. The chemisorbed oxygen species which are utilized to oxidize the analyte gas molecules released the electrons back to the conduction band as  $R + O_{ads}^- \rightarrow RO + e^-$ . Hence, electron depletion layer is narrowed, conductance of the films are retained. Usually, desorption of RO happens in higher temperature. Screen printed ZnO films obtained from glycine and citric acid respond to ammonia gas at low operating temperature. Highest response  $\sim 8$  was found in ZnO obtained from glycine system. Release of electrons from chemisorbed molecular oxygen back to the conduction band when exposed to  $NH_3$  as follows (equ. 5.13) (Wagh et al. 2006);



Maximum ethanol gas sensitivity  $\sim 4$  was found in ZnO films synthesized from glycine fuel-system at 100 °C. Carbon-di-oxide and water are produced by the release of electrons to the conduction band, when ethanol reacts with  $O_2^-$ , as equation 5.14 (Patil et al. 2007);

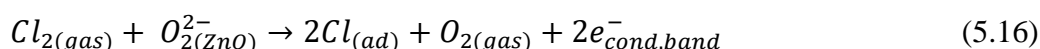


Butane (55 %) is the major constituents of LPG with  $CH_4$  (6%),  $C_2H_6$  (8%),  $C_4H_8$  (11.5%) and  $C_5H_{12}$  (4.5%). At higher temperature, alkanes are decomposed thereby generates  $H^+$ , which combines with anion super oxide  $O_2^-$  to release water and molecular oxygen. When alkanes react with chemisorbed  $O_2^-$ , a complex reaction take place as follows (equ. 5.15) (Patil et al. 2006);



Maximum sensitivity to LPG gases is ~ 6 at operating temperature 350 °C in ZnO sensor from citric acid system and it decreases with increasing temperature.

A maximum response of ~ 2.75 at operating temperature of 200 °C to chlorine gas is found in ZnO films obtained from glycine, but ZnO films obtained from the urea fuel system show poor response to chlorine gas, as because of the substitution of oxygen by chlorine is not easier. In the present case the feasible reaction is shown as equation 5.16;



Further, H<sub>2</sub>S gas sensing properties of ZnO films obtained from various films were estimated when it was exposed 50 ppm concentration at operating temperature varies from room temperature to 450 °C depicted in fig. 5.20. The film of ZnO obtained from glycine shows maximal response ~ 10 at operating temperature 100 °C compared to ZnO synthesized from other fuel-system towards 50 ppm of H<sub>2</sub>S gas. The reaction of H<sub>2</sub>S with O<sub>2</sub><sup>-</sup> in order to increase the conductance of the ZnO films, is as follows (equ.5.17) (Kim et al. 2011);

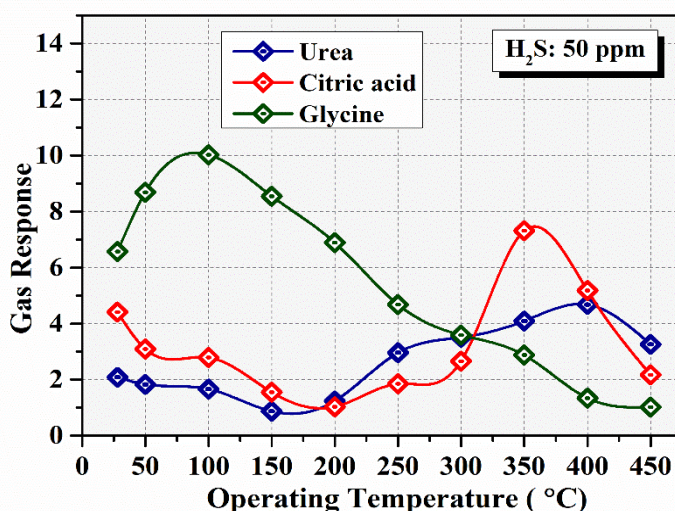
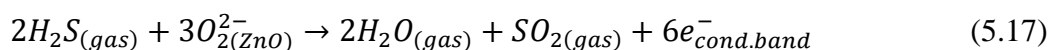


Fig. 5.20 Gas response as a function of the operating temperature of a screen- printed films of ZnO obtained from different fuel system exposed to a 50 ppm of hydrogen sulphide in the air.

The response of ZnO films towards the analyte gases exhibited an increasing trend up to a maximum value with an operating temperature then follows a decreasing trend.

The semiconductor metal oxide sensor operates only within a particular temperature window, when they are exposed to certain concentration of target gas. High sensitivity of ZnO was noticed towards the gases such as NH<sub>3</sub> and C<sub>2</sub>H<sub>5</sub>OH at low temperature. It is obvious that, formation of chemisorbed oxygen species O<sup>-</sup> and O<sup>2-</sup> is depends on temperature. At lower temperature, higher concentration of O<sup>2-</sup> chemisorbed which promotes effective interaction between H<sub>2</sub> and O<sup>2-</sup> ions and resulted into the high sensitivity. At higher temperatures, concentration of O<sup>2-</sup> depletes as a result there will be less interaction between analyte gases, which leads to the decrement of sensitivity (Lupan et al. 2010). But sensitivity value becomes high, when it is exposed to LPG and Cl<sub>2</sub> gases at high operating temperatures 350 °C and 200 °C, respectively. The reason behind this, at low temperature the formation of chemisorbed oxygen species is less, also passivates the films surface for additional adsorption of oxygen (Windischmann and Mark 1979). Moreover, H<sub>2</sub> ions forms after decomposition of alkanes at higher temperature and also interaction of O<sup>2-</sup> with chlorine gas is not easier at lower temperature. Apart from the adsorption and desorption, the operating temperature influences the charge carrier-concentration, Debye length, and work function of the semiconductor. Carrier-concentration (conductivity) increases and Debye length shortens, when temperature is relatively high; as a result the sensitivity get decreased (Mizsei 1995). Crystallites in polycrystalline metal oxide are connected to their neighbours either by necks or by grain boundary contacts. Grain boundary control ( $D_v \gg 2L$ ), neck control ( $D_v \geq 2L$ ) and grain control ( $D_v \ll 2L$ ) are three sintering mechanisms solely depends on crystallite size ( $D_v$ ) relative to twice the space charge ( $2L$ ).  $D_v$  of the synthesized powders by three fuel system are larger than the  $2L$ . When  $D_v \gg 2L$ , charge carriers move across a potential barrier at each grain boundary, the barrier height of which alters with the surrounding atmosphere, i.e. sensing gases (Ansari et al. 1997). Gas sensitivity via the change in electrical resistance is controlled by the grain boundary contacts through which carrier flow. Lattice distortion in the ZnO synthesized from urea-fuel system is larger than ZnO synthesized by the other two fuel system. Lower sensitivity was observed with screen-printed film of ZnO synthesized from the urea system. With the higher lattice distortion, charge carrier scattering will be dominant, resulted into a small resistance modulation in the film when exposed to analyte gases and hence the lower sensitivity is obtained (Sahay and Nath 2008).

Table 5.4 Particle size, stoichiometry, crystallite size and lattice distortion of ZnO sensors.

Fuel system	Particle size ( $\mu\text{m}$ )	Stoichiometry (O: Zn)	Crystallite Size (nm)		Lattice distortion ( $\epsilon \times 10^{-3}$ )
			Scherrer	W-H ISM	
Urea	0.4, 7.5	1.44	34	38	0.616
Citric Acid	0.94, 7.5	1.35	36	39	0.159
Glycine	0.84	1.46	39	44	0.335

Due to larger particle size and non-uniform particle size distribution in the ZnO sensor from citric acid fuel system hinders gas sensitivity, even though have less lattice distortion. ZnO films from glycine fuel system possess good UV and gas sensing characteristics, the reasons may be due to smaller particle size, uniform particle size distribution, crystallite size and less lattice distortion (as shown in Table 5.4). These factors may be caused to increase the exposed surface area and porosity, hence the diffusion of atmospheric oxygen and target gas molecules is increased (Dey 2018; Xu et al. 2000).

The response and recovery characteristics of glycine-combusted ZnO thick films towards the 100 ppm of  $\text{NH}_3$  at working temperature  $50^\circ\text{C}$  was recorded with time as shown in fig. 5.21.

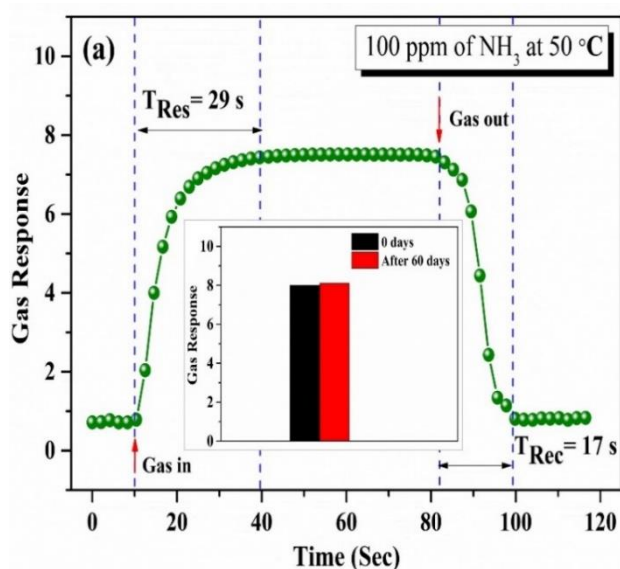


Fig. 5.21 Response and recovery time and long-term stability (Inset) of screen-printed films of ZnO synthesized from glycine fuel system when exposed to 100 ppm  $\text{NH}_3$  at  $50^\circ\text{C}$ .

It can be noticed that dynamic of the sensor is very fast whose response and recovery times are 29 s and 17 s respectively. Long-term stability of the gas sensing properties of screen-printed thick films of ZnO synthesized from glycine fuel system was investigated after 60 days for the 100 ppm of NH<sub>3</sub> at operating temperature 50 °C as shown in the inset of fig. 5.21. No change was observed in the gas response of the screen printed ZnO sensor exposed to the gas. Sensor showed good stability as the variation in response under the exposure of NH<sub>3</sub> was less than 6%.

### 5.3.2.3 Pristine, Sr-doped ZnO and RuO<sub>2</sub> activated Sr doped ZnO screen printed films

The XRD patterns of the pristine and RuO<sub>2</sub> activated Sr-doped ZnO heterostructure films are shown in fig. 5.22. Wurtzite Sr doped ZnO has diffraction peaks at 31.76°, 34.46°, 36.31°, 47.62°, 56.69°, 68.08° and 69.23° which are assigned to reflection planes of (1 0 0), (0 0 2), (1 0 1), (1 0 2), (1 1 0), (2 0 0), (1 1 2) and (2 0 1) (ICDD 01–079–0205). There is a slight shift of (101) peak towards the higher diffraction angle and is shown in fig. 5.22 (b); it may be due to the doping of Sr element in ZnO caused the aberrance of ZnO crystal lattice.

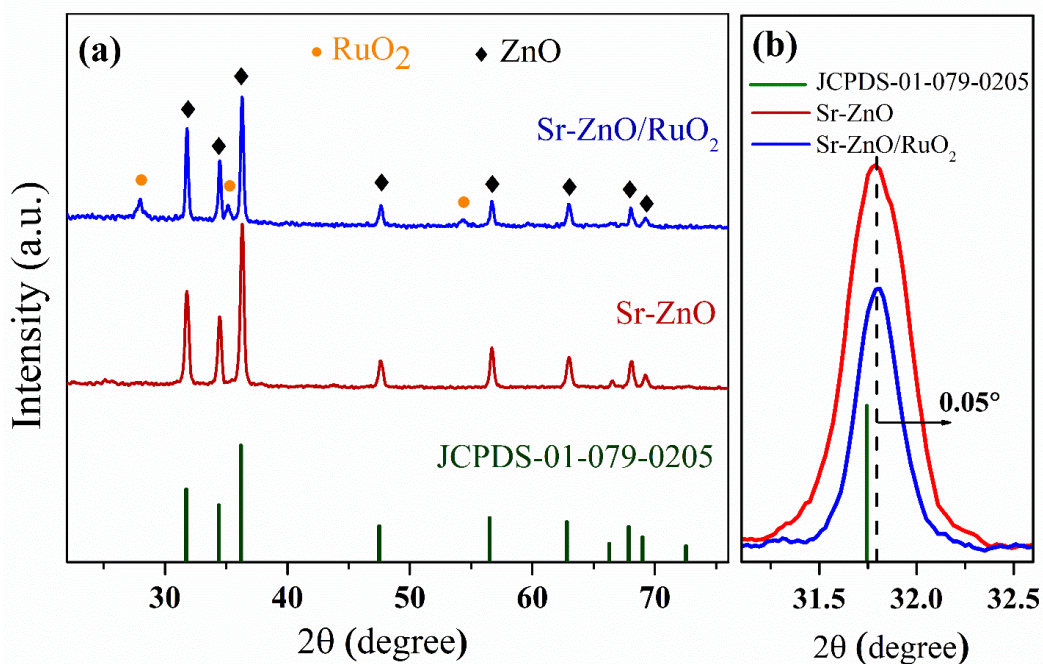


Fig. 5.22 XRD patterns of pristine and surface activated Sr-doped ZnO screen-printed films



There is a slight shift of (101) peak towards the higher diffraction angle and is shown in fig. 5.22 (b); it may be due to the doping of Sr element in ZnO caused the aberrance of ZnO crystal lattice. Vijayan et al. reported a similar shift of diffraction peaks to higher angles in Sr doped ZnO (Vijayan et al. 2008). ZnO films are associated with some intrinsic point defects such as Zn interstitial, oxygen vacancy etc. With the doping of Sr atoms in the ZnO lattice, variations of point defects density and their distribution may lead to the changes in the lattice constant, lattice strain and stress. Three additional peaks are observed at 27.6°, 34.8° and 54° in surface activated Sr-doped ZnO heterostructure films confirming the presence of RuO<sub>2</sub> (ICDD 03-065-2824). Surface activation of Sr-doped ZnO and followed by annealing at 500 °C for 30 min resulted into the formation of RuO<sub>2</sub> from RuCl<sub>3</sub>.

Cohen's analysis method is employed to calculate the precise lattice constants 'a' and 'c', so that systematic and random errors are minimized. (The steps involved in the calculation of the lattice parameter of Sr-doped ZnO using Cohen's method is shown in Appendix IV). Unit cell volumes and bond length (l) of the Zn-O are calculated using the relations (3.19) and (3.20). Lattice constants of the Sr-doped ZnO and RuO<sub>2</sub> activated Sr-doped ZnO screen printed films are  $a = 3.21 \text{ \AA}$ ,  $c = 5.19 \text{ \AA}$  and  $a = 3.22 \text{ \AA}$ ,  $c = 5.19 \text{ \AA}$  respectively. Axial ratio (c/a) of hexagonal close-packed crystal structure for both the films are found to be 1.61 and 1.612, respectively. Bond length (Zn-O) and unit volume of Sr-doped ZnO films are calculated to be 1.96 Å and 46.78 Å<sup>3</sup> respectively, whereas for RuO<sub>2</sub> activated Sr-doped ZnO films are found to be 1.96 Å and 46.6 Å<sup>3</sup> respectively.

Crystallite size of pristine and RuO<sub>2</sub> activated Sr-doped ZnO screen-printed films obtained by Scherrer (3.7), W-H ISM (3.9), W-H ASM (3.10) and W-H EDM (3.12) equations (Plots of W-H ISM, W-H ASM and W-H EDM for the calculation of crystallite size are shown in Appendix V) are tabulated in Table 5.5. The average crystallite size of the films obtained from various models is comparable. The crystallite size of ZnO phase in RuO<sub>2</sub> activated Sr-doped ZnO films increased from 28 nm to 40 nm after the successive annealing of films at 500 °C for 30 min after dipping in the RuCl<sub>3</sub> aqueous solution.

Table 5.5 The estimated microstructural parameters of pristine and RuO<sub>2</sub> activated Sr-doped ZnO screen-printed films.

Screen printed thick films	Crystallite size of ZnO using different methods						
	Scherrer	W-H ISM		W-H ASM		W-H EDM	
	$D_V$ (nm)	$D_V$	$\epsilon \times 10^{-3}$	$D_V$	$\sigma$ (MPa)	$D_V$	$u$ (kJ·m <sup>-3</sup> )
	(nm)	(nm)		(nm)		(nm)	
<b>Sr-doped ZnO</b>	24	28	0.477	27	43	27	8.65
<b>RuO<sub>2</sub> activated Sr-doped ZnO</b>	29	40	0.834	39	95	39	48

The morphological analysis of pristine and RuO<sub>2</sub> activated Sr-doped ZnO screen printed films are depicted in fig. 5.23 and inset shows photograph of the sensor comprises films with two silver electrodes. Screen-printed films of Sr-doped ZnO particles are porous with foam-like structure; which facilitates the more active sites on which the oxygen species can be adsorbed. It enables the mobilization of gas molecules through pore channels and facilitates the gases to have contact with the underneath particles. Whereas in RuO<sub>2</sub> activated films sub-micron particles are randomly distributed over the substrate with the less porous structure compared to pristine one, it may be due to the collapse of the foam-like structure after dipping the Sr-doped ZnO film in ruthenium chloride aqueous solution.

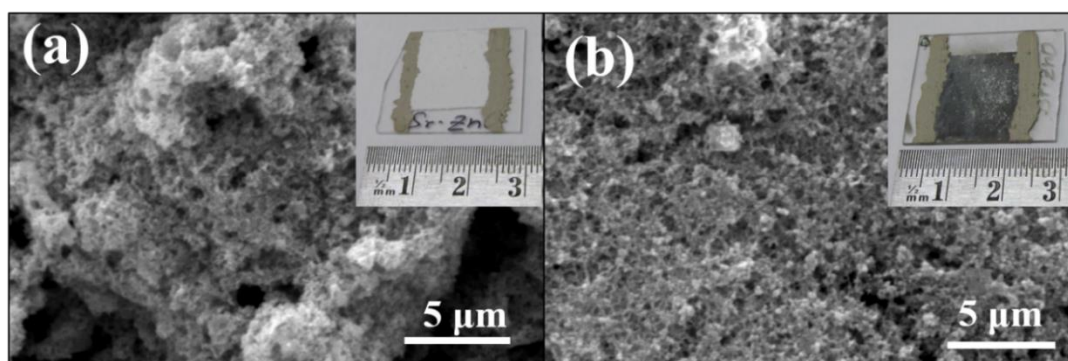


Fig. 5.23 SEM spectra of (a) pristine and (b) RuO<sub>2</sub> activated Sr-doped ZnO screen-printed films.

Elemental composition of Sr-doped ZnO and ruthenium activated Sr-doped ZnO is depicted in fig. 5.24 (a) and (b), which confirms the doping concentration of Sr element in ZnO is ~ 1 at. %. Approximate areal porosity of films is found to be 22 % and 7 %

for Sr-doped ZnO and RuO<sub>2</sub> activated Sr-doped ZnO screen-printed films respectively as shown in fig. 5.24 (c) and (d).

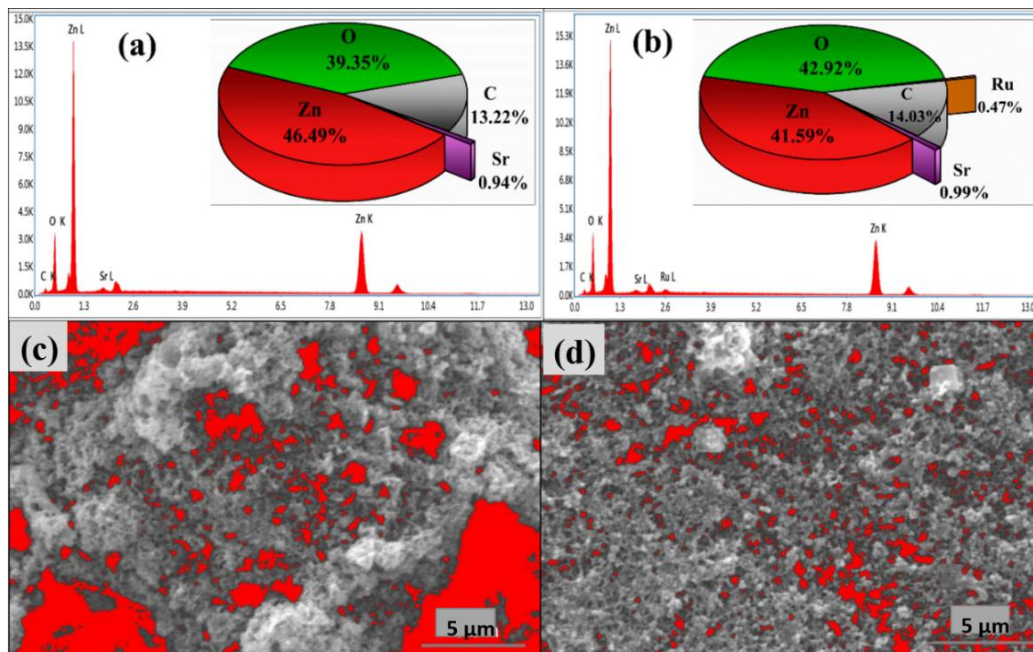


Fig. 5.24 Elemental composition of (a) Sr-doped ZnO and (b) RuO<sub>2</sub> activated Sr-doped ZnO screen printed films. Areal porosity of (c) Sr-doped ZnO and (d) RuO<sub>2</sub> activated Sr-doped ZnO screen printed films.

XPS survey scan reveals the presence of zinc (Zn), oxygen (O), strontium (Sr), ruthenium (Ru) and carbon (C) in the respective screen-printed films and is shown in the fig. 5.25 (a). The C 1s XPS spectra of undoped ZnO, Sr-doped ZnO and RuO<sub>2</sub> activated Sr-doped ZnO screen printed films depicted in fig 5.25 (b), (c) and (d), were fit with four synthetic peaks centred at 284.6 (C-H, peak A), A + 1.5 (C-O, peak B), A + 3.0 (O=C, peak C), and A + 4.5 eV (CO<sub>3</sub><sup>2-</sup> peak D). The positions of these peaks were allowed to vary by  $\pm 0.2$  eV. But, C 1s spectra of RuO<sub>2</sub> activated Sr-doped ZnO is quite complex, because deconvoluted C 1s spectra has two more components at 280.7 eV and 281.8 eV assigned to the Ru 3d<sub>5/2</sub> in addition to the four synthetic peaks as explained earlier. Peaks at 280.7 eV and 281.8 eV represent the valence state of Ru<sup>4+</sup> and Ru<sup>3+</sup> confirms the presence of RuO<sub>2</sub> and RuCl<sub>3</sub> respectively (Iriondo et al. 2010; Lemay et al. 1986; Shen et al. 1991).

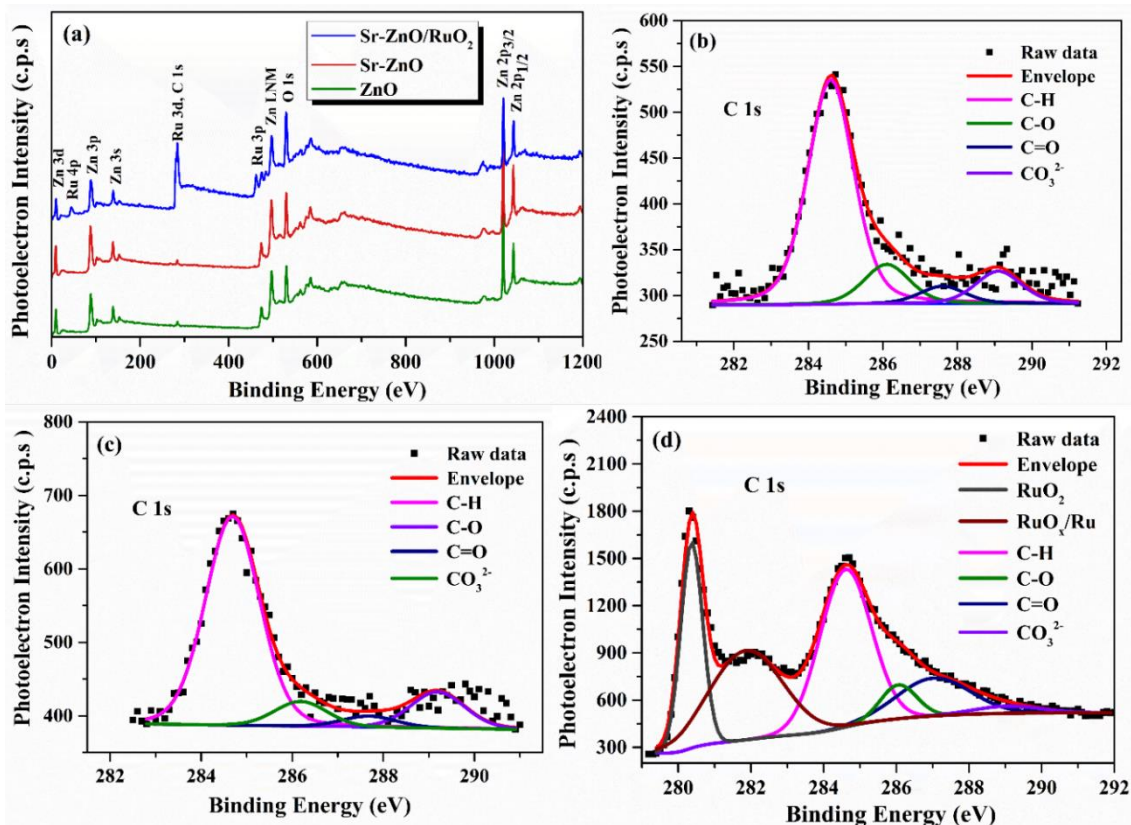


Fig. 5.25 (a) XPS survey scan, (b), (c) and (d) deconvoluted C 1s peaks of ZnO, Sr-doped ZnO and RuO<sub>2</sub> activated Sr-doped ZnO screen printed films.

Fig. 5.26 (a), (b) and (c) shows the high-resolution XPS spectra of the Zn 2p, Sr 3d<sub>3/2</sub>, Ru 3p<sub>3/2</sub> of RuO<sub>2</sub> activated Sr-doped ZnO heterostructure screen printed films. Two strong peaks observed at binding energies of 1046.9 eV and 1023.9 eV in Zn 2p spectra correspond to the spin-orbit of Zn 2p<sub>1/2</sub> and Zn 2p<sub>3/2</sub> respectively, which confirms the presence of element Zn in wurtzite ZnO structure in the form of divalent (Zn<sup>2+</sup>) oxidation state (Navaneethan et al. 2017). In narrow scan spectra of Sr 3d<sub>3/2</sub> reveals that valence state of Sr element in the Sr-doped screen-printed films are Sr (II) and Sr (0). It clearly shows that peak at 134 eV and 133.5 eV attribute to Sr atoms in the wurtzite and non-wurtzite structure, respectively (Liao et al. 2006; Sosulnikov and Teterin 1992). The deconvoluted Ru 3p<sub>3/2</sub> peak has two components with binding energies of 462.03 eV and 464.56 eV. The strong peak at 462.03 eV assigns to the Ru<sup>4+</sup> valence state, confirms the presence of conducting RuO<sub>2</sub> (Wang et al. 2014). To support this, the XRD pattern of RuO<sub>2</sub> activated Sr-doped ZnO screen-printed film shows the presence of RuO<sub>2</sub> phase of rutile structure. The low-intensity deconvoluted

peak at 464.56 eV corresponds to the formation of  $RuO_3/Ru$  from the  $RuO_2$  as per the following reaction (equ. 5.18) (Shen et al. 1991):

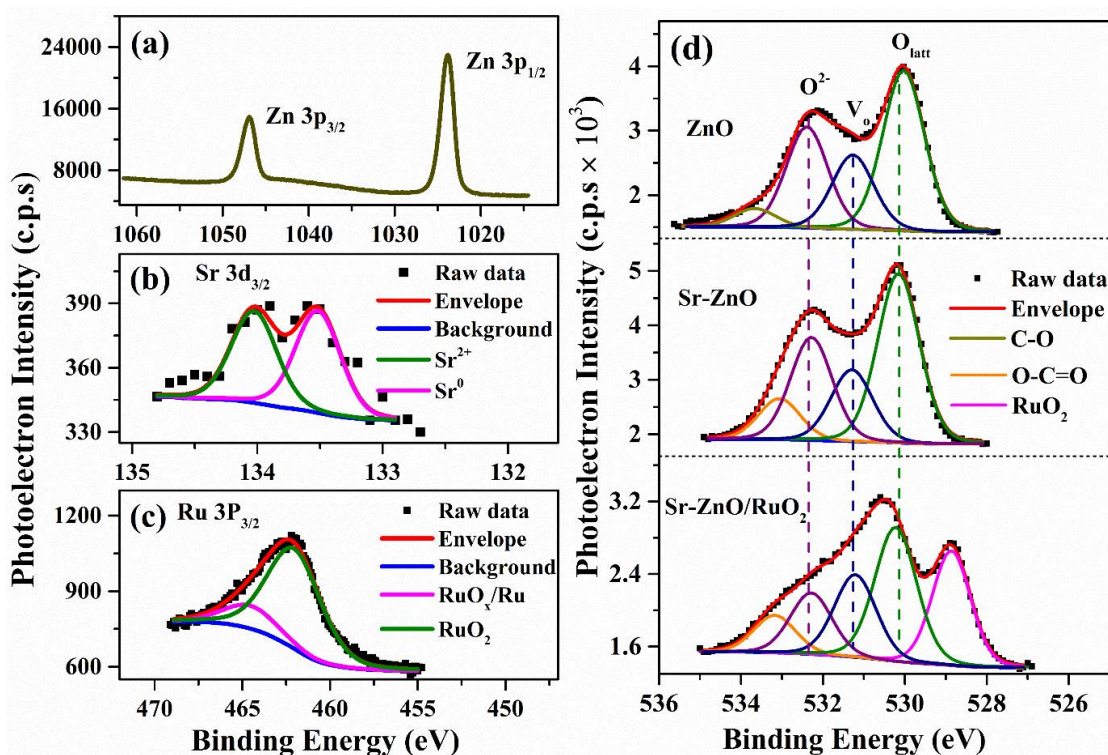
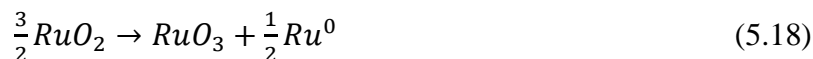


Fig. 5.26 XPS spectra of the (a) Zn, (b) Sr 3d<sub>3/2</sub> and (c) Ru 3p<sub>3/2</sub> elements present in the  $RuO_2$  activated Sr-doped ZnO screen printed films and (d) deconvoluted O 1s peak of the undoped ZnO, Sr-doped ZnO and  $RuO_2$  activated Sr-doped ZnO screen printed films.

The O 1s peak of all the screen-printed films are deconvoluted and shown in fig. 5.26 (d). All deconvoluted O 1s spectra has three components at binding energies of  $530 \pm 0.2$  eV,  $531.1 \pm 0.2$  eV and  $532.2 \pm 0.2$  eV. The peak at  $530 \pm 0.2$  eV corresponds to the  $O^{2-}$  ions in the wurtzite structure of  $Zn^{2+}$  ion array, and also the  $O^{2-}$  anions are surrounded by Sr atoms and Zn atoms in Sr-doped ZnO films. The peak at a binding energy of  $531.1 \pm 0.2$  eV attributes to the  $O^{2-}$  ions signifies the non-stoichiometry and point defects due to oxygen vacancies ( $V_O^{**}$ ) (Q. Zhu et al. 2014). The peak at  $532.2 \pm 0.2$  eV reveals the presence of chemisorbed oxygen species on the surface of films. The peak at  $533.2 \pm 0.2$  eV is associated with the oxygen of

carboxymethyl ether (COO<sup>-</sup>) group presence in Na-carboxy methylcellulose. The additional component at 529 ± 0.2 eV observed in the O 1s spectra of RuO<sub>2</sub> activated Sr-ZnO films is assigned to the RuO<sub>2</sub> (Shen et al. 1991).

Crystallite size, lattice strain, ratio of concentration of oxygen vacancies to the lattice oxygen (V<sub>o</sub>/M-O-M), the ratio of the concentration of the chemisorbed oxygen species to the lattice oxygen (O<sup>2-</sup>/M-O-M), and areal porosity of undoped ZnO, Sr-doped ZnO and RuO<sub>2</sub> activated Sr-doped ZnO films are tabulated in Table 5.6. Strontium dopant controls the crystallite growth in Sr-doped ZnO, leads to the formation of smaller crystallites than the undoped ZnO. Increase in crystallite size is found in the RuO<sub>2</sub> activated Sr-doped ZnO due to subsequent annealing of Sr-doped ZnO films after RuO<sub>2</sub> activation. Lattice strain in the Sr-doped ZnO films is quite smaller than the other two screen-printed films. Less concentration of chemisorbed oxygen species and oxygen vacancies (V<sub>o</sub>) is found in RuO<sub>2</sub> activated Sr-doped ZnO films than the other two films. Percentage of areal porosity of Sr-doped ZnO films is 22 %, is higher than RuO<sub>2</sub> activated Sr-doped ZnO thick films (7%).

Table 5.6 Crystallite size, lattice distortion, chemisorbed oxygen to lattice oxygen, oxygen vacancies to lattice oxygen and areal porosity of ZnO, Sr-ZnO and RuO<sub>2</sub> activated Sr-doped ZnO sensor.

	Crystallite Size (nm)	Lattice Strain	O <sup>2-</sup> /M-O-M	V <sub>o</sub> /M-O-M	Areal porosity (in %)
<b>ZnO</b>	42	0.678	0.63	0.46	-
<b>Sr-ZnO</b>	27	0.477	0.60	0.423	22
<b>RuO<sub>2</sub> activated Sr-doped ZnO</b>	39	0.834	0.26	0.345	7

The variation of absorbance in the UV-Vis-IR regions of Sr-doped ZnO and RuO<sub>2</sub> activated Sr-doped ZnO screen-printed films are shown in fig. 5.27. In UV-vis spectrum, screen printed ZnO films have an absorbance in the visible region (~380 nm), which is a characteristic of ZnO. Model for direct interband transitions gives a relationship between the absorbance coefficient ( $\alpha$ ) and bandgap (E<sub>g</sub>) and the relation is denoted by the equation. 5.5. The optical band gap of ZnO synthesized by the glycine nitrate combustion process is observed to be 3.25 eV reported in the fig. 5.17 (a).

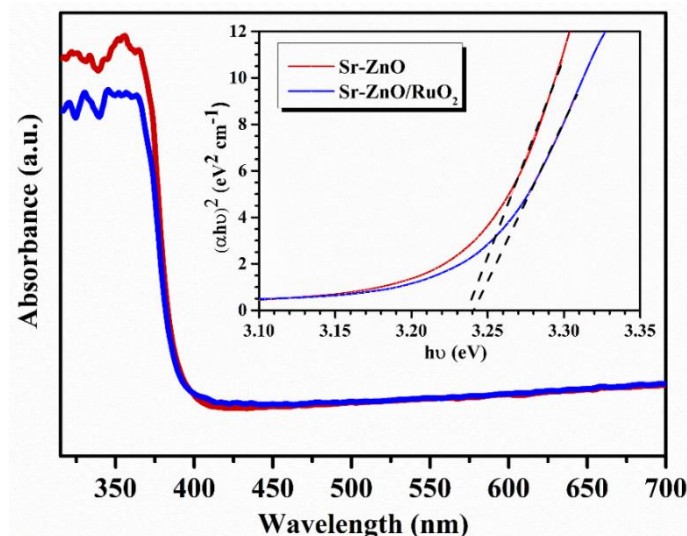


Fig. 5.27 Absorbance spectra and Tauc's plot of pristine and RuO<sub>2</sub> activated Sr-ZnO screen-printed films.

The optical bandgap for the screen-printed films of pristine and RuO<sub>2</sub> activated Sr-doped ZnO is found to be 3.227 eV and 3.228 eV, respectively. Similar fact was reported in the literature, where incorporation of Sr atoms in the ZnO lattice resulted in a decrease in the bandgap ( $E_g$ ). This redshift of the bandgap may be due to sp-d exchange interactions between the band electrons and localized d-electrons. The s-d and p-d exchange interactions are expected to contribute positive and negative corrections to the valence band (VB) and conduction band (CB) respectively, thereby, the bandgap gets reduced (Raj et al. 2016).

The gas response of the undoped ZnO, Sr-doped ZnO and RuO<sub>2</sub> activated Sr-doped ZnO screen-printed sensors against various concentration (1 - 50 ppm) of NH<sub>3</sub> gas at room temperature is shown in fig. 5.28 (a). It is observed that Sr-doped ZnO sensor exhibited high response than the other sensors. Notably, the gas response is enhanced to 1.1, 2, 2.7, 3 and 9 times higher than the undoped ZnO, when exposed towards 1, 5, 10, 25 and 50 ppm of ammonia gas, respectively. Gas response of RuO<sub>2</sub> activated Sr-doped ZnO was diminished drastically 0.73, 0.45, 0.31, 0.35, 0.3 times in comparison with undoped ZnO, with increase in the concentration of ammonia from 1 to 50 ppm. This means that the gas response of Sr-doped ZnO was decreased from 70 to 1.2 against 50 ppm of ammonia gas after the RuO<sub>2</sub> activation.

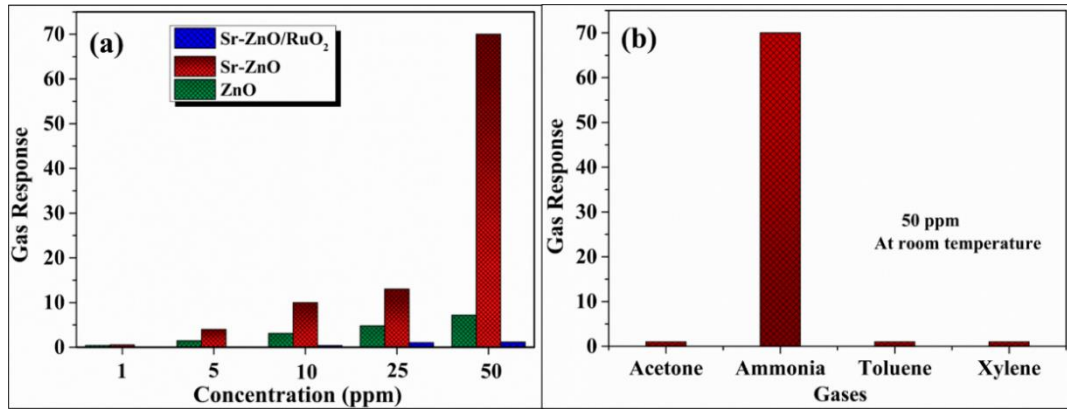
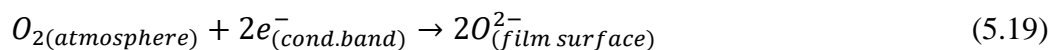


Fig. 5.28 (a) NH<sub>3</sub> gas response of undoped ZnO, Sr-doped ZnO and RuO<sub>2</sub> activated Sr-doped ZnO sensor exposed to various concentration at room temperature. (b) Response of Sr-doped ZnO sensor towards the 50 ppm of different gases at room temperature (28 °C).

The selectivity of Sr-doped ZnO sensor was investigated upon exposure to 50 ppm of acetone, ammonia, toluene, and xylene at room temperature, as shown in fig. 5.28 (b). Sr-doped ZnO based sensor exhibited excellent selectivity towards the ammonia gas. The main two reasons caused to the high selectivity towards NH<sub>3</sub> against some of the VOCs such as acetone, toluene, xylene are; firstly, NH<sub>3</sub> molecule has lone electron pair and strong electron donating ability. It can be transferred easily to the sensing material, results into the change in resistance considerably when it comes in contact. Secondly, the kinetic diameter of the NH<sub>3</sub> gas is lower than the kinetic diameter of acetone, toluene and xylene molecules, which facilitates the ease diffusion of gas into the sensing layer (Navaneethan et al. 2017).

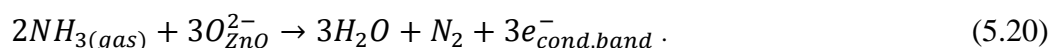
The gas sensing mechanism of semiconductor metal oxides solely depends on the modulation of its electrical resistance upon exposure to analyte gases (Fig. 5.29). Initially, atmospheric oxygen molecules are physisorbed on the semiconductor metal oxide surface sites. The physisorbed oxygen molecules get converted into chemisorbed oxygen species (O<sup>-</sup> or O<sup>2-</sup>) by capturing electrons in the conduction band is shown in equation 5.19, thereby an electron depletion region is created; it results into an increment in electrical resistance (R<sub>a</sub>) of the semiconductor metal oxides.





The lower bandgap stimulates the formation of chemisorbed oxygen species ( $O^-$  or  $O^{2-}$ ) on the sensor surface. The concentration of chemisorbed oxygen can also be increased by decreasing particle size, increasing oxygen vacancies and depreciating the desorption (Zhu and Zeng 2017).

In all screen-printed films, donor defects  $Zn_i^*$  (neutral), which act as an electron donor and electrons are extricated as  $Zn_i^* \leftrightarrow Zn_i + e^-$ . In parallel, the  $NH_3$  gas reacts with chemisorbed oxygen species present on the surface and induces oxidation of target gas molecules. The chemisorbed species are utilized to oxidize the  $NH_3$  gas molecules, results in the release of electrons from the chemisorbed molecular oxygen species to the conduction band, as shown in equation 5.20. Hence, released electrons are participated in the conduction, results in the shrinkage of electron depletion layer and decrease of electrical resistance ( $R_g$ ) of the films (Wagh et al. 2006).



The gas response of all screen-printed films enhanced with the increase in analyte gas concentration. High  $NH_3$  concentration promotes the involvement of more chemisorbed oxygen species  $O^{2-}$ , leads to the release of more electrons to the conduction band of semiconductor metal oxides. Thereby, a decrement in electrical resistance is found considerably.

The reasons behind the enhancement of gas response in the Sr-doped ZnO sensor are mainly due to smaller crystallite size and lesser lattice distortion (Table 5.6). Smaller crystallite size in Sr-doped ZnO films reduces the potential barrier for the flow of electrons by neck control contacts whereas undoped ZnO with larger crystallite size possess higher potential barrier due to grain boundary contact between two neighbouring grains, thereby restricts the flow of electrons. Also, Sr-doped ZnO particles offered high BET specific surface area  $12.05 \text{ m}^2/\text{g}$ , with an average smaller particle size of  $0.53 \pm 0.1$  microns compared to previously reported undoped ZnO particles ( $6.97 \text{ m}^2/\text{g}$  and  $0.84$  microns). Smaller particles size with the higher specific surface area may provide more active sites for the adsorption and desorption of oxygen and analyte gas molecules (Zhu and Zeng 2017). In addition to this, lattice distortion ( $\epsilon$ ) with higher values  $0.678$  and  $0.834$  in undoped ZnO and  $RuO_2$  activated Sr-doped ZnO heterostructure sensor respectively, may be caused to more scattering of charge

carriers and resulted into a smaller resistance modulation when exposed to ammonia gas.

Even though the crystallite size ( $D_v$ ) and lattice distortion ( $\epsilon$ ) of  $\text{RuO}_2$  activated Sr-doped ZnO heterostructure sensor are almost same as undoped ZnO, still exhibits lower response which is nearly half the value of gas response of the undoped ZnO sensor. It is because of the decreased concentration of oxygen vacancies ( $V_o$ ) and chemisorbed oxygen species ( $\text{O}^{2-}$ ) in  $\text{RuO}_2$  activated Sr-doped ZnO sensor compared to other sensors. Formation of  $\text{RuO}_2$  layer over the Sr-doped ZnO sensor may be acted as a passivation layer for the adsorption of oxygen species over the surface resulted into formation of lesser concentration of the chemisorbed oxygen species. Furthermore, adsorbed oxygen species may be utilized to oxidize the  $\text{RuO}_2$  to  $\text{RuO}_3$  and caused to the less availability of physisorbed oxygen species; hence no-spillover mechanism is observed as shown in fig. 5.29.

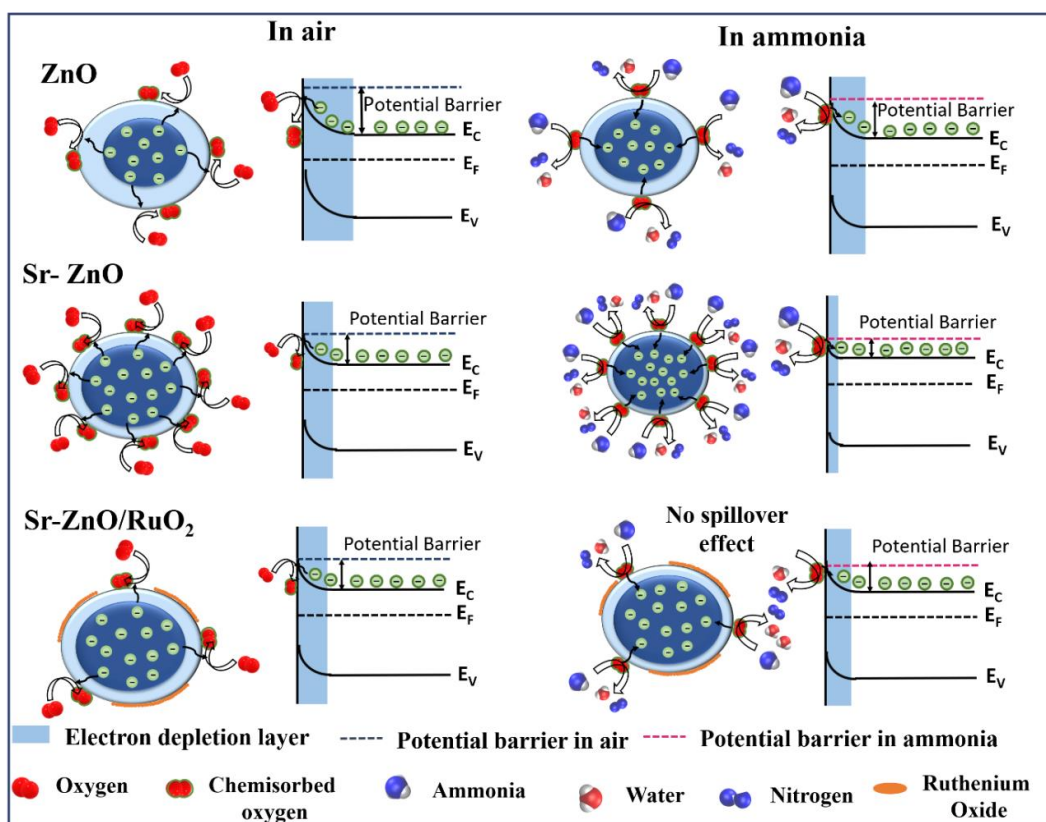


Fig. 5.29 Schematic representation of gas sensing mechanism of undoped ZnO, Sr doped ZnO and  $\text{RuO}_2$  activated Sr-doped ZnO sensor with band diagram when exposure to air and ammonia.

The same phenomenon was noticed in Pt and Pd decorated over SnO<sub>2</sub> particles which were oxidized using adsorbates to form PtO and PdO, and ended up into less concentration of chemisorbed oxygen species due to no-spill over catalytic activity, hence the gas response was decreased in case of decorated SnO<sub>2</sub> (Liu et al. 2015).

Five-time cycling response of undoped ZnO, Sr-doped ZnO and RuO<sub>2</sub> activated Sr-doped ZnO sensors for different concentration of NH<sub>3</sub> gas is depicted in Fig. 5.30 (a), (b) and (c). Transient response of the sensors varies with the concentration and depends on the adsorption and desorption of oxygen molecules on the surface of the sensors. When the airflow replaces the NH<sub>3</sub> gas flow, the electrical resistance returns to its original value implies the complete desorption of NH<sub>3</sub> molecules. After RuO<sub>2</sub> activation, the resistance of Sr-doped ZnO film decreases from 350 MΩ to 0.13 MΩ as shown in fig. 5.30 (c), may due to the consistent metallic conductivity of RuO<sub>2</sub>.

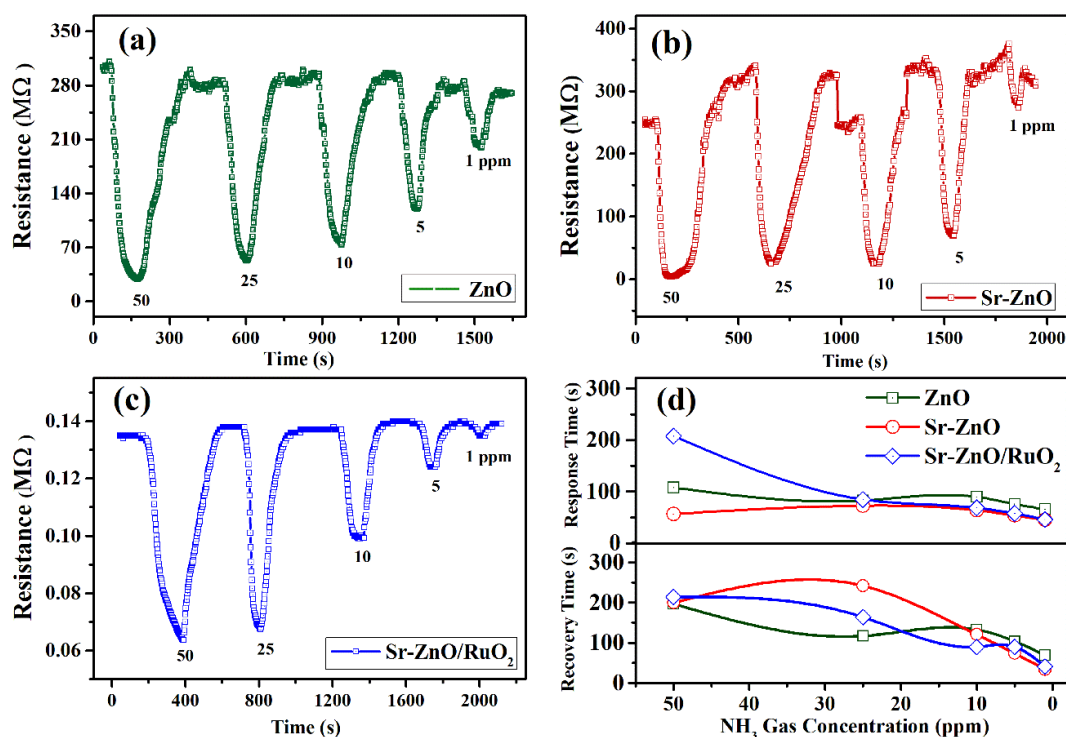


Fig. 5.30 Transient response of (a) ZnO (b) Sr-doped ZnO, (c) RuO<sub>2</sub> activated Sr-doped ZnO films and (d) response time and recovery time of screen-printed films towards different concentration of NH<sub>3</sub>.

Fig. 5.30 (d) depicts the response and recovery time of all sensors against the various concentration of NH<sub>3</sub>. It is observed that the Sr-doped ZnO sensor having

smaller crystallite size exhibited the faster response compared to the other two sensors. Crystallite size, oxygen vacancies ( $V_o$ ) influence the sensor kinetics characteristics mainly response time of the gas sensor. Usually, metal oxide semiconductor sensors detect gases by modulating its resistance. When sensors exposed to target gas, change in resistance observed because of the series of reactions and diffusion as explained earlier. When diffusion influences the sensor kinetics, smaller crystallite size offers a shorter distance for it. The crystallite size has a role to accommodate the successive reactions of vacancy among surface, grain boundary and volume. Therefore, Sr-doped ZnO sensor with smaller crystallite size exhibited a quick response to the ammonia gas than the other screen-printed sensors.

### **5.3.3 Screen printed pristine and La-doped BaSnO<sub>3</sub> films – gas sensing applications**

The X-ray diffraction patterns of BSO, LBSO, CLBSO and RLBSO films are shown in fig. 5.31 (a). The pristine BSO films exhibited the presence of pure cubic perovskite BaSnO<sub>3</sub> phase (ICDD: 15-0780) with diffraction peaks (110), (111), (200), (211), (220) and (310). The existence of La-doped BaSnO<sub>3</sub> phase without any secondary phases was detected in LBSO film, whereas additional small traces of CeO<sub>2-x</sub> (ICDD: 49-1415), CeO<sub>1.66</sub> (ICDD: 01-089-8434) and Ba<sub>5</sub>Ru<sub>2</sub>O<sub>10</sub> (ICDD: 01-089-7866), BaRuO<sub>3</sub> (ICDD: 01-074-4486) phases are found with LBSO phase in CLBSO and RLBSO films respectively. A right shift in the (110) plane in LBSO compared to BSO film is observed (fig. 5.31 (b)) and this shift may be due to the partial substitution of Ba<sup>2+</sup> ions by La<sup>3+</sup> ions, which confirms the successful doping of La in BaSnO<sub>3</sub>. The magnified region highlighting the mentioned additional phases in CLBSO and RLBSO films are shown in fig. 5.31 (c), respectively. The formation of the additional cerium oxide phases and ruthenates in CLBSO and RLBSO films is attributed to the oxidation of CeCl<sub>3</sub> and RuCl<sub>3</sub> while annealing the dipped film as a part of surface sensitization. It is noticed that the intensity of (110) main peak of BSO film is almost same as of (110) main peak of LBSO film, but the FWHM of (110) main peak of LBSO film is increased compared to BSO main peak, this is attributed to the decrease in the crystallite size. The average crystallite size of the BSO, LBSO, CLBSO and RLBSO films is estimated by using the Scherrer equation (3.7), and found to be 34, 29, 28 and 28 nm respectively,

as shown fig. 5.31 (d). It is noticed that the crystallite size of BSO has reduced after doping with La. The reason behind the formation of smaller crystallite size upon doping can be attributed to the inhibition of grain growth of BSO by dopant La even at high processing temperature (Dey 2018).

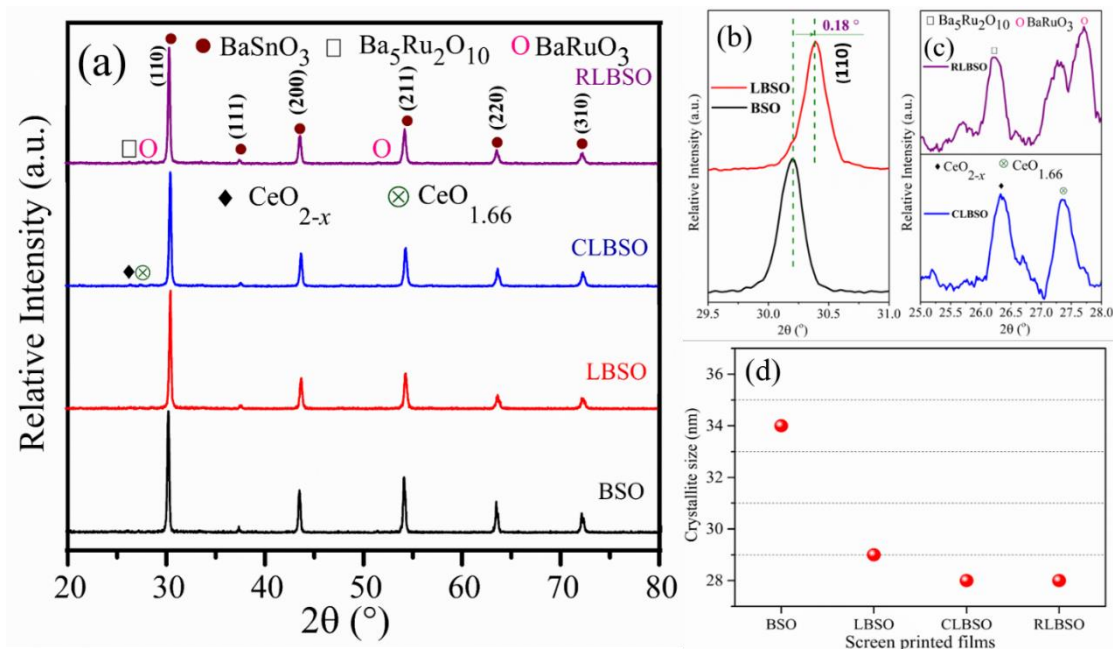


Fig. 5.31 (a) X-ray diffraction patterns of BSO, LBSO, CLBSO and RLBSO screen printed films, (b) Peak shift of (110) diffraction plane of LBSO (c) magnified region showing the additional phases appeared in CLBSO and RLBSO screen printed films, respectively, and (d) Crystallite size of the BSO, LBSO, CLBSO and RLBSO screen printed films.

Morphological features of all the BSO based screen printed films characterised using FESEM are shown in fig. 5.32 (a-d). Micrograph of pristine BSO screen-printed film (shown in fig. 5.32 (a)) revealed that the presence of small needle-like structures on the agglomerated micro-sized particles. Morphology with grown needle-like structures with an average D/L ratio of 0.1 on the smaller agglomerated particles is observed in the LBSO screen printed films as shown in fig. 5.32 (b). It is noticed that morphology of the LBSO is quite different from BSO screen printed films. The reason behind this could be the dopant La inhibited the grain growth of  $\text{BaSnO}_3$  in two directions and allowed to grow in only one direction, thereby the small needle-like structures on the agglomerated micro-sized particles in BSO film has been transformed to a morphology comprising lengthier needles in LBSO film. So many literature

reported that the dopant La yields control over the morphology of La-BaSnO<sub>3</sub> system (Purushothamreddy et al. 2020). Similar needle-like structures appeared partially from granular morphology after doping of La in perovskite SrTiO<sub>3</sub> also recognised in the previous report (Songwattanasin et al. 2019).

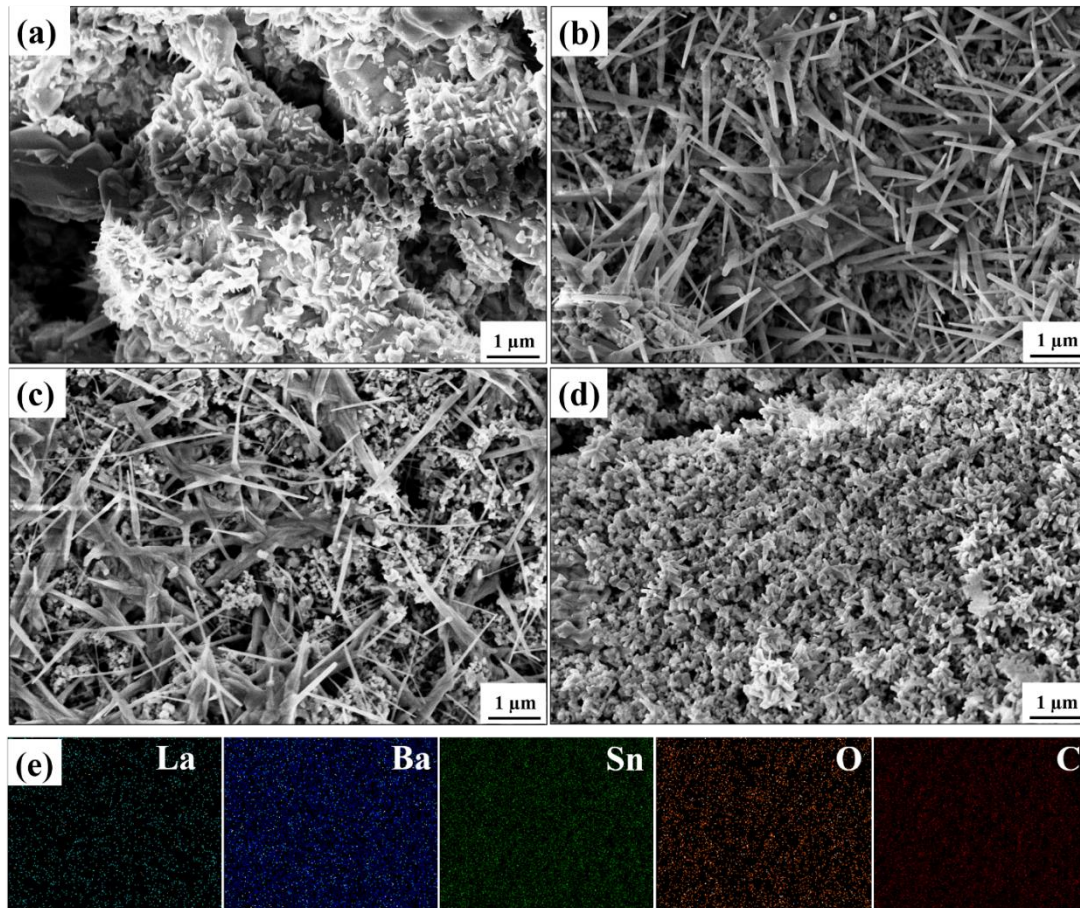


Fig. 5.32 FESEM images of the (a) BSO, (b) LBSO, (c) CLBSO (d) RLBSO screen printed films and (e) EDS elemental mapping of the LBSO screen printed film.

In the CLBSO films, some needles are clubbed and formed twisted-root structure along with the agglomerated particles and also the reduction in the concentration of needle-like morphology is observed, as shown in fig. 5.32 (c). Morphology of RLBSO film resembled the grouped star-fish structure, which leads to less porosity in the film as depicted in fig. 5.32 (d) and notably the presence of needle-like structures is completely disappeared after the immersion in the LBSO film the aqueous ruthenium chloride solution. The reason behind this could be the ruthenium chloride combined with the LBSO phase and caused the formation of separate phases of barium ruthenate by involving the atoms of Ba from the LBSO crystal structure. Formation of the secondary

phases using the atoms of the parent phase LBSO might have caused the disappearance of needle-like morphology in RLBSO film. The EDS elemental mapping of the nanostructured LBSO screen printed film is depicted in fig. 5.32 (e). which revealed the uniform distribution of elements such as lanthanum (La), barium (Ba), Tin (Sn), oxygen (O) and carbon (C).

The XPS wide scan spectra of all the BSO based screen-printed films is depicted in fig. 5.33 (a), which revealed the presence of elements such as barium (Ba), tin (Sn), oxygen (O), lanthanum (La), cerium (Ce), and ruthenium (Ru) in the respective films. The Carbon 1s (C 1s) peak centred at 284.6 eV is used for calibration of the XPS spectra. The peak fitting of the C 1s peak is performed to determine the position of the C-H peak for accounting the charge correction. (The deconvoluted C 1s XPS spectra and details of BSO based screen printed films are shown in Appendix VI and VII). The deconvoluted high-resolution spectra of O 1s peak of all the BSO based screen printed films are represented in fig. 5.33 (b-e). The O 1s peak is coherently fitted into four peaks centred at binding energies of  $530 \pm 0.3$  eV,  $531.1 \pm 0.3$  eV,  $532.5 \pm 0.3$  eV and  $534.3 \pm 0.3$  eV. The binding energies located at  $530 \pm 0.3$  eV,  $531.1 \pm 0.3$  eV,  $532.5 \pm 0.3$  eV corresponds to the lattice oxygen ( $O_L$ ), oxygen vacancies ( $O_V$ ) and surface adsorbed oxygen molecules ( $O_A$ ) respectively (Xi et al. 1992; Yang et al. 2020). The component at  $534.3 \pm 0.3$  eV associated with C=O is attributed to the hydroxyethyl cellulose, which is used as a binder in this study (Lhoest et al. 1995). The respective position, area of the O 1s deconvoluted components, and the ratio of the  $O_V/O_L$  of all the BSO based screen printed films are shown in Appendix VIII. The  $O_V/O_L$  ratio for the BSO, LBSO, CLBSO and RLBSO screen printed films is found to be  $\sim 1.7$ ,  $\sim 2.6$ ,  $\sim 1.1$  and  $\sim 1.5$  respectively as shown in fig. 5.33 (f). It is observed that the oxygen vacancy concentration is raised in LBSO film compared to pristine BSO film, whereas a reduction of it is observed in sensitized CLBSO and RLBSO films. The attractive force between  $La^{3+}$  and  $O^{2-}$  is less compared to  $Ba^{2+}$  and  $O^{2-}$ . This is due to the different electronegativity values of  $Ba^{2+}$  (0.89),  $La^{3+}$  (1.1) and  $O^{2-}$  (3.44), which indicates that ions of Ba have the ability to attract strongly with ions of O (Luo et al. 2015). Because of the low attraction between La and O, the chances of escaping of O atoms from the lattice will be high, forming high oxygen vacancy concentration in LBSO film compared to pristine BSO film.

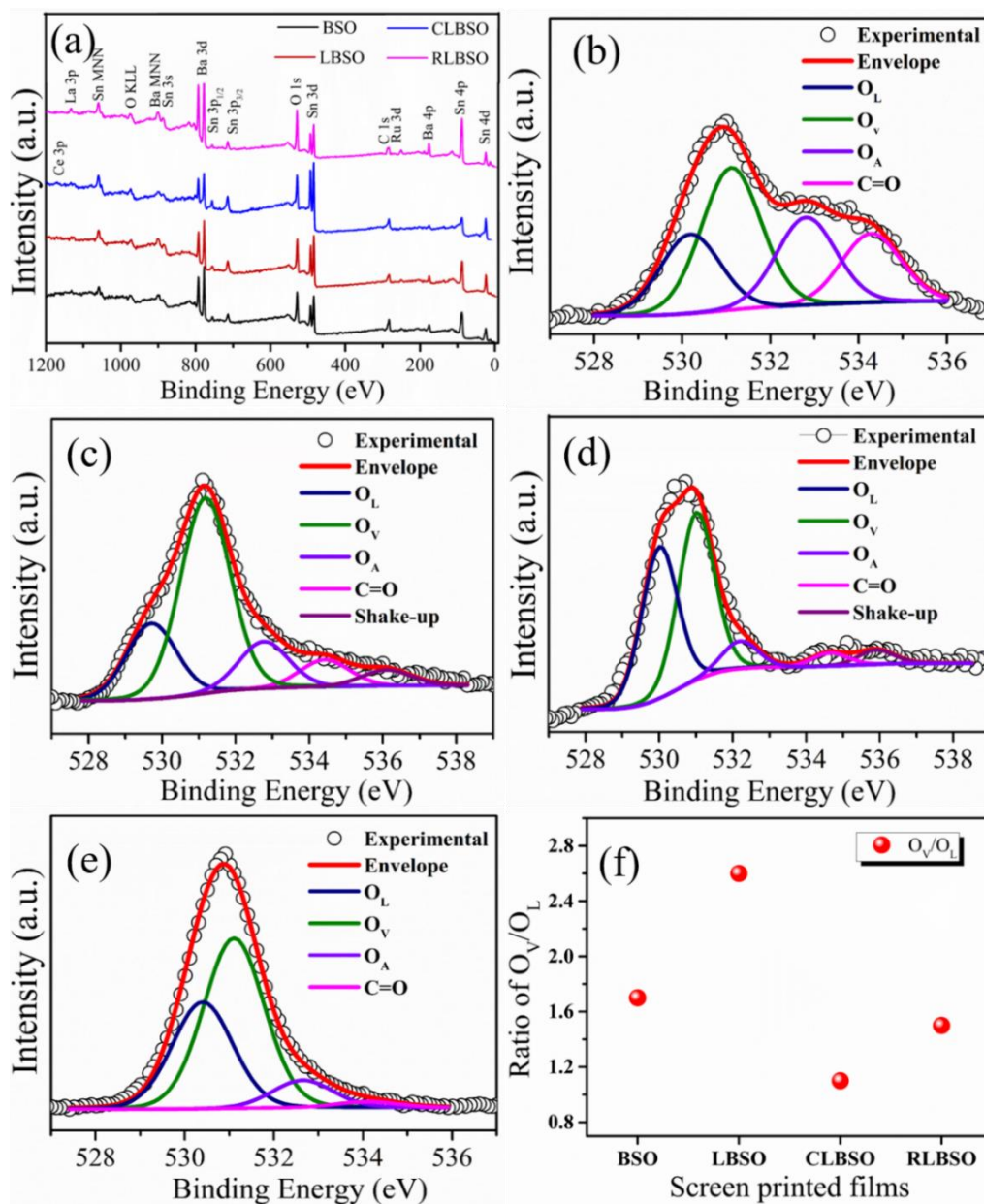


Fig. 5.33 (a) XPS wide scan spectrum, high-resolution spectra of O 1s peak (b) BSO, (c) LBSO, (d) CLBSO and (e) RLBSO films, and (f) ratio of O<sub>V</sub> to O<sub>L</sub> for the BSO based screen printed films.

Ceria displays a cubic fluorite structure, because of its fluorite structure it has attained a large oxygen storage capacity (Hamedani et al. 2012). Due to the storage efficiency of ceria, CLBSO film might have shown a low oxygen vacancy concentration in this study. Barium ruthenate phases are considered as good stable materials and the partial reduction of these phases ( $\text{BaRuO}_{3-x}$ ) is an unfavourable reaction. Even though partially reduced barium ruthenate phase occurs during annealing, it has the capability



to undergo reoxidation with atmospheric O<sub>2</sub> smoothly (Kamata et al. 2018). So, the chances of oxygen vacancies formation are comparatively less in RLBSO film, therefore a reduction in oxygen vacancy formation is observed.

The UV-Vis absorption spectra of all the BSO based screen printed films are depicted in fig. 5.34 (a). It is observed that the absorption edge of the LBSO film and its sensitized films exhibited a slight blue shift compared to the pristine BSO film, revealing an increment in the optical energy bandgap. The indirect band gap transition of all the screen-printed films was estimated by employing the Tauc's plot of Kubelka-Munk function. The relation of Kubelka-Munk function is shown in the following equation 5.21.

$$F(R) = \frac{\alpha}{S} = \frac{(1-R)^2}{2R} \quad (5.21)$$

Where F(R) is the Kubelka-Munk function,  $\alpha$  is the absorption coefficient, S is the scattering coefficient and R is the diffused reflectance of the film (Antunez et al. 2014; Patel et al. 2016). The Tauc's plot of Kubelka-Munk function revealed an indirect band gap transition of 2.73 eV for the pristine BSO film. The estimated band gap value is in accordance with the band gap value of barium stannate mentioned in the previous reports (Deepa et al. 2011; Slassi 2015; Zidi et al. 2010). The indirect band gap transition has further increased to 2.8 eV in LBSO film. A similar trend is observed in the literature, where the optical energy bandgap has increased with La doping in BaSnO<sub>3</sub> (Huang et al. 2016; James et al. 2015; Tiwari and Wong 2020). Increment in the value of bandgap transition can be the result of the substitution of La<sup>3+</sup> over Ba<sup>2+</sup> sites in the BSO perovskite structure. Also, the increment can be attributed to the defects augmentation, which results in the enhancement of localized energy levels. It is also observed that the indirect bandgap transition of LBSO film has increased to 3.08 eV and 3.04 eV after sensitization with ceria and ruthenate, respectively. The reason behind the increment could be the presence of ceria/ruthenate, which inhibits or suppresses the grain growth of LBSO and causes to the formation of smaller grains of LBSO. Due to the higher content, the ceria/ruthenate nucleates as secondary phase and transfers to the surface of the LBSO. Thus, the content of ceria and ruthenate in CLBSO and RLBSO leads to the blue shift of the LBSO bandgap (Bayal and Jeevanandam, 2014). In support of this statement, XRD reveals the crystal growth of the LBSO

(crystallite size 29 nm) is completely inhibited after the ceria/ruthenate sensitization of LBSO (29 nm).

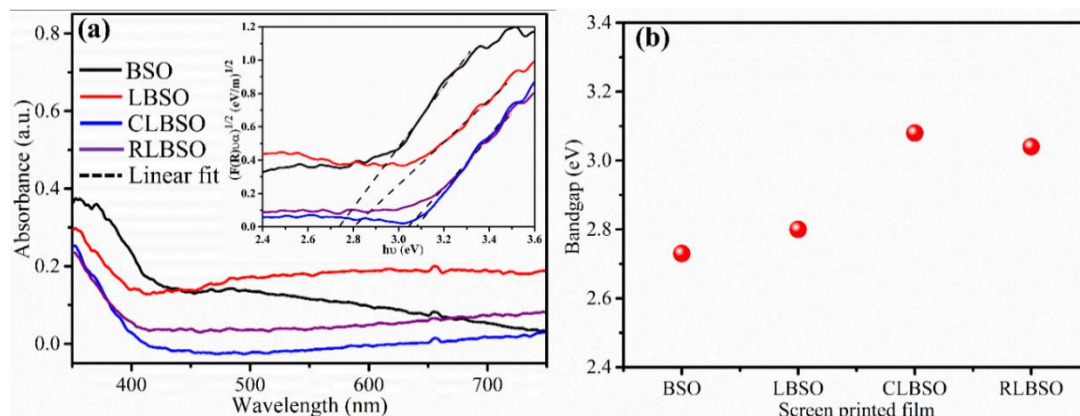


Fig. 5.34 (a) Absorbance spectra of BSO based screen printed films, inset shows the respective Tauc's plots of Kubelka-Munk function corresponding indirect bandgap transition and (b) estimated bandgap transition values of all BSO based screen printed films.

The gas-sensing performance of all the BSO based screen-printed sensors towards analyte gases ( $\text{NH}_3$  and  $\text{HCHO}$ ) at room temperature are shown in fig. 5.35 (a) and (b), respectively. It is observed that with the increase in analyte gas concentration, the gas response of all the BSO based screen-printed sensors has increased substantially. Importantly, it is noticed that the LBSO sensor exhibited superior gas response compared to the other sensors upon exposure various different concentration (5-50 ppm) of analyte gases. The gas response of the BSO, LBSO, CLBSO and RLBSO sensors towards 50 ppm of  $\text{NH}_3$  gas is found to be 35, 65, 14 and 3 respectively.

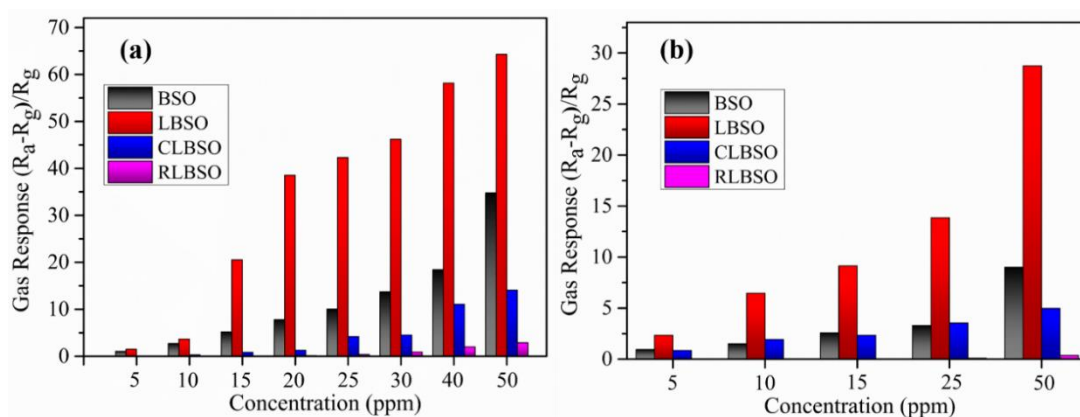


Fig. 5.35 The Gas response of BSO based sensors towards different concentrations of (a) ammonia and (b) formaldehyde gases at room temperature.

It is noticed that the gas sensitivity of the LBSO sensor enhanced by  $\sim 3$  times compared to the pristine BSO sensor against the various concentrations of HCHO gas (fig. 5.35 (b)). Further, the gas response value of LBSO screen-printed sensor towards HCHO gas decreased drastically to the  $1/6^{\text{th}}$  after ceria sensitization, whereas ruthenate sensitized LBSO exhibited the sensing capability with negligible value.

Fig. 5.36 (a) depicts the dynamic response and recovery behaviour of all BSO based screen-printed sensors when exposed to the various concentrations of  $\text{NH}_3$  gas at room temperature. It is observed that BSO, LBSO and CLBSO sensors are capable of detecting wide range of  $\text{NH}_3$  concentrations (5 to 50 ppm) distinctly, whereas RLBSO sensor lacked the capability to detect the  $\text{NH}_3$  gas with concentration less than 20 ppm.

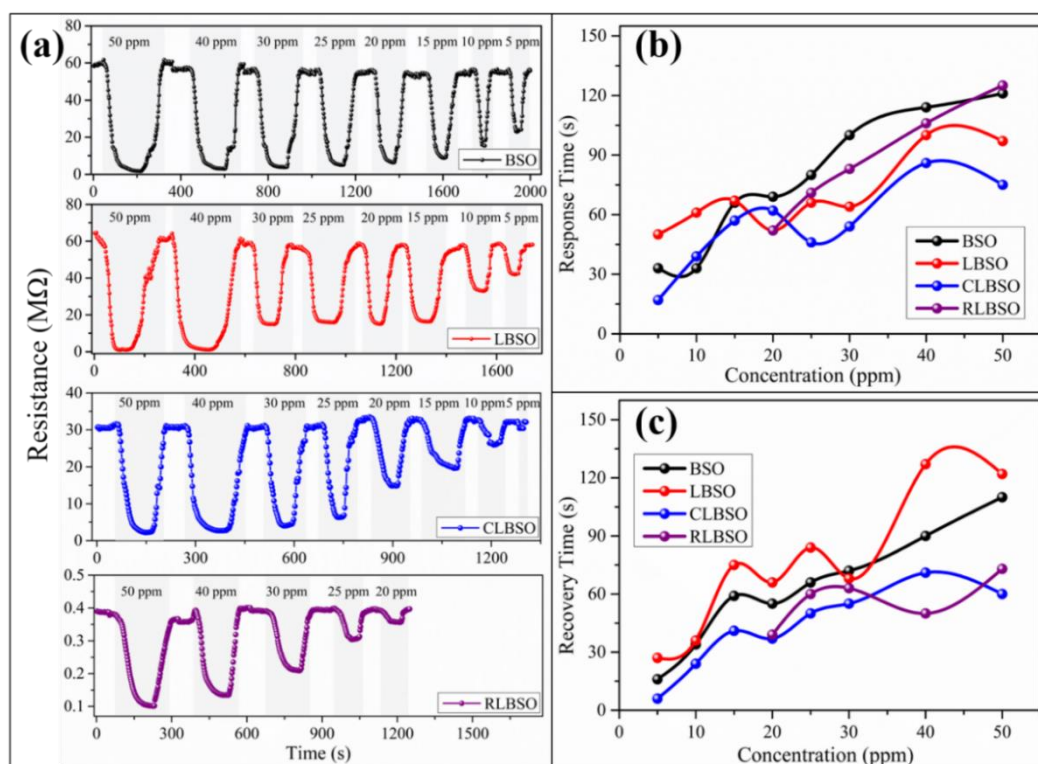
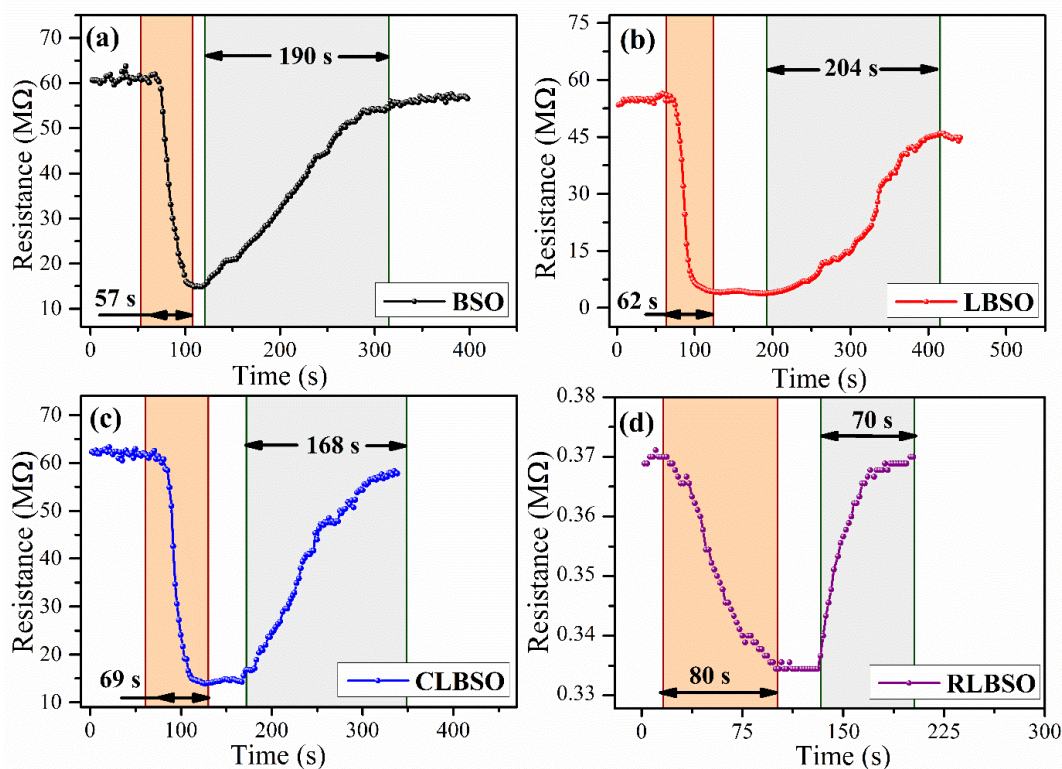


Fig. 5.36 (a) Transient resistance measurement of BSO based sensors towards different concentrations of ammonia gas, (b) response and (c) recovery time of BSO based sensors as a function of ammonia gas concentration.

Response and recovery time of all BSO based sensors towards various concentrations of  $\text{NH}_3$  gas are evaluated through their respective transient sensing curves, shown in fig. 5.36 (b) and (c), respectively. The response time range is found to be 33-121 s, 50-97 s, 17-75 s and 52-125 s for BSO, LBSO, CLBSO and RLBSO

sensors, respectively. It is observed that LBSO and CLBSO sensors exhibited an expeditious response towards the different concentrations of  $\text{NH}_3$  gas compared to other sensors. CLBSO sensor has recovered its original resistance quickly (6-60 s) upon unloading of  $\text{NH}_3$  gas than BSO (16-110 s), LBSO (27-122 s) and RLBSO (52-73 s) sensors (fig. 5.36 (c)). The reason behind the faster recovery in CLBSO sensor compared to other sensors could be the presence of fluorite structured ceria, which can store a large number of oxygen atoms in crystal planes, allows rapid diffusion of oxygen vacancies and facilitates rapid oxidization of  $\text{NH}_3$  gas (Hamedani et al. 2012).

The response and recovery time of all BSO sensors upon exposure to 25 ppm of HCHO gas at room temperature is depicted in fig. 5.37. The response time of BSO, LBSO, CLBSO and RLBSO sensors are found to be 57, 62, 69, and 80 s respectively. It is observed that LBSO sensor exhibited faster response with high sensitivity value ( $S = 15$ ) compared to other sensors. Whereas, the original resistance is recovered in 190, 204, 168 and 70 s for the BSO, LBSO, CLBSO and RLBSO sensors respectively after the desorption of formaldehyde gas.



**Fig. 5.37** Transient response of (a) BSO, (b) LBSO, (c) CLBSO and (d) RLBSO sensors respectively towards 25 ppm of formaldehyde gas at room temperature.

Response and recovery time of all BSO based sensors towards various concentration of HCHO gas are determined and tabulated in Table 5.7. It is observed that RLBSO sensor showed a faster recovery rate compared to other BSO based sensors. The reason could be the less porous morphology may not allow the more atmospheric oxygen molecules to diffuse underneath the film to extract electrons to form chemisorbed oxygen species.

Table 5.7 Response and Recovery time of BSO based screen printed sensors towards formaldehyde gas of different concentration at room temperature.

	Response Time (s)				Recovery Time (s)			
	BSO	LBSO	CLBSO	RLBSO	BSO	LBSO	CLBSO	RLBSO
<b>5 ppm</b>	43	50	8	-	86	38	62	-
<b>10 ppm</b>	52	55	63	-	116	50	156	-
<b>15 ppm</b>	54	63	48	-	136	176	127	-
<b>25 ppm</b>	57	62	69	80	190	204	168	70
<b>50 ppm</b>	73	77	77	166	218	352	276	137

As the gas selectivity is the main criterion for the usage of gas sensors in practical applications, the selectivity of the highly responded LBSO sensor was studied against the 50 ppm of ammonia, formaldehyde, methanol, ethanol, toluene and xylene gases, respectively, at room temperature (fig. 5.38 (a)). LBSO sensor exhibited a high selectivity against the ammonia gas followed by formaldehyde than the other interference gases. Notably, the LBSO sensor exhibited no response towards methanol, toluene and xylene gases. The probabilistic speculations behind the high gas selectivity of LBSO could be primarily due to the presence of a single pair of electrons in the ammonia gas. In addition to this, the kinetic diameter of the analyte gas molecules also influences the gas selectivity characteristic. Ammonia gas molecules with a lesser kinetic diameter (0.36 nm) might diffuse through the sensing layer and come in contact with chemisorbed oxygen species quickly than the other analyte gas molecules and this might resulted into an expeditious response (Navaneethan et al. 2017). The long-term stability of the gas sensing properties of LBSO sensors is tested after 240 days for the 50 ppm of NH<sub>3</sub> and HCHO, and shown in (fig. 5.38 (b)). It is observed that the LBSO sensor exhibited good stability as the variation in the gas response under the exposure of NH<sub>3</sub> and HCHO is less than 3 % and 10 % respectively.

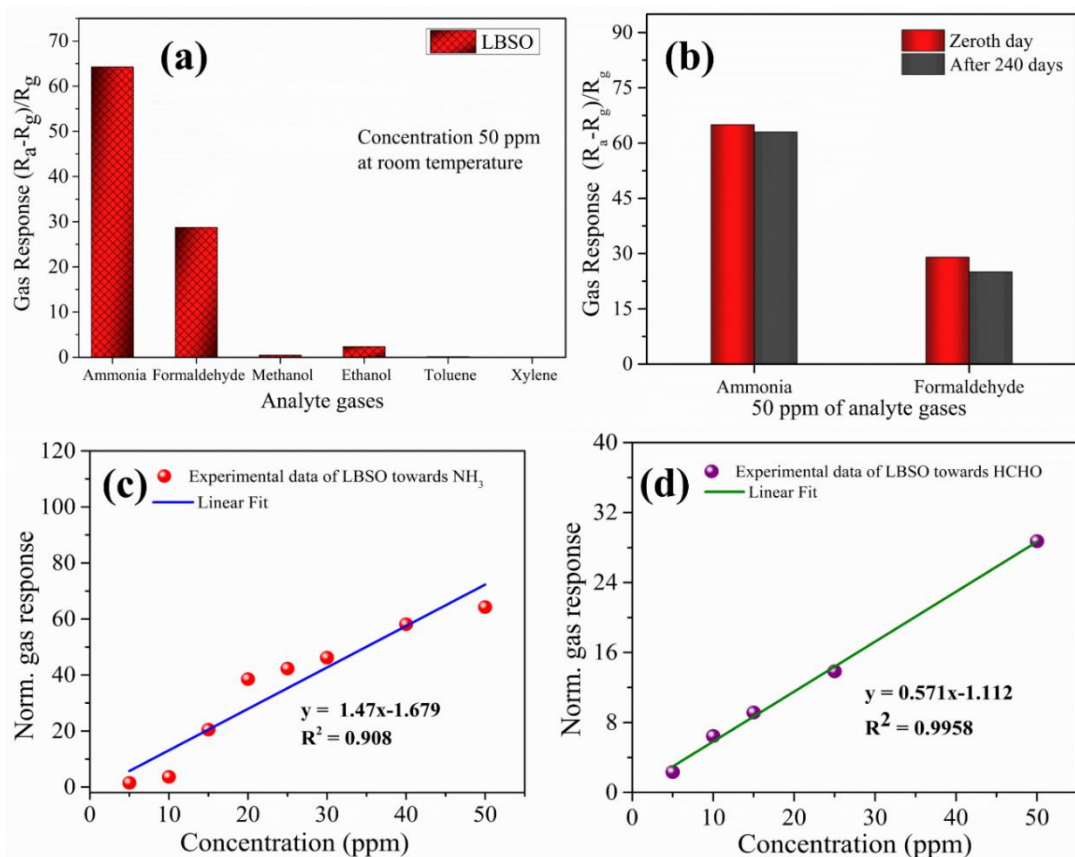
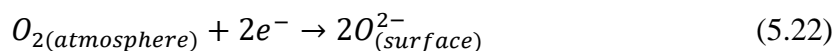


Fig. 5.38 (a) Gas Selectivity of LBSO sensor towards 50 ppm concentration of different gases at room temperature, (b) Stability of LBSO sensor towards 50 ppm of ammonia and formaldehyde gases after 240 days, (c) and (d) normalized response of LBSO sensor as a function of the concentration of ammonia and formaldehyde gases at room temperature, respectively.

Fig. 5.38 (c) and (d) shows the plot of response value of the LBSO sensor against the concentration of  $\text{NH}_3$  and  $\text{HCHO}$  gases respectively. The values are fitted linearly with an equation  $y = 1.47x - 1.6790$  ( $R^2=0.908$ ) and  $y = 0.571x - 1.112$  ( $R^2=0.995$ ) for the ammonia and formaldehyde gases respectively. The limit of detection of the LBSO sensor towards the  $\text{NH}_3$  and  $\text{HCHO}$  gases is estimated using the above-mentioned equations and found to be  $\sim 1$  ppm and  $\sim 2$  ppm respectively.

The mechanism of gas sensing of semiconducting metal oxides (SMO) is based on the variation of its electrical resistance upon loading and unloading of the analyte gases. Under ambient conditions, numerous oxygen molecules get adsorbed on the nanostructured BSO (n-type) semiconductor surface. These physisorbed oxygen

molecules disassociate and each oxygen atom extracts the free electron from the conduction band of the oxide to complete the bond and resulted into the formation of chemisorbed oxygen species ( $O^-$  and  $O^{2-}$ ) as shown in equation 5.22 (Bhattacharya et al. 2019).



When the electrons involve in the chemisorption process, the electron density in the material decreases, hence the electrical resistance increases. The physisorbed dissociated oxygen atoms can extract the electrons up to a certain depth (Debye length) from the surface, and the region within the Debye-length is called electron depletion layer (Miller et al. 2014). when the analyte gas ( $NH_3$  or  $HCHO$ ) is introduced, it reacts with chemisorbed oxygen species distributed over nanostructured BSO surface and gets oxidised. Simultaneously electrons return to the conduction band of the SMOs, thereby the electron depletion layer decreases resulting in the decrement of the electrical resistance. The possible reactions take place upon loading of  $NH_3$  or  $HCHO$  gases are represented as equations (5.23) and (5.24) respectively (Bhattacharya et al. 2019; Wagh et al. 2006);

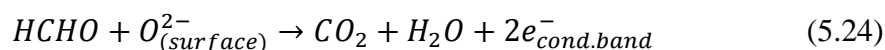
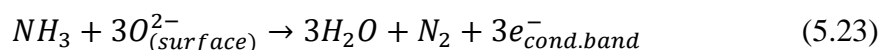


Table 5.8 Crystalline size, optical band gap, estimation of oxygen vacancies and gas responses of screen printed BSO, LBSO, CLBSO and RLBSO sensors.

Screen printed films	Crystallite size (nm)	Optical band gap (eV)	Ratio of $O_V/O_L$	Gas response (50 ppm)	
				$NH_3$	HCHO
BSO	34	2.94	1.7	35	9
LBSO	29	3.08	2.6	65	29
CLBSO	28	3.18	1.1	14	5
RLBSO	28	3.22	1.5	3	0.4

The notable results obtained from the BSO based screen-printed sensors using various characterisation techniques are summarised and tabulated in Table. 5.8. LBSO screen-printed sensor exhibited the higher sensitivity compared to the pristine BSO sensor and the probabilistic reasons behind this could be as follows: (i) Dopant La act as an

impurity which inhibited the grain growth in BSO resulting into the smaller grains (Table. 5.8). The relatively smaller grains in the LBSO sensor facilitate the larger Debye-length, which encourages the extraction of more electrons from the oxide material and primes to the development of more active sites for the reaction between the analyte gas and oxide surface, ensuing in high gas sensitivity (Shan et al. 2013). (ii) The high specific area due to needle-like morphology encourages the formation of higher concentration of chemisorbed oxygen species ( $O_2^-$ ) (Zhao et al. 2015). (iii) Most importantly, doping of La in BSO causes lattice deformation and increase in oxygen vacancies because of the variation in the ionic radius and valency of  $La^{3+}$  (1.36 Å) and  $Ba^{2+}$  (1.61 Å). It is noticed that LBSO possessed high oxygen vacancy concentration compared to all other sensors (Table.5.8). The high oxygen vacancy concentration encourages the participation of electrons in large numbers in the chemisorption process. It leads to the formation of the more active sites over the surface (Zeng et al. 2020). Simultaneously, LBSO depletes with electrons in large amount, causes the formation of thicker depletion layer than the pristine BSO during the chemisorption process as shown in fig. 5.39 (a). Afterwards, the involvement of high concentration chemisorbed oxygen species in the oxidation of analyte gas leads to the release of more electrons back to the conduction band of the LBSO sensor. Thereby, the depletion layer of LBSO shrunken to a larger extent than BSO and resulted into larger resistance modulation. The presence of  $CeO_2$  phase over the semiconducting metal oxide surface can have both positive and negative effects on the gas sensing properties. In this case, the superabundant  $CeO_2$  phase in CLBSO sensor might have acted as an insulator and reduced the active adsorption sites. In addition to this, less oxygen vacancy concentration in CLBSO sensor retard the formation of chemisorbed oxygen species in a large number (as shown in fig. 5.39 (b)), thereby oxidation of analyte gases will be reduced and resulted into the inferior gas sensing properties (Hamedani et al. 2012). In the case of RLBSO, when the amount of ruthenate oxide dispersed over the surface becomes more than the optimum, it results in the dense distribution of Ru atoms. The densely distributed Ru atoms over the sensor surface inhibit the formation of chemisorbed oxygen species in larger extent (fig. 5.39 (c)). So, the less number of electrons participated in the chemisorption process, thereby smaller resistance modulation is observed under air. When the analyte gases are exposed, lesser



chemisorbed oxygen species react with analyte gases and fewer electrons are released back to the conduction band of the RLBSO sensor. Hence, overall resistance modulation upon the exposure of analyte gas becomes smaller, which leads to the inferior gas sensitivity (Wagh et al. 2006). It is observed that the gas response of the LBSO sensor towards both the analyte gases has been decreased after ceria and ruthenate sensitization. It can be concluded that the ceria and ruthenate phases emerge as an inhibitor to the gas response of LBSO sensor.

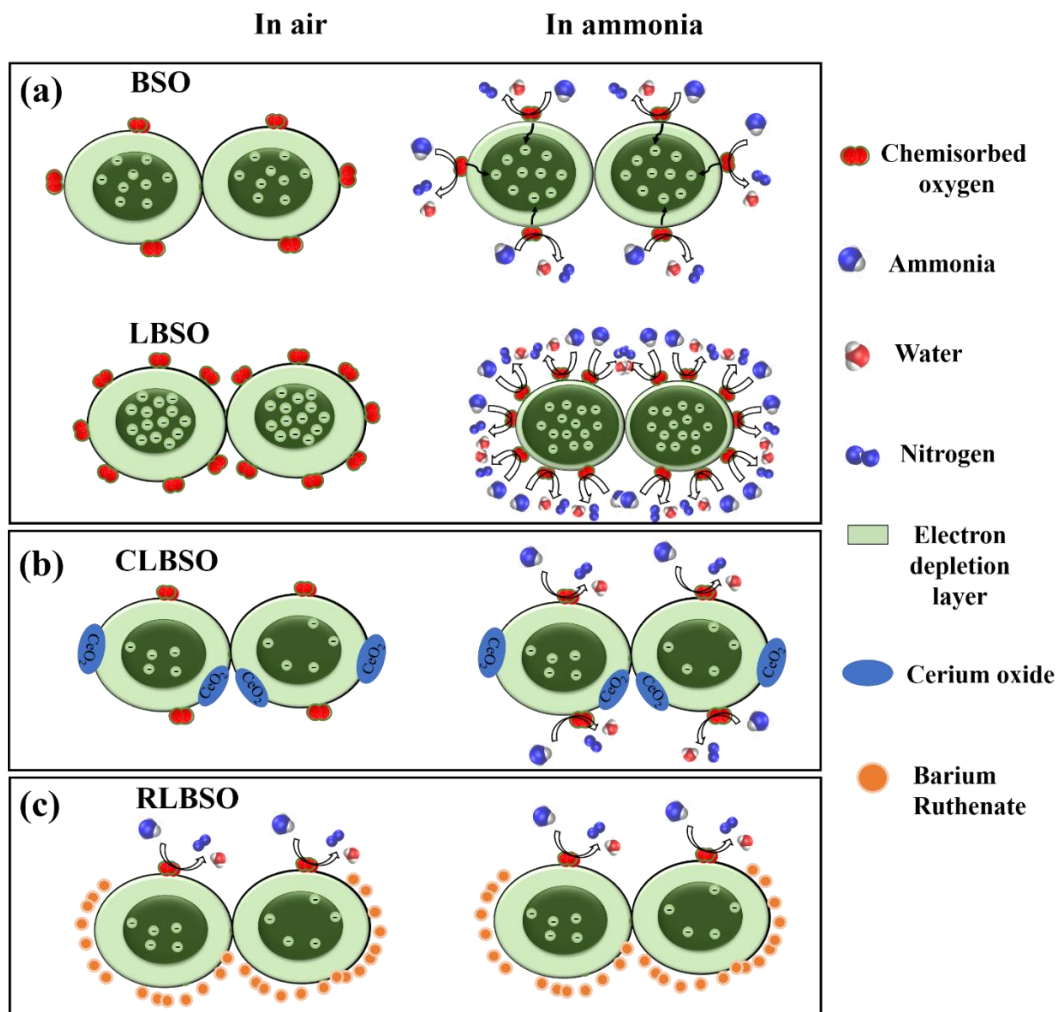


Fig. 5.39 Schematic illustration of ammonia gas sensing mechanism for the (a) pristine BSO, (b) LBSO, (c) CLBSO and (d) RLBSO sensors.

These inhibitors can be utilised to reduce the sensitivity of over-reactive catalytic combustible gas sensors (pellistors) which are used in the fire extinguishers and used in the multi-toxic gas detecting instruments to avoid the cross-sensitivity of the sensors.

## 5.4 Conclusions

Crystalline silver films were developed at a low curing temperature of 200 °C in 20 min. on glass substrates exhibited electrical conductivities  $2.6 \times 10^6$ ,  $4.0 \times 10^6$  and  $8.2 \times 10^6 \text{ S.m}^{-1}$  using Ink-1, Ink-2, and Ink-3, respectively. Whereas on a flexible polyamide substrate, a conductivity of  $2.6 \times 10^6 \text{ Sm}^{-1}$  was achieved using Ink-2. High resolution printed films with a minimum thickness of  $\sim 3 \mu\text{m}$  and roughness of 43.1 nm were obtained using Ink-2. Hence, minimal thickness (3  $\mu\text{m}$ ) with high dimensional accuracy was achieved in high conductive films and used as electrode for TFTs. The BGTC TFTs with amorphous IZTO- and sodium  $\beta$ -alumina as the active layer and gate dielectrics, were fabricated on the screen-printed silver gate, exhibited  $\mu_{\text{sat}}$ ,  $I_{\text{on}}/I_{\text{off}}$ , and  $V_{\text{th}}$  of  $0.88 \text{ cm}^2 \text{ V}^{-1} \text{ s}^{-1}$ ,  $10^2$ , and  $\sim 0.3 \text{ V}$ , respectively.

Adhered phase pure screen printed ZnO films is fabricated using particle-free ZnO screen printing inks and followed by annealing at 400 and 500 °C. Screen printed ZnO sensors processed at 500 °C showed significantly high  $\text{NH}_3$  response  $\sim 336$  and moderate HCHO response  $\sim 16.4$  towards the 5 ppm and 10 ppm of the respective gases under ambient conditions. Sensor-based on the screen-printed ZnO processed at 500 °C showed superior ammonia gas selectivity against various gases and LOD values were found to be 0.58 and 2.93 ppm for  $\text{NH}_3$  and HCHO.

Particle-based screen printed ZnO films with a thickness of  $\sim 15 \mu\text{m}$ , with high porosity were fabricated. Adhesion of printed ZnO films is designated as 4B (ASTM D3359). ZnO films obtained from glycine fuel system exhibited a high response to UV irradiation of exposure time  $\sim 90\text{s}$ . ZnO sensor were exposed to 100 ppm of  $\text{NH}_3$ ,  $\text{C}_2\text{H}_5\text{OH}$ ,  $\text{Cl}_2$  and 50 ppm of  $\text{H}_2\text{S}$ ; glycine fuel system exhibited good gas sensitivity of  $\sim 8$ , 5, 3 and 10 at operating temperature of 50 °C, 100 °C, 200 °C and 100 °C, respectively with quicker response and recovery speed. But, ZnO films from citric acid fuel system showed high sensitivity  $\sim 6$  with a 100 ppm of LPG gas at 350 °C.

Sr-doped ZnO sensor exhibited the highest response 70 towards the 50 ppm of  $\text{NH}_3$  gas compared to the pristine and  $\text{RuO}_2$ -activated Sr-doped ZnO sensors.  $\text{NH}_3$  gas response of  $\text{RuO}_2$ - activated Sr-doped ZnO heterostructure sensor was decreased from 70 to  $\sim 2$  when compared to Sr-doped ZnO, because of the larger crystallite size (40 nm), lesser concentration of oxygen vacancies, and chemisorbed oxygen.

Favourable parameters such as smaller crystallites, needle-like morphology and high concentration of oxygen vacancies contribute the LBSO sensor to exhibit a high gas response of ~ 65 and ~ 29 towards 50 ppm of ammonia and formaldehyde, respectively, at room temperature. Limit of detection of LBSO sensors was estimated to be ~ 1 and ~ 2 ppm against NH<sub>3</sub> and HCHO respectively.



## CHAPTER 6

### CONCLUSIONS

- ⇒ Ag and Ag-Cu alloy NPs capped with PVP were synthesized by two-step reduction polyol method with an average size of  $33 \pm 19$  and  $48 \pm 15$  nm, respectively.
- ⇒ The electrical conductivity of the solution combustion derived CVO films annealed at  $140\text{ }^\circ\text{C}$  was found to be  $\sim 3\text{ S}\cdot\text{cm}^{-1}$ .
- ⇒ Phase pure, non-stoichiometric, highly reactive, nanocrystalline pristine and Sr-doped ZnO with wurtzite structure was synthesized by the SCS route with an average particle size of  $0.84$  and  $0.45\text{ }\mu\text{m}$ , respectively.
- ⇒ Formulated water-based reducible particle-free silver precursor screen-printable inks possess thixotropic and shear thinning properties, which are decent for screen printing with curing temperature  $\sim 176\text{ }^\circ\text{C}$ .
- ⇒ Aqueous combustible particle-free ZnO screen printing inks made of zinc nitrate, glycine, Na-CMC and water with curing temperature  $\sim 400\text{ }^\circ\text{C}$  was formulated.
- ⇒ The minimum curing temperature of the particle-based ZnO/Sr-doped ZnO screen printing inks are found to be  $400\text{ }^\circ\text{C}$ .
- ⇒ Silver films were processed at  $200\text{ }^\circ\text{C}$  on glass substrates using formulated inks exhibited electrical conductivities of the order  $10^4\text{ S}\cdot\text{cm}^{-1}$ .
- ⇒ High conductive films with a minimum thickness ( $\sim 3\text{ }\mu\text{m}$ ) and high dimensional accuracy are used as the bottom gate electrode for TFTs, which exhibit an acceptable performance with static performance parameters, such as  $\mu_{\text{sat}}$ ,  $I_{\text{on}}/I_{\text{off}}$ , and  $V_{\text{th}}$  of  $0.88\text{ cm}^2\text{ V}^{-1}\text{ s}^{-1}$ ,  $10^2$ , and  $\sim 0.3\text{ V}$ , respectively.

- ⇒ Particle-free screen printed ZnO sensors processed at 500 °C showed a significantly high gas response ( $S = 336$ ) and selectivity towards 5 ppm of  $\text{NH}_3$  under ambient conditions.
- ⇒ Particle-based ZnO sensors obtained from the glycine fuel system depicted a good sensitivity to UV irradiation and gases like  $\text{NH}_3$ ,  $\text{C}_2\text{H}_5\text{OH}$ , and  $\text{Cl}_2$  than the ZnO sensors obtained from the urea and citric acid fuel system.
- ⇒ Sr-doped ZnO sensor exhibited superior room temperature gas sensing properties towards  $\text{NH}_3$  gas compared to the pristine and  $\text{RuO}_2$ -activated Sr-doped ZnO sensors.
- ⇒ La-doped  $\text{BaSnO}_3$  sensor exhibited superior gas response upon exposure of both the  $\text{NH}_3$  and  $\text{HCHO}$  gases than the  $\text{BaSnO}_3$  and sensitized La-doped  $\text{BaSnO}_3$  sensors.

### **Scope for the future work**

The result and analysis of the present study demonstrated the formulation and screen printing of metal and metal oxides and their applications. The present study offers a scope for further work are:

1. Fabrication of screen-printed conductive alloys electrodes such as Ag-Cu in place of Ag to reduce the cost.
2. A theoretical model can be established to investigate the effect of screen-printing parameters on the thickness and roughness of the films.
3. Demonstration of  $\text{NH}_3$  prototype sensor using particle-free screen printed ZnO as an active layer, for perceiving the state/progression of end-stage renal and chronic kidney diseases.
4. Screen printing of doped and co-doped indium oxides for gas sensing applications using particle free approach.

APPENDIX

Appendix I

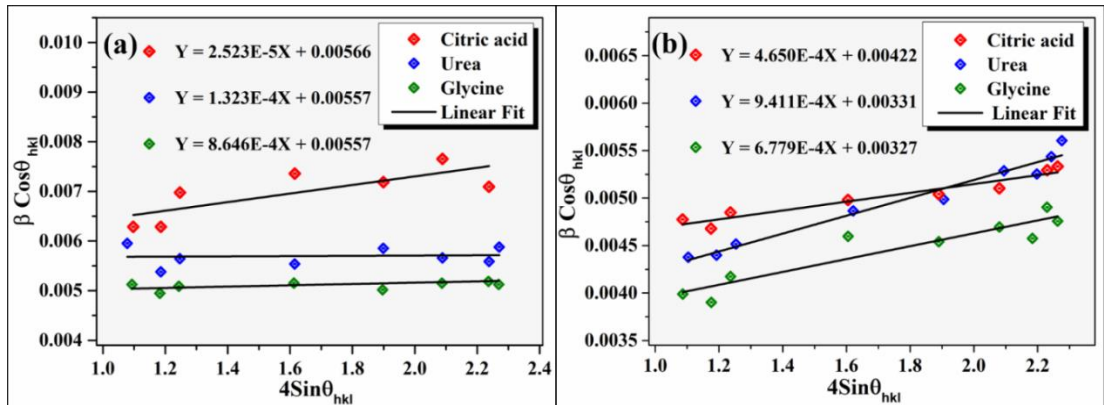


Figure I-a. Williamson Hall-ISM plot of ZnO synthesized by different fuel-system, (a) as-combusted and (b) calcined at 600 °C for 2 hrs

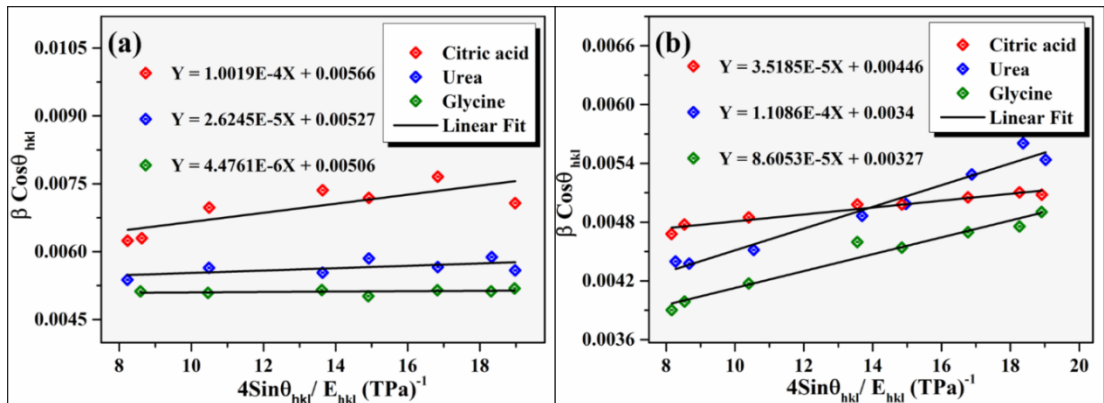


Figure I-b. Williamson Hall-ASM plot of synthesized ZnO by different fuel-system; (a) as-combusted and (b) calcined at 600 °C for 2 hrs

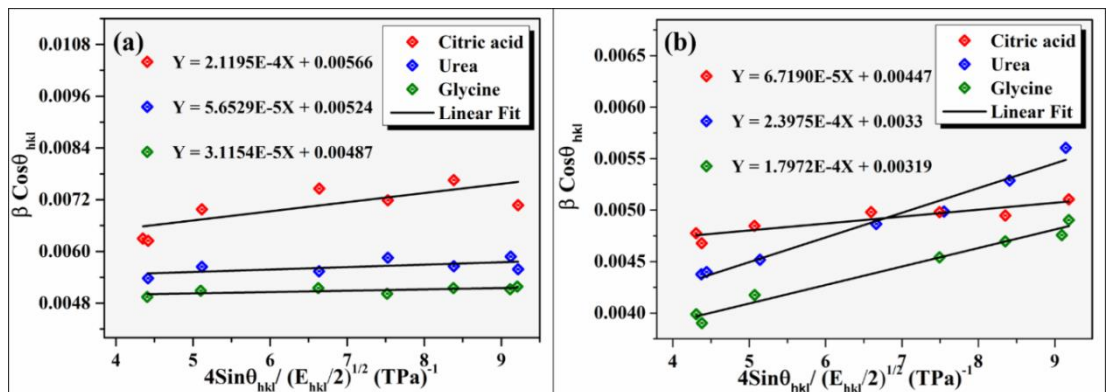


Figure I-c. Williamson Hall-UDM plot of synthesized ZnO by different fuel-system; (a) as-combusted and (ii) calcined at 600 °C for 2 hrs.

## Appendix II

Table -II Spreadsheet of cohen's analysis for the calculation of precise lattice parameter 'a' and 'c' of particle-free screen printed ZnO films annealed at 400 °C.

<b>2θ</b>	<b>θ</b>	<b>h</b>	<b>k</b>	<b>l</b>	<b>α</b>	<b>γ</b>	<b>δ</b>	<b>α<sup>2</sup></b>	<b>αγ</b>	<b>αδ</b>	<b>γ<sup>2</sup></b>	<b>γδ</b>	<b>δ<sup>2</sup></b>	<b>α(sinθ)</b>	<b>γ(Sinθ)</b>	<b>δ(Sinθ)</b>
<b>31.996</b>	15.998	1	0	0	1	0	0.280	1	0	0.2807	0	0	0.078	0.075	0	0.0213
<b>34.654</b>	17.327	0	0	2	0	4	0.323	0	0	0	16	1.293	0.104	0	0.354	0.028
<b>36.457</b>	18.228	1	0	1	1	1	0.353	1	1	0.353	1	0.353	0.124	0.097	0.097	0.034
<b>47.793</b>	23.896	1	0	2	1	4	0.548	1	4	0.5486	16	2.194	0.300	0.16	0.656	0.089
<b>56.789</b>	28.394	1	1	0	3	0	0.699	9	0	2.097	0	0	0.488	0.678	0	0.158
<b>63.051</b>	31.525	1	0	3	1	9	0.794	1	9	0.7946	81	7.151	0.631	0.273	2.460	0.217
<b>68.175</b>	34.087	1	1	2	3	4	0.861	9	12	2.5853	16	3.447	0.742	0.942	1.256	0.270
								<b>Σα<sup>2</sup>=22</b>	<b>Σαγ=26</b>	<b>Σαδ=6.659</b>	<b>Σγ<sup>2</sup>=130</b>	<b>Σγδ=14.439</b>	<b>Σδ<sup>2</sup>=2.471</b>	<b>Σα(sinθ)=2.231</b>	<b>Σγsinθ=4.825</b>	<b>Σδsinθ=0.82</b>

$$\alpha = (h^2 + k^2 + l^2)$$

$$\gamma = l^2, \delta = \sin^2 2\theta$$

$$22A + 26B + 6.659C = 2.231$$

$$26A + 130B + 14.439C = 4.825$$

$$6.659A + 14.439B + 2.471C = 0.82$$

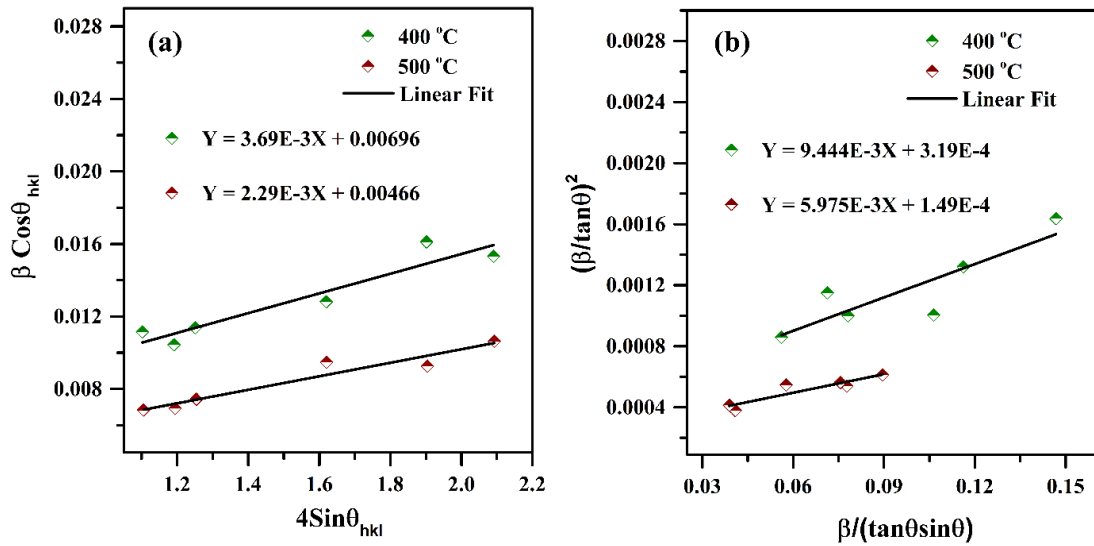
$$a = \frac{\lambda}{(3A)^{1/2}} = 3.25 \text{ \AA}$$

$$c = \frac{\lambda}{(4B)^{1/2}} = 5.21 \text{ \AA}$$



### Appendix III

Figure III (a) Williamson–Hall and (b) Halder -Wagner analysis plots of screen-printed ZnO films annealed at different temperatures.



### Appendix IV

Table-IV Spreadsheet of cohen's analysis for the calculation of precise lattice parameter 'a' and 'c' of particle-based screen-printed Sr-doped ZnO films.

<b>2θ</b>	<b>θ</b>	<b>h</b>	<b>k</b>	<b>l</b>	<b>a</b>	<b>γ</b>	<b>δ</b>	<b>α<sup>2</sup></b>	<b>αγ</b>	<b>αδ</b>	<b>γ<sup>2</sup></b>	<b>γδ</b>	<b>δ<sup>2</sup></b>	<b>α(sinθ)</b>	<b>γ(Sinθ)</b>	<b>δ(Sinθ)</b>
<b>31.796</b>	15.898	1	0	0	1	0	0.277	1	0	0.277	0	0	0.077	0.075	0	0.020
<b>34.467</b>	17.233	0	0	2	0	4	0.320	0	0	0	16	1.28	0.102	0	0.35	0.028
<b>36.304</b>	18.152	1	0	1	1	1	0.350	1	1	0.350	1	0.35	0.122	0.09706	0.097	0.034
<b>47.626</b>	23.813	1	0	2	1	4	0.545	1	4	0.545	16	2.18	0.297	0.163	0.652	0.088
<b>56.698</b>	28.349	1	1	0	3	0	0.698	9	0	2.095	0	0	0.487	0.672	0	0.156
<b>62.989</b>	31.494	1	0	3	1	9	0.793	1	9	0.793	81	7.143	0.629	0.2729	2.4561	0.216
<b>68.085</b>	34.042	1	1	2	3	4	0.860	9	12	2.582	16	3.442	0.74	0.9399	1.2532	0.269
<b>69.235</b>	34.617	2	0	1	4	1	0.874	16	4	3.497	1	0.874	0.764	1.2908	0.3227	0.282

$$\alpha = (h^2 + k^2 + l^2)$$

$$\gamma = l^2, \quad \delta = \sin^2 2\theta$$

$$\Sigma\alpha^2=38 \quad \Sigma\alpha\gamma=36 \quad \Sigma\alpha\delta=10.142 \quad \Sigma\gamma^2=131 \quad \Sigma\gamma\delta=15.274 \quad \Sigma\delta^2=3.223 \quad \Sigma\alpha(\sin\theta)=3.51 \quad \Sigma\gamma\sin\theta=5.131 \quad \Sigma\delta\sin\theta=1.096$$

$$38A + 30B + 10.1423C = 3.51$$

$$30A + 131B + 15.2745C = 5.131$$

$$10.1423A + 15.2745B + 3.223C = 1.096$$

$$a = \frac{\lambda}{(3A)^{1/2}} = 3.21 \text{ \AA}, \quad c = \frac{\lambda}{(4B)^{1/2}} = 5.19 \text{ \AA}$$

## Appendix V

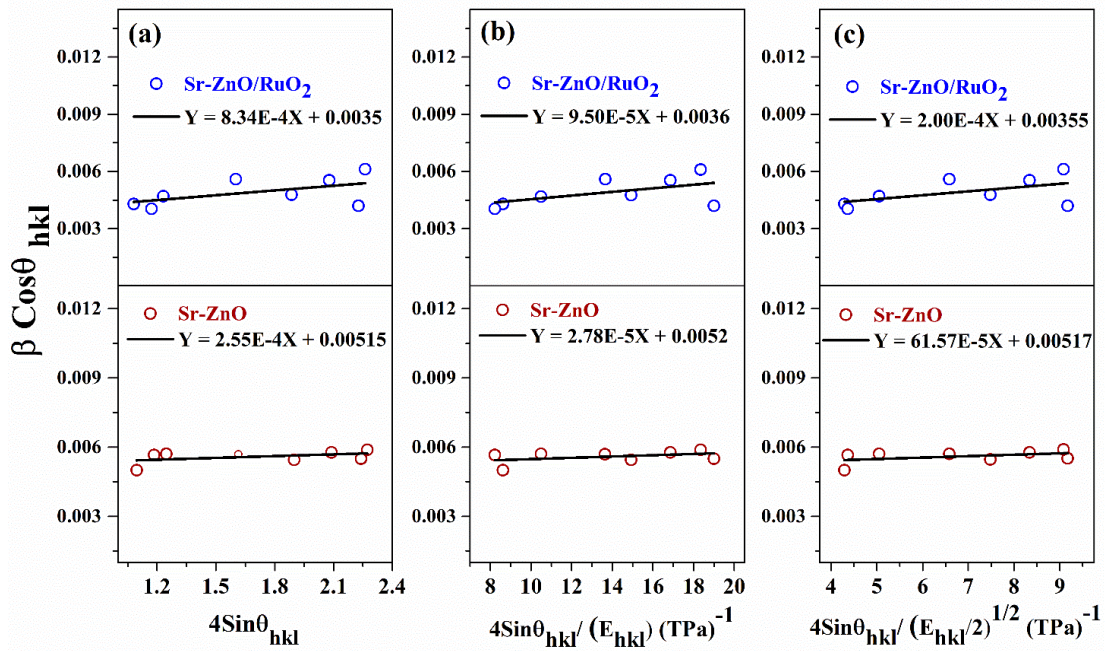


Figure V. The W–H analysis plots of pristine and RuO<sub>2</sub> activated Sr-doped ZnO screen printed films assuming (a) Iso-strain model, (b) Anisotropic model, and (c) Energy Density model.

## Appendix VI

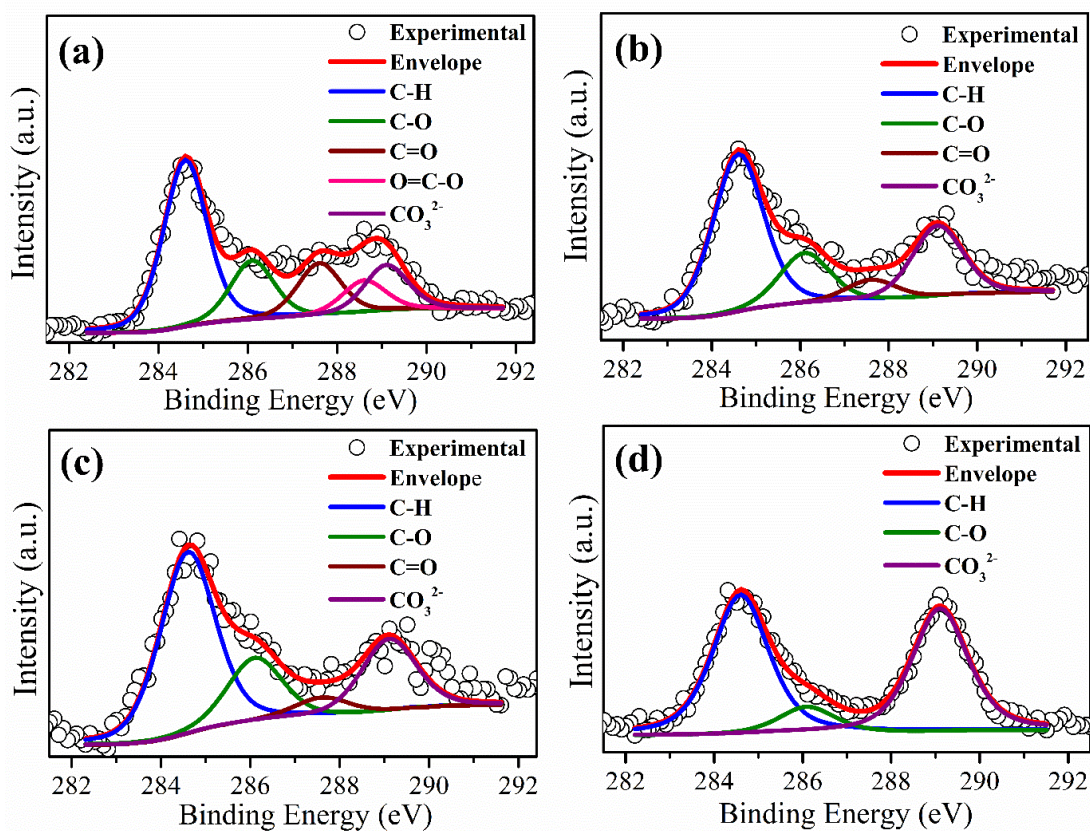


Figure VI. C 1s XPS spectra of (a) BSO, (b) LBSO, (c) CLBSO and (d) RLBSO

## Appendix VII

Table-VII C 1s XPS Peak fit parameters of BSO, LBSO, CLBSO and RLBSO screen printed films

Screen printed films	Deconvoluted peak	Position constraints	Position (eV)	FWHM	GL ratio	Area (cps.eV)
<b>BSO</b>	C-H (peak I)	--	284.6	1.15	30	372.01
	C-O (peak II)	Peak I + 1.5 eV	286.1	1.15	30	131.55
	C=O (peak III)	Peak I + 3.0 eV	287.6	1.15	30	116.8
	O=C-O (peak IV)	Peak I + 4.0 eV	288.6	1.15	30	71.12
	CO <sub>3</sub> <sup>2-</sup> (peak V)	Peak I + 4.5 eV	289.1	1.15	30	101.77
<b>LBSO</b>	C-H (peak I)	--	284.6	1.35	30	296.86
	C-O (peak II)	Peak I + 1.5 eV	286.1	1.35	30	94.85
	C=O (peak III)	Peak I + 3.0 eV	287.6	1.35	30	38.59
	CO <sub>3</sub> <sup>2-</sup> (peak IV)	Peak I + 4.5 eV	289.1	1.35	30	132.65
<b>CLBSO</b>	C-H (peak I)	--	284.6	1.45	30	250.26
	C-O (peak II)	Peak I + 1.5 eV	286.1	1.45	30	86.73
	C=O (peak III)	Peak I + 3.0 eV	287.6	1.45	30	25.38
	CO <sub>3</sub> <sup>2-</sup> (peak IV)	Peak I + 4.5 eV	289.1	1.45	30	99.02
<b>RLBSO</b>	C-H (peak I)	--	284.6	1.5	50	506.02
	C-O (peak II)	Peak I + 1.5 eV	286.1	1.5	50	94.85
	CO <sub>3</sub> <sup>2-</sup> (peak III)	Peak I + 4.5 eV	289.1	1.5	50	446.8

### Appendix VIII

Table-VIII Binding energies, peak areas of the O 1s deconvoluted components and ratio of concentration of  $O_V/O_L$ .

Screen printed films	Peak name	Peak position (eV)	Area (cps.eV)	Conc. ratio of $O_V/O_L$
<b>BSO</b>	$O_L$	530.1	604.7	1.7
	$O_V$	531.1	1081.9	
	$O_A$	532.8	670.4	
	C=O	534.2	524.7	
<b>LBSO</b>	$O_L$	529.4	771.8	2.6
	$O_V$	530.8	1995	
	$O_A$	532.4	479.8	
	C=O	534.1	276.2	
	Shake-up	535.8	162.8	
<b>CLBSO</b>	$O_L$	530.0	828.4	1.1
	$O_V$	531.0	915.0	
	$O_A$	532.2	150.9	
	C=O	534.6	71.97	
	Shake-up	535.9	79.15	
<b>RLBSO</b>	$O_L$	530.4	1665.5	1.5
	$O_V$	531.1	2655.5	
	$O_A$	532.6	430.4	
	C=O	534.1	98.2	

## REFERENCES

- Adhikari, K. K., Jung, Y., Park, H., Cho, G., and Kim, N.-Y. (2015). "Silver-nanoparticle-based screen-printing and film characterization of a disposable, dual-band, bandstop filter on a flexible polyethylene terephthalate substrate". *J. Nanomater.*, 16(1), 395.
- Agnihotri, S., Mukherji, S., and Mukherji, S. (2014). "Size-controlled silver nanoparticles synthesized over the range 5–100 nm using the same protocol and their antibacterial efficacy". *RSC Adv.*, 4(8), 3974-3983.
- Alharbi, N.D., and Guirguis, O.W. (2019). "Macrostructure and optical studies of hydroxypropyl cellulose in pure and Nano-composites forms". *Results Phys.*, 15, 102637.
- Al-Hashem, M., Akbar, S., and Morris, P. (2019). "Role of oxygen vacancies in nanostructured metal-oxide gas sensors: a review". *Sens. Actuators B Chem.*, 301, 126845.
- Aleeva, Y., and Pignataro, B. (2014). "Recent advances in upscalable wet methods and ink formulations for printed electronics". *J. Mater. Chem.*, 2(32), 6436-6453.
- Anand, K., Kaur, J., Singh, R. C., and Thangaraj, R. (2016). "Structural, optical and gas sensing properties of pure and Mn-doped In<sub>2</sub>O<sub>3</sub> nanoparticles". *Ceram. Int.*, 42(9), 10957-10966.
- Ang, T.P., and Chin, W.S. (2005). "Dodecanethiol-Protected Copper/Silver Bimetallic Nanoclusters and Their Surface Properties". *J. phys.Chem.B.*, 109, 22228-22236.
- Anisimov, V. I. i. (2010). "Electronic structure of strongly correlated materials". Paper presented at the AIP Conference Proceedings.
- Ansari, S., Borojerdian, P., Sainkar, S., Karekar, R., Aiyer, R., and Kulkarni, S. (1997). "Grain size effects on H<sub>2</sub> gas sensitivity of thick film resistor using SnO<sub>2</sub> nanoparticles". *Thin Solid Films.*, 295(1-2), 271-276.

- Antunez, P. D., Torelli, D. A., Yang, F., Rabuffetti, F. A., Lewis, N. S., and Brutchey, R. L. (2014). "Low temperature solution-phase deposition of SnS thin films". *Chem. Mater.*, 26(19), 5444-5446.
- Ardelean, I., Andronache, C., Cimpean, C., and PĂȘCUȚĂ, P. (2004). "Structural Investigation of  $x\text{Fe}_2\text{O}_3 \cdot (100-x)[\text{P}_2\text{O}_5 \cdot \text{CaO}]$  and  $x(\text{Fe}_2\text{O}_3 \cdot \text{V}_2\text{O}_5) \cdot (100-x)[\text{P}_2\text{O}_5 \cdot \text{CaO}]$  Glass Systems by IR Spectroscopy". *Mod Phys Lett B.*, 18(01), 45-49.
- Ayeshamariam, A., Kashif, M., Bououdina, M., Hashim, U., Jayachandran, M., and Ali, M. (2014). "Morphological, structural, and gas-sensing characterization of tin-doped indium oxide nanoparticles". *Ceram. Int.*, 40(1), 1321-1328.
- Bai, S., Li, D., Han, D., Luo, R., Chen, A., and Chung, C. L. (2010). "Preparation, characterization of  $\text{WO}_3\text{-SnO}_2$  nanocomposites and their sensing properties for  $\text{NO}_2$ ". *Sens. Actuators B Chem.*, 150(2), 749-755.
- Bai, Z., Xie, C., Zhang, S., Zhang, L., Zhang, Q., Xu, W., and Xu, J. (2010). "Microstructure and gas sensing properties of the ZnO thick film treated by hydrothermal method". *Sens. Actuators B Chem.*, 151(1), 107-113.
- Bao, X., Lee, N.-C., Raj, R. B., Rangan, K., and Maria, A. (1998). "Engineering solder paste performance through controlled stress rheology analysis". *Solder. Surf. Mt. Technol.*, 10(2), 26-35.
- Barnes, H. A., Hutton, J. F., and Walters, K. (1989). *An introduction to rheology*: Elsevier.
- Barsan, N., Koziej, D., and Weimar, U. (2007). "Metal oxide-based gas sensor research: How to?". *Sens. Actuators B Chem.*, 121(1), 18-35.
- Bayan, S., and Chakraborty, P. (2014). "Secondary ion mass spectrometry and photoluminescence study on microstructural characteristics of chemically synthesized ZnO nanowalls". *Appl. Surf. Sci.*, 303, 233-240.
- Bayan, S., and Mohanta, D. (2013). "Fragmentation of elongated-shaped ZnO nanostructures into spherical particles by swift ion impact". *Physica E Low Dimens. Syst. Nanostruct.*, 54, 288-294.



- Bayal, N., and Jeevanandam, P. (2014). "Synthesis of TiO<sub>2</sub>-MgO mixed metal oxide nanoparticles via a solgel method and studies on their optical properties". *Ceram. Int.*, 40, 15463-15477.
- Beck, S., Sclauzero, G., Chopra, U., and Ederer, C. (2018). "Metal-insulator transition in CaVO<sub>3</sub> thin films: Interplay between epitaxial strain, dimensional confinement, and surface effects". *Phys. Rev. B.*, 97(7), 075107.
- Bernabò, M., Pucci, A., Ramanitra, H. H., and Ruggeri, G. (2010). "Polymer nanocomposites containing anisotropic metal nanostructures as internal strain indicators". *Materials.*, 3(2), 1461-1477.
- Bhattacharya, A., Jiang, Y., Gao, Q., Chu, X., Dong, Y., Liang, S., and Chakraborty, A. K. (2019). "Highly responsive and selective formaldehyde sensor based on La<sup>3+</sup> - doped barium stannate microtubes prepared by electrospinning". *Mater. Res.*, 34(12), 2067-2077.
- Bochenkov, V., and Sergeev, G. (2010). "Sensitivity, selectivity, and stability of gas-sensitive metal-oxide nanostructures". *Metal oxide nanostructures and their applications*, 3, 31-52.
- Bonet, F., Grugeon, S., Dupont, L., Urbina, R. H., Guery, C., and Tarascon, J. (2003). "Synthesis and characterization of bimetallic Ni–Cu particles". *J. Solid State Chem.*, 172(1), 111-115.
- Căldăraru, M., Sprinceana, D., Popa, V., and Ionescu, N. (1996). "Surface dynamics in tin dioxide-containing catalysts II. Competition between water and oxygen adsorption on polycrystalline tin dioxide". *Sens. Actuators B Chem.*, 30(1), 35-41.
- Cao, X., Chen, H., Gu, X., Liu, B., Wang, W., Cao, Y., Wu, F., and Zhou, C. (2014). "Screen printing as a scalable and low-cost approach for rigid and flexible thin-film transistors using separated carbon nanotubes". *ACS nano*, 8(12), 12769-12776.
- Carotta, M., Cervi, A. d., Di Natale, V., Gherardi, S., Giberti, A., Guidi, V., Puzzovio, B., Vendemiati, G., Martinelli, M., and Sacerdoti, D. (2009). "ZnO gas sensors: a comparison between nanoparticles and nanotetrapods-based thick films". *Sens. Actuators B Chem.*, 137(1), 164-169.

- Cerdà, J., Arbiol, J., Dezanneau, G., Diaz, R., and Morante, J. (2002). "Perovskite-type BaSnO<sub>3</sub> powders for high temperature gas sensor applications". *Sens. Actuators B Chem.*, 84(1), 21-25.
- Chahal, R. P., Mahendia, S., Tomar, A., and Kumar, S. (2010). "Effect of ultraviolet irradiation on the optical and structural characteristics of in situ prepared PVP-Ag nanocomposites". *Dig. J. Nanomater. Biostructures.*, 5, 569-575.
- Chaudhary, P., Singh, P., and Kumar, V. (2018). "Synthesis and characterization of pure ZnO and La-doped ZnO (Zn<sub>0.98</sub>La<sub>0.02</sub>O) films via novel sol-gel screen-printing method". *Optik*, 158, 376-381.
- Chen, A., Huang, X., Tong, Z., Bai, S., Luo, R., and Liu, C. C. (2006). "Preparation, characterization and gas-sensing properties of SnO<sub>2</sub>-In<sub>2</sub>O<sub>3</sub> nanocomposite oxides". *Sens. Actuators B Chem.*, 115(1), 316-321.
- Chen, H.-L., Lu, Y.-M., and Hwang, W.-S. (2005). "Characterization of sputtered NiO thin films". *Surf. Coat. Technol.* 198(1-3), 138-142.
- Chen, X., Deng, N., Zhang, X., Yang, Y., Li, J., Hong, B., and Peng, X. (2019). "Preparation of Fe-doped In<sub>2</sub>O<sub>3</sub> gas sensing semiconductor by one-step impregnation with enhanced ethanol sensing". *Chem. Phys. Lett.*, 722, 96-103.
- Choi, E., Lee, S., and Piao, Y. (2015). "A solventless mix-bake-wash approach to the facile controlled synthesis of core-shell and alloy Ag-Cu bimetallic nanoparticles". *CrystEngComm*, 17(31), 5940-5946.
- Choudhury, B., Chetri, P., and Choudhury, A. (2015). "Annealing temperature and oxygen-vacancy-dependent variation of lattice strain, band gap and luminescence properties of CeO<sub>2</sub> nanoparticles". *J. Exp. Nanosci.*, 10(2), 103-114.
- Chu, D. H., Vinoba, M., Bhagiyalakshmi, M., Baek, I. H., Nam, S. C., Yoon, Y., and Jeong, S. K. (2013). "CO<sub>2</sub> mineralization into different polymorphs of CaCO<sub>3</sub> using an aqueous-CO<sub>2</sub> system". *RSC Advances*, 3(44), 21722-21729.
- Cui, J., Shi, L., Xie, T., Wang, D., and Lin, Y. (2016). "UV-light illumination room temperature HCHO gas-sensing mechanism of ZnO with different nanostructures". *Sens. Actuators B Chem.*, 227, 220-226.

- Cui, Z. (2016). *Printed electronics: Materials, technologies and applications*: John Wiley & Sons.
- Cullity, B. D., and Stock, S. R. (2014). *Elements of X-ray Diffraction*: Pearson Education.
- Nath, D., Singh, F., and Das, R (2020). "X-ray diffraction analysis by Williamson-Hall, Halder-Wagner and size-strain plot methods of CdSe nanoparticles-a comparative study". *Mater. Chem. Phys.*, 239, 122021.
- de Lacy Costello, B., Ewen, R., Jones, P., Ratcliffe, N., and Wat, R. (1999). "A study of the catalytic and vapour-sensing properties of zinc oxide and tin dioxide in relation to 1-butanol and dimethyldisulphide". *Sens. Actuators B Chem.*, 61(1-3), 199-207.
- Deepa, A., Vidya, S., Manu, P., Solomon, S., John, A., and Thomas, J. (2011). "Structural and optical characterization of BaSnO<sub>3</sub> nanopowder synthesized through a novel combustion technique". *J. Alloys Compd.*, 509(5), 1830-1835.
- Deepa, S., Kumari, K. P., and Thomas, B. (2017). "Contribution of oxygen-vacancy defect-types in enhanced CO<sub>2</sub> sensing of nanoparticulate Zn-doped SnO<sub>2</sub> films". *Ceram. Int.*, 43(18), 17128-17141.
- Deganello, F., and Tyagi, A. K. (2018). "Solution combustion synthesis, energy and environment: Best parameters for better materials". *Prog. Cryst. Growth Charact. Mater.*, 64(2), 23-61.
- Deo, G., Hardcastle, F., Richards, M., Hirt, A., and Wachs, I. E. (1990). "Raman spectroscopy of vanadium oxide supported on alumina". *Novel materials in heterogeneous catalysis*, 437, 317.
- Dev, S., Kumar, P., Rani, A., Agarwal, A., and Dhar, R. (2020). "Development of indium doped ZnO thin films for highly sensitive acetylene (C<sub>2</sub>H<sub>2</sub>) gas sensing". *Superlattices Microstruct.*, 145, 106638.
- Dey, A. (2018). "Semiconductor metal oxide gas sensors: A review". *Mater Sci Eng B Solid State Mater Adv Technol.*, 229, 206-217.
- Do, J.-S., Yu, S.-H., and Cheng, S.-F. (2003). "Thick-film nickel–metal-hydride battery based on porous ceramic substrates". *J. Power Sources.*, 117(1-2), 203-211.

- Doroshenko, I., Pogorelov, V., and Sablinskas, V. (2013). "Infrared absorption spectra of monohydric alcohols". *Dataset Papers in Science*, 2013.
- Ducamp-Sanguesa, C., Herrera-Urbina, R., and Figlarz, M. (1992). "Synthesis and characterization of fine and monodisperse silver particles of uniform shape". *J. Solid State Chem.*, 100(2), 272-280.
- Dudric, R., Vladescu, A., Rednic, V., Neumann, M., Deac, I., and Tetean, R. (2014). "XPS study on  $\text{La}_{0.67}\text{Ca}_{0.33}\text{Mn}_{1-x}\text{Co}_x\text{O}_3$  compounds". *J. Mol. Struct.*, 1073, 66-70.
- Durairaj, R., Mallik, S., Seman, A., Marks, A., and Ekere, N. (2009). "Rheological characterisation of solder pastes and isotropic conductive adhesives used for flip-chip assembly". *J. Mater. Process. Technol.*, 209(8), 3923-3930.
- Durairaj, R., Ramesh, S., Mallik, S., Seman, A., and Ekere, N. (2009). "Rheological characterisation and printing performance of Sn/Ag/Cu solder pastes". *Mater. Des.*, 30(9), 3812-3818.
- Durairaj, R., Seman, A., and Ekere, N. (2006). "Development of quality control (QC) tools for solder pastes used for flip chip assembly based on oscillatory tests". Paper presented at the 2006 1<sup>st</sup> Electronic Systemintegration Technology Conference.
- El-Sheikh, M., El-Rafie, S., Abdel-Halim, E., and El-Rafie, M. (2013). "Green synthesis of hydroxyethyl cellulose-stabilized silver nanoparticles". *J. Polym.*,
- El Fawal, G. F., Abu-Serie, M. M., Hassan, M. A., and Elnouby, M. S. (2018). "Hydroxyethyl cellulose hydrogel for wound dressing: Fabrication, characterization and in vitro evaluation". *Int. J. Biol. Macromol.*, 111, 649-659.
- Eranna, G., Joshi, B., Runthala, D., and Gupta, R. (2004). "Oxide materials for development of integrated gas sensors—a comprehensive review". *Crit. Rev. Solid State Mater. Sci.*, 29(3-4), 111-188.
- Faddoul, R., Reverdy-Bruas, N., and Blayo, A. (2012). "Formulation and screen printing of water based conductive flake silver pastes onto green ceramic tapes for electronic applications". *Mater Sci Eng B Solid State Mater Adv Technol.*, 177(13), 1053-1066.

- Faddoul, R., Reverdy-Bruas, N., and Bourel, J. (2012). "Silver content effect on rheological and electrical properties of silver pastes. *J. Mater. Sci.: Mater.*", 23(7), 1415-1426.
- Fereshteh, Z., Rojaee, R., and Sharifnabi, A. (2016). "Effect of different polymers on morphology and particle size of silver nanoparticles synthesized by modified polyol method". *Superlattices Microstruct.*, 98, 267-275.
- Ferrando, R., Jellinek, J., and Johnston, R. L. (2008). "Nanoalloys: from theory to applications of alloy clusters and nanoparticles". *Chem. Rev.*, 108(3), 845-910.
- Fievet, F., Fievet-Vincent, F., Lagier, J.-P., Dumont, B., and Figlarz, M. (1993). "Controlled nucleation and growth of micrometre-size copper particles prepared by the polyol process". *J. Mater. Chem.*, 3(6), 627-632.
- Fortunato, G., Oswald, H., and Reller, A. (2001). "Spinel-type oxide catalysts for low temperature CO oxidation generated by use of an ultrasonic aerosol pyrolysis process". *J. Mater. Chem.*, 11(3), 905-911.
- Frederickson, L., and Hausen, D. (1963). "Infrared Spectra-Structure Correlation Study of Vanadium-Oxygen Compounds". *Anal. Chem.*, 35(7), 818-827.
- Fukushima, A., Iga, F., Inoue, I. H., Murata, K., and Nishihara, Y. (1994). "Annealing effects on transport and magnetic properties of perovskite-type vanadium oxide  $\text{CaVO}_3$ ". *J. Phys. Soc. Jpn.*, 63(2), 409-412.
- Gallo Stampino, P., Omati, L., Cristiani, C., and Dotelli, G. (2010). "Characterisation of Nanocarbon-Based Gas Diffusion Media by Electrochemical Impedance Spectroscopy". *Fuel Cells.*, 10(2), 270-277.
- Ganesh, R. S., Durgadevi, E., Navaneethan, M., Patil, V., Ponnusamy, S., Muthamizhchelvan, C., and Hayakawa, Y. (2018). "Tuning the selectivity of  $\text{NH}_3$  gas sensing response using Cu-doped ZnO nanostructures". *Sens. Actuator A Phys.*, 269, 331-341.
- Garcia-Jaca, J., Larramendi, J. I. R., Insausti, M., Arriortua, M. I., and Rojo, T. (1995). "Synthesis, crystal structure and transport properties of a new non-stoichiometric  $\text{CaVO}_{3+\delta}$  phase". *J. Mater. Chem.*, 5(11).

- Girija, K., Somasundaram, K., Debnath, A., Topkar, A., and Vatsa, R. (2018). "Enhanced H<sub>2</sub>S sensing properties of Gallium doped ZnO nanocrystalline films as investigated by DC conductivity and impedance spectroscopy". *Mater. Chem. Phys.*, 214, 297-305.
- Goldberg, H. D., Brown, R. B., Liu, D. P., and Meyerhoff, M. E. (1994). "Screen printing: a technology for the batch fabrication of integrated chemical-sensor arrays". *Sens. Actuators B Chem.*, 21(3), 171-183.
- Gu, J., and Yan, B. (2009). "Hydrothermal synthesis and luminescent properties of Ca<sub>2</sub>V<sub>2</sub>O<sub>7</sub>: Eu<sup>3+</sup> phosphors". *J. Alloys Compd.*, 476(1-2), 619-623.
- Gu, X., Xu, L., Tian, F., and Ding, Y. (2009). "Au-Ag alloy nanoporous nanotubes". *Nano Res.*, 2(5), 386-393.
- Guo, J., and Peng, C. (2015). "Synthesis of ZnO nanoparticles with a novel combustion method and their C<sub>2</sub>H<sub>5</sub>OH gas sensing properties". *Ceram. Int.*, 41(2), 2180-2186.
- Gupta, B., Pujar, P., Mal, S. S., Gupta, D., and Mandal, S. (2018). "Retention of high dielectric constant sodium beta alumina via solution combustion: Role of aluminum ions complexation with fuel". *Ceram. Int.*, 44(2), 1500-1511.
- Hamedani, N. F., Mahjoub, A. R., and Mortazavi, Y. (2012). "CeO<sub>2</sub> doped ZnO flower-like nanostructure sensor selective to ethanol in presence of CO and CH<sub>4</sub>". *Sens. Actuators B Chem.*, 169, 67-73.
- Hashimoto, A., Yasuho, T., Hayama, M., and Miura, K. (2002). Conductive paste. In: Google Patents.
- Haverinen, H. M., Myllylä, R. A., and Jabbour, G. E. (2010). "Inkjet printed RGB quantum dot-hybrid LED". *Journal of display technology.*, 6(3), 87-89.
- Henglein, A. (1993). "Physicochemical properties of small metal particles in solution: "microelectrode" reactions, chemisorption, composite metal particles, and the atom-to-metal transition". *J. Phys. Chem.*, 97, 5457-5471.
- Heinze, T., and Pfeiffer, K. (1999). "Studies on the synthesis and characterization of carboxymethylcellulose". *Die Angewandte Makromolekulare Chemie.*, 266(1), 37-45.

- Hirsimäki, M., Lampimäki, M., Lahtonen, K., Chorkendorff, I., and Valden, M. (2005). "Investigation of the role of oxygen induced segregation of Cu during Cu<sub>2</sub>O formation on Cu {1 0 0}, Ag/Cu {1 0 0} and Cu (Ag) alloy". *Surf. Sci.*, 583(2-3), 157-165.
- Hornyak, G. L., Dutta, J., Tibbals, H. F., and Rao, A. (2008). *Introduction to nanoscience*: CRC press.
- Hosseini, Z., and Mortezaali, A. (2015). "Room temperature H<sub>2</sub>S gas sensor based on rather aligned ZnO nanorods with flower-like structures". *Sens. Actuators B Chem.*, 207, 865-871.
- Hu, J., Wang, T., Wang, Y., Huang, D., He, G., Han, Y., and Zhang, Y. (2018). "Enhanced formaldehyde detection based on Ni doping of SnO<sub>2</sub> nanoparticles by one-step synthesis". *Sens. Actuators B Chem.*, 263, 120-128.
- Huang, C., Wang, X., Wang, X., Liu, X., Shi, Q., Pan, X., and Li, X. (2016). "Preparation of BaSnO<sub>3</sub> and Ba<sub>0.96</sub>La<sub>0.04</sub>SnO<sub>3</sub> by reactive core-shell precursor: formation process, CO sensitivity, electronic and optical properties analysis". *RSC Adv.*, 6(30), 25379-25387.
- Huang, Y.-F., Huang, K.-M., and Chang, H.-T. (2006). "Synthesis and characterization of Au core-Au-Ag shell nanoparticles from gold seeds: impacts of glycine concentration and pH". *J. Colloid Interface Sci.*, 301(1), 145-154.
- Hyun, W. J., Lim, S., Ahn, B. Y., Lewis, J. A., Frisbie, C. D., and Francis, L. F. (2015). "Screen printing of highly loaded silver inks on plastic substrates using silicon stencils". *ACS Appl. Mater. Interfaces.*, 7(23), 12619-12624.
- Ibupoto, Z. H., Khun, K., Beni, V., Liu, X., and Willander, M. (2013). "Synthesis of novel CuO nanosheets and their non-enzymatic glucose sensing applications". *Sensors*, 13(6), 7926-7938.
- Iriondo, A., Guemez, M., Requies, J., Barrio, V., Cambra, J., Arias, P., and Fierro, J. (2010). "Butyraldehyde production by butanol oxidation over Ru and Cu catalysts supported on ZrO<sub>2</sub>, TiO<sub>2</sub> and CeO<sub>2</sub>". *Stud Surf Sci Catal.*, 175, 453-456.

Ito, M., Miyazaki, C., Ishizaki, M., Kon, M., Ikeda, N., Okubo, T., and Sekine, N. (2008). "Application of amorphous oxide TFT to electrophoretic display". *J. Non-Cryst. Solids.*, 354(19-25), 2777-2782.

Izdebska-Podsiadły, J., and Thomas, S. (2015). *Printing on polymers: fundamentals and applications*: William Andrew.

Izu, N., Shin, W., Matsubara, I., and Murayama, N. (2003). "The effects of the particle size and crystallite size on the response time for resistive oxygen gas sensor using cerium oxide thick film". *Sens. Actuators B Chem.*, 94(2), 222-227.

Izumi, F., and Ikeda, T. (2015). Implementation of the Williamson-Hall and Halder-Wagner Methods into RIETAN-FP.

Jiang, H., Moon, K., and Wong, C. (2005). "Synthesis of Ag-Cu alloy nanoparticles for lead-free interconnect materials". *International Symposium on Advanced Packaging Materials: Processes, Properties and Interfaces*, 2005.

Jiang, Z., Zhao, R., Sun, B., Nie, G., Ji, H., Lei, J., and Wang, C. (2016). "Highly sensitive acetone sensor based on Eu-doped SnO<sub>2</sub> electrospun nanofibers". *Ceram. Int.*, 42(14), 15881-15888.

Joseph, A. M., Nagendra, B., Bhoje Gowd, E., and Surendran, K. P. (2016). "Screen-printable electronic ink of ultrathin boron nitride nanosheets". *Acs Omega*, 1(6), 1220-1228.

Ju, D., Xu, H., Xu, Q., Gong, H., Qiu, Z., Guo, J., and Cao, B. (2015). "High triethylamine-sensing properties of NiO/SnO<sub>2</sub> hollow sphere P-N heterojunction sensors". *Sens. Actuators B Chem.*, 215, 39-44.

Kamata, K., Sugahara, K., Kato, Y., Muratsugu, S., Kumagai, Y., Oba, F., and Hara, M. (2018). "Heterogeneously Catalyzed Aerobic Oxidation of Sulfides with a BaRuO<sub>3</sub> Nanoperovskite". *ACS Appl. Mater. Interfaces.*, 10(28), 23792-23801.

Karaguzel, B., Merritt, C., Kang, T., Wilson, J., Nagle, H., Grant, E., and Pourdeyhimi, B. (2009). "Flexible, durable printed electrical circuits". *J. Text. Inst.*, 100(1), 1-9.



- Karthik, T. V. K., Olvera, M. D. I. L., Maldonado, A., and Gomez Pozos, H. (2016). "CO Gas sensing properties of pure and Cu-incorporated SnO<sub>2</sub> nanoparticles: A study of Cu-induced modifications". *Sensors*, 16(8), 1283.
- Katoch, A., Sun, G.-J., Choi, S.-W., Byun, J.-H., and Kim, S. S. (2013). "Competitive influence of grain size and crystallinity on gas sensing performances of ZnO nanofibers". *Sens. Actuators B Chem.*, 185, 411-416.
- Kell, A. J., Paquet, C., Mozenon, O., Djavani-Tabrizi, I., Deore, B., Liu, X., and Shaker, J. (2017). "Versatile molecular silver ink platform for printed flexible electronics". *ACS Appl. Mater. Interfaces.*, 9(20), 17226-17237.
- Khan, S., Lorenzelli, L., and Dahiya, R. S. (2014). "Technologies for printing sensors and electronics over large flexible substrates: a review". *IEEE Sens. J.*, 15(6), 3164-3185.
- Kim, M.-G., Kanatzidis, M. G., Facchetti, A., and Marks, T. J. (2011). "Low-temperature fabrication of high-performance metal oxide thin-film electronics via combustion processing". *Nat. Mater.*, 10(5), 382-388.
- Kind, C., Weber, A., and Feldmann, C. (2012). "Easy access to Cu<sup>0</sup> nanoparticles and porous copper electrodes with high oxidation stability and high conductivity". *J. Mater. Chem.*, 22(3), 987-993.
- Korotcenkov, G. (2007). Metal oxides for solid-state gas sensors: "What determines our choice? ". *Mater Sci Eng B Solid State Mater Adv Technol.*, 139(1), 1-23.
- Korotcenkov, G. (2008). "The role of morphology and crystallographic structure of metal oxides in response of conductometric-type gas sensors". *Mater. Sci. Eng. R Rep.*, 61(1-6), 1-39.
- Korotcenkov, G., Brinzari, V., Cerneavschi, A., Ivanov, M., Cornet, A., Morante, J., and Arbiol, J. (2004). "In<sub>2</sub>O<sub>3</sub> films deposited by spray pyrolysis: gas response to reducing (CO, H<sub>2</sub>) gases". *Sens. Actuators B Chem.*, 98(2-3), 122-129.
- Korotcenkov, G., Brinzari, V., Cerneavschi, A., Ivanov, M., Golovanov, V., Cornet, A., and Arbiol, J. (2004). "The influence of film structure on In<sub>2</sub>O<sub>3</sub> gas response". *Thin Solid Films.*, 460(1-2), 315-323.

- Kou, X., Wang, C., Ding, M., Feng, C., Li, X., Ma, J., and Lu, G. (2016). "Synthesis of Co-doped SnO<sub>2</sub> nanofibers and their enhanced gas-sensing properties". *Sens. Actuators B Chem.*, 236, 425-432.
- Kou, X., Xie, N., Chen, F., Wang, T., Guo, L., Wang, C., and Zhang, H. (2018). "Superior acetone gas sensor based on electrospun SnO<sub>2</sub> nanofibers by Rh doping". *Sens. Actuators B Chem.*, 256, 861-869.
- Krebs, F. C., Jørgensen, M., Norrman, K., Hagemann, O., Alstrup, J., Nielsen, T. D., and Kristensen, J. (2009). "A complete process for production of flexible large area polymer solar cells entirely using screen printing—first public demonstration". *Sol. Energy Mater. Sol. Cells.*, 93(4), 422-441.
- Kulandaisamy, A. J., Reddy, J. R., Srinivasan, P., Babu, K. J., Mani, G. K., Shankar, P., and Rayappan, J. B. B. (2016). "Room temperature ammonia sensing properties of ZnO thin films grown by spray pyrolysis: Effect of Mg doping". *J. Alloys Compd.*, 688, 422-429.
- Kumar, R. A., Vizhi, R. E., Sivakumar, N., Vijayan, N., and Babu, D. R. (2012). "Crystal growth, optical and thermal studies of nonlinear optical  $\gamma$ -glycine single crystal grown from lithium nitrate". *Optik*, 123(5), 409-413.
- Kunnari, E., Valkama, J., Keskinen, M., and Mansikkamäki, P. (2009). "Environmental evaluation of new technology: printed electronics case study". *J. Clean. Prod.*, 17(9), 791-799.
- Lahti, M., and Lantto, V. (2001). "Passive RF band-pass filters in an LTCC module made by fine-line thick-film pastes". *J. Eur. Ceram. Soc.*, 21(10-11), 1997-2000.
- Lee, E.-J., Kim, Y.-H., Hwang, D. K., Choi, W. K., and Kim, J.-Y. (2016). "Synthesis and optoelectronic characteristics of 20 nm diameter silver nanowires for highly transparent electrode films". *RSC Adv.*, 6(14), 11702-11710.
- Lemay, G., Kaliaguine, S., Adnot, A., Nahar, S., Cozak, D., and Monnier, J. (1986). "Synthesis of some ring-substituted ruthenocenes and their use in the preparation of Ru/ZSM-5 catalysts". *Can. J. Chem.*, 64(9), 1943-1948.

- Lhoest, J.-B., Bertrand, P., Weng, L., and Dewez, J.-L. (1995). "Combined time-of-flight secondary ion mass spectrometry and X-ray photoelectron spectroscopy study of the surface segregation of poly (methyl methacrylate)(PMMA) in bisphenol A polycarbonate/PMMA blends". *Macromolecules.*, 28(13), 4631-4637.
- Li, C., Shuford, K. L., Chen, M., Lee, E. J., and Cho, S. O. (2008). "A facile polyol route to uniform gold octahedra with tailorable size and their optical properties". *ACS nano*, 2(9), 1760-1769.
- Li, J., Mayer, J., and Colgan, E. (1991). "Oxidation and protection in copper and copper alloy thin films". *J. Appl. Phys.*, 70(5), 2820-2827.
- Li, X. G., Huang, M. R., and Bai, H. (1999). "Thermal decomposition of cellulose ethers". *J. Appl. Polym. Sci.*, 73(14), 2927-2936.
- Lian, X., Li, Y., Tong, X., Zou, Y., Liu, X., An, D., and Wang, Q. (2017). "Synthesis of Ce-doped SnO<sub>2</sub> nanoparticles and their acetone gas sensing properties". *Appl. Surf. Sci.*, 407, 447-455
- Liang, J., Tong, K., and Pei, Q. (2016). "A water-based silver-nanowire screen-print ink for the fabrication of stretchable conductors and wearable thin-film transistors". *Adv. Mater.*, 28(28), 5986-5996.
- Liang, T.-X., Sun, W., Wang, L.-D., Wang, Y., and Li, H.-D. (1996). "Effect of surface energies on screen printing resolution". *IEEE Trans Compon Packaging Manuf Technol.*, 19(2), 423-426.
- Liangyuan, C., Shouli, B., Guojun, Z., Dianqing, L., Aifan, C., and Liu, C. C. (2008). "Synthesis of ZnO–SnO<sub>2</sub> nanocomposites by microemulsion and sensing properties for NO<sub>2</sub>". *Sens. Actuators B Chem.*, 134(2), 360-366.
- Liao, J., Yang, C., Tian, Z., Yang, H., and Jin, L. (2006). "The influence of post-annealing on the chemical structures and dielectric properties of the surface layer of Ba<sub>0.6</sub>Sr<sub>0.4</sub>TiO<sub>3</sub> films". *J. Phys. D: Appl. Phys.*, 39(11), 2473.
- Lim, S. C., Kim, S. H., Yang, Y. S., Lee, M. Y., Nam, S. Y., and Ko, J. B. (2009). "Organic thin-film transistor using high-resolution screen-printed electrodes". *Jpn. J. Appl. Phys.*, 48(8R), 081503.

- Lin, H.-W., Chang, C.-P., Hwu, W.-H., and Ger, M.-D. (2008). "The rheological behaviors of screen-printing pastes". *J. Mater. Process. Technol.*, 197(1-3), 284-291.
- Linde, R. K. (1966). "Lattice Parameters of Metastable Silver-Copper Alloys". *J. Appl. Phys.*, 37(2), 934-934.
- Liu, A., Zhu, H., Sun, H., Xu, Y., and Noh, Y.Y. (2018). "Solution processed metal oxide high- $\kappa$  dielectrics for emerging transistors and circuits". *Adv. Mater.*, 30(33), 1706364.
- Liu, C., Kuang, Q., Xie, Z., and Zheng, L. (2015). "The effect of noble metal (Au, Pd and Pt) nanoparticles on the gas sensing performance of SnO<sub>2</sub>-based sensors: a case study on the {221} high-index faceted SnO<sub>2</sub> octahedra". *CrystEngComm.*, 17(33), 6308-6313.
- Liu, J., Jiang, M., and Zeng, X. (2013). "Electrical conductivity of thick films made from silver methylcarbamate paste". *J. Electron. Mater.*, 42(10), 2990-2997.
- Liu, L., Shen, Z., Zhang, X., and Ma, H. (2021). "Highly conductive graphene/carbon black screen printing inks for flexible electronics". *J. Colloid Interface Sci.*, 582, 12-21.
- Liu, Y., Liu, J., Li, Y., Wang, D., Ren, L., and Zou, K. (2016). "Effect of annealing temperature on the structure and properties of vanadium oxide films". *Opt. Mater. Express.*, 6(5), 1552-1560.
- Liu, Z., Tian, S., Yang, J., Liu, H., Liu, X., Jia, H., and Xu, B. (2016). "Sulfur ion-induced shape evolution of Ag nanocrystals by microwave-assisted polyol process". *Mater. Lett.*, 164, 647-650.
- Lupan, O., Postica, V., Hoppe, M., Wolff, N., Polonskyi, O., Pauporté, T., and Faupel, F. (2018). "PdO/PdO<sub>2</sub> functionalized ZnO: Pd films for lower operating temperature H<sub>2</sub> gas sensing". *Nanoscale.*, 10(29), 14107-14127.
- Lupan, O., Ursaki, V., Chai, G., Chow, L., Emelchenko, G., Tiginyanu, I., and Redkin, A. (2010). "Selective hydrogen gas nanosensor using individual ZnO nanowire with fast response at room temperature". *Sens. Actuators B Chem.*, 144(1), 56-66.

- Lupo, D., Clemens, W., Breitung, S., and Hecker, K. (2013). "OE-A roadmap for organic and printed electronics". In *Applications of Organic and Printed Electronics* (pp. 1-26): Springer.
- Ma, G., Li, J., Feng, K., Zhang, B., and Zhang, S. (2019). "Ultrafast methanol sensing properties of nano-spindle like  $\text{In}_2\text{O}_3$  hierarchical structures with oxygen vacancies". *Ceram. Int.*, 45(6), 7295-7301.
- Ma, Z.-H., Yu, R.-T., and Song, J.-M. (2020). "Facile synthesis of Pr-doped  $\text{In}_2\text{O}_3$  nanoparticles and their high gas sensing performance for ethanol". *Sens. Actuators B Chem.*, 305, 127377.
- Machado, G. S., Arízaga, G. G., Wypych, F., and Nakagaki, S. (2010). "Immobilization of anionic metalloporphyrins on zinc hydroxide nitrate and study of an unusual catalytic activity". *J. Catal.*, 274(2), 130-141.
- Mani, G. K., and Rayappan, J. B. B. (2016). "ZnO nanoarchitectures: ultrahigh sensitive room temperature acetaldehyde sensor". *Sens. Actuators B Chem.*, 223, 343-351.
- Mbarek, H., Saadoun, M., and Bessaïs, B. (2006). "Screen-printed Tin-doped indium oxide (ITO) films for  $\text{NH}_3$  gas sensing". *Mater. Sci. Eng. C.*, 26(2-3), 500-504.
- Meti, S., Rahman, M.R., Ahmad, I., and Bhat, K.U. (2018). "Chemical free synthesis of graphene oxide in the preparation of reduced graphene oxide-zinc oxide nanocomposite with improved photocatalytic properties". *Appl. Surf. Sci.*, 451, 67-75.
- Merilampi, S., Laine-Ma, T., and Ruuskanen, P. (2009). "The characterization of electrically conductive silver ink patterns on flexible substrates". *Microelectron Reliab.*, 49(7), 782-790.
- Michel, B., Bernard, A., Bietsch, A., Delamarche, E., Geissler, M., Juncker, D., and Schmid, H. (2001). "Printing meets lithography: Soft approaches to high-resolution patterning". *IBM J Res Dev.*, 45(5), 697-719.
- Miller, D. R., Akbar, S. A., and Morris, P. A. (2014). "Nanoscale metal oxide-based heterojunctions for gas sensing: a review". *Sens. Actuators B Chem.*, 204, 250-272.
- Mizsei, J. (1995). "How can sensitive and selective semiconductor gas sensors be made?" *Sens. Actuators B Chem.*, 23(2-3), 173-176.

Mohamed, S. H. (2011). "Synthesis, structural and ellipsometric evaluation of oxygen-deficient and nearly stoichiometric zinc oxide and indium oxide nanowires/nanoparticles". *Philos. Mag. Lett.*, 91(27), 3598-3612.

Montazeri, A., and Jamali-Sheini, F. (2017). "Enhanced ethanol gas-sensing performance of Pb-doped In<sub>2</sub>O<sub>3</sub> nanostructures prepared by sonochemical method". *Sens. Actuators B Chem.*, 242, 778-791.

Mote, V., Purushotham, Y., and Dole, B. (2012). "Williamson-Hall analysis in estimation of lattice strain in nanometer-sized ZnO particles". *Int. J. Theor. Phys.*, 6(1), 6.

Mücke, R., Büchler, O., Menzler, N., Lindl, B., Vaßen, R., and Buchkremer, H. (2014). "High-precision green densities of thick films and their correlation with powder, ink, and film properties". *J. Eur. Ceram. Soc.*, 34(15), 3897-3916.

Muruganandam, S., Anbalagan, G., and Murugadoss, G. (2017). "Structural, electrochemical and magnetic properties of codoped (Cu, Mn) CdS nanoparticles with surfactant PVP". *Optik (Stuttg.)*, 131, 826-837.

Na, C. W., Woo, H.-S., Kim, I.-D., and Lee, J.-H. (2011). "Selective detection of NO<sub>2</sub> and C<sub>2</sub>H<sub>5</sub>OH using a Co<sub>3</sub>O<sub>4</sub>-decorated ZnO nanowire network sensor". *ChemComm.*, 47(18), 5148-5150.

Nadargi, D. Y., Dateer, R. B., Tamboli, M. S., Mulla, I. S., and Suryavanshi, S. S. (2019). "A greener approach towards the development of graphene–Ag loaded ZnO nanocomposites for acetone sensing applications". *RSC Adv.*, 9(58), 33602-33606.

Nalawade, P., Mukherjee, T., and Kapoor, S. (2012). "High-yield synthesis of multispiked gold nanoparticles: Characterization and catalytic reactions". *Colloids Surf. A Physicochem. Eng. Asp.*, 396, 336-340.

Navaneethan, M., Mani, G. K., Ponnusamy, S., Tsuchiya, K., Muthamizhchelvan, C., Kawasaki, S., and Hayakawa, Y. (2017). "Influence of Al doping on the structural, morphological, optical, and gas sensing properties of ZnO nanorods". *J. Alloys Compd.*, 698, 555-564.

- Naveen, C., Dinesha, M., and Jayanna, H. (2013). "Effect of fuel to oxidant molar ratio on structural and DC electrical conductivity of ZnO nanoparticles prepared by simple solution combustion method". *J Mater Sci Technol.*, 29(10), 898-902.
- Ni, Y.-h., Wei, X.-w., Hong, J.-m., and Ye, Y. (2005). "Hydrothermal preparation and optical properties of ZnO nanorods". *Mater Sci Eng B Solid State Mater Adv Technol.*, 121(1-2), 42-47.
- Niknafs, Y., Amirjani, A., Marashi, P., and Fatmehsari, D. H. (2017). "Synthesis of Ag-Cu and Ag-Cu<sub>2</sub>O alloy nanoparticles using a seed-mediated polyol process, thermodynamic and kinetic aspects". *Mater. Chem. Phys.*, 189, 44-49.
- Nithya, N., Bhoopathi, G., Magesh, G., and Balasundaram, O. (2019). "Synthesis and characterization of yttrium doped titania nanoparticles for gas sensing activity". *Mater Sci Semicond Process.*, 99, 14-22.
- Ogawa, H., Nishikawa, M., and Abe, A. (1982). "Hall measurement studies and an electrical conduction model of tin oxide ultrafine particle films". *J. Appl. Phys.*, 53(6), 4448-4455.
- Paint, A. C. D.-o., Related Coatings, M., and Applications. (2009). *Standard Test Methods for Measuring Adhesion by Tape Test*: ASTM International.
- Pan, J., Tonkay, G. L., and Quintero, A. (1999). "Screen printing process design of experiments for fine line printing of thick film ceramic substrates". *Journal of Electronics Manufacturing*, 9(03), 203-213.
- Pan, X., Ren, G., Hoque, M. N. F., Bayne, S., Zhu, K., and Fan, Z. (2014). "Fast supercapacitors based on graphene-bridged V<sub>2</sub>O<sub>3</sub>/VO<sub>x</sub> core-shell nanostructure electrodes with a power density of 1 MW kg<sup>-1</sup>". *Adv. Mater. Interfaces.*, 1(9), 1400398.
- Pang, Z., Fu, J., Luo, L., Huang, F., and Wei, Q. (2014). "Fabrication of PA6/TiO<sub>2</sub>/PANI composite nanofibers by electrospinning-electrospraying for ammonia sensor". *Colloids Surf. A Physicochem.*, 461, 113-118.
- Parashkov, R., Becker, E., Riedl, T., Johannes, H.-H., and Kowalsky, W. (2005). "Large area electronics using printing methods". *Proc IEEE Inst Electr Electron Eng.*, 93(7), 1321-1329.

- Park, B. K., Jeong, S., Kim, D., Moon, J., Lim, S., and Kim, J. S. (2007). "Synthesis and size control of monodisperse copper nanoparticles by polyol method". *J. Colloid Interface Sci.*, 311(2), 417-424.
- Park, K., Seo, D., and Lee, J. (2008). "Conductivity of silver paste prepared from nanoparticles". *Colloids Surf. A Physicochem.*, 313, 351-354.
- Park, S.-S., and Mackenzie, J. (1996). "Thickness and microstructure effects on alcohol sensing of tin oxide thin films". *Thin Solid Films.*, 274(1-2), 154-159.
- Parra, M. R., and Haque, F. Z. (2014). "Aqueous chemical route synthesis and the effect of calcination temperature on the structural and optical properties of ZnO nanoparticles". *J. Mater. Res.*, 3(4), 363-369.
- Patel, M., Chavda, A., Mukhopadhyay, I., Kim, J., and Ray, A. (2016). "Nanostructured SnS with inherent anisotropic optical properties for high photoactivity". *Nanoscale.*, 8(4), 2293-2303.
- Pathak, T. K., Kumar, A., Swart, C., Swart, H., and Kroon, R. (2016). "Effect of fuel content on luminescence and antibacterial properties of zinc oxide nanocrystalline powders synthesized by the combustion method". *RSC Adv.*, 6(100), 97770-97782.
- Patil, D., and Patil, L. (2007). "Room temperature chlorine gas sensing using surface modified ZnO thick film resistors". *Sens. Actuators B Chem.*, 123(1), 546-553.
- Patil, D., and Patil, L. (2009). "Cr<sub>2</sub>O<sub>3</sub>-modified ZnO thick film resistors as LPG sensors". *Talanta*, 77(4), 1409-1414.
- Patil, D., Patil, L., and Amalnerkar, D. (2007). "Ethanol gas sensing properties of Al<sub>2</sub>O<sub>3</sub>-doped ZnO thick film resistors". *Bull. Mater. Sci.*, 30(6), 553-559.
- Patil, D., Patil, L., Jain, G., Wagh, M., and Patil, S. (2006). "Surface activated ZnO thick film resistors for LPG gas sensing". *Sens. Transducers.*, 74(12), 874-883.
- Peng, S., Wang, Z., Liu, R., Bi, J., and Wu, J. (2019). "Controlled oxygen vacancies of ZnFe<sub>2</sub>O<sub>4</sub> with superior gas sensing properties prepared via a facile one-step self-catalyzed treatment". *Sens. Actuators B Chem.*, 288, 649-655.



- Phair, J. W., Lundberg, M., and Kaiser, A. (2009). "Leveling and thixotropic characteristics of concentrated zirconia inks for screen-printing". *Rheol. Acta.*, 48(2), 121-133.
- Poloju, M., Jayababu, N., and Reddy, M. R. (2018). "Improved gas sensing performance of Al doped ZnO/CuO nanocomposite based ammonia gas sensor". *Mater Sci Eng B Solid State Mater Adv Technol.*, 227, 61-67.
- Popovic, Z., Stergiou, V., Raptis, Y., Konstantinovic, M., Isobe, M., Ueda, Y., and Moshchalkov, V. (2002). "High-pressure Raman study of  $\text{CaV}_2\text{O}_5$ ". *J. Phys. Condens. Matter.*, 14(32), L583-L589.
- Potti, P. R., and Srivastava, V. C. (2012). "Comparative studies on structural, optical, and textural properties of combustion derived ZnO prepared using various fuels and their photocatalytic activity". *Ind. Eng. Chem. Res.*, 51(23), 7948-7956.
- Pudas, M., Halonen, N., Granat, P., and Vähäkangas, J. (2005). "Gravure printing of conductive particulate polymer inks on flexible substrates". *Prog. Org. Coat.*, 54(4), 310-316.
- Pujar, P., Gupta, D., and Mandal, S. (2019). "High-performance low voltage operation of indium zinc tin oxide thin film transistors using chemically derived sodium  $\beta$ -alumina dielectric". *J. Mater. Sci. Mater. Electron.*, 30(10), 9097-9105.
- Pushpamalar, V., Langford, S. J., Ahmad, M., and Lim, Y. Y. (2006). "Optimization of reaction conditions for preparing carboxymethyl cellulose from sago waste". *Carbohydr. Polym.*, 64(2), 312-318.
- Rahman, L.-u., Qureshi, R., Yasinzai, M. M., and Shah, A. (2012). "Synthesis and spectroscopic characterization of Ag-Cu alloy nanoparticles prepared in various ratios". *C R Chim.*, 15(6), 533-538.
- Rahman, L.-u., Shah, A., Lunsford, S. K., Han, C., Nadagouda, M. N., Sahle-Demessie, E., and Dionysiou, D. D. (2015). "Monitoring of 2-butanone using a Ag-Cu bimetallic alloy nanoscale electrochemical sensor". *RSC Adv.*, 5(55), 44427-44434.

- Raj, K. P., Sadaiyandi, K., Kennedy, A., and Thamizselvi, R. (2016). "Structural, optical, photoluminescence and photocatalytic assessment of Sr-doped ZnO nanoparticles". *Mater. Chem. Phys.*, 183, 24-36.
- Ramakritinan, C., Kaarunya, E., Shankar, S., and Kumaraguru, A. (2013). "Antibacterial effects of Ag, Au and bimetallic (Ag-Au) nanoparticles synthesized from red algae". *Solid State Phenom.*, 201, 211-230.
- Ramyadevi, J., Jeyasubramanian, K., Marikani, A., Rajakumar, G., and Rahuman, A. A. (2012). "Synthesis and antimicrobial activity of copper nanoparticles". *Mater. Lett.*, 71, 114-116.
- Rane, S., Khanna, P., Seth, T., Phatak, G., Amalnerkar, D., and Das, B. (2003). "Firing and processing effects on microstructure of fritted silver thick film electrode materials for solar cells". *Mater. Chem. Phys.*, 82(1), 237-245.
- Rani, M., Rudhzhiah, S., Ahmad, A., and Mohamed, N. (2014). "Biopolymer electrolyte based on derivatives of cellulose from kenaf bast fiber". *Polymers*, 6(9), 2371-2385.
- Rani, M. S. A., Rudhzhiah, S., Ahmad, A., and Mohamed, N. S. (2014). "Biopolymer electrolyte based on derivatives of cellulose from kenaf bast fiber". *Polymers*, 6(9), 2371-2385.
- Rao, G. T., and Rao, D. T. (1999). "Gas sensitivity of ZnO based thick film sensor to NH<sub>3</sub> at room temperature". *Sens. Actuators B Chem.*, 55(2-3), 166-169.
- Ravichandran, K., Santhosam, A. J., and Sridharan, M. (2020). "Effect of tungsten doping on the ammonia vapour sensing ability of ZnO thin films prepared by a cost effective simplified spray technique". *Surf. Interfaces.*, 18, 100412.
- Ravikumar, N., Dilip, R., and Elango, P. (2020). "Gas sensing nature and characterization of Zr doped TiO<sub>2</sub> films prepared by automated nebulizer spray pyrolysis technique". *Optik.*, 206, 164347.
- Renitta, A., and Vijayalakshmi, K. (2016). "Highly sensitive hydrogen safety sensor based on Cr incorporated ZnO nano-whiskers array fabricated on ITO substrate". *Sens. Actuators B Chem.*, 237, 912-923.

- Ried, P., Lorenz, C., Brönstrup, A., Graule, T., Menzler, N. H., Sitte, W., and Holtappels, P. (2008). "Processing of YSZ screen printing pastes and the characterization of the electrolyte layers for anode supported SOFC". *J. Eur. Ceram. Soc.*, 28(9), 1801-1808.
- Rudež, R., Pavlič, J., and Bernik, S. (2015). "Preparation and influence of highly concentrated screen-printing inks on the development and characteristics of thick-film varistors". *J. Eur. Ceram. Soc.*, 35(11), 3013-3023.
- Sahay, P., & Nath, R. (2008). "Al-doped ZnO thin films as methanol sensors". *Sens. Actuators B Chem.*, 134(2), 654-659.
- Salian, A., Pujar, P., and Mandal, S. (2019). "Facile in situ formation of high conductive Ag and Cu<sub>x</sub>O<sub>y</sub> composite films: a role of aqueous spray combustion". *J. Mater. Sci.: Mater. Electron.*, 30(3), 2888-2897.
- Sanson, A., Roncari, E., Boldrini, S., Mangifesta, P., and Doubova, L. (2010). "Eco-friendly screen-printing inks of gadolinia doped ceria". *J Fuel Cell Sci Technol.*, 7(5).
- Sarkar, S., and Das, R. (2017). "PVP capped silver nanocubes assisted removal of glyphosate from water-a photoluminescence study". *J. Hazard. Mater.*, 339, 54-62.
- Sarkar, S., Veluri, P., and Mitra, S. (2014). "Morphology controlled synthesis of layered NH<sub>4</sub>V<sub>4</sub>O<sub>10</sub> and the impact of binder on stable high rate electrochemical performance". *Electrochim. Acta.*, 132, 448-456.
- Schuetz, W. M., and Buhro, W. E. (2013). "Silver chloride as a heterogeneous nucleant for the growth of silver nanowires". *Acs Nano*, 7(5), 3844-3853.
- Schüler, T., Asmus, T., Fritzsche, W., and Möller, R. (2009). "Screen printing as cost-efficient fabrication method for DNA-chips with electrical readout for detection of viral DNA". *Biosens. Bioelectron.*, 24(7), 2077-2084.
- Seo, D., Park, J. C., and Song, H. (2006). "Polyhedral gold nanocrystals with O<sub>h</sub> symmetry: From octahedra to cubes". *J. Am. Chem. Soc.*, 128(46), 14863-14870.
- Seo, D., Yoo, C. I., Chung, I. S., Park, S. M., Ryu, S., and Song, H. (2008). "Shape adjustment between multiply twinned and single-crystalline polyhedral gold

nanocrystals: decahedra, icosahedra, and truncated tetrahedra". *J. Phys. Chem. C.*, 112(7), 2469-2475.

Shan, H., Liu, C., Liu, L., Li, S., Wang, L., Zhang, X., and Chi, X. (2013). "Highly sensitive acetone sensors based on La-doped  $\alpha$ -Fe<sub>2</sub>O<sub>3</sub> nanotubes". *Sens. Actuators B Chem.*, 184, 243-247.

Sharma, M. K., Buchner, R. D., Scharmach, W. J., Papavassiliou, V., and Swihart, M. T. (2013). "Creating conductive copper–silver bimetallic nanostructured coatings using a high temperature reducing jet aerosol reactor". *Aerosol Sci Technol.*, 47(8), 858-866.

Sharma, S., and Spitz, J. (1980). "Hillock formation, hole growth and agglomeration in thin silver films". *Thin Solid Films*, 65(3), 339-350.

Shen, J., Adnot, A., and Kaliaguine, S. (1991). "An ESCA study of the interaction of oxygen with the surface of ruthenium". *Appl. Surf. Sci.*, 51(1-2), 47-60.

Shingange, K., Tshabalala, Z., Ntwaeaborwa, O., Motaung, D., and Mhlongo, G. (2016). "Highly selective NH<sub>3</sub> gas sensor based on Au loaded ZnO nanostructures prepared using microwave-assisted method". *J. Colloid Interface Sci.*, 479, 127-138.

Silversmit, G., Depla, D., Poelman, H., Marin, G. B., and De Gryse, R. (2004). "Determination of the V<sub>2p</sub> XPS binding energies for different vanadium oxidation states (V<sup>5+</sup> to V<sup>0+</sup>)". *J Electron Spectros Relat Phenomena.*, 135(2-3), 167-175.

Singh, G., and Singh, R. C. (2017). "Synthesis and characterization of Gd-doped SnO<sub>2</sub> nanostructures and their enhanced gas sensing properties". *Ceram. Int.*, 43(2), 2350-2360.

Singh, G., and Singh, R. C. (2019). "Highly sensitive gas sensor based on Er-doped SnO<sub>2</sub> nanostructures and its temperature dependent selectivity towards hydrogen and ethanol". *Sens. Actuators B Chem.*, 282, 373-383.

Singh, M., Sinha, I., and Mandal, R. (2009). "Synthesis of nanostructured Ag–Cu alloy ultra-fine particles". *Materials letters*, 63(26), 2243-2245.

Singh, T. B., and Sariciftci, N. S. (2006). "Progress in plastic electronics devices". *Annu. Rev. Mater. Res.*, 36, 199-230.

- Slassi, A. (2015). "Ab initio study of a cubic perovskite: Structural, electronic, optical and electrical properties of native, lanthanum-and antimony-doped barium tin oxide". *Mater Sci Semicond Process.*, 32, 100-106.
- Smitha, S., Nissamudeen, K., Philip, D., and Gopchandran, K. (2008). "Studies on surface plasmon resonance and photoluminescence of silver nanoparticles". *Spectrochim. Acta A Mol. Biomol.*, 71(1), 186-190.
- Sneha, C., Prabukumar, C., Jayalakshmi, M., Bhat, S., and Bhat, K. U. (2017). "Effect of substrate temperature on the characteristics of ZnO films produced by a combination of thermal vapor deposition and oxidation processes". *J. Mater. Sci. Mater. Electron.*, 28(21), 15959-15966.
- Soltabayev, B., Yıldırım, M. A., Ateş, A., and Acar, S. (2019). "The effect of indium doping concentration on structural, morphological and gas sensing properties of IZO thin films deposited SILAR method". *Mater Sci Semicond Process.*, 101, 28-36.
- Somalu, M., Yufit, V., and Brandon, N. (2013). "The effect of solids loading on the screen-printing and properties of nickel/scandia-stabilized-zirconia anodes for solid oxide fuel cells". *Int. J. Hydrog. Energy.*, 38(22), 9500-9510.
- Somalu, M. R., and Brandon, N. P. (2012). "Rheological studies of nickel/scandia-stabilized-zirconia screen printing inks for solid oxide fuel cell anode fabrication". *J. Am. Ceram. Soc.*, 95(4), 1220-1228.
- Somalu, M. R., Muchtar, A., Baboli, M. G., Yufit, V., Shapiro, I. P., Xiao, P., and Brandon, N. P. (2013). "Understanding the relationship between ink rheology and film properties for screen-printed nickel/scandia-stabilized-zirconia anodes". *ECS Trans.*, 57(1), 1321-1330.
- Somalu, M. R., Muchtar, A., Daud, W. R. W., and Brandon, N. P. (2017). "Screen-printing inks for the fabrication of solid oxide fuel cell films: a review". *Renew. Sust. Energ. Rev.*, 75, 426-439.
- Somalu, M. R., Yufit, V., and Brandon, N. (2013). "The effect of solids loading on the screen-printing and properties of nickel/scandia-stabilized-zirconia anodes for solid oxide fuel cells". *Int. J. Hydrog. Energy.*, 38(22), 9500-9510.

Song, C., Li, C., Yin, Y., Xiao, J., Zhang, X., Song, M., and Dong, W. (2015). "Preparation and gas sensing properties of partially broken WO<sub>3</sub> nanotubes". *Vacuum.*, 114, 13-16.

Song, P., Feng, J.-J., Guo, F.-Y., and Wang, A.-J. (2015). "Simple polyol synthesis of porous coral-like palladium–silver alloy nanostructures with enhanced electrocatalytic activity for glycerol oxidation reaction". *J. Mater. Chem.*, 3(31), 15920-15926.

Songping, W. (2007). "Preparation of micron size flake silver powders for conductive thick films". *J. Mater. Sci. Mater. Electron.*, 18(4), 447-452.

Songwattanasin, P., Karaphun, A., Phokha, S., Hunpratub, S., Maensiri, S., Amornkitbamrung, V., and Swatsitang, E. (2019). "Influence of La concentration on structural, morphological, optical and magnetic properties of Sr<sub>1-x</sub>La<sub>x</sub>TiO<sub>3</sub> nanopowders". *Physica B Condens. Matter.*, 571, 213-221.

Sosulnikov, M., and Teterin, Y. A. (1992). "X-ray photoelectron studies of Ca, Sr and Ba and their oxides and carbonates". *J Electron Spectros Relat Phenomena.*, 59(2), 111-126.

Sowade, E., Ramon, E., Mitra, K. Y., Martínez-Domingo, C., Pedró, M., Pallarès, J., and Terés, L. (2016). "All-inkjet-printed thin-film transistors: manufacturing process reliability by root cause analysis". *Sci. Rep.*, 6, 33490.

Sun, G., Chen, H., Li, Y., Chen, Z., Zhang, S., Ma, G., and Wang, X. (2016). "Synthesis and improved gas sensing properties of NiO-decorated SnO<sub>2</sub> microflowers assembled with porous nanorods". *Sens. Actuators B Chem.*, 233, 180-192.

Sun, P., Zhou, X., Wang, C., Wang, B., Xu, X., and Lu, G. (2014). "One-step synthesis and gas sensing properties of hierarchical Cd-doped SnO<sub>2</sub> nanostructures". *Sens. Actuators B Chem.*, 190, 32-39.

Sun, Y., and Xia, Y. (2002). "Shape-controlled synthesis of gold and silver nanoparticles". *science*, 298(5601), 2176-2179.

Takahashi, Y., Kanamori, M., Kondoh, A., Minoura, H., and Ohya, Y. (1994). "Photoconductivity of ultrathin zinc oxide films". *Jpn. J. Appl. Phys.*, 33(12R), 6611.

- Thibert, S., Jourdan, J., Bechevet, B., Chaussy, D., Reverdy-Bruas, N., and Beneventi, D. (2014). "Influence of silver paste rheology and screen parameters on the front side metallization of silicon solar cell". *Mater Sci Semicond Process.*, 27, 790-799.
- Tiwari, A., and Wong, M.-S. (2020). "Role of oxygen partial pressure on structure and properties of sputtered transparent conducting films of La-doped BaSnO<sub>3</sub>". *Thin Solid Films*, 137986.
- Tolaymat, T. M., El Badawy, A. M., Genaidy, A., Scheckel, K. G., Luxton, T. P., and Suidan, M. (2010). "An evidence-based environmental perspective of manufactured silver nanoparticle in syntheses and applications: a systematic review and critical appraisal of peer-reviewed scientific papers". *Sci. Total Environ.*, 408(5), 999-1006.
- Trchová, M., and Stejskal, J. (2010). "The reduction of silver nitrate to metallic silver inside polyaniline nanotubes and on oligoaniline microspheres". *Synth. Met.*, 160(13-14), 1479-1486.
- Tshabalala, Z. P., Shingange, K., Cummings, F. R., Ntwaeaborwa, O. M., Mhlongo, G. H., and Motaung, D. E. (2017). "Ultra-sensitive and selective NH<sub>3</sub> room temperature gas sensing induced by manganese-doped titanium dioxide nanoparticles". *J. Colloid Interface Sci.*, 504, 371-386.
- Tsuji, M., Hikino, S., Sano, Y., and Horigome, M. (2009). "Preparation of Cu@ Ag core-shell nanoparticles using a two-step polyol process under bubbling of N<sub>2</sub> gas". *Chem. Lett.*, 38(6), 518-519.
- Tsuji, M., Hikino, S., Tanabe, R., Matsunaga, M., and Sano, Y. (2010). "Syntheses of Ag/Cu alloy and Ag/Cu alloy core Cu shell nanoparticles using a polyol method". *CrystEngComm.*, 12(11), 3900-3908.
- Tsuji, M., Hikino, S., Tanabe, R., and Yamaguchi, D. (2010). "Synthesis of Ag@ Cu Core-Shell Nanoparticles in High Yield Using a Polyol Method". *Chem. Lett.*, 39(4), 334-336.
- Tsuji, M., Miyamae, N., Lim, S., Kimura, K., Zhang, X., Hikino, S., and Nishio, M. (2006). "Crystal structures and growth mechanisms of Au@ Ag core-shell

nanoparticles prepared by the microwave– polyol method". *Cryst. Growth Des.*, 6(8), 1801-1807.

Tsuji, M., Yamaguchi, D., Matsunaga, M., and Alam, M. J. (2010). "Epitaxial Growth of Au@ Cu Core– Shell Nanocrystals Prepared Using the PVP-Assisted Polyol Reduction Method". *Cryst. Growth Des.*, 10(12), 5129-5135.

Ueda, Y. (1998). "Oxygen Nonstoichiometry, Structures, and Physical Properties of  $\text{CaVO}_{3-\delta}$ : I. A Series of New Oxygen-Deficient Phases". *J. Solid State Chem.*, 135(1), 36-42.

Ureña-Begara, F., Crunteanu, A., and Raskin, J.-P. (2017). "Raman and XPS characterization of vanadium oxide thin films with temperature". *Appl. Surf. Sci.*, 403, 717-727.

Vahur, S., Teearu, A., Peets, P., Joosu, L., and Leito, I. (2016). "ATR-FT-IR spectral collection of conservation materials in the extended region of  $4000\text{-}80\text{ cm}^{-1}$ ". *Anal. Bioanal. Chem.*, 408(13), 3373-3379.

Varma, A., Mukasyan, A. S., Rogachev, A. S., and Manukyan, K. V. (2016). "Solution combustion synthesis of nanoscale materials". *Chem. Rev.*, 116(23), 14493-14586.

Venkateswarlu, K., Bose, A. C., and Rameshbabu, N. (2010). "X-ray peak broadening studies of nanocrystalline hydroxyapatite by Williamson–Hall analysis". *Physica B Condens. Matter.*, 405(20), 4256-4261.

Vest, R. (1986). "Material science of thick film technology". *Am. Ceram. Soc. Bull.*, 65(4), 631-636.

Viau, G., Piquemal, J.-Y., Esparrica, M., Ung, D., Chakroune, N., Warmont, F., and Fiévet, F. (2003). "Formation of assembled silver nanowires by reduction of silver thiolate in polyol/toluene medium". *ChemComm.*, (17), 2216-2217.

Vijayan, T., Chandramohan, R., Valanarasu, S., Thirumalai, J., and Subramanian, S. (2008). "Comparative investigation on nanocrystal structure, optical, and electrical properties of ZnO and Sr-doped ZnO thin films using chemical bath deposition method". *J. Mater. Sci.*, 43(6), 1776-1782.



- Viricelle, J.-P., Rivière, B., and Pijolat, C. (2005). "Optimization of SnO<sub>2</sub> screen-printing inks for gas sensor applications". *J. Eur. Ceram. Soc.*, 25(12), 2137-2140.
- Von Dollen, P., and Barnett, S. (2005). "A study of screen printed yttria-stabilized zirconia layers for Solid oxide fuel cells". *J. Am. Ceram. Soc.*, 88(12), 3361-3368.
- Vuong, N. M., Hieu, N. M., Hieu, H. N., Yi, H., Kim, D., Han, Y.-S., and Kim, M. (2014). "Ni<sub>2</sub>O<sub>3</sub>-decorated SnO<sub>2</sub> particulate films for methane gas sensors". *Sens. Actuators B Chem.*, 192, 327-333.
- Wagh, M., Jain, G., Patil, D., Patil, S., and Patil, L. (2006). "Modified zinc oxide thick film resistors as NH<sub>3</sub> gas sensor". *Sens. Actuators B Chem.*, 115(1), 128-133.
- Wang, C., Yin, L., Zhang, L., Xiang, D., and Gao, R. (2010). "Metal oxide gas sensors: sensitivity and influencing factors". *Sensors.*, 10(3), 2088-2106.
- Wang, J., Zou, B., Ruan, S., Zhao, J., and Wu, F. (2009). "Synthesis, characterization, and gas-sensing property for HCHO of Ag-doped In<sub>2</sub>O<sub>3</sub> nanocrystalline powders". *Mater. Chem. Phys.*, 117(2-3), 489-493.
- Wang, S. F., Dougherty, J. P., Huebner, W., and Pepin, J. G. (1994). "Silver-palladium thick-film conductors". *J. Am. Ceram. Soc.*, 77(12), 3051-3072.
- Wang, W., Guo, S., Lee, I., Ahmed, K., Zhong, J., Favors, Z., and Ozkan, C. S. (2014). "Hydrous ruthenium oxide nanoparticles anchored to graphene and carbon nanotube hybrid foam for supercapacitors". *Sci. Rep.*, 4, 4452.
- Waqas, H., Salman, M. S., Riaz, A., Riaz, N., and Shabbir, S. (2015). "Unique morphologies of zinc oxide synthesized by thermal decomposition and co-precipitation routes: Ultraviolet absorption and luminescence characteristics". *Cryst. Res. Technol.*, 50(5), 379-388.
- Wei, D., Huang, Z., Wang, L., Chuai, X., Zhang, S., and Lu, G. (2018). "Hydrothermal synthesis of Ce-doped hierarchical flower-like In<sub>2</sub>O<sub>3</sub> microspheres and their excellent gas-sensing properties". *Sens. Actuators B Chem.*, 255, 1211-1219.
- Wiley, B., Herricks, T., Sun, Y., and Xia, Y. (2004). "Polyol synthesis of silver nanoparticles: use of chloride and oxygen to promote the formation of single-crystal, truncated cubes and tetrahedrons". *Nano Lett.*, 4(9), 1733-1739.

Windischmann, H., and Mark, P. (1979). "A model for the operation of a thin-film SnO<sub>x</sub> conductance-modulation carbon monoxide sensor". *J. Electrochem. Soc.*, 126(4), 627.

Woo, H.-S., Na, C. W., Kim, I.-D., and Lee, J.-H. (2012). "Highly sensitive and selective trimethylamine sensor using one-dimensional ZnO–Cr<sub>2</sub>O<sub>3</sub> hetero-nanostructures". *Nanotechnology.*, 23(24), 245501.

Xi, L., Xiaoxun, L., Baokun, X., and Muyu, Z. (1992). "XPS study of adsorbed oxygen of nanocrystalline LaFeO<sub>3</sub> materials". *J. Alloys Compd.*, 186(2), 315-319.

Xiao, Y. (2001). Conductive ink composition. In: Google Patents.

Xing, R., Wang, X., Zhang, C., Wang, J., Zhang, Y., Song, Y., and Guo, Z. (2011). "Superparamagnetic magnetite nanocrystal clusters as potential magnetic carriers for the delivery of platinum anticancer drugs". *J. Mater. Chem.*, 21(30), 11142-11149.

Xiong, Y., Siekkinen, A. R., Wang, J., Yin, Y., Kim, M. J., and Xia, Y. (2007). "Synthesis of silver nanoplates at high yields by slowing down the polyol reduction of silver nitrate with polyacrylamide". *J. Mater. Chem.*, 17(25), 2600-2602.

Xu, C., Tamaki, J., Miura, N., and Yamazoe, N. (1991). "Grain size effects on gas sensitivity of porous SnO<sub>2</sub> -based elements". *Sens. Actuators B Chem.*, 3(2), 147-155.

Xu, J., Pan, Q., and Tian, Z. (2000). "Grain size control and gas sensing properties of ZnO gas sensor". *Sens. Actuators B Chem.*, 66(1-3), 277-279.

Yabuki, A., and Arriffin, N. (2010). "Electrical conductivity of copper nanoparticle thin films annealed at low temperature". *Thin Solid Films.*, 518, 7033-7037.

Yamazoe, N., Sakai, G., and Shimanoe, K. (2003). "Oxide semiconductor gas sensors". *Catalysis Surveys from Asia*, 7(1), 63-75.

Yang, K., Ma, J., Qiao, X., Cui, Y., Jia, L., and Wang, H. (2020). "Hierarchical Porous LaFeO<sub>3</sub> nanostructure for efficient trace detection of formaldehyde". *Sens. Actuators B Chem.*, 128022.

Yi, Z., Xu, X., Tan, X., Liu, L., Zhang, W., Yi, Y., and Duan, T. (2017). "Microwave-assisted polyol method rapid synthesis of high quality and yield Ag nanowires". *Surf. Coat. Technol.*, 327, 118-125.

- Yin, W., Lee, D.-H., Choi, J., Park, C., and Cho, S. M. (2008). "Screen printing of silver nanoparticle suspension for metal interconnects". *Korean J Chem Eng.*, 25(6), 1358-1361.
- Yoo, R., Güntner, A. T., Park, Y., Rim, H. J., Lee, H.-S., and Lee, W. (2019). "Sensing of acetone by Al-doped ZnO". *Sens. Actuators B Chem.*, 283, 107-115.
- Yoo, R., Li, D., Rim, H. J., Cho, S., Lee, H.-S., and Lee, W. (2018). "High sensitivity in Al-doped ZnO nanoparticles for detection of acetaldehyde". *Sens. Actuators B Chem.*, 266, 883-888.
- Yu, L., Guo, F., Liu, S., Yang, B., Jiang, Y., Qi, L., and Fan, X. (2016). "Both oxygen vacancies defects and porosity facilitated NO<sub>2</sub> gas sensing response in 2D ZnO nanowalls at room temperature". *J. Alloys Compd.*, 682, 352-356.
- Yun, J., Cho, K., Park, B., Kang, H. C., Ju, B.-K., and Kim, S. (2008). "Optical heating of ink-jet printable Ag and Ag–Cu nanoparticles". *Jpn. J. Appl. Phys.*, 47(6S), 5070.
- Zeng, Q., Cui, Y., Zhu, L., and Yao, Y. (2020). "Increasing oxygen vacancies at room temperature in SnO<sub>2</sub> for enhancing ethanol gas sensing". *Mater Sci Semicond Process.*, 111, 104962.
- Zeng, W., Liu, T., and Wang, Z. (2010). "Sensitivity improvement of TiO<sub>2</sub>-doped SnO<sub>2</sub> to volatile organic compounds". *Physica E Low Dimens. Syst. Nanostruct.*, 43(2), 633-638.
- Zhang, D., Li, C., Han, S., Liu, X., Tang, T., Jin, W., and Zhou, C. (2003). "Ultraviolet photodetection properties of indium oxide nanowires". *Appl. Phys. A.*, 77(1), 163-166.
- Zhang, H.-X., Siegert, U., Liu, R., and Cai, W.-B. (2009). "Facile fabrication of ultrafine copper nanoparticles in organic solvent". *Nanoscale Res. Lett.*, 4(7), 705-708.
- Zhang, W., Liu, T., Hu, X., and Gong, J. (2012). "Novel nanofibrous composite of chitosan–CaCO<sub>3</sub> fabricated by electrolytic biomineralization and its cell biocompatibility". *RSC Adv.*, 2(2), 514-519.
- Zhang, Y., Liu, Y., Zhou, L., Liu, D., Liu, F., Liu, F., and Lu, G. (2018). "The role of Ce doping in enhancing sensing performance of ZnO-based gas sensor by adjusting the proportion of oxygen species". *Sens. Actuators B Chem.*, 273, 991-998.

Zhang, Y., Zhu, P., Li, G., Zhao, T., Fu, X., Sun, R., and Wong, C.-p. (2014). "Facile preparation of monodisperse, impurity-free, and antioxidation copper nanoparticles on a large scale for application in conductive ink". *ACS Appl. Mater. Interfaces.*, 6(1), 560-567.

Zhao, J., Han, Z., Lu, H., Wang, X., and Chen, J. (2011). "Synthesis and photoluminescence properties of ZnO powder by solution combustion method". *J. Mater. Sci.: Mater. Electron.*, 22(9), 1361-1365.

Zhao, Q., Ju, D., Deng, X., Huang, J., Cao, B., and Xu, X. (2015). "Morphology-modulation of SnO<sub>2</sub> hierarchical architectures by Zn doping for glycol gas sensing and photocatalytic applications". *Sci. Rep.*, 5, 7874.

Zhao, T., Sun, R., Yu, S., Zhang, Z., Zhou, L., Huang, H., and Du, R. (2010). "Size-controlled preparation of silver nanoparticles by a modified polyol method". *Colloids Surf. A Physicochem. Eng. Asp.*, 366(1-3), 197-202.

Zhao, Y., Li, Y., Wan, W., Ren, X., and Zhao, H. (2018). "Surface defect and gas-sensing performance of the well-aligned Sm-doped SnO<sub>2</sub> nanoarrays". *Mater. Lett.*, 218, 22-26.

Zhao, Y., Zhang, Y., Li, Y., and Yan, Z. (2012). "Soft synthesis of single-crystal copper nanowires of various scales". *New J. Chem.*, 36(1), 130-138.

Zhu, L., and Zeng, W. (2017). "Room-temperature gas sensing of ZnO-based gas sensor: A review". *Sens. Actuator A Phys.*, 267, 242-261.

Zhu, Q., Xie, C., Li, H., Yang, C., Zhang, S., and Zeng, D. (2014). "Selectively enhanced UV and NIR photoluminescence from a degenerate ZnO nanorod array film". *J. Mater. Chem. C.*, 2(23), 4566-4580.

Zidi, N., Omeiri, S., Hadjarab, B., Bouguelia, A., Akroun, A., and Trari, M. (2010). "Transport properties and photo electrochemical characterization of oxygen-deficient A<sub>2</sub>SnO<sub>3-δ</sub> (A= Ca, Sr and Ba)". *Physica B Condens. Matter.*, 405(16), 3355-3359.

## LIST OF PUBLICATIONS AND CONFERENCES

### PUBLICATIONS

1. **G Manjunath**, P Nagaraju, Saumen Mandal. “Ultra-sensitive clogging free combustible molecular precursor-based screen-printed ZnO sensors: A detection of ammonia and formaldehyde breath markers”. Journal of Materials Science: Materials in Electronics 32 (2021) 5713.
2. **G Manjunath**, Robbi Vivek Vardhan, P Nagaraju, Saumen Mandal. “CeO<sub>2</sub> and RuO<sub>2</sub> -sensitized La<sub>x</sub>Ba<sub>1-x</sub>SnO<sub>3-δ</sub> (x = 0 and 0.05) screen printed sensor towards the detection of ammonia and formaldehyde gas at room temperature”. Applied Physics A: Materials & Processing 127 (2021) 116.
3. **G Manjunath**, P Nagaraju, Saumen Mandal. “A comparative study on enhancer and inhibitor of glycine nitrate combusted ZnO screen printed sensor: Detection of low concentration ammonia at room temperature”. Journal of Materials Science: Materials in Electronics 31 (2020) 10366.
4. **G Manjunath**, Sanjay Pujari, D. R. Patil, Saumen Mandal. “A scalable screen-printed high performance ZnO-UV and Gas Sensor: Effect of solution combustion”. Materials Science in Semiconductor Processing 107 (2020) 104828
5. **G Manjunath**, Pavan Pujar, Bikesh Gupta, Dipti Gupta, Saumen Mandal. “Low-temperature reducible particle-free screen-printable silver ink for the fabrication of high conductive electrodes”. Journal of Materials Science: Materials in Electronics 30 (2019) 18647.
6. **G Manjunath**, Robbie Vivek Vardhan, Ashritha Salian, Rashi Jagannatha, Mayank Kedia, Saumen Mandal, “Effect of annealing-temperature-assisted phase evolution on conductivity of solution combustion processed calcium vanadium oxide films”. Bulletin of Materials Science 41 (2018) 126.
7. **G Manjunath**, P Anusha, Ashritha Salian, Bikesh Gupta, Saumen Mandal, “Effect of O<sub>2</sub>, N<sub>2</sub> and H<sub>2</sub> on annealing of pad printed high conductive Ag–Cu nano-alloy electrodes”. Material Research Express 5 (2018) 014014.

## CONFERENCE PRESENTATIONS

1. **G Manjunath**, Sanjay P, D.R. Patil and Saumen Mandal “Screen printing of solution combustion processed ZnO - a promising UV and gas sensors”, Third International Conference on Advanced Materials (ICAM-2019) 9-11 August 2019, Mahatma Gandhi University, Kottayam, Kerala, India (Oral presentation).
2. **G Manjunath**, Bikesh Gupta and Saumen Mandal “A novel, cost-effective and efficient approach to screen printable silver conductor by direct reduction of initial precursor for printable electronics”, 5th International Conference on Nanoscience and Nanotechnology (ICONN-2019) SRM University, Kattankulathur, India (Oral presentation).
3. **G Manjunath**, Robbi Vivek Vardhan, Ashritha Salian, Rashi Jagannatha, Mayank Kedia, Saumen Mandal “Development of combustion synthesized high conductive calcium vanadium oxide ( $\text{CaVO}_3$ ) thin film electrodes”, International Conference on Nanoscience and Technology (ICONSAT-2018), March 21-23 2018, Bengaluru, India (Poster presentation).
4. **G Manjunath**, P Anusha, Ashritha Salian, Bikesh Gupta and Saumen Mandal, “Effect of  $\text{O}_2$ ,  $\text{N}_2$ , and  $\text{H}_2$  on annealing of pad printed high conductive Ag-Cu Nano-alloys electrodes”, International conference on Nanoscience and Nanotechnology (ICONN-2017), August 9-11, 2017, Chennai, India (Oral presentation).

## **BIO DATA**

Name : Manjunath G  
Father's name : Gangaiah. K  
Date of birth : 1<sup>st</sup> August 1987  
Permanent Address : #11, New channel road  
Appagere, Channapatna Taluk  
Ramanagram Dist- 562160  
Karnataka, India.  
Mobile : +91-9632854737  
E-mail : [manjunathg1857@gmail.com](mailto:manjunathg1857@gmail.com)

### **Academic qualification:**

Bachelor of Engineering (B.E.) in Mechanical Engineering from B.M.S. College of Engineering Bangalore, Karnataka (Overall aggregate- 67 %).

Mater of Technology (M. Tech) in Production Engineering and System Technology from National Institute of Engineering Mysore, Karnataka (CGPA: 8.79 out of 10).